IECO

Volume 7 No 4 Year 2024

- **Volume** 7
- **No** 4
- **Year** 2024

International Journal Of
Industrial Electronics Control and Optimization
IECO

University of
Sistan and Baluchestan

Iranian Association of
Electrical and Electronics Engineers

International Journal Of
Industrial Electronics Control and Optimization

In This Issue:

Research Articles:

About Journal

The University of Sistan and Baluchestan entered into strategic partnership with Iranian Association of Electrical and Electronic Engineers (IAEEE) to publish the **International Journal of Industrial Electronics Control and Optimization (IECO)**. The IECO is a refereed international journal which presents to the international scientific community important results of work in these fields, whether in the form of modeling simulation, analysis, fundamental research, development, application, design or real-time implementation. The scope of IECO is broad, encompassing all aspects of Industrial Electronics, Control and Optimization.

Note: International Journal of Industrial Electronics, Control and Optimization (IECO) has qualified to **ACADEMIC RESEARCH JOURNAL (ELMI-PAJOHESHI)** status certified by the ministry of Science, Research and Technology of Iran (No. 231566/3/18 dated 1396/10/09), and is published by the University of Sistan and Baluchestan through a formal partnership (No. 952/2/1500 dated 1395/11/04) with Iranian Association of Electrical and electronic Engineers (IAEEE) in order to develop scientific and research cooperation.

Aims and Scope

International Journal of Industrial Electronics, Control and Optimization (IECO) is a Peer reviewed journal of advanced and state-of-the-art in the science and engineering of Industrial Electronics, Control and Optimization. Its Scope encompasses the applications of Industrial Electronics, power systems, control, optimization and computational intelligence for the enhancement of industrial and manufacturing system and processes. The scope of the journal include the following:

I. Industrial Electronics

- Low and high-power converters
- Renewable energy
- Drive control techniques
- Techniques for advanced power semiconductor devices
- Power quality and utility applications
- Communications
- Flexible AC Transmission Systems (FACTS)
- Control in power electronics
- Electromagnetic and thermal performance of electronic power converters
- Motion control, robotics, sensors and actuators
- Fault detection and diagnosis
- Power systems
- Factory automation, communication, and computer networks

II. Control

- Adaptive control
- Control of process systems
- Control theory
- Data processing
- Design of control systems
- Hybrid systems
- Identification and observation
- Intelligent systems
- Model-predictive control
- Optimal control
- Robust control
- Fractional order systems

III. Optimization

- Ant Colony
- Chaos Theory
- Evolutionary Computing
- Fuzzy Computing
- Hybrid Methods
- Immunological Computing
- Neuro Computing
- Particle Swarm
- Probabilistic Computing
- Rough Sets
- Wavelet

Director-in-Charge:
Dr. S. Masoud Barakati

Editor-in-Chief
Dr. Gevork B. Gharehpetian

Editorial Board
Dr. S. Masoud Barakati- University of Sistan and Baluchestan
Dr. Gevork B. Gharehpetian- University of Technology (Tehran Polytechnic)
Dr. Ebrahim Babaei-University of Tabriz & Near East University
Dr. Seyyed Hossein Hosseini-University of Tabriz
Dr. Hasan Bevrani-University of Kordestan
Dr. Amirnaser Yazdani-Toronto Metropolitan University
Dr. Mehrdad Kazerani-Ryerson University
Dr. Hossein Askarian-Abyaneh-Amirkabir University of Technology (Tehran Polytechnic)
Dr. Hasan Monsef-University of Tehran
Dr. Massoud Rashidi Nejad-University of Shahid Bahonar Kerman
Dr. Mohammad Monfared- Ferdowsi University of Mashhad
Dr. Saeed Tavakoli-University of Sistan and Baluchestan
Dr. Mahmood Joorabian-Shahid Chamran University of Ahvaz
Dr. Mehri Mehrjoo-University of Sistan and Baluchestan
Dr. Mohammad Reza Aghaebrahimi- University of Birjand
Dr. Reza Ghazi-Ferdowsi University of Mashhad
Dr. Bin Wu- Toronto Metropolitan University
Dr. Tahere Fanaei Sheikhosleslami-University of Sistan and Baluchestan
Dr. Mahmoud Okati Sadegh-University of Sistan and Baluchestan

Assistant Editors
Dr. Ahmad khajeh-University of Sistan and Baluchestan
Dr. Hamde Torabi-University of Sistan and Baluchestan
Dr. Mojgan MollahassaniPour-University of Sistan and Baluchestan
Dr. Poria Jafari-University of Sistan and Baluchestan
Dr. Abbas-Ali Zamani-Technical and vocational University

IECO International Journal Of Industrial Electronics Control and Optimization
Print ISSN: 3517-2645
Online ISSN: 3568-2645
Homepage: https://ieco.usb.ac.ir/

Connectivity Maintenance of Nonlinear Multi-Agent Robotic System Subject to Minimizing Channel Path Attenuation

Sorush Akhlaghi [1] | Naser Pariz [1] | Mohammad Bagher Naghibi Sistani [1]

Engineering Faculty, Electrical Department, Ferdowsi University of Mashhad[1]
Corresponding author's email: n-pariz@um.ac.ir

Article Info

Article type:
Research Article

Article history:
Received: 07-February-2024
Received in revised form:
23-Jun-2024
Accepted: 20-July-2024
Published online: 21-Dec-2024

Keywords:
Multi-agent,
Connectivity maintenance,
Channel fading,
Sliding mode control.

ABSTRACT

In this paper, we address the problem of connectivity maintenance for a group of robots connected via wireless communication. We consider fading in the wireless channel between agents, where the exchange of information is possible at permissible distances. A distributed controller is designed to maintain the global connectivity of the network communication graph. On the other hand, obtaining the best communication quality between agents is the definition of good network connectivity. Therefore, the Laplacian matrix is defined as a weighted graph according to the communication parameters. Initially, the controller uses the supergradient algorithm to remake the network Laplacian matrix for having a greater second eigenvalue. While each agent in the network only has access to the neighbor's information. The control algorithm uses a multi-agent estimator to find the eigenvector corresponding to the second small eigenvalue. The formation problem has been considered in the second step after the reference topology has been obtained. Because of the nonlinear dynamics of the agents, the sliding mode controller has been used for this purpose. This robust controller could be a suitable choice due to the modeling and sensor measurement uncertainties. Finally, an example of multi-agent robots is provided to evaluate the algorithm.

I. Introduction

With the advancement of communication networks, multi-agent systems have been considered in many types of research and applications [1],[2],[3]. In these systems, independent units are interconnected and work together for various purposes. They consist of autonomous units, related to each other and working together to meet a common goal. e.g., the participation of a series of exploration robots or mobile sensor networks in an unknown area [4],[5]. Usually, in multi-agent systems, there are some limitations, and information is not always fully available to all agents. In a group of robots, it is assumed that each agent has access to data from its neighbors at certain intervals only depending on its place and conditions. Therefore, achieving network goals such as average consensus requires the permanent connection of the robot's set in a network.

Because of different plans that can be considered for agents and the existence of disturbances in the workplace, changes in network topology are always likely. In these systems, communication is limited only in the range of specific distances due to hardware limitations, and the movement of agents can cause changes in the communication graph [6],[7]. This problem makes it necessary to set a controller to keep the distances of the agents in an acceptable range. In this case, the controller is designed by assuming the initial connection of the communication graph to prevent the separation or collision of agents over time [8]. In some cases, arranging robots at certain intervals in a rigid network is the primary purpose [9],[10].

Keeping agents at a constant distance is not possible in many applications. For instance, in some cases, secondary goals in

Publisher: University of Sistan and Baluchestan

the group or obstacle avoidance purposes can make disturbing and stubborn agents [11],[12]. So, the continued maintenance of initial distances imposes many limitations on the agents. However, achieving global connectivity is usually a higher priority than local connectivity. Therefore, in many papers, the connectivity of agents has been studied and controlled according to global characteristics. The second small eigenvalue of the Laplacian matrix is used in the network connection graph to assess global communication [13]. In [14], connectivity in the graph is described as a Semidefinite Programming (SDP) problem. The optimal topology is determined for this optimization problem by considering some constraints.

Connectivity maintenance in distance-based networks has been reviewed in [15] which the states of agents are set to form the best possible communication graph. Due to the lack of access to information for each node in the distributed multi-agent systems, estimating the eigenvalues or eigenvectors is necessary for the global connectivity maintenance process. In [16], the distributed PI estimator and in [17], the decentralized Orthogonal Iteration Algorithm are used for this purpose. The dynamics of the agents in the multi-agent system can be different in modeling (linear or nonlinear). Accordingly, there are used lots of methods like [18],[19],[20] to maintain the connectivity of graph communications.

Multi-agent networks also have a great variety in terms of the type of agent communication. Numerous studies have been carried out on major problems such as packet loss and time delay [21]. In [22], the consensus problem in a multi-agent system is addressed, and the permissible delay boundaries are determined. Also, in [23], the formation control for a second-order multi-agent network, despite the delay in the channel, is designed. In [24], communication links are considered with the possibility of disruption, and the consensus problem is analyzed.

The use of wireless communication networks to exchange information in multi-agent systems is widely used [25],[26]. In this case, communication signals are always at risk of being lost, and part of it is usually converted to heat or absorbed by the environment. So, The received signal power at the receiver will differ from the transmitted power depending on the environment. One of the conventional models in wireless communication is the fading channel. The fading channel is usually modeled as a random time process. Many factors, such as geographic area and radio frequency, affect the fading channel.

Shadow and multipath propagation are two phenomena observed in the fading channel. Rayleigh model [27] is one of the models used in fading channels. In this model, changes and attenuation of the signal (communication quality) are modeled over time by changing the path loss power. So the fading phenomenon is related to the path losses that are increased by distance. In [28], fading channels are used in multi-agent systems, and sufficient condition for consensusability is given. Multipath propagation may cause some information to be lost, and the packet loss rate increases in the network.

In this paper, the connectivity problem for nonlinear multi-agent systems under fading channels is investigated. Due to the fading, the exchange of information is associated with errors, and it causes data loss. In other words, changing the distances between agents will change the channel's specification. So, we can define the connectivity maintenance problem based on achieving the best formation of agents. In this case, connectivity means placing the agents at desired distances to have the lowest information loss rate. With the distributed estimator, the controller in each agent determines the ideal distances to reach the best conditions over time. A robust sliding mode controller was used due to the nonlinear dynamics of the agents and the presence of uncertainties in modeling.

Additionally, this paper considers the fading effect in the communication between agents. In such a communication channel, the signal appears with varying degrees of attenuation, which can generally lead to non-convergence of the multi-agent system. The multi-agent system must be capable of establishing or strengthening effective communications between agents when necessary to maintain connectivity, thereby avoiding non-convergence or slower, weaker convergence; For this purpose, a sliding mode controller is used in this paper.

The remainder of the paper is organized as follows. Section 2 presents the Problem Formulation and introduces signal fading in the wireless communication network. It also describes the optimal topology to achieve the best connectivity conditions and provides the optimization solution with the supergradient algorithm. In Section 3, the design of the distributed controller is considered. A sliding mode controller is used to achieve the reference topology over the undirected graph, despite the presence of the fading effect.

The necessary and sufficient conditions for stability are also studied. In Section 4, the algorithm is tested by using numeric simulation in MATLAB software. Concluding remarks are drawn in Section 5.

II. Problem Formulation

A network consisting of N mobile robots is assumed with the directional graph $\mathcal{G} = (\mathcal{V}, \mathcal{E})$ that the robots form the graph nodes, and there is an edge between each connected robot. The set of nodes is $\mathcal{V} = \{1.2 \dots . n\}$ and the set of edges $\mathcal{E}$ consists of two subsets of $\mathcal{V}$ from the beginning and end of each edge. The existence of an edge between pairs $(i.j)$ is possible if j is at a certain distance.

$r_{ij} = \|x_i - x_j\|$ is the distance between two agents i and j in two dimensions, which can be connected in a wireless communication channel. Regardless of the disturbing agents in the communication channel, here, the phenomenon of communication path losses will be considered as a criterion for evaluating the quality of network communication. Path loss or path attenuation refers to the reduction in the power density of an electromagnetic wave as it propagates through space. Eq.(1) is used to compute the path loss.

$$P_{ij} = P_{L0} + 10\gamma \log(10)\left(\frac{r_{ij}}{r_0}\right) \tag{1}$$

In this equation, P_{L0} is the initial value of the path loss interference in reference distance r_0 . γ is the path loss exponent, and r_{ij} is the current distance between two agents in each dimension. Fig.1 shows this function relative to the changes in r_{ij}. For each agent within a range of less than r_0, the path loss power is assumed to be the lowest, and for further distances, this value increases slowly.

In this paper, the path losses, which are proportional to the network hardware equipment in the transmitter and receiver of an agent, are considered only in proportion to the distance of the agent to its neighbors. As a result, the adjacency matrix A, which represents the matrix of connections between robots in the graph is: $[\mathcal{A}(\mathcal{G})]_{ij} = P_{L0}/P_{ij}$.

The neighbors of ith agent are a subset of agents located in a circle with radius ρ and the center of ith agent. In other words, the C_i neighborhood is:

$$C_i \triangleq \{ j\epsilon\mathcal{V}, j \neq i : r_{ij} = \left\|x_i - x_j\right\| \leq \rho\} \tag{2}$$

Eq.(3) shows the Laplacian matrix $\mathcal{L}(z)$, which represents the network communication graph,

$$\mathcal{L}(x) = \mathcal{D}(x) - \mathcal{A}(x) \tag{3}$$

$\mathcal{D}(x)$ is the diagonal matrix and $\mathcal{D}_i = \sum_{j=1\ldots N} \mathcal{A}_{ij}$ are the main diagonal elements.

The dynamic of each agent in the network where $x_i \epsilon R^2$ and $u_i \epsilon R^2$ is as follows,

$$\dot{x}_i(t) = f(x_i) + u_i(t) \tag{4}$$

The state vector for all network agents is: $x_i = (y_{1i}, y_{2i})$, and $f(x_i) = [f_1(y_{1i}) \quad f_2(y_{2i})]^T$ is a generic nonlinear function of x_i and $\|f(x_i)\| \leq \tilde{\Upsilon}$, *where* $\tilde{\Upsilon}$ *is a positive scaller constant.*

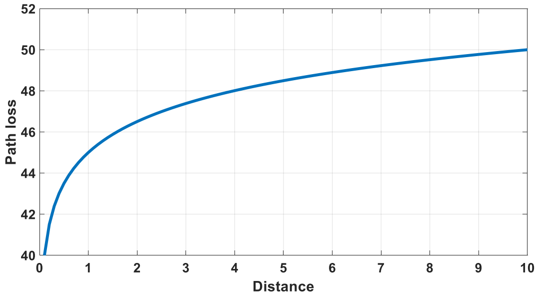

Fig. 1. The function $P(r_{ij})$ for $\gamma = 0.5$, $P_{L0} = 40$, $r_0 = 1$.

In an actual multi-agent system, agents often receive only partial or weakened information from their neighboring agents, rather than precise data. This occurrence can be described by the random attenuation of real-state information, meaning the true information is scaled by a random variable ranging between 0 and 1. This phenomenon is known as signal fading . In this study, signal fading is observed during transmission between followers, as described by the following fading model:

$$x_{ij} = \xi_{ij}\, x_j \tag{5}$$

Where x_{ij} represents the signal received by the i-th agent from its neighboring agent j. The fading effect of the transmission channel from agent j to agent i is captured by the random variable ξ_{ij}, which falls within the range (0, 1) and has a mean value of $\bar{\xi}$.

A. *Optimal Laplacian matrix*

Finding an optimal structure for the best second eigenvalue of the Laplacian matrix in the network, $\lambda(\mathcal{L})$, is considered in this Section. According to Eq.(1) and Eq.(2), this problem is expressed as follows,

$$\max_{L} \lambda_2(\mathcal{L}) \tag{6}$$

$\mathcal{L}^*$ is the answer to the above problem and determines the optimal topology During the process, this matrix is considered independent of states. It`s noted that $\lambda_2(\mathcal{L})$ is a concave function [15].

Hence the optimization problem (5) can be solved in the form of an SDP (Semidefinite program) problem. Here, the solution to the problem is in distributed form due to the necessity of using local control commands in agents. In other words, it is not possible to know the location of all agents for each of them, and every agent is able to make decisions using only the information of neighbors. The distributed supergradient optimization algorithm [29] can be a good choice for use in this algorithm.

Definition: Let F be a concave function from R^N to R. If $y \neq x$ and,

$$F(y) \leq F(x) + G^T(y - x) \tag{7}$$

The vector G is the supergradient of F in x. We can use the following updating rule by knowing the value of G in kth step,

$$x_{(k+1)} = x_{(k)} + \alpha_{(k)} G_{(k)} \tag{8}$$

$\alpha_{(k)} > 0$ is a constant coefficient.

According to the above definition, it is shown that the matrix $G = v_2 v_2^T$ is considered as a supergradient function for$\lambda_2(\mathcal{L})$ [15]. By assuming $\tilde{\mathcal{L}} \neq \mathcal{L}$ and $v_2 \epsilon 1^{\perp}$ the following equation holds,

$$\lambda_2(\tilde{\mathcal{L}}) \leq \lambda_2(\mathcal{L}) + < v_2 v_2^T . (\tilde{\mathcal{L}} - \mathcal{L}) > \tag{9}$$

And the L matrix update rule is specified as follows,

$$\mathcal{L}^*_{(k+1)} = \mathcal{L}^*_k + \alpha_{(k)} G_{(k)} \tag{10}$$

While each agent has access only to the neighbors, this rule must be defined in a distributed form. So, for computing the appropriate $\mathcal{L}(x)$ matrix, the agent only needs to update the values of one row of the matrix.

The vector $m = (m_{ij})$ is a part of matrix $\mathcal{L}$ is defined as follows,

$$m_{ij} = \mathcal{L}_{ij}. \quad i = 1.\cdots.N. \quad j > i \tag{11}$$

The matrix $\tilde{\mathcal{L}}_{ij}$ is considered for each pair $(i.j)$ with the elements of $\tilde{\mathcal{L}}_{ij_{ii}} = \tilde{\mathcal{L}}_{ij_{jj}} = -1$, $\tilde{\mathcal{L}}_{ij_{ij}} = \tilde{\mathcal{L}}_{ij_{ji}} = 1$, and other elements equal to zero. The Laplacian $\mathcal{L}$ matrix is:

$$\mathcal{L} = \sum_{j>i} \tilde{\mathcal{L}}_{ij}\, m_{ij}, \quad i = 1.\dots.N. \tag{12}$$

And the main optimization problem is expressed as follows,

$$max\, \lambda_2 \left(\sum_{j>i} \tilde{\mathcal{L}}_{ij}\, m_{ij} \right), \quad i = 1.\dots.N. \tag{13}$$

$$s.t. \quad -1 \leq m_{ij} \leq 0 \quad \forall (i.j)$$

As mentioned, $\lambda_2(p)$ is a concave function on m[15]. The supergradient vector corresponding to each m_{ij} is defined as follows,

$$G_{ij} = v_2^T \tilde{\mathcal{L}}_{ij} v_2 = -\left(v_{2i} - v_{2j}\right)^2 \tag{14}$$

The v_2 in a network must be estimated by each agent using available information. So, we can write the update rule similar to (7):

$$m^*_{ij,(k+1)} = m^*_{ij,(k)} + \alpha_{(k)} G_{ij,(k)} \tag{15}$$

$\alpha_{(k)}$ is the step-size coefficient, and $\mathrm{G}_{\mathrm{ij},(\mathrm{k})}$ is the function of the supergradient in the step k. The $m^*_{ij,(k+1)}$ should be on the feasible set of (12), and if $\alpha_k \mathrm{G}_{\mathrm{ij},(\mathrm{k})} \leq 0$, the update rule guarantees that the inequality $m^*_{ij,(k+1)} \leq m^*_{ij,(k)}$ is true. Therefore, to have a solution on a feasible set, $m^*_{ij,(k+1)} \geq -1$ must be met. It leads to the Eq. (15) [15].

$$p^*_{ij,(k+1)} = max(p^*_{ij,(k+1)}, -1) \tag{16}$$

The updated values are determined as follows,

$$\mathcal{L}^*_{ii,(k+1)} = -\sum_{j=1.j\neq i}^{N} \mathcal{L}^*_{ij,(k+1)} \quad .i = 1.\cdots.N \tag{17}$$

The above results show that each agent can find the related row values of the updated Laplacian matrix by using the supergradient algorithm. As can be seen, it is important to know the elements of the second eigenvector for ith agent and its neighbors. The following Section presents a method for estimating the second eigenvalue in a connected graph.

In the problem of eigenvalue estimation, the fading effect of the channel in the exchange between agents has been disregarded.

B. Decentralized power iteration

This section introduces an algorithm to estimate the second small eigenvalue (λ_2) for the weighted Laplacian matrix (3). During the process, it is assumed that $\mathcal{L}$ is approximately independent of the change in states. Since all eigenvalues of the Laplacian matrix ($\mathcal{L}$) are non-negative, the Power Iteration Algorithm can be used for $\mathrm{I} - \alpha\mathcal{L}$ with small and positive α-values to find the second small eigenvalue of a matrix [16].

The vector $\tilde{v} = (\tilde{v}^1 \dots \tilde{v}^n)^T \in R^n$ is assumed as an estimate of the eigenvector v_2. The algorithm includes the following three parts,

I. $\dot{\tilde{v}} = -Ave(\{\tilde{v}^i\})\mathbb{1}$

II. $\dot{\tilde{v}} = -\alpha\mathcal{L}\tilde{v}$

III. $\dot{\tilde{v}} = -(Ave(\{(\tilde{v}^i)^2\}) - 1)\tilde{v}$

Where $Ave(\{\tilde{v}^i\}) \triangleq (\sum_i \tilde{v}_i)/n$ and $\mathbb{1}$ is the eigenvector corresponding to the largest eigenvalue of the $\mathrm{I} - \alpha\mathrm{L}$ matrix. The first step is driving $\tilde{v}$ to the null space $\mathbb{1}$ (the space is spanned by eigenvectors $(v_2, \dots, v_n)$. For most of the initial values for $\tilde{v}$, the second step directs $\tilde{v}$ to the $v_1 = \mathbb{1}$, but if $\mathbb{1}^T\tilde{v} = 0$, $\tilde{v}$ converges to the second eigenvector v_2. The third step move $\tilde{v}$ to the sphere of radius $\sqrt{n}$ [16].

The three steps of this algorithm lead to the weighted equations as follows, where the weight parameters k_1, k_2, k_3 are scalar values.

$$\begin{aligned} \dot{\tilde{v}} = -k_1 Ave(\{\tilde{v}^i\})\mathbb{1} - k_2 L\tilde{v} \\ - k_3(Ave(\{(\tilde{v}^i)^2\}) - 1)\tilde{v} \end{aligned} \tag{18}$$

Theorem [16]: For each initial value $\tilde{v}(t_0)$ and the weights $k_1, k_2, k_3 > 0$, as long as $v^2\tilde{v}(t_0) \neq 0$, for system (17), where$\|\tilde{v}_2\| = \sqrt{n(\frac{k_3 - k_2\lambda_2}{k_3})}$, the following conditions for convergence λ_2 to the weight matrix L is necessary and sufficient.

$$\begin{aligned} k_1 > k_2\lambda_2 \\ k_3 > k_2\lambda_2 \end{aligned} \tag{19}$$

The estimate equation (18) requires access to all elements of $\tilde{v}$, but agent i only has access to some of them with local communication. Therefore, a decentralized algorithm should be proposed. In other words, the estimate of λ_2^i will be considered for each agent. The most critical problem in the power iteration algorithm is the Ave operator for $\tilde{v}^i$ and $(\tilde{v}^i)^2$. In [16], the average consensus PI estimator has been used to overcome this problem. Since there are two unknown average variables in (18), two estimators will be required.

This estimator is designed for n separate agents so that each agent can get the value of $a^i(t)$ to compute $\bar{a}(t) = \frac{1}{n}\sum_i a^i(t)$ by measuring using local connections. The PI estimator is considered as follows:

$$\begin{aligned} \dot{z}^i = \gamma(a^i - z^i) - K_p \sum_{j\in N_i(t)} (z^i - z^j) \\ + K_I \sum_{j\in N_i(t)} (w^i - w^j) \end{aligned} \tag{20}$$

$$\dot{w}^i = -K_I \sum_{j\in N_i(t)} (z^i - z^j)$$

$z^i \epsilon R^2$ is the average estimate, $z^i(1)$ for $Ave(\{\tilde{v}^i\})$ and $z^i(2)$ for $Ave(\{(\tilde{v}^i)^2\})$. K_p and K_I are estimator weights, and constant γ determines the effect of past information on the estimate. The estimator error is:

$$e^i(t) = x^i(t) - \frac{1}{n}\sum_{i=1}^{n} a^i(t) \tag{21}$$

In the proposed algorithm, the ith agent, according to the neighborhood radius and the number of adjacent agents, can have access to the variables $\{\tilde{v}^j, z^{j,1}, w^{j,1}, z^{j,2}, w^{j,2}\}$.

The second eigenvector $\tilde{v}$, the variable needed to build the supergradient function, is estimated by each agent. By estimating the unknown variables, the kth step of the supergradient algorithm to determine the optimal structure will be considered as follows,

I. Calculate the second small special value $\tilde{v}_i^{(k)}$ and receive $\tilde{v}_{j,(k)}$ from the neighbors
II. Update $G_{ij,(k)}$ values according to Equ.(13)
III. Update $\mathcal{L}^*_{ij,(k+1)}$ values according to Equ.(14) and Equ.(15).
IV. Update $\mathcal{L}^*_{ii,(k+1)}$ values according to Equ.(16)

III. Design decentralized controller

A decentralized controller will be required to move agents from their current state to the desired status. Defining the topology of the graph in the previous Section is performed without considering that the Laplacian matrix can be different by changing the position of the agents during the estimation process. Therefore, the movement of agents causes a constant error in elements of the Laplacian matrix in each step. So, the controller should be as fast as possible despite the input limitation and have a minimum steady-state error.

According to each $\mathcal{L}^*_{i,(k)}$, based on the definition of the Laplacian matrix Equ.(3) and the adjacency matrix, and the use of the inverse operator, the desired distance between the connected agents can be achieved as follows,

$$d_{ij,(k)} = A_{ij}^{-1}(\mathcal{L}^*_{ij,(k)}) \tag{22}$$

It should be noted that the connections between the agents are affected by the distance between them, or as mentioned in the introduction, the strength of communication and packet loss phenomenon in the network is different in various positions. It is possible that the reference values obtained for the distances Equ.(21), don't be in the detectable range of agents.

The agents in the multi-agent network should present at the appropriate distance from each other in the least possible time according to the desired topology in Equ.(21). We use the answer obtained from the optimization problem as a reference in the decentralized controller. In other words, the problem in this part will be as follows,

$$\min_{x_i} \left\| \mathcal{L}_i(x) - \mathcal{L}^*_{i,(k)} \right\|_2^2 \tag{23}$$

Where $\mathcal{L}_i(x)$ is the ith row of the Laplacian matrix, generally a function of system states. $\mathcal{L}^*_{i,(k)}$ is the row corresponding to the ith agent, which is estimated in the kth iteration from the previous Section optimization problem.

The sliding error $s_i(t)$ for every possible (i,j) is defined as the weighted sum function as follows,

$$s_i(t) = \sum_{j\in C} s_{ij}(t)\,, \qquad i = 1.\dots.N \tag{24}$$

Where,

$$s_{ij}(t) = \|r_{ij}\| - d_{ij,(k)}\,, \qquad j \in C \tag{25}$$

The sliding surface for all agents will generally be as follows,

$$S(t) = \begin{bmatrix} s_1(t) \\ s_2(t) \\ \vdots \\ s_N(t) \end{bmatrix} \tag{26}$$

It should be noted that the sliding surface is defined locally and in a distributed form. It is linear with respect to the $\mathcal{L}$ (Laplacian matrix). The reaching rule is defined as follows for the sliding mode controller,

$$\dot{s}_i(t) = \sum_{j\in C} \left(-\psi\, s_{ij}(t) - \phi\, sgn\left(s_{ij}(t)\right)\right) \tag{27}$$

By substituting Equ. (4) and with the assumption that the position changes of the neighbors are limited in each estimation run, $\dot{x}_j \cong 0, \quad \forall j \in C$, we get,

$$\begin{aligned} \dot{s}_i(t) &= \left(\sum_{j\in C} \nabla_{x_i}\left(s_{ij}(t)\right)\right)\left(f(x_i) + u_i(t)\right) \\ &= \sum_{j\in C}\Big(-\psi\, s_{ij}(t) \\ &\quad - \phi\, sgn\left(s_{ij}(t)\right)\Big) \end{aligned} \tag{28}$$

By rewriting the above relation, the control signal is written as follows.

$$\begin{aligned} u_i(t) = \Bigg(\sum_{j\in C} -\left(\nabla_{x_i}\left(s_{ij}(t)\right)\right)^{-1}\Big(-\psi\, s_{ij}(t) \\ - \phi\, sgn\left(s_{ij}(t)\right)\Big)\Bigg) - f(x_i) \end{aligned} \tag{29}$$

Theorem: Consider dynamics of the agents as Equ(4). With the distributed controller (29) and by setting parameters $\phi > 0$ and $\psi > 0$, the sliding surface $S(t) = 0$ in a finite time with the boundary $\sum_{j\in C} \left|s_{ij}(0)\right|$ is achievable.

Proof: The following Lyapunov function is a candidate for the networked system,

$$V(t) = \frac{1}{2}\, S(t)^T S(t) \tag{30}$$

By taking the derivative of Lyapunov's function,

$$\dot{V}(t) = S(t)^T . \dot{S}(t) \tag{31}$$
$$= \sum_{i \in N} \left(\sum_{j \in C} s_{ij}(t) . \sum_{j \in C} \left(-\psi \, s_{ij}(t) - \phi \, sgn\left(s_{ij}(t) \right) \right) \right)$$

By replacing the Equ.(23) and Equ.(25), we get,

$$\dot{V}(t) = \left(\sum_{j \in C} s_{ij}(t) \right)^T . \sum_{j \in C} \left(-\psi \, s_{ij}(t) - \phi \, sgn\left(s_{ij}(t) \right) \right) \tag{32}$$
$$\leq -\phi \sum_{j \in C} \frac{s_{ij}(t)^T \, s_{ij}(t)}{\left| s_{ij}\,(t) \right|}$$
$$\leq -\phi \sum_{j \in C} \left| s_{ij}\,(t) \right|$$

With the help of the above Lyapunov function and the appropriate selection the $\phi > 0$, the access time t_r at the boundary $\sum_{j \in \mathrm{C}} \left| s_{ij}\,(0) \right|$ is limited. It should be noted that achieving the better structure for the communication graph increases the convergence time in the control Section.

Theorem: Consider dynamics of the agents as Equ(4). In sliding phase, when $S(t) = 0$, the assumed system will converge to $\tilde{\mathcal{L}}^* \subset \mathcal{L}^*$.

Proof: As long as the matrix $\mathcal{L}$ is positive definite and,

$$S(t) = \mathcal{L} \sum_{j \in C} s_{ij}(t) = 0 \tag{33}$$

We can conclude the following equation.

$$\left\| r_{ij} \right\| - d_{ij,(k)} = 0 \,, \qquad j \in C \tag{34}$$

This equation shows that the two agents i and j are at the desired distance r_{ij}.

Theorem: Consider dynamics of the agents as Equ(4). In sliding phase, when $S(t) = 0$, the assumed system will converge to $\tilde{\mathcal{L}}^* \subset \mathcal{L}^*$.

Proof: As long as the matrix $\mathcal{L}$ is positive definite and,

$$S(t) = \mathcal{L} \sum_{j \in C} s_{ij}(t) = 0 \tag{35}$$

Considering the fading effect in the channel, the mathematical expression for r_{ij} is modified as follows:

$$\hat{r}_{ij} = \left\| x_i - x_{ij} \right\| \tag{36}$$

As a result,

$$\bar{s}_{ij}(t) = \left\| \hat{r}_{ij} \right\| - d_{ij,(k)} \tag{37}$$
$$= \left\| x_i - \xi_{ij} \, x_j \right\| - d_{ij,(k)}$$

In this case, by substituting the above expression into equation (28), the control signal is defined as follows:

$$u_i(t) = \left(\sum_{j \in C} - \left(\nabla_{x_i} \left(\bar{s}_{ij}(t) \right) \right)^{-1} \left(-\psi \, \bar{s}_{ij}(t) - \phi \, sgn\left(\bar{s}_{ij}(t) \right) \right) \right) - f(x_i) \tag{38}$$

To compensate for the impact of fading on the measured distance values, the new sliding surface is defined as follows using the mean value $\bar{\xi}$:

$$\hat{s}_{ij}(t) = 1/\,\bar{\xi} \ \left\| r_{ij} \right\| - d_{ij,(k)} \,, \qquad j \in C \tag{39}$$

The sliding error $s_i(t)$ for every possible (i, j) is defined as

$$\hat{s}_i(t) = \sum_{j \in C} \hat{s}_{ij}(t) \,, \qquad i = 1. \dots . N \tag{40}$$

And the sliding surface for all agents will generally be as follows,

$$\hat{S}(t) = \begin{bmatrix} \hat{s}_1(t) \\ \hat{s}_2(t) \\ \vdots \\ \hat{s}_N(t) \end{bmatrix} \tag{41}$$

To analyze the stability of the closed-loop system in the presence of measured values from neighboring nodes affected by fading channels, a control signal in the form of Equ(38) is proposed. By substituting this control signal into the sliding surface (41), the stability of the closed-loop system is guaranteed through the following theorem.

Theorem: Consider dynamics of the agents as Equ(4) and the sliding surface defined by Equ(41), With the distributed controller (38) and by setting parameters $\phi > 0$ and $\psi > 0$, the sliding surface $\hat{S}(t) = 0$ in a finite time with the boundary $\sum_{j \in \mathrm{C}} \left| \hat{s}_{ij}(0) \right|$ is achievable.

Proof: The following Lyapunov function is a candidate for the networked system,

$$V(t) = \frac{1}{2} \, \hat{S}(t)^T \hat{S}(t) \tag{42}$$

By taking the derivative of Lyapunov's function,

$$\dot{V}(t) = \hat{S}(t)^T . \dot{\hat{S}}(t) \tag{43}$$
$$= \sum_{\mathrm{i} \in \mathrm{N}} \left(\frac{1}{\bar{\xi}} \right)^2 \left(s_i(t) \left(-\psi \, \bar{s}_i(t) - \phi \, sgn\left(\bar{s}_i(t) \right) \right) \right)$$
$$= \sum_{\mathrm{i} \in \mathrm{N}} \left(\frac{1}{\bar{\xi}} \right)^2 \left(\left(-\psi \, s_i(t) \bar{s}_i(t) - \phi \, s_i(t) sgn\left(\bar{s}_i(t) \right) \right) \right)$$

Using Young's inequality for products with $\varepsilon_2, \varepsilon_2 > 0$, we have the following:

$$\dot{V}(t) = \sum_{i\in N}\left(\frac{1}{\bar{\bar{\xi}}}\right)^2\left(\left(-\frac{1}{\varepsilon_1}\,s_i(t)^2 - \frac{\psi^2}{\varepsilon_2}\,\bar{s}_i(t)^2 - \frac{1}{\varepsilon_1}\,s_i(t)^2 - \frac{\phi^2}{\varepsilon_2}\,sgn\left(\bar{s}_i(t)\right)^2\right)\right) < \sum_{i\in N}\left(\frac{1}{\bar{\bar{\xi}}}\right)^2\left(\left(-\frac{\psi}{\varepsilon_2}\,\bar{s}_i(t)^2\right)\right) \tag{44}$$

from (24) and (39), we have $E(s) = E(\hat{s})$. Take the expectation of both sides of the expression (18), we have,

$$E[\dot{V}(t)] \leq \sum_{i\in N}\frac{1}{\bar{\bar{\xi}}}\left(-\frac{\psi}{\varepsilon_2}\,E[V(t)]\right) \tag{45}$$

With the help of the above Lyapunov function and the appropriate selection the $\psi > 0$, the access time t_r at the boundary $\sum_{j\in C}\left|\hat{s}_{ij}\,(0)\right|$ is limited. It should be noted that achieving the better structure for the communication graph increases the convergence time of consensus in the multiagent system. Equ(45) shows that if $\hat{S}(t) \neq 0$, the trajectories outside the $\hat{S}(t) = 0$ will reach it in a limited time.

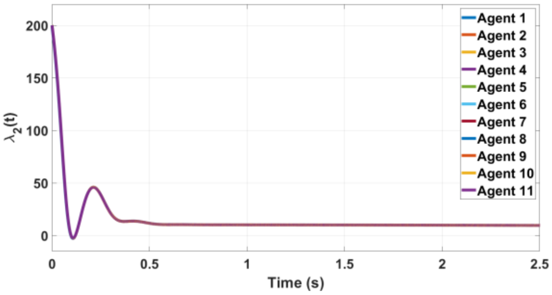

Fig. 2. The graph connectivity λ_2 estimated over time by each agent.

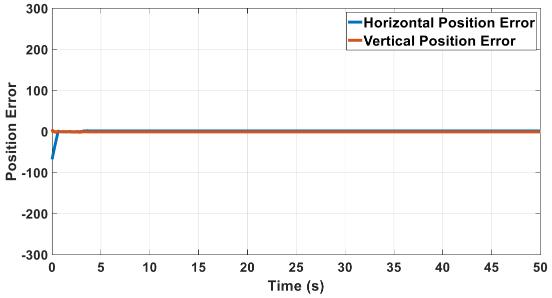

Fig. 3. The closed-loop tracking error for agent#5 under normal conditions, without considering fading in the communication channel.

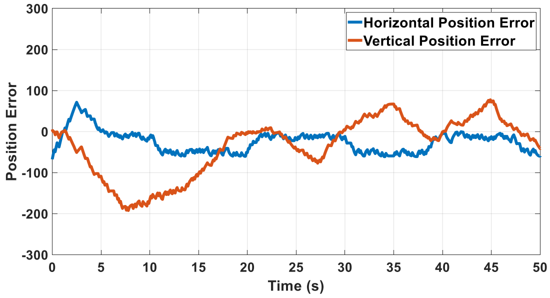

Fig. 4. The closed-loop tracking error for agent #5, considering fading in the communication channel, using conventional control similar to the [15].

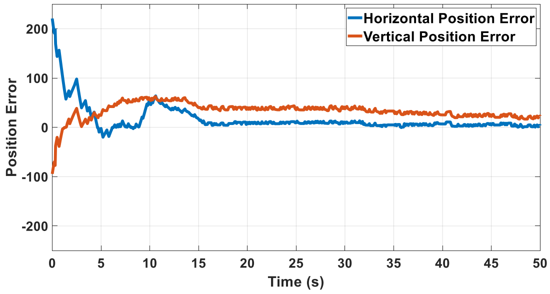

Fig. 5. The closed-loop tracking error for agent #5, considering fading in the communication channel, using the sliding mode controller.

In the above case, in general, there is no guarantee that all neighbors are available and the graph forms a tree, so the Therefore, the convergence study of the supergradient algorithm in the upper layer can be affected by the possible error.

In other words, the difference error between the Laplacian matrix and the desired matrix should not affect the convergence of the algorithm to find the optimal eigenvalue.

Assuming that $m^*_{(k+1)}$ is the updated vector in the matrix $L^*_{(k+1)}$ in the iteration $(k + 1)$ of the supergradient calculations because there is no guarantee to find non-neighboring agents, the formation leads to form the agents with the error ε.

In this case, instead of obtaining the vector $m^*_{(k+1)}$, we will reach the vector $\tilde{p}^{(k+1)}$, which is:

$$\tilde{m}_{(k+1)} = m^*_{(k+1)} + \varepsilon_{(k+1)} \tag{46}$$

$e_{(k+1)} = m^*_{(k+1)} - \mathrm{m}^*$ is the error of the supergradient algorithm relative to the final optimal value of m^*. It is shown that the assumed error will not affect the convergence of the estimator to the optimal value and the error between $\tilde{\mathrm{m}}_{(k+1)}$ and the optimal value m^* has a finite bound. The error between the optimal eigenvalue and the eigenvalue reached with the supergrdient algorithm can be defined as follows [15],

As a result, the error between the optimal eigenvalue and the eigenvalue reached with the supergrdient algorithm can be defined as:

$$\lambda_2^* - \lambda_2(\widetilde{m}_{(k)}) \leq \left\|\widetilde{m}_{(k)} - m^*\right\|^2 + \frac{\sum_{i=1}^{k}\left\|\square_{(i+1)}\right\|^2}{2\sum_{i=1}^{k}\alpha_{(i)}} + \frac{\sum_{i=1}^{k}\alpha_{(i)}{}^2\, g_{(i)}}{2\sum_{i=1}^{k}\alpha_{(i)}} \tag{47}$$

The difference between the eigenvalue obtained in k^{th} step with the desired optimal value is in a specific band by setting the square and summable values of $\alpha_{(i)}$ and assuming the norm of the supergradient function is bounded $\left\|\mathrm{G}_{\mathrm{ij},(\mathrm{k})}\right\| < \bar{G}$ and $\left\|\varepsilon_{(k)}\right\|$ is not divergent.

IV. Simulation results

In this Section, the proposed algorithm has been tested using simulation. A multi-agent system is composed of 11 autonomous agents. The maximum permissible range is $R = 10$, and the input signal changes in the range $-1 < U < 1$. The minimum distance is $r_0 = 1$. Assume the graph of the network is initially connected. By choosing $\alpha^{(k)} = \frac{1}{k+1}$ the algorithm is convergent.

The estimated signal of the second small eigenvalue λ for each agent can be seen in Fig.2. It can be seen that the estimates values of all agents converge to the algebraic connectivity of the graph.

Fig.3 shows the closed-loop tracking error for agent#5 under normal conditions, without considering fading in the communication channel. Fig.4 shows the closed-loop tracking error, considering fading in the communication channel, using conventional control similar to the [15] and Fig.5 shows the closed-loop tracking error, considering fading in the communication channel, using the sliding mode controller.

Fig. 6 shows the movement of agents over a period of time. As can be seen from the movement of robots, agents are moving towards more effective communication across the network. This is also shown in Fig. 7, where the second eigenvalue changes are plotted. The small second eigenvalue is $\lambda = 2$ in the first, and its final value is $\lambda = 9$.

In another example, the algorithm was investigated by considering uncontrollable agents in the network. The results are plotted in Fig. 8 and Fig. 9. In some iterations, due to inaccessible agents, the second small eigenvalue may decrease, but the final position of the agents eventually changes to improve the overall connectivity of the graph.

Compared to [15], the obtained results have more robustness to noise in controlling the position of agents. The algorithm of the mentioned article will not guarantee control and reach the optimal formation in every iteration.

Also, comparing the results with [28] and [30] shows that the use of sliding mode control can be effective in maintaining connectivity despite fading in communication channels.

In these papers, the subject of average consensus among agents has been discussed, which does not guarantee connectivity and convergence over time if the structure of the communication network is variable. The use of global preservation connectivity algorithm can be a guarantee of this.

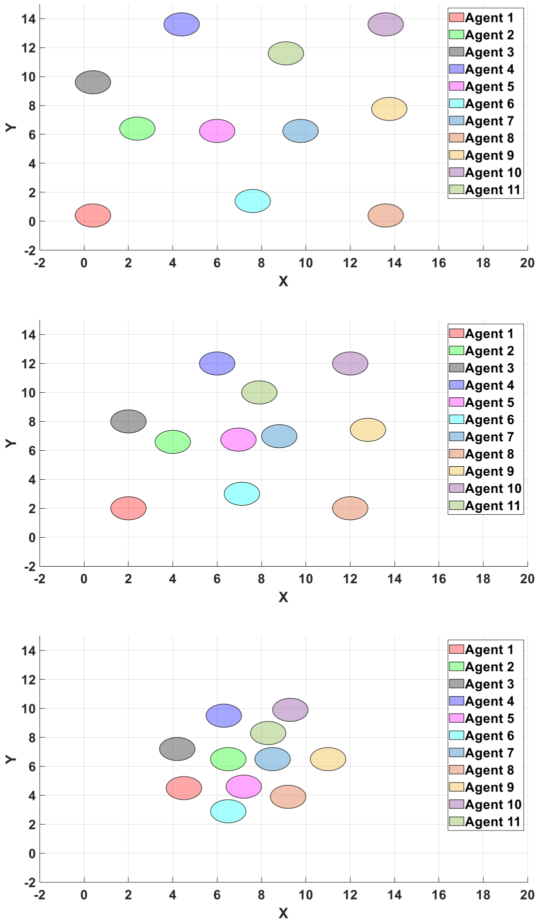

Fig. 6. Changes the position of agents on the plane in order to achieve the maximum second small eigenvalue.

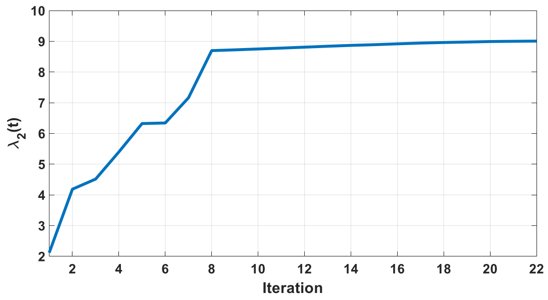

Fig. 7. Value of maximum second small eigenvalue $\lambda_2(t)$ during the first simulation.

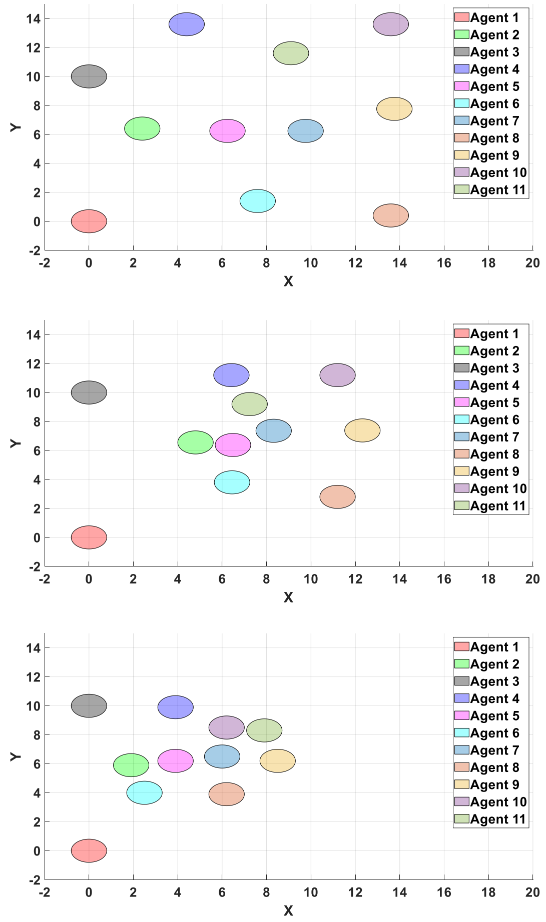

Fig. 8. Changes the position of agents on the plane by considering uncontrollable agents (Agent 1 and Agent 3).

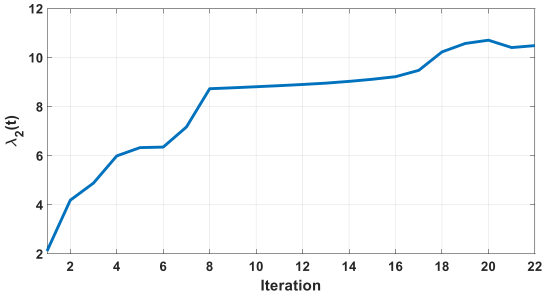

Fig. 9. Value of maximum second small eigenvalue $\lambda_2(t)$ during the second simulation.

I. Conclusion

In this paper, the problem of connectivity maintenance in a robotic multi-agent system with nonlinear dynamics was investigated. Wireless communication is used to exchange information, and according to the fading channel model for a wireless network, the quality of communication is in a specific range in the best condition to have the least packet lost. This goal is achieved by maximizing the second small eigenvalue of the Laplacian matrix $\mathcal{L}(x)$. Distributed sliding mode controller was designed to achieve the best topology for the information exchange. Finally, the results were evaluated through numerical simulations.

REFERENCES

[1] H. S. Ahn, Formation Control: Approaches for Distributed Agents: Springer International Publishing, 2019.

[2] S. Martínez and F. Bullo, "Optimal sensor placement and motion coordination for target tracking," Automatica, vol. 42, pp. 661-668, 2006/04/01/ 2006.

[3] M. Otte, M. J. Kuhlman, and D. Sofge, "Auctions for multi-robot task allocation in communication limited environments," Autonomous Robots, vol. 44, pp. 547-584, 2020/03/01 2020.

[4] E. Olcay, J. Bodeit, and B. Lohmann, "Sensor-based Exploration of an Unknown Area with Multiple Mobile Agents," IFAC-PapersOnLine, vol. 53, pp. 9621-9627, 2020/01/01/ 2020.

[5] S. Rahili, J. Lu, W. Ren, and U. M. Al-Saggaf, "Distributed Coverage Control of Mobile Sensor Networks in Unknown Environment Using Game Theory: Algorithms and Experiments," IEEE Transactions on Mobile Computing, vol. 17, pp. 1303-1313, 2018.

[6] J. Cortes, S. Martínez, and F. Bullo, "Robust Rendezvous for Mobile Autonomous Agents via Proximity Graphs in Arbitrary Dimensions," Automatic Control, IEEE Transactions on, vol. 51, pp. 1289-1298, 09/01 2006.

[7] S. Ponda, L. Johnson, A. Kopeikin, H.-L. Choi, and J. How, "Distributed Planning Strategies to Ensure Network Connectivity for Dynamic Heterogeneous Teams," Selected Areas in Communications, IEEE Journal on, vol. 30, pp. 861-869, 06/01 2012.

[8] H. Su, X. Wang, and G. Chen, "A connectivity-preserving flocking algorithm for multi-agent systems based only on position measurements," International Journal of Control, vol. 82, pp. 1334-1343, 2009/07/01 2009.

[9] D. Zelazo, A. Franchi, P. Allgöwer, H. Bülthoff, and P. Giordano, "Rigidity Maintenance Control for Multi-Robot Systems," 2012.

[10] D. Zelazo, A. Franchi, H. H. Bülthoff, and P. Robuffo Giordano, "Decentralized rigidity maintenance control with range measurements for multi-robot systems," The International Journal of Robotics Research, vol. 34, pp. 105-128, 2015/01/01 2014.

[11] L. Zhang, J. Wang, Z. Lin, L. Lin, Y. Chen, and B. He, "Distributed Cooperative Obstacle Avoidance for Mobile Robots Using Independent Virtual Center Points," Journal of Intelligent & Robotic Systems, vol. 98, pp. 791-805, 2020/06/01 2020.

[12] K. Khateri, M. Pourgholi, M. Montazeri, and L. Sabattini, "Effect of Stubborn Agents on Bounded Confidence Opinion Dynamic systems: Unanimity in Presence of Stubborn Agents," in 2019 27th Iranian Conference on Electrical Engineering (ICEE), 2019, pp. 875-880.

[13] C. D. G. G. Royle, C. Godsil, and G. F. Royle, Algebraic Graph Theory: Springer, 2001.

[14] R. Dai and M. Mesbahi, "Optimal topology design for dynamic networks," in 2011 50th IEEE Conference on Decision and Control and European Control Conference, 2011, pp. 1280-1285.

[15] M. C. D. Gennaro and A. Jadbabaie, "Decentralized Control of Connectivity for Multi-Agent Systems," in Proceedings of the 45th IEEE Conference on Decision and Control, 2006, pp. 3628-3633.

[16] P. Yang, R. A. Freeman, G. J. Gordon, K. M. Lynch, S. S.

Srinivasa, and R. Sukthankar, "Decentralized estimation and control of graph connectivity for mobile sensor networks," Automatica, vol. 46, pp. 390-396, 2010/02/01/ 2010.

[17] D. Kempe and F. McSherry, "A decentralized algorithm for spectral analysis," Journal of Computer and System Sciences, vol. 74, pp. 70-83, 2008/02/01/ 2008.

[18] X. Xue, X. Yue, and J. Yuan, "Connectivity preservation and collision avoidance control for spacecraft formation flying in the presence of multiple obstacles," Advances in Space Research, 2020/06/06/ 2020.

[19] S. J. Yoo and B. S. Park, "Connectivity-Preserving Approach for Distributed Adaptive Synchronized Tracking of Networked Uncertain Nonholonomic Mobile Robots," IEEE Transactions on Cybernetics, vol. 48, pp. 2598-2608, 2018.

[20] C. P. Bechlioulis and K. J. Kyriakopoulos, "Robust model-free formation control with prescribed performance and connectivity maintenance for nonlinear multi-agent systems," in 53rd IEEE Conference on Decision and Control, 2014, pp. 4509-4514.

[21] R. Olfati-Saber and R. M. Murray, "Consensus problems in networks of agents with switching topology and time-delays," IEEE Transactions on automatic control, vol. 49, pp. 1520-1533, 2004.

[22] Y. Zhang and Y.-P. Tian, "Allowable delay bound for consensus of linear multi-agent systems with communication delay," International Journal of Systems Science, vol. 45, pp. 2172-2181, 2014/10/03 2014.

[23] A. Nejadvali, R. Esfanjani, A. Farnam, and G. Crevecoeur, "Delay dependent criteria for the consensus of second-order multi-agent systems subject to communication delay," IET Control Theory and Applications, vol. 15, pp. 1-10, 05/07 2021.

[24] R. Mu and A. Wei, "Consensus disturbance rejection for linear multi-agent systems based on output feedback," in 2019 Chinese Control Conference (CCC), 2019, pp. 6094-6099.

[25] R. Carli, G. Como, P. Frasca, and F. Garin, "Distributed averaging on digital erasure networks," Automatica, vol. 47, pp. 115-121, 01/31 2011.

[26] J. Mou, Q. He, Z. Xia, and J. Wang, "Consensus of the Distributed Multiagent System with the Framework of the Small-World Network," Mathematical Problems in Engineering, vol. 2021, p. 6193508, 2021/02/15 2021.

[27] E. Carrillo, S. Yeotikar, S. Nayak, M. K. M. Jaffar, S. Azarm, J. W. Herrmann, et al., "Communication-Aware Multi-Agent Metareasoning for Decentralized Task Allocation," IEEE Access, vol. 9, pp. 98712-98730, 2021.

[28] X. Gu, T. Jia, and Y. Niu, "Consensus tracking for multi-agent systems subject to channel fading: a sliding mode control method," International Journal of Systems Science, vol. 51, pp. 1-9, 07/30 2020.

[29] S. Boyd, A. Ghosh, B. Prabhakar, and D. Shah, "Gossip algorithms: design, analysis and applications," in Proceedings IEEE 24th Annual Joint Conference of the IEEE Computer and Communications Societies., 2005, pp. 1653-1664 vol. 3.

[30] J. Li, Y. Niu and Y. Zou, "Sliding Mode Control for Networked Control System Under Fading Channels," 2019 IEEE Conference on Control Technology and Applications (CCTA), Hong Kong, China, 2019, pp. 561-566.

Sorush Akhlaghi received the B.S. degree in Electrical Engineering from Shahroud University, Semnan, Iran, in 2010, the M.S. degree at control engineering from the Shiraz University, Shiraz, Iran, in 2014. He is currently working toward the Ph.D. degree in electrical and computer engineering with Ferdowsi University of Mashhad, Mashhad, Iran. His research interests include control and optimization of multi-agent systems.

Naser Pariz received the B.S. and M.Sc degree in Electrical Engineering from Ferdowsi University of Mashhad, Iran, in 1988 and 1991 respectively. He received his Ph.D. from the Department of Electrical Engineering at Ferdowsi University of Mashhad in 2001. He is a Professor at Ferdowsi University. His research interests are nonlinear and control systems.

Mohammad Bagher Naghibi Sistani received the B.S. degree in electronics from the University of Tehran, Tehran, Iran, in 1991, the M.S. degree at control engineering from the University of Tehran, Tehran, Iran, in 1995, and the Ph.D. degree in control engineering from the Ferdowsi University of Mashhad, Iran, in 2005. He currently is Associate Professor at the Department of Electrical Engineering and Biomedical Engineering, Ferdowsi University of Mashhad. His research interests include reinforcement learning, soft computing, optimal control, multi- agent systems, and machine learning. He has published over 70 journal and conference papers.

IECO
International Journal Of
Industrial Electronics Control and Optimization
Print ISSN: 3517-2645
Online ISSN: 3568-2645
Homepage: https://ieco.usb.ac.ir/

An Optimal Self-Tuning Fuzzy Tilted Integral Derivative Controller for Load Frequency Control of Multi-Interconnected Power Plants

Morteza Janfaza[1] | Abbas-Ali Zamani[2]

Department of Electrical Engineering, Faculty of Engineering, University of Saravan, Saravan, Iran.[1]
Department of Electrical Engineering, National University of Skills (NUS), Tehran, Iran.[2]
Corresponding author's email: m.janfaza@saravan.ac.ir

Article Info

Article type:
Research Article

Article history:
Received: 02-June-2024
Received in revised form: 03-August-2024
Accepted: 06-August-2024
Published online: 21-Dec-2024

Keywords:
Load frequency control,
Multi-source power systems,
self-tuning fuzzy,
Renewable energy sources,
Tilted integral derivative.

ABSTRACT

A new framework for controlling load frequency in a complex, interconnected power system with multiple sources has been developed. This framework combines a fuzzy logic controller (FLC) and a tilted integral derivative (TID) controller, creating a self-tuning fuzzy tilted integral derivative (STFTID) controller. The purpose of this controller is to conduct and reduce load frequency perturbations during the operation of a multi-area interconnected multi-source power system. The STFTID controller is optimized using a particle swarm optimization algorithm to minimize the frequency fluctuations effectively. Investigations of the proposed STFTID controller were performed for power systems with generation units of a conventional system and renewable energy sources. In the design process of the STFTID controller, various nonlinearities, uncertainties, and fluctuations are considered to simulate practical challenges. These challenges include generation rate constraints, governor deadband, and communication time delays (as the sources of nonlinearity), as well as fluctuations caused by step load switching and the connection of renewable power plants to the system. The STFTID controller is compared with the proportional integral derivative (PID), titled integral derivative, and integral tilted-derivative (I-TD) controllers. Simulation results show that the developed STFTID controller significantly enhances the system frequency control under various applied conditions, including multi-step load perturbation, renewable power plant integration, communication time delays, and generation rate constraints.

I. Introduction

The power system has the critical task of maintaining a balance between the supply of electricity and the demand for it. This delicate balance can be influenced by uncertainties on either the demand side or the supply side. Moreover, hybrid power systems are designed to address the integration between conventional and renewable energy sources (RESs) for power generation. The discrepancies that may arise between the generation of electricity and its consumption may be increased in such cases, especially when the weather and daylight cause severe switching oscillations in the system's response. By integrating multiple RESs, such as wind and solar energy, these systems can improve overall efficiency and achieve an optimal balance in electricity generation [1, 2]. However, the connection of such systems to the power grid may introduce perturbations to the output frequency and power.

Nowadays, the new challenges that hybrid power systems face are unpredictable because of the intrinsically volatile nature of the RESs and the variations in power demand. Therefore, integrating the RESs into the power grid system

Publisher: University of Sistan and Baluchestan

decreases inertia, negatively affecting system stability in higher load frequency and power deviations. Conventional power-generating systems face such challenges, but they become more severe when RESs are added to the grid, impacting the reliability and safety of the power system [3, 4]. To maintain a steady grid frequency and manage the power distribution between various power system regions, it is crucial to have load frequency control (LFC) [5-8].

To control power systems, various control methods have been employed to address the LFC problem. These methods include robust control [9, 10], model predictive control [11, 12], fuzzy logic control [13, 14], and artificial intelligence control [15, 16]. Furthermore, PID controllers have attracted the attention of researchers due to their effectiveness and relatively simple implementation [17, 18]. However, determining the appropriate PID parameters can be challenging, especially when dealing with uncertain or nonlinear systems. This often requires trial-and-error techniques. To tackle this challenge, one can employ numerical optimization algorithms to calculate the best PID parameters [19-22]. Overcoming the fluctuations of real power and load angle of a synchronous generator in both transient and permanent conditions of the system and expanding the range of stable operation of the generator using a PID controller, is one of the important issues in power systems [19]. In [20], a PID controller is used to control the real output power and load angle of the synchronous generator, whose parameters are set using the genetic algorithm. The Harris Hawk optimization algorithm is used to optimally adjust the coefficients of the PID controller to control the load angle of a synchronous generator [21]. In [22], using an arithmetic optimization algorithm, PID controller coefficients are set with two approaches reducing the settling time and reducing the amount of overshoot of the step response to control the load angle of a three-phase synchronous generator.

Furthermore, there has been increased research focus on using fractional-order (FO) controllers in recent years. The reason behind such interest in FO controllers is their ability to expand the stability range and provide more flexibility in controller design [23, 24]. Specifically, the TID controller, which falls under the category of FO controllers, has been utilized to address LFC issues [25]. This controller effectively handles disturbances, meets the required specifications for the closed-loop system, and ensures a satisfactory level of robustness [25-27]. An optimal TID controller for the LFC problem is constructed in [28] by taking a cost function into account and applying a GA algorithm. For a two-area multi-source interlinked power system made up of thermal-hydro-gas generating units with nonlinearities, a cascade type of TID controller is suggested in [29]. In [30], an optimal TID controller is formed for the LFC problem of a multi-area networked reorganized power system. With the use of a hungry games search algorithm, the recommended TID controller settings are adjusted. However, a significant challenge in this research area remains unsolved: the controller parameters of the TID controller are considered fixed after optimization in the design phase and cannot be modified dynamically.

Several authors have recommended the utilization of the Fuzzy Logic Controller along with the conventional controllers to improve the performance of the LFC system [13, 14]. In a fuzzy control system, the input variables are usually represented by fuzzy sets. These sets consist of membership functions (MFs) that can be adjusted to obtain the desired efficiency of the system. Several algorithms have been proposed in the literature to modify the gains of the fuzzy controller, including the Whale Optimization Algorithm [31], the Ennoble Class Topper Algorithm [32], and the Particle Swarm Optimization (PSO) [13, 14]. Furthermore, for frequency stability in hybrid systems, a Fuzzy-PIDF controller has been presented based on the PSO algorithm and the Competition over Resources (COR) method [33]. Moreover, a fuzzy self-tuning PID controller has also been proposed for LFC that uses the Tribe-DE optimization method to handle parametric uncertainties and external disturbances. Previous fuzzy-based LFC structures have shown satisfactory system responsiveness. However, these controllers cannot be considered fully optimized because only the input and output scaling factors were optimized in these structures. Additionally, the limitations of the membership functions were solely determined based on the designer's expertise and may not be fully optimized [34].

This study introduces a new adaptive framework called the self-tuning fuzzy tilted integral derivative controller, dedicated to LFC of power systems. This controller addresses the issues with the FLC and TID controllers mentioned earlier. The STFTID parameters are adjusted using the PSO algorithm. Then, two-area interconnected power systems are considered to evaluate the performance of the proposed STFTID controller based on PSO: one system for conventional power generating systems and another for RESs. In the first two-area interconnected power system, each area consists of various traditional generation units (thermal, gas, and hydraulic power plants). In contrast, in the second one, renewable generation units (wind and solar power) are considered. The design of the proposed controller considers various nonlinearities in the system, including generation rate constraints, governor deadband, and communication time delays. It also addresses uncertainties in the fluctuations in load and RESs.

To validate the effectiveness of the STFTID controller, its performance is investigated by comparing it with other control techniques discussed in the literature, including the PID controller, TID controller, and I-TD controller. The I-TD controller is an improved version of the TID controller proposed for the LFC of a power system in [35-37]. The paper's contributions are summarized as follows.

- A load frequency control framework based on a self-tuning fuzzy tilted integral derivative controller is proposed.
- The proposed STFTID combines a fuzzy logic controller and a tilted integral derivative controller.
- A hybrid power system including various conventional generation units (thermal, gas, and hydraulic power plants), and renewable generation units (wind and solar power) is considered for evaluating the proposed STFTID.
- The performance assessments of the proposed STFTID controller are done taking into account various nonlinearities in the system, including generation rate constraints, governor deadband, and communication time delays.
- The performance of the proposed STFTID controller is compared with traditional PID, TID, and I-TD controllers.
- The improvement of performance indicators of the proposed STFTID controller was evaluated and shown during four different scenarios.

The organization of the remains of the paper is as follows: Section 2 introduces the description of the hybrid power system models investigated in this study. Section 3 describes the PSO algorithm used for optimization. Section 4 focuses on the structure of the proposed STFTID controller. In Section 5, the parameters of the system being studied are presented, as well as the definition of four different scenarios. Then, the proposed control method is numerically analyzed, and the improved performance of the proposed STFTID structure is studied and discussed for these scenarios. Finally, the conclusion is presented in the last section.

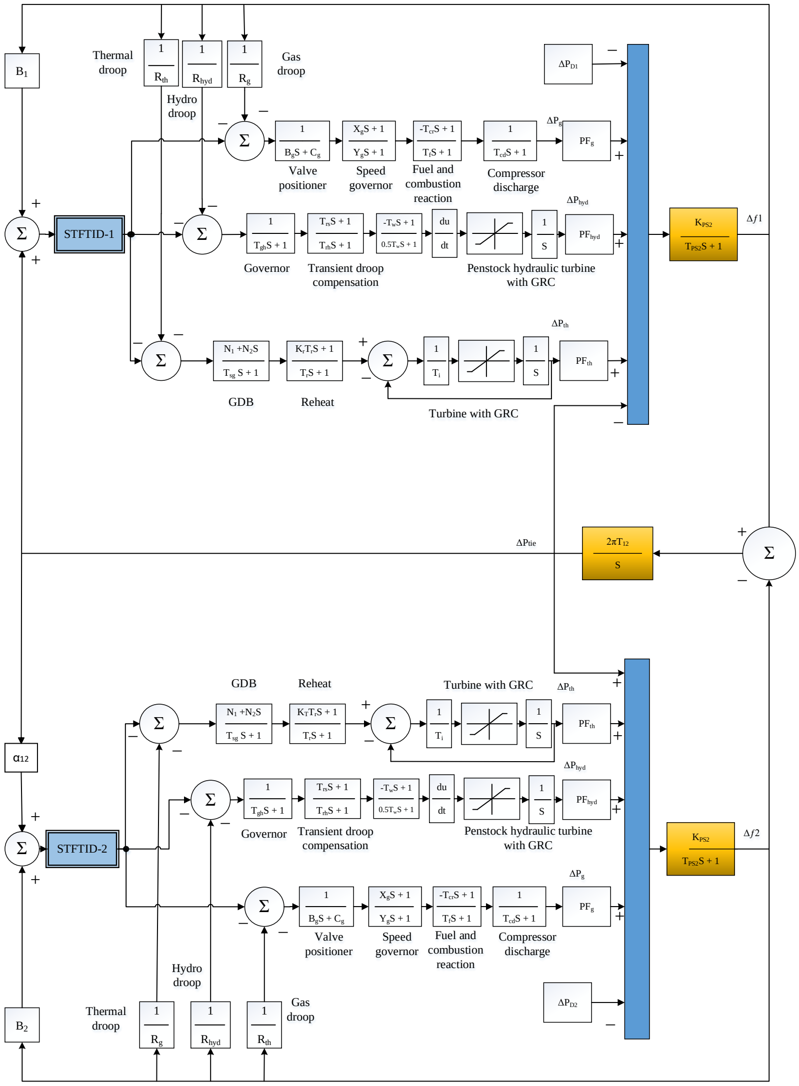

Fig. 1. The interconnected dynamic model for a two-area multi-source power system, including gas, hydro, and reheat thermal power plants.

II. Dynamic Modeling of the Studied Power System

Firstly, we have examined a two-area diverse-unit power system [35-37]. Fig.1 shows the MATLAB SIMULINK modeling structure used for this purpose. The assumption for this structure is presented here.

There are dedicated building blocks for different power plants in these areas, including i) gas, ii) hydro, and iii) reheat thermal power plants. The gas power plant contains transfer functions for the valve positioner, speed governor, fuel and combustion reaction, and compressor discharge. The transfer functions are shown in the building blocks of Fig. 1. The hydro power plant comprises its governor, transient droop compensator, and a penstock hydraulic turbine with a generation rate constraint (GRC). The reheat thermal power plant includes a governor deadband (GDB), and its transfer function provides the input for a turbine with a nonlinear steam turbine and a GRC.

GDB and GRC limit the capability of the power system to reject disturbances immediately. Therefore, reliable, realistic, and precise results depend on the considered physical constraints and multi-source power generations in each control unit/area. To study such effects, we define the GDB as a function of the sustained speed change magnitude resulting from mechanical frictions, valve overlaps in hydraulic relays, and backlash. It should be noted that the position of the valve in the thermal turbine is considered fixed. GDB prevents immediate reaction of the governor until the input reaches a specific value. This increases the fluctuations, and the stability of the power system reduces accordingly. Such an effect leads to sinusoidal oscillations with a fundamental frequency of 0.5 Hz. GDB equation nonlinearity may be decreased by variations in the speed/speed rate. The linear model for a GDB with 0.5% backlash can be written as Eq. 1.

$$GDB = \frac{N_1 + N_2 S}{T_{sg} S + 1} \tag{1}$$

This model is solved for N_1= 0.8 and N_2= -0.2/π for the reheat thermal power plant.

GRC allows for the maximum variations of the practical generation rate for both the hydro and thermal units. For the rising and falling rates of the hydro unit, generation variations of 270% and 360% are assumed, respectively, while a GRC of 10% is considered for the reheat thermal units [35-37].

The effects of renewable energy penetrations are modeled by dynamic blocks of a two-area power system for wind and solar energies, as shown in Fig. 2. These units are modeled based on the assumptions and considerations of Sections 2.1 and 2.2, respectively.

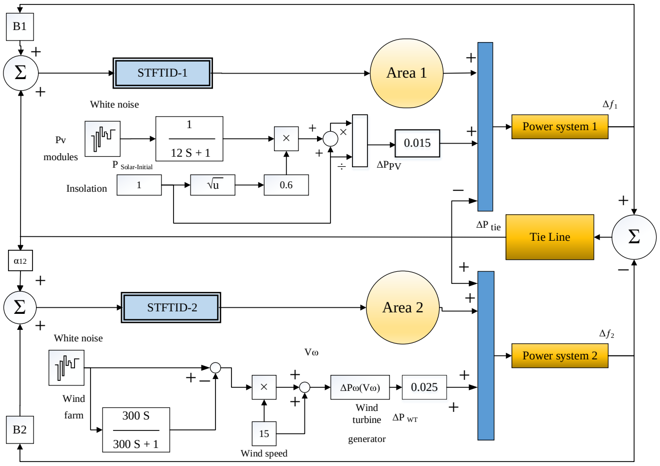

Fig. 2. The interconnected dynamic model for a two-area double-source power system, including PV and wind power plants.

A. PV System Model

The PV system is constantly affected by diverse environmental factors. Such factors, including seasonal changes in sun irradiation, variations in irradiation time during the 24-hour day, and weather conditions, should be considered. Additionally, the irregular output power of the PV systems generates significant frequency deviations, posing a threat to the stability of the system. Thus, careful consideration should be given to both the uniform and non-uniform deviations in insolation when estimating the output power of PV systems. To this end, the oscillated output power of this system is simulated using white noise. These variations are then added to the output power of the PV system [35-37]:

$$\Delta P_{Solar} = 0.6\sqrt{P_{Solar}} \tag{2}$$

B. Wind Generation Unit Model

The behavior of the wind is random as well. To account for this randomness, another white noise block is applied to multiply the wind speed. Consequently, the computed output power from the wind generation unit (P_W) is determined by equation (3) [35-37], where the density of air, the area swept by the rotor, and the wind-rated speed are represented as ρ, A_T, and V_W, respectively.

$$P_W = \frac{1}{2}\rho A_T V_W^3 C_P(\lambda, \beta) \tag{3}$$

Moreover, the parameter of the rotor blades is given by C_P as in (4);

$$C_P(\lambda, \beta) = C_1 \times \left(\frac{C_2}{\lambda_I} - C_3\beta - C_4\beta^2 - C_5\right) \times e^{\frac{C_6}{\lambda_I}} + C_7\lambda_T \tag{4}$$

Here, coefficients C_1 to C_7 represent the wind turbine parameters (see Table 1), and the pitch angle is β. Furthermore, λ_T and λ_I are the optimum tip-speed ratio (TSR) and the intermittent TSR, which can be calculated from (5) and (6):

$$\lambda_T = \lambda_T^{OP} = \frac{\omega_T \times r_T}{V_W} \tag{5}$$

$$\frac{1}{\lambda_I} = \frac{1}{\lambda_T + 0.08\beta} - \frac{0.035}{\beta^3 + 1} \tag{6}$$

In (5), ω_T and r_T are the rotational speed and the radius of the rotor, respectively. Therefore, P_W can be calculated as 750 kW for the coefficients of Table 1.

TABLE 1 THE PARAMETERS OF THE WIND GENERATION UNIT [35-37]

Coefficient	Value	Coefficient	Value
$\boldsymbol{C_1}$	−0.6175	ρ	1.225 Kg · m³
$\boldsymbol{C_2}$	116	A_T	1684 m²
$\boldsymbol{C_3}$	0.4	V_W	15 m/s
$\boldsymbol{C_4}$	0	r_T	22.9 m
$\boldsymbol{C_5}$	5	λ_T	22.5rpm
$\boldsymbol{C_6}$	21	P_W	750KW
$\boldsymbol{C_7}$	0.1405	P_W	750KW

The photovoltaic (PV) system and wind power plants of Fig. 2 are connected to areas 1 and 2, with power rates of 50 MW and 70 MW, respectively. The obtained output power deviations, calculated with the model for the PV power plant and the wind turbine, are shown in Fig. 3.

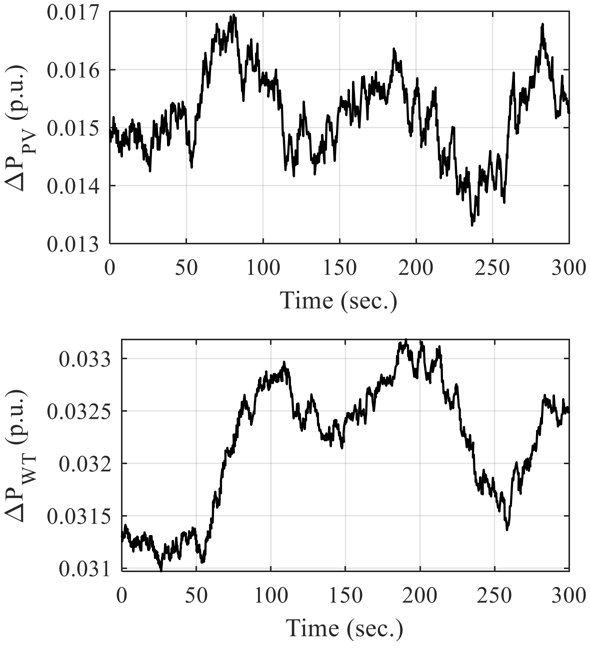

Fig. 3. The RESs output power deviations are calculated from the model shown in Fig. 2.

III. Particle Swarm Optimization Algorithm

PSO is an optimization technique in which a simplified social model simulates populations called swarms. Each population is composed of particles (similar to a bird's swarm), in which the particles fly through the problem space and look for the optimal position, just as a bird swarm searches for food. This evolutionary technique solves multiple conditions simultaneously and collaborates on the solutions to yield the final results. Each particle corrects its position based solely on the knowledge from its own experience and that of its neighbors. The initial population is random, while the algorithm updates the particles and populations in generations.

For an *N*-dimensional search space, particle *i* has N-dimensional position and velocity vectors, namely $x_i = (x_{i1}, x_{i2}, ..., x_{iN})$ and $v_i = (v\ v_{i1}, v_{i2}, ..., v_{iN})$, respectively. The objectives of the optimization problem monitor the fitness of particles, and the best position previously visited by particle i is considered as its best experience and indexed as $Pi = (p_{i1}, p_{i2}, ..., p_{iN})$, while the best position of the whole population is considered as the best global position, indexed as $G = (g\ g_1, g_2, ..., g_N)$.

Having data for each search step, i.e., x_i, v_i, P_i, and G, the new positions of each particle change according to the x and v vectors based on Eq. 7. In Eq. 7, w represents the inertia weight which controls the impact of the v vector from previous steps, r_j, and c_j are random variables (in the range of [0, 1]) and positive acceleration constants, respectively.

$$\begin{aligned} v_i(k+1) = w^2 v_i(k) + c_1 \cdot r_1 \\ \cdot (P_i(k) - x_i(k)) + c_2 \cdot r_2 \\ \cdot (G(k) - x_i(k)) \end{aligned} \tag{7}$$

$$x_i(k+1) = x_i(k) + v_i(k) \tag{8}$$

The velocity vector is limited in the range of [$-v_{\max}$, and $v_{\max}$], so that the particle's roaming outside the search space can be controlled, and excessive roaming is prevented.

IV. Proposed Self-Tuning Fuzzy Tilted Integral Derivative Controller

The most crucial aspect of operating an interconnected power system is ensuring frequency stability. Fluctuations in such systems arise from an imbalance between production and demand. In real-world scenarios, electrical loads within a power system are constantly changing. Consequently, the production rate must be carefully managed to maintain a sustained balance between production and demand. To achieve such a balance, the power system should be able to restructure the integration between the conventional power units and the RESs. In order to study the behavior of the operation and control of a power system, uncertainties should be considered during standard operational intervals. Various technical problems can be used to reduce system fluctuations and maintain a balanced production and demand cycle [1, 2]. The STFTID controller proposed in this section is a self-tuning fuzzy-based structure that utilizes a TID controller, as shown in Fig. 4.

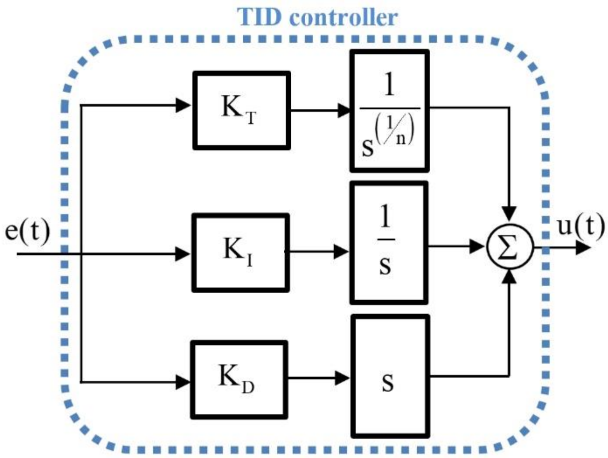

Fig. 4. The tilted integral derivative controller scheme.

The TID controller offers enhanced performance and control, with increased sensitivity to system parameter variations and improved disturbance rejection. System tuning is also made more accessible [27, 35, 38]. As is obvious from Fig. 4, the structure of the TID controller is similar to a PID, in which the proportional component is replaced by a titled integral derivative with a transfer function of $1/s^{1/n}$. In other words, for a PID controller, the transfer function is generally shown as (9), while it is modified as (10) for a TID.

$$PID = K_P + \frac{K_I}{S} + K_D S \tag{9}$$

$$TID = \frac{K_T}{S^{(1/n)}} + \frac{K_I}{S} + K_D S \tag{10}$$

With K_P, K_T, K_I, and K_D as the proportion, proportional tilt gain, integral, and differential coefficients, the transfer functions govern the controller systems. Moreover, the tilt fractional component is shown by n in (10) which may be tuned in the valid range of [1 10]. The modified system performance is a result of considering the tilt fractional component *n*, allowing the improved system performance to face disturbances and uncertainties. Therefore, the overall tuning process can be simplified. Additionally, a self-adjusting control structure is crucial in new power systems with diverse sources of uncertainty. Thus, a self-tuning fuzzy tilted-integral-derivative controller is proposed to regulate the load frequency, utilizing the advantageous TID controllers illustrated in Fig. 5. This STFTID structure is employed in a system comprising *i* regions.

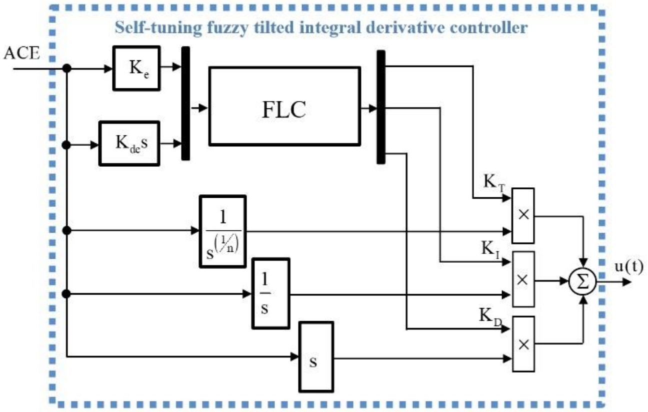

Fig. 5. The proposed optimal STFTID control structure.

The FLC block in the STFTID control structure of Fig. 5 is a Mamdani type, including two inputs and three outputs, which sets the values of the TID controller coefficients for areas in a self-tuning manner. Coefficients K_T, K_I, and K_D, get values based on the rules summarized in Table 2. In this table, NB, N, Z, and P show negative, zero, and positive values, respectively. In contrast, S, M, and B abbreviate small, middle, and significant values, and V is the acronym for the word "very".

TABLE 2 RULES FOR THE FUZZY CONTROLLER USED IN THE PROPOSED CONTROLLER.

K_T, K_I, K_D		$\frac{dACE}{dt}$						
		NB	NM	NS	Z	PS	PM	PB
ACE	NB	VB/VS/M	VB/VS/SM	B/S/S	B/S/VS	BM/SM/S	BM/M/SM	M/M/M
	NM	VB/VS/M	B/S/SM	B/S/S	BM/S/VS	BM/M/S	M/M/SM	SM/M/M
	NS	B/S/M	B/S/SM	BM/SM/S	BM/M/VS	M/M/S	SM/M/SM	SM/BM/M
	Z	B/S/BM	BM/SM/M	BM/M/SM	M/M/S	SM/M/SM	SM/BM/M	S/B/BM
	PS	BM/SM/B	BM/M/BM	M/M/M	SM/M/SM	SM/BM/M	S/B/BM	S/B/B
	PM	BM/M/VB	M/M/B	SM/M/BM	S/BM/M	S/B/BM	S/B/B	VS/VB/VB
	PB	M/M/VB	SM/M/B	SM/BM/B	S/B/BM	S/B/B	VS/VB/B	VS/VB/VB

The self-tuning manner of the STFTID controller of Fig. 4, working based on the rules applied by Table 2, updates the values of K_T, K_I, and K_D to feed the TID controller structure. This is repeated for each time step, while the value of parameter n and two scaling factors K_e and K_{de} are updated based on implementing the optimization process in these steps. The style of input membership functions for the fuzzy block is exhibited in Fig. 6.

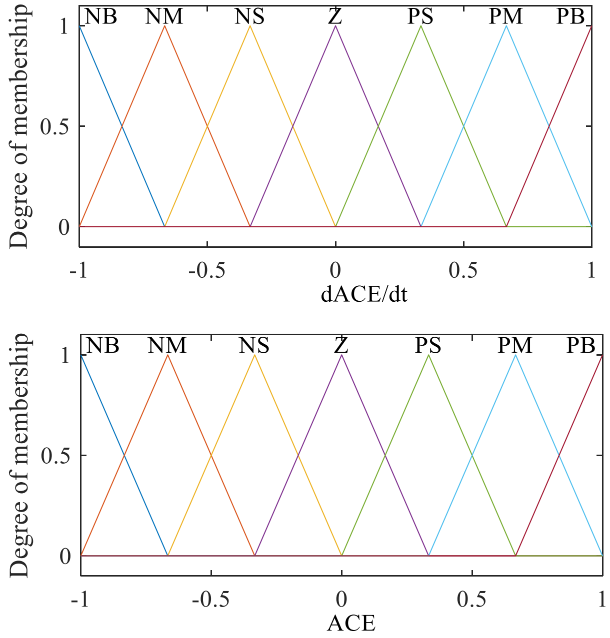

Fig. 6. The input MFs for the STFTID controller.

The K_T, K_I, and K_D represent the outputs from the fuzzy block. These MFs of the outputs are illustrated in Fig. 7, wherein B_T, B_I, and B_D are considered for the parameters of the upper bands. During the design process, a PSO algorithm can specify these parameters. When the values of B_T, B_I, and B_D are determined, the following equations are employed to calculate the magnitude of the output membership functions' centers.

$$\begin{aligned} a_1^i &= \frac{1}{6}B_i \\ a_2^i &= \frac{2}{6}B_i \\ a_3^i &= \frac{3}{6}B_i \\ a_4^i &= \frac{4}{6}B_i \\ a_5^i &= \frac{5}{6}B_i \end{aligned} \tag{11}$$

Here, index i is set as T, I, and D to satisfy all the necessary parameters. For the optimal design process in our proposed controller, a design vector X_D is used as shown in (12):

$$X_D = [B_T, B_I, B_D, K_e, K_{de}, n]. \tag{12}$$

To complete the optimization procedure, a cost function was also used in the STFTID controller based on (13).

$$G_c(X_D) = \int_{t=0}^{t=T_{sim}} t.((\Delta f_1)^2 + (\Delta f_2)^2 + (\Delta p_{tie})^2)dt \tag{13}$$

Finally, the design intervals for the parameters are considered based on (14).

$$\begin{aligned} &0 < B_T \leq 10 \\ &0 < B_I \leq 10 \\ &0 < B_D \leq 10 \\ &0 < K_e \leq 1 \\ &0 < K_{de} \leq 1 \\ &1 \leq n \leq 10 \end{aligned} \tag{14}$$

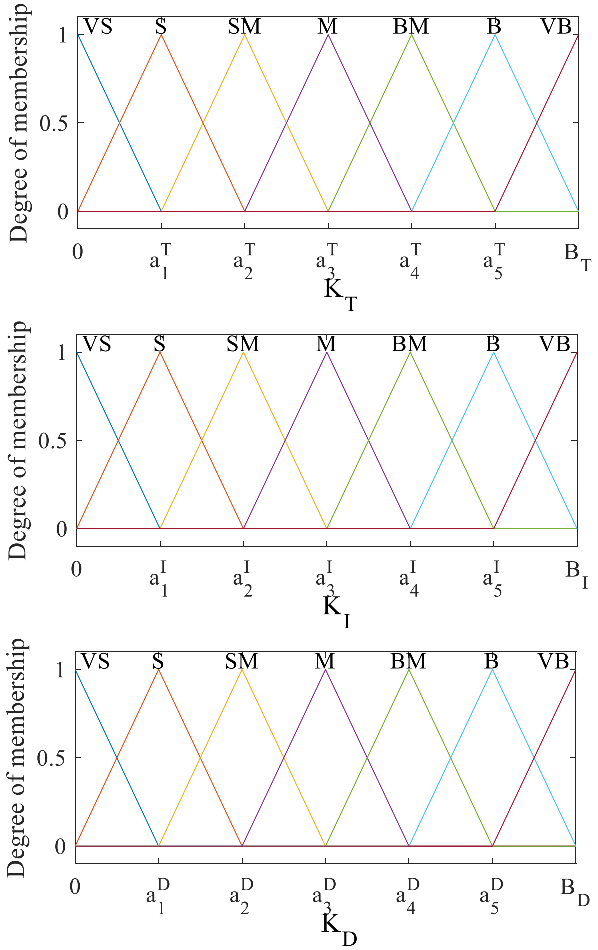

Fig. 7. The considered output membership functions for the STFTID controller.

V. Performance Validation and Simulation Results

To validate the performance of the proposed controller, four different scenarios were investigated and the results from the proposed STFTID controller were compared to [36-38]. The parameters of the hybrid power system are as follows: The governor speed regulation parameters of the gas, hydro, and thermal units are $R_g=R_{hyd}=R_{th}=2.4$. The first and second Fourier coefficients in the GDB transfer function are $N_1=0.8$ and $N_2=-0.2/\pi$, respectively. The time constants of the transient droop, Governor of the steam turbine, and steam turbine are $Trh=28.749$, $Tsg=0.06$, and $Tt=0.3$, respectively. The starting time of water in the hydro turbine, the steam turbine reheats constant, and the steam turbine reheat time constant are $T_w=1.1$, $K_r=0.3$, and $T_r=10.2$, respectively.

The first and second power system time constants are T_{ps1}=T_{ps2}=11.49. The first and second power system gains are K_{ps1}=K_{ps2}=68.965. The synchronizing coefficient is T_{12}=0.0433. The participation factors of gas, hydro, thermal, PV system, and wind generation units are PF_g=0.2873, PF_{hyd}=0.138, PF_{Th}=0.5747, PF_{pv}=0.015, and P_{FWT}=0.025, respectively. The lead and lag time constant of gas turbine governor are X_g=0.6, and Y_g=1.1. The time constant of the value positioner, Hydro turbine governor, and Compressor discharge volume are B_g=0.049, T_{gh}=0.2, and T_{cd}=0.2, respectively. The valve positioner, fuel time constant, and combustion reaction time delay of the gas turbine are C_g=1, T_f=0.239, and T_{cr}=0.01, respectively. The hydro turbine speed governor reset time and frequency bias coefficients are T_{rs}=4.9 and B_1=B_2=0.4312.

A. *First Scenario*

For the first scenario, we compared our proposed STFTID controller with the PID, TID, and I-TD controllers in [35], with a 1% step load only in the first area of the two-area power system shown in Fig. 1. The comparison was based on the parameters listed in Table 3 for the STFTID controller parameters.

TABLE 3 PARAMETERS OF THE PROPOSED STFTID CONTROLLER FOR THE FIRST SCENARIO

	B_T	B_I	B_D	K_e	K_{de}	n
Area-1	8.5316	9.0135	6.1037	0.3912	0.4692	2.1976
Area-2	5.9136	6.8601	4.0671	0.4168	0.5318	2.3671

The results of Fig. 8 confirm the convergence between the output of all considered controllers. As can be seen from the results of this figure, the characteristics of the TID and I-TD controllers are better than those of the PID. The STFTID performance is the best in terms of the maximum overshoot and undershoot (MO and MU), as well as the settling time (ST), rise time (RT), peak time (PT), and the index of the integral time square error (ITSE). To quantify these factors to evaluate of the dynamic system performance, they are summarized in Table 4.

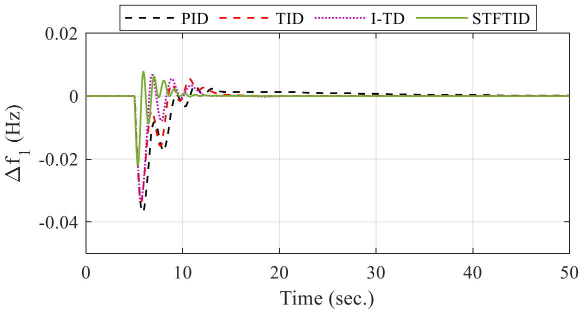

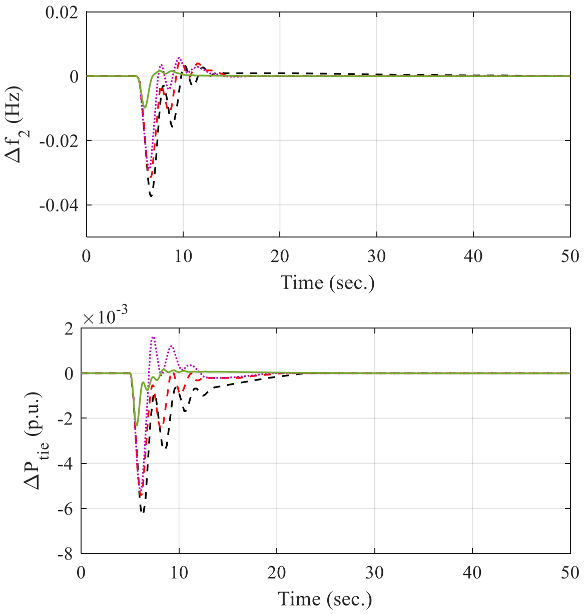

Fig. 8. The time history of the studied controllers for the first scenario.

TABLE 4 THE DYNAMIC SYSTEM PERFORMANCE INDICES FOR THE FIRST SCENARIO.

		PID	TID	I-TD	STFTID
Δf_1	ST	25	15	11	10
	MO	0.004	0.005	0.006	0.006
	MU	-0.04	-0.034	-0.033	-0.021
	RT	1.01	0.92	0.88	0.31
	PT	6.21	5.82	5.76	5.41
		PID	TID	I-TD	STFTID
Δf_2	ST	30	16	13	7.5
	MO	0.001	0.005	0.0051	0.001
	MU	-0.038	-0.031	-0.029	-0.010
	RT	1.28	0.94	0.90	0.26
	PT	6.76	6.11	5.98	5.54
		PID	TID	I-TD	STFTID
ΔP_{tie}	ST	20	25	25	8
	MO	0	0	0.002	0.0001
	MU	-0.006	-0.005	-0.005	-0.002
	RT	1.22	0.91	0.84	0.26
	PT	6.49	6.02	5.87	5.32
		PID	TID	I-TD	STFTID
ITSE		0.0056	0.0035	0.0022	0.0007

B. *Second Scenario*

To further evaluate the performance of the proposed STFTID controller, in the second scenario, we applied a multi-step load perturbation (MSLP) to area 1 of the two-area power system shown in Fig. 1 to simulate a more realistic situation. This MSLP, shown in Fig. 9, can represent a series of forced shutdowns occurring for the power-generating units, and unexpected loading switches. The results of the system's response are shown in Fig. 10 for different controllers, namely TID, I-TD, and STFTID, for this scenario.

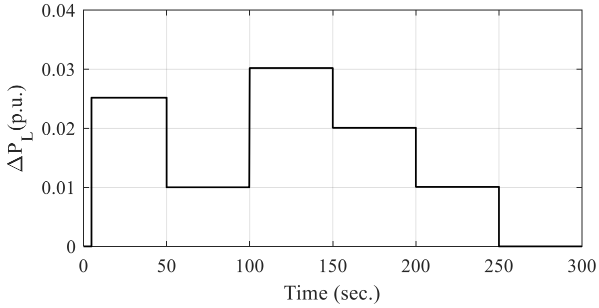

Fig. 9. The step load pattern for the second scenario.

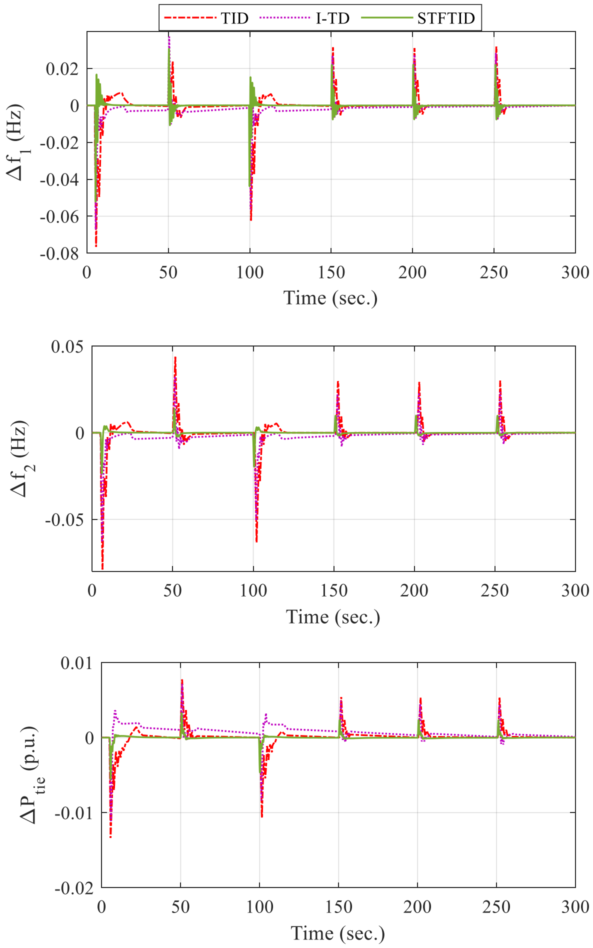

Fig. 10. The time history of the studied controllers for the second scenario.

The optimized parameters for the proposed STFTID are summarized in Table 5, whereas the dynamic system performance under this situation can be seen in Table 6. As is evident from Fig. 10 and Table 6, the best ST, MO, MU, RT, and PT are the results of the proposed STFTID, for all the loading variations of the applied MSLP. Therefore, this STFTID controller can be a practical, high-performance solution for the LFC problems, giving the best damping performance for the forced MSLP.

TABLE 5 PARAMETERS OF THE PROPOSED STFTID CONTROLLER FOR THE SECOND SCENARIO.

	B_T	B_I	B_D	K_e	K_{de}	n
Area-1	7.6319	8.9137	5.6186	0.4961	0.4169	2.9135
Area-2	5.3619	6.0371	3.9135	0.3916	0.4692	2.6912

TABLE 6 THE SYSTEM DYNAMIC PERFORMANCE INDICES FOR THE SECOND SCENARIO.

		TID	I-TD	TFTID
Δf_1	ST	20	200	10
	MO	0.05	0.03	0.03
	MU	-0.08	-0.07	-0.04
	RT	1.06	1.26	0.86
	PT	5.56	5.87	5.21
		TID	I-TD	STFTID
Δf_2	ST	20	200	9
	MO	0.05	0.03	0.010
	MU	-0.08	-0.06	-0.021
	RT	0.97	1.12	0.79
	PT	5.31	5.58	5.14
		TID	I-TD	STFTID
ΔP_{tie}	ST	30	200	10
	MO	0.008	0.007	0.001
	MU	− 0.014	− 0.01	-0.005
	RT	0.92	1.10	0.75
	PT	5.23	5.47	5.11
		TID	I-TD	STFTID
ITSE		35	25	3.11

C. Third Scenario

The third scenario compares the performance of three controllers, i.e. TID, I-TD, and STFTID, under load disturbances with various applied patterns, as shown in Fig. 11. This scenario evaluates the performance of the proposed STFTID for RES fluctuations in the interconnected dynamic model shown in Fig. 2. To this end, three controllers under investigation are examined for solar energy and wind penetrations, wherein the PV system and the wind power plants are connected to area 1 and 2, respectively, with rated powers of 50 and 70 MW. The parameters for the STFID controller are presented in Table 7 for this scenario, and the maximum iteration and search number agents are set to 50 and 10.

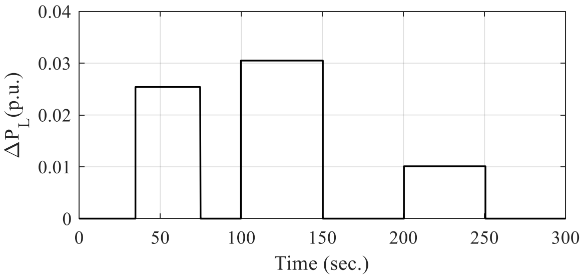

Fig. 11. The step load pattern for the third scenario.

TABLE 7 PARAMETERS OF THE PROPOSED STFTID CONTROLLER FOR THE THIRD SCENARIO.

	B_T	B_I	B_D	K_e	K_{de}	n
Area-1	4.3671	1.6138	2.9376	0.3371	0.4923	5.9637
Area-2	3.8613	1.3812	3.3682	0.4631	0.5037	2.6381

This time, the simulations, including controllers under series load disturbance in area 1, as shown in Fig. 11, are performed for the wind power plant and the PV system connected after 100 and 250 s, respectively. It should be noted that this figure represents the frequency deviations for the two-area model and the variations of the tie-line power under the second scenario. One can easily conclude from the results of Fig. 12 (summarized in Table 8) that severe oscillations occur during the multistep load and RES connection time intervals for the frequencies and tie-line power. However, the proposed controller performance is superior to the TID and I-TD controllers and can reduce the ST in Δf_2 and ΔP_{tie}. The TID performance is better for decreasing the ST for Δf_1. In all other evaluated parameters, i.e., MO, MU, and ITSE, the STFTID performance is superior to the TID and I-TD. In addition to this, the STFTID controller has better convergence compared to the other two controllers under investigation.

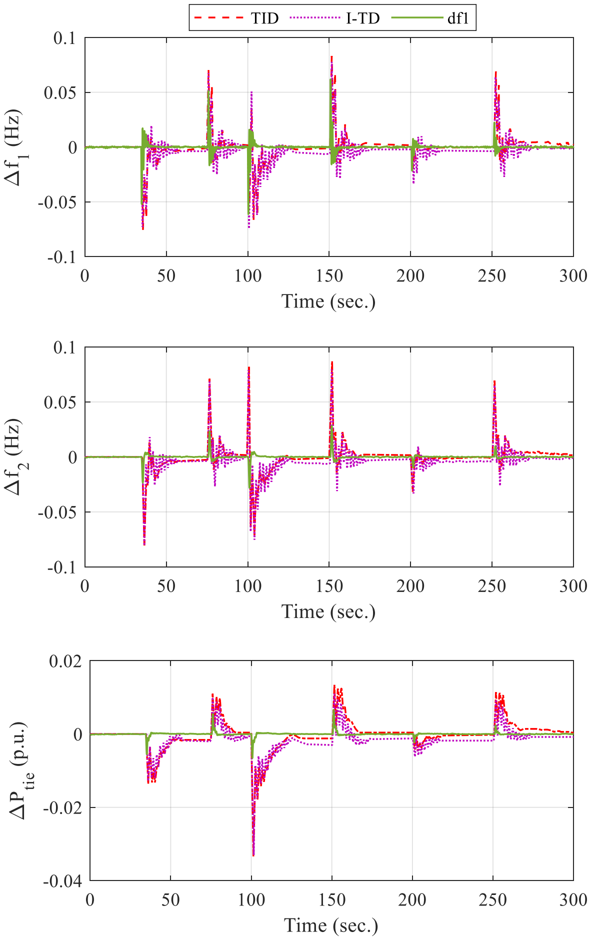

Fig. 12. The time history of the studied controllers for the third scenario.

TABLE 8 THE SYSTEM DYNAMIC PERFORMANCE INDICES FOR THE THIRD SCENARIO.

		TID	I-TD	STFTID
Δf_1	ST	120	150	150
	MO	0.07	0.06	0.05
	MU	-0.07	-0.06	-0.05
	RT	1.11	1.25	0.93
	PT	101.95	102.86	101.02
		TID	I-TD	STFTID
Δf_2	ST	120	150	101
	MO	0.07	0.06	0.021
	MU	-0.07	-0.06	-0.026
	RT	1.09	1.23	0.91
	PT	101.86	102.68	101.01
		TID	I-TD	STFTID
ΔP_{tie}	ST	120	150	102
	MO	0.012	0.01	0.005
	MU	-0.035	-0.035	-0.005
	RT	1.03	1.18	0.88
	PT	101.24	102.14	101.01
		TID	I-TD	STFTID
ITSE		28.12	23.45	12.55

D. Fourth Scenario

In our last scenario, a 0.1 s communication time delay (CTD) was introduced to the controller's output. Additionally, load disturbances of 0.01 and 0.05 p.u. were considered for areas 1 and 2, respectively. In this scenario, the PV system and wind turbines were connected after 80 and 220 seconds, respectively, and the load disturbances were applied to areas 1 and 2 after 10 and 150 seconds. Based on the parameters in Table 9, the STFTID was configured, and its results are shown in Fig. 13 for TID, I-TD, and STFTID controllers.

TABLE 9 PARAMETERS OF THE PROPOSED STFTID CONTROLLER FOR THE FOURTH SCENARIO.

	B_T	B_I	B_D	K_e	K_{de}	n
Area-1	2.1394	2.1835	3.9613	0.3687	0.5316	1.6631
Area-2	1.9385	1.8624	4.0136	0.4531	0.3286	1.8671

The perturbations in the output of the controller lead to oscillations of the system, as is evident in the frequency deviations of the two-area system, and the tie-line power response. Once again, the response of the proposed STFTID controller remains more stable, with significantly lower MO and MU values (see Table 10). However, the ST is also lower for the proposed controller than the TID and I-TD controllers.

From Fig. 13, it can be seen that more severe oscillations contribute to the system response at 150 and 220 s, while the step load disturbance in area 2 and the PV system connection occur. In both cases, the STFTID controller is more effective in dampening the oscillations. However, the TID shows worse performance.

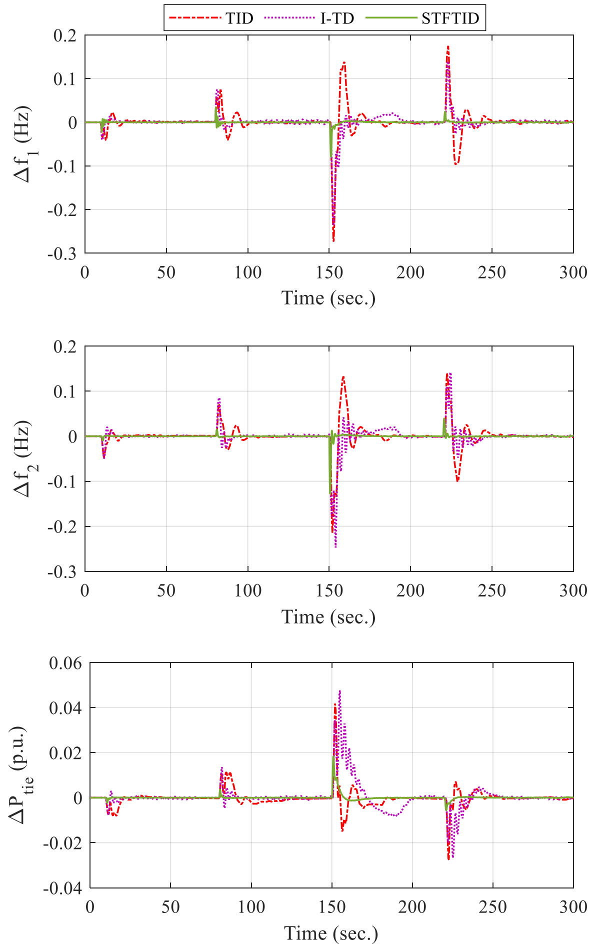

Fig. 13. The time history of the studied controllers for the fourth scenario.

TABLE 10 THE SYSTEM DYNAMIC PERFORMANCE INDICES FOR THE FOURTH SCENARIO.

		TID	I-TD	STFTID
Δf_1	ST	250	250	232
	MO	0.15	0.13	0.05
	MU	-0.29	-0.25	-0.07
	RT	1.23	1.34	1.11
	PT	152.92	152.98	151.09
		TID	I-TD	STFTID
Δf_2	ST	250	250	223
	MO	0.1	0.1	0.05
	MU	-0.25	-0.2	-0.11
	RT	1.21	1.26	1.09
	PT	152.65	152.71	151.05
		TID	I-TD	STFTID
ΔP_{tie}	ST	250	250	223
	MO	0.05	0.04	0.017
	MU	-0.02	-0.02	-0.005
	RT	1.18	1.20	1.02
	PT	152.13	152.16	150.98
		TID	I-TD	STFTID
ITSE		53.1	39.2	12.64

VI. Results and Discussion

The preceding part presents the results of four scenarios in which the performance of the proposed STFTID controller is compared with that of the PID, TID, and I-TD controllers [35-37]. This allows for an evaluation of the controller's performance. In conclusion, the suggested STFTID controller can reduce the ST, MO, MU, RT, PT, and ITSE in every scenario.

In the first scenario, for example, the STFTID controller reduced the ST index for Δf_1 to 60%, 33.3%, and 9.1%, respectively, compared to the PID, TID, and I-TD controllers. These reductions for the MU index are 47.5%, 38.2%, and 36.4%, in that order. In comparison to the PID, TID, and I-TD controllers, the RT index for Δf_2 was reduced by the STFTID controller to 79.7%, 72.3%, and 71.1%, respectively. The PT index for ΔP_{tie} fell to 18%, 11.6%, and 9.4%, while the ITSE index also decreased to 87.5%, 80%, and 68.2%, respectively.

The ST index for Δf_1 dropped to 50% and 95% compared to the TID and I-TD controllers for the second scenario, which involves imposing an MSLP onto area 1 of a two-area power system. The MU index for Δf_2 has been reduced by 73.8% and 65%, respectively. The STFTID controller decreased the RT index for ΔP_{tie} to 18.5% and 31.8%, respectively, in contrast to the TID and I-TD controllers. In addition to the ITSE index, which dropped to 91.1% and 87.5%, respectively.

The third scenario results in a reduction in the MO index for Δf_1 to 28.6% and 16.7%, respectively, when renewable power plants are taken into account. Compared to the TID and I-TD controllers, the STFTID controller reduced the MU index for Δf_2 to 62.9% and 56.7%, respectively. Apart from the ST index for ΔP_{tie}, which decreased to 15% and 32%, and the RT index fell to 14.6% and 25.4%, respectively. Also, the ITSE index fell to 55.3% and 46.5%, respectively.

In the fourth scenario, in addition to connecting the PV and wind power plants at different time steps, two-step load disturbances and a communication time delay were enforced. With a 66.7% and 61.5% drop in the MO index for Δf_1 compared to the TID and I-TD controllers, respectively, this scenario further demonstrates the superior performance of the STFTID controller. Apart from the MU index for Δf_2, which fell to 56% and 45%, respectively, there was a decrease in the ST index to 10.8% and 10.7%, a reduction in the RT index to 9.9% and 13.5%, respectively. Also, a significant decrease in the ITSE index to 76.2% and 67.8% was achieved, respectively. The findings collected from all scenarios show that the STFTID controller performs better than the PID, TID, and I-TD controllers in [35-37], despite having a more complex structure than the latter three kinds of controllers.

VII. Conclusions

A control structure is presented in this paper, a self-tuning fuzzy tilted integral derivative control structure, to control the load frequency response of a hybrid power system.

The hybrid power system contains different power plants, including conventional (gas, hydro, and thermal plants) and renewable (PV and wind turbine). Nonlinear factors such as generation rates, governor deadband, and communication time delays are considered for the system. To evaluate the performance of the proposed STFTID control system, we present the results of four scenarios in which the results of STFTID are compared with those achieved by PID, TID, and I-TD controllers, confirming the performance of the proposed system. In summary, this system can mitigate the settling time, rise time, peak time, maximum overshoot/undershoot, and integral time square error in all scenarios. The STFTID controller decreased the ITSE index compared to the PID, TID, and I-TD in the first scenario down to 87.5%, 80%, and 68.2%, respectively, where a 1% step load is only applied to the first area of a two-area power system. For the second scenario, in which a multi-step load perturbation is forced onto area 1 of a two-area power system, ITSE decreased to 91.1% and 87.5% compared to the TID and I-TD controllers. In the third scenario, considering renewable power plants, this parameter was reduced to 55.3% and 46.5%, respectively. In this scenario, load disturbances were applied with various rectangular functions at different time intervals, and wind and PV power plants were connected at different times. For the last scenario, a communication time delay and two-step load disturbances were forced onto the controller's output, in addition to connecting the PV and wind power plants at other time steps. This scenario also exhibits the better performance of the STFTID system, with a 76.2% and 67.8% reduction in the ITSE compared to the TID and I-TD controllers, respectively. Overall, the proposed STFTID controller presents more sustainability than other control methods.

REFERENCES

[1] Y. Arya, R. Ahmad, I. Nasiruddin, and M. F. Ahmer, "LFC performance advancement of two-area RES penetrated multi-source power system utilizing CES and a new CFOTID controller," Journal of Energy Storage, Vol. 87, p. 111366, 2024.

[2] R. Singh, J. Kumar, J. Singh, and G. S. Chaurasia, "Renewable Energy - Based Load Frequency Controller and Model with a Reduced Order for a Large - Scale Power System," Energy Technology, Vol. 12, No. 1, p. 2300618, 2024.

[3] M. Khamies, A. H. Elkasem, M. H. Hassan, and S. Kamel, "Enhancing frequency stability in diverse power systems with conventional and renewable energy sources based on an innovative LFC and controlled energy storage integration," Journal of Energy Storage, Vol. 73, p. 108960, 2023.

[4] S. Biswas, P. K. Roy, and K. Chatterjee, "FACTS-based 3DOF-PID controller for LFC of renewable power system under deregulation using GOA," IETE Journal of Research, Vol. 69, No. 3, p. 1486-1499, 2023.

[5] G. Wang, C. Wang, Q. Hao, and M. Shahidehpour, "Load Frequency Control Method for Cyber-Physical Power Systems with 100% Renewable Energy," IEEE Transactions on Power Systems, 2023.

[6] A. M. A. Soliman, M. Bahaa, and M. A. Mehanna, "PSO tuned interval type-2 fuzzy logic for load frequency control of two-area multi-source interconnected power system," Scientific Reports, Vol. 13, No. 1, p. 8724, 2023.

[7] M. Ranjan and R. Shankar, "A literature survey on load frequency control considering renewable energy integration in power system: Recent trends and future prospects," Journal of Energy Storage, Vol. 45, p. 103717, 2022.

[8] A. A. Abou El-Ela, R. A. El-Sehiemy, A. M. Shaheen, and A. E.-G. Diab, "Design of cascaded controller based on coyote optimizer for load frequency control in multi-area power systems with renewable sources," Control engineering practice, Vol. 121, p. 105058, 2022.

[9] P. Sharma and S. Neeli, "Computation of stability boundary locus of robust PID controller for time delayed LFC system," International Journal of Dynamics and Control, p. 1-11, 2023.

[10] J. Ansari, M. Homayounzade, and A. R. Abbasi, "Load frequency control in power systems by a robust backstepping sliding mode controller design," Energy Reports, Vol. 10, p. 1287-1298, 2023.

[11] F. Amiri and M. H. Moradi, "Improving the MPC performance of the model in order to improve the frequency stability of the two-area microgrid," International Journal of Industrial Electronics Control and Optimization, 2024.

[12] A. M. Taher et al., "Optimal model predictive control of energy storage devices for frequency stability of modern power systems," Journal of Energy Storage, Vol. 57, p. 106310, 2023.

[13] A. Karimi, Y. Jafarian, H. Bevrani, and R. Mirzaei, "Frequency response improvement in microgrids: a fuzzy–based virtual synchronous generator approach," International Journal of Industrial Electronics Control and Optimization, Vol. 3, No. 2, p. 147-158, 2020.

[14] J. Vinitha, G. Ramadas, and P. U. Rani, "PSO based fuzzy logic controller for load frequency control in EV charging station," Journal of Electrical Engineering & Technology, Vol. 19, No. 1, p. 193-208, 2024.

[15] A. Karimipouya, S. Karimi, and H. Abdi, "Microgrid frequency control using the virtual inertia and ANFIS-based Controller," International Journal of Industrial Electronics Control and Optimization, Vol. 2, No. 2, p. 145-154, 2019.

[16] R. K. Singh and V. Verma, "ANN-tuned PIDN controller for LFC with modified HVDC tie-line in deregulated environment," International Journal of Information Technology, Vol. 15, No. 8, p. 4193-4210, 2023.

[17] B. Dhanasekaran, J. Kaliannan, A. Baskaran, N. Dey, and J. M. R. Tavares, "Load frequency control assessment of a PSO-PID controller for a standalone multi-source power system," Technologies, Vol. 11, No. 1, p. 22, 2023.

[18] J. Biswas, P. Bera, and K. Chakrabarty, "Determination of control area and design of fuzzy rule-tuned PID controller for LFC of multimachine power system," Electric Power Systems Research, Vol. 221, p. 109411, 2023.

[19] S. Korram and H. R. ezadfar, "Use of genetic algorithm in optimal control of real power and load angle of synchronous generator," International conference on recent trends in engineering and materials science, 2016, Dubai, UAE, p. 1-15.

[20] S. M. Hosseini, R. Abdollahi, and M. Karrari, "Inclusive design and implementation of online load angle measurement for real-time transient stability improvement of a synchronous generator in a smart grid,"

IEEE Transactions on Industrial Electronics, Vol. 65, No. 11, p. 8966-8972, 2018.

[21] M. Abdolhosseini and R. Abdollahi, "Design of HHO-PID Controllers for Load Angle of Power Plant Synchronous Generators," International Transactions on Electrical Energy Systems, Vol. 2022, No. 1, p. 7746062, 2022.

[22] R. Abdollahi, "Modeling by order reducing the load angle of a three-phase synchronous generator and designing an AOA-PID controller to control the load angle," Journal of Modeling in Engineering, Vol. 21, p 83-99, 2023.

[23] R. Choudhary, J. Rai, and Y. Arya, "Cascade FOPI-FOPTID controller with energy storage devices for AGC performance advancement of electric power systems," Sustainable Energy Technologies and Assessments, Vol. 53, p. 102671, 2022.

[24] A. Kumar and S. Pan, "Design of fractional order PID controller for load frequency control system with communication delay," ISA transactions, Vol. 129, p. 138-149, 2022.

[25] P. N. Topno and S. Chanana, "Load frequency control of a two-area multi-source power system using a tilt integral derivative controller," Journal of Vibration and Control, Vol. 24, No. 1, p. 110-125, 2018.

[26] A. Rai and D. K. Das, "The development of a fuzzy tilt integral derivative controller based on the sailfish optimizer to solve load frequency control in a microgrid, incorporating energy storage systems," Journal of Energy Storage, Vol. 48, p. 103887, 2022.

[27] S. A. Kumar, M. S. S. Narayana, and K. J. Gowd, "Application of a TID Controller for the LFC of a Multi Area System using HGS Algorithm," Engineering, Technology & Applied Science Research, Vol. 13, No. 3, p. 10691-10697, 2023.

[28] S. Semwal, A. Mittal, S. Kumar, S. Goyal, and A. Singh, "Comparative Analysis of Two-Area Load Frequency Control Using Tilted-Integral-Derivative (TID) and Proportional-Integral-Derivative (PID) Controllers," in 2024 1st International Conference on Trends in Engineering Systems and Technologies (ICTEST), 2024: IEEE, pp. 1-5.

[29] S. Kumari and G. Shankar, "Design of SSA Tuned Cascaded TI-TID Controller for Load Frequency Control of Multi-Source Power System with Electric Vehicle," Industrial Control Systems, p. 255-283, 2024.

[30] S. A. Kumar, M. S. S. Narayana, and K. J. Gowd, "Application of a TID Controller for the LFC of a Multi Area System using HGS Algorithm," Engineering, Technology & Applied Science Research, Vol. 13, No. 3, p 10691-10697, 2023.

[31] N. C. Patel and M. K. Debnath, "Whale optimization algorithm tuned fuzzy integrated PI controller for LFC problem in thermal-hydro-wind interconnected system," in Applications of Computing, Automation and Wireless Systems in Electrical Engineering: Proceedings of MARC 2018, 2019: Springer, p. 67-77.

[32] A. Rai and D. K. Das, "Ennoble class topper optimization algorithm based fuzzy PI-PD controller for micro-grid," Applied Intelligence, Vol. 52, No. 6, p. 6623-6645, 2022.

[33] K. Ullah, A. Basit, Z. Ullah, S. Aslam, and H. Herodotou, "Automatic generation control strategies in conventional and modern power systems: A comprehensive overview," Energies, Vol. 14, No. 9, p. 2376, 2021.

[34] N. Jalali, H. Razmi, and H. Doagou-Mojarrad, "Optimized fuzzy self-tuning PID controller design based on Tribe-DE optimization algorithm and rule weight adjustment method for load frequency control of interconnected multi-area power systems," Applied Soft Computing, Vol. 93, p. 106424, 2020.

[35] M. Ahmed, G. Magdy, M. Khamies, and S. Kamel, "Modified TID controller for load frequency control of a two-area interconnected diverse-unit power system," International Journal of Electrical Power & Energy Systems, Vol. 135, p. 107528, 2022.

[36] J. Morsali, K. Zare, and M. T. Hagh, "Performance comparison of TCSC with TCPS and SSSC controllers in AGC of realistic interconnected multi-source power system," Ain shams engineering journal, Vol. 7, No. 1, p. 143-158, 2016.

[37] J. Morsali, K. Zare, and M. T. Hagh, "Comparative performance evaluation of fractional order controllers in LFC of two-area diverse-unit power system with considering GDB and GRC effects," Journal of electrical systems and Information Technology, Vol. 5, No. 3, p. 708-722, 2018.

[38] S. Tavakoli, A.-A. Zamani, and A. Khajehoddin, "Efficient load frequency control in multi-source interconnected power systems using an innovative intelligent control framework," Energy Reports, Vol. 11, p. 2805-2817, 2024.

Morteza Janfaza received B.S., M.S., and Ph.D. degrees in Electrical Engineering from the University of Sistan and Baluchestan, Zahedan, Iran, in 2011, 2013, and 2019, respectively. He is currently an assistant professor in the Departement of Electrical Engineering, Higher Education Complex of Saravan, Saravan, Iran. His current research interests include graphene, nano-optics, plasmonics, optoelectronic devices, nanoelectronics, and sensors.

Abbas-Ali Zamani was was born in 1986 in Isfahan, Iran. He earned a B.Sc. degree in electronic engineering from Hakim Sabzevari University in Iran in 2009, and an M.Sc. degree in control engineering from Isfahan University of Technology in 2011. In 2018, he received his Ph.D. in control engineering from the University of Sistan and Baluchestan in Iran. Dr. Zamani is currently an assistant professor in the Department of Electrical Engineering, National University of Skills (NUS), Tehran, Iran. Seismic control, power system control, smart grids, renewable energies, and artificial intelligence are among his research interests.

IECO

This page intentionally left blank.

IECO International Journal Of
Industrial Electronics Control and Optimization
Print ISSN: 3517-2645
Online ISSN: 3568-2645
Homepage: https://ieco.usb.ac.ir/

A Single Switch Transformer-Less DC-DC Converter with Continuous Input Current for Photovoltaic Applications

Sirous Toofan | Babak Fathipour | Ebrahim Babaei

Faculty of Electrical and Computer Engineering, University of Tabriz, Tabriz, Iran.
Corresponding author's email: s.toofan@tabrizu.ac.ir

Article Info

Article type:
Research Article

Article history:
Received: 29-March-2024
Received in revised form:
18-June-2024
Accepted: 20-June-2024
Published online:21-Dec-2024

Keywords:
Non-Isolated DC-DC Converter,
Maximum Power Point Tracking,
Continuous Input Current,
Turn Ratio Reduction.

ABSTRACT

In this paper, a single switch transformer-less DC-DC converter with continuous input current for photovoltaic applications is proposed. The suggested configuration utilizes a $CL^1C^2D^2$ structure to achieve a high voltage gain and alleviate voltage stress on the semiconductor components. The voltage gain of the proposed converter is enhanced through a reduction in the turn ratio of the coupled inductor, offering a significant benefit in minimizing the overall size of the converter. The reduction in the turns ratio of the coupled inductor results in lowered voltage stress on the semiconductor elements. Additionally, employing just one power switch in the converter simplifies control and reduces expenses. With its continuous input current, this converter is particularly well-suited for integration in photovoltaic systems. Simulation results conducted using PSCAD/EMTDC software validate the efficacy of the proposed power converter. Furthermore, the maximum power output of the photovoltaic module through an MPPT (Maximum Power Point Tracking) controller under varying irradiance levels is determined, and simulations are executed using PSCAD/EMTDC.

I. Introduction

Renewable energy technologies like solar (photovoltaic), fuel cells, and wind power are gaining popularity due to the increasing energy demands [1, 2]. This trend has spurred power industry professionals, organizations, and regulators to deepen their investigation of renewable energy sources [3, 4]. Solar PV panels primarily generate direct current (DC) with relatively low voltage levels. To efficiently elevate this voltage to higher levels, a high voltage conversion ratio converter is essential as an intermediary between the renewable energy source and the end user. A topology with high voltage gain, compact size, and low power losses is crucial for this task. DC-DC converters play a vital role in increasing voltage levels to match the load or DC bus requirements [5, 6]. Consequently, the development of high-voltage-gain converters has emerged as a significant solution to leverage renewable resources effectively [7, 8]. Various types of high-step-up DC-DC converters are being explored, broadly categorized into isolated and non-isolated classes for renewable energy applications [9, 10]. Non-isolated DC-DC converters offer advantages like smaller size, higher efficiency, and reduced production costs due to the absence of a transformer. In solar PV setups, DC-DC converters handle input voltage conversion from 12-60 V to a fixed output ranging from 24 V to 760 V. The demands for high-step-up DC-DC boost converters arise from the necessity for very high output voltages with limited input voltage ranges. It is critical for the DC-DC converters deployed in renewable energy systems to exhibit minimal input current ripple, as high ripple can reduce the lifespan of the solar panels and overall system efficiency. Hence, there arises a requirement for an appropriate input filter for the utilized DC-DC converter, and the filter used in these converters must be carefully selected to avoid an excessive increase in converter size and cost. Traditional DC-DC converters achieve high voltage gains through wide duty cycles,

Publisher: University of Sistan and Baluchestan

leading to increased conduction losses and electromagnetic interference (EMI) issues [11, 12]. Furthermore, the voltage gain is limited in practice due to power losses in switches/diodes and the equivalent series resistance of capacitors and inductors. The enhancement of voltage conversion ratio through the use of switched capacitors and/or switched inductor units has been a subject of research [13, 14]. However, concerns related to electromagnetic interference (EMI) impose limitations on voltage boosting due to high duty cycle levels. Additionally, operational challenges arise at high step-up voltage ratios, leading to increased current stress levels that can result in component failures and reduced element lifetime [15, 16]. To address these issues, alternative traditional DC-DC converters such as forward, push-pull, and fly-back converters can be employed by adjusting the transformer's turns ratio. Various isolated converters have been presented to achieve high voltage conversion ratios, but their implementation comes with increased cost and volume due to the isolated configuration. To mitigate these challenges, non-isolated DC-DC converters offer a viable solution, presenting advantages such as lower cost and smaller volume. Various high-gain converters leveraging coupled inductors with minimal core loss can be employed. These converter topologies achieve high voltage gain by adjusting the duty cycle of the power switch and the turns ratio of the coupled inductor. An introduced non-isolated topology in [17] is suited for microgrid inverters; however, the high input current ripple associated with this design may diminish the operational lifespan of the input PV panels. Another high step-up structure presented in [18] involves a voltage multiplier cell (VMC) and coupled inductor, yet it also suffers from high input current ripple and a high component count, leading to reduced efficiency. Several DC-DC converters with high voltage gain benefits are presented in the literature. Despite these advancements, challenges persist in high step-up DC-DC converters, including issues such as high input current ripple, elevated voltage stress on semiconductor components, diode reverse recovery troubles, increased component count, and lower overall efficiency. In [19], an economical and effective converter known as the Z-source DC-DC converter was introduced. This converter implements the Z-source network using two inductors and two capacitors. The unique X-shaped interconnection of the inductors and capacitors in the Z-source network enables its integration with other converters and methodologies like the boost converter, switched-inductor, and switched capacitor [20-22]. However, due to its atypical non-grounded configuration, the basic Z-source converter is limited in its applications. To enhance the voltage gain, a combination of the switched-inductor and Z-source network was explored in [23], but this approach exhibited complexities, increased costs, and larger dimensions. Another prospect involved integrating a switched capacitor into a Z-source DC-DC converter [24], leading to a similarly intricate and expensive design that lacks common ground. Recent research efforts have aimed at addressing common grounding and reducing voltage stresses in such converters [25, 26]. For instance, a quasi-Z-source converter was introduced in [27] to mitigate issues like discontinuous input current and leakage current attributable to the absence of a common grounded connection between the output null and input negative terminal in the Z-source converter. The quasi-Z-source converter, akin to the Z-source counterpart, can be synergistically combined with techniques like switched capacitor and switched inductor to enhance characteristics such as voltage gain and voltage stress [28, 29]. Nevertheless, these combined converters necessitate additional components, escalating their complexity and cost. Moreover, the duty cycle of these converters is constrained by design limitations. In [30], a high-gain transformer-less converter employing a switched inductor, capacitor, and active network is presented. This configuration incorporates two switches, resulting in elevated conduction losses. Another converter described in [31] utilizes a coupled inductor and VMC, but the achieved voltage gain is modest. A high step-up structure with continuous input current is detailed in [32], utilizing a coupled inductor and voltage multiplier cell. Although a high voltage gain is achieved through increased turns ratio, this design suffers from high voltage stress on the main switch.

In this study, a single-switch transformer-less DC-DC converter with continuous input current is introduced. The proposed converter features a $CL^1C^2D^2$ network and offers several advantages, including high step-up gain with a low turn ratio of the coupled inductor, low voltage stress on the semiconductor devices, and a shared ground. The proposed converter features a straightforward design with a single power switch, devoid of any additional complexity in its topology. Simulation results conducted using PSCAD/EMTDC software are presented to verify the performance of the proposed converter. Additionally, the simulations involved the utilization of a photovoltaic module as an input source and the MPPT capability of the converter is confirmed.

II. Proposed DC-DC Converter

The configuration of the proposed converter is illustrated in Fig. 1. It comprises one power switch (S), three diodes (D_1, D_2, and D_3), one inductor (L), one coupled inductor (CL), four capacitors (C_1, C_2, C_3, and C_o). The proposed converter incorporates a conventional boost switching configuration with inductors L, switch S, diode D_1, and capacitor C_1 (resembling a conventional boost converter). Additionally, a $CL^1C^2D^2$ network is introduced, consisting of coupled inductor CL, capacitors C_2, C_3, diodes D_2, and D_3, situated between the conventional boost switching arrangement and the output capacitor C_o. The integration of the $CL^1C^2D^2$ network enhances the voltage gain of the proposed converter while alleviating the voltage stress on the semiconductor components.

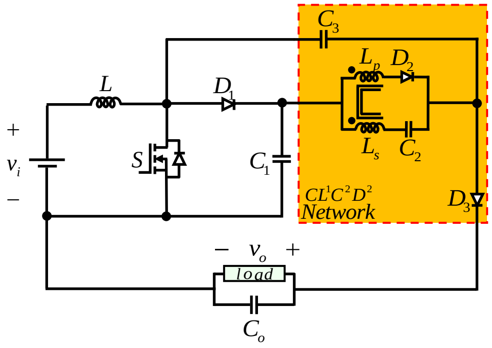

Fig. 1. The proposed converter.

The key waveforms for the proposed converter are depicted in Fig. 2. The proposed converters exhibit two distinct operational states: the shoot-through (ST) state, lasting DT_s, and the non-shoot-through (NST) state, lasting $(1\text{-}D)T_s$. In the proposed converter, the coupled inductor is conceptualized as a dual-headed transformer, depicted in Fig. 3. This transformer incorporates a magnetizing inductance (L_m) aligned in parallel with the primary winding. Therefore, the turns ratio of the coupled inductor is denoted as $n=N_S/N_P$. To express the conceptual performance of the proposed converter, several assumptions are considered in the analysis of the proposed converter: 1) Continuous conduction mode (CCM) is consistently maintained, 2) All components are assumed to be ideal, 3) The input DC source is constant, 4) The capacitors and inductors are sufficiently large, allowing for the application of the small ripple principle.

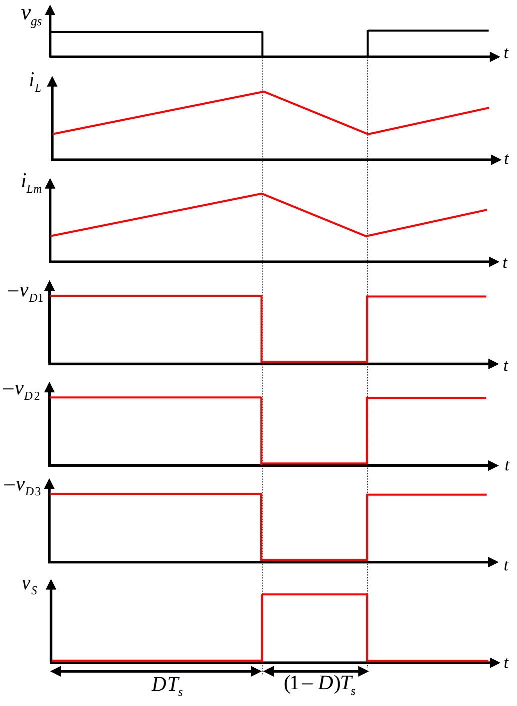

Fig. 2. Key waveforms of the proposed converter.

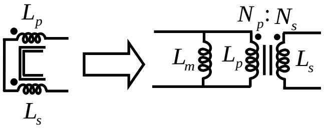

Fig. 3. Transformer modelling of the coupled inductor.

Shoot-through (ST) state: Fig. 4(a) demonstrates the corresponding circuitry depicting the ST state. During this state, the switch S is activated. The inductor L is charged in parallel with a voltage source via the S paths. Diodes D_1-D_3 are reverse-biased, preventing current flow. Furthermore, capacitors C_1 and C_2 are discharged while C_3 is being charged. Capacitor C_o delivers the necessary energy to the load and subsequently is discharged. By employing Kirchhoff's Voltage Law (KVL) and Kirchhoff's Current Law (KCL) in this operational state, the following equations can be formulated:

$$v_L = v_i \tag{1}$$

$$v_{Ls} = v_{C1} + v_{C2} - v_{C3} \tag{2}$$

$$v_{Co} = v_o \tag{3}$$

$$i_{Co} = -i_o \tag{4}$$

$$i_{C1} = i_{C2} = -i_{C3} = -i_{Ls} \tag{5}$$

$$i_{Lp} = i_{Lm} \tag{6}$$

Non-shoot-through (NST) state: This mode begins when the switch S is deactivated. Diodes D_1-D_3 transition to a forward bias state, enabling current conduction. The voltage across inductors L and magnetizing inductor L_m turns negative, leading to a linear reduction in their respective currents. Additionally, capacitors C_1, C_2, and C_o are charged, while C_3 is discharged during this state. Fig. 4(b) illustrates the equivalent circuitry representing this operational state. By applying KVL and KCL in this mode, the following equations can be expressed:

$$v_L = v_i - v_{C1} \tag{7}$$

$$v_{Lm} = -v_{C3} \tag{8}$$

$$v_{Ls} = v_{C2} - v_{C3} \tag{9}$$

$$v_{Co} = v_{C1} + v_{C3} \tag{10}$$

$$i_{C3} = i_{Lm} + i_{Ls} - i_{Lp} - i_{Co} - i_o \tag{11}$$

$$i_{C2} = -i_{Ls} \tag{12}$$

$$i_{C1} = i_L + i_{C3} + i_{Lp} - i_{Lm} - i_{Ls} \tag{13}$$

By applying the voltage balance principle to inductors L and L_m according to equations (1-3) and (7-10), the voltage across capacitors and the voltage gain of the proposed converter can be calculated as illustrated below:

$$v_{C1} = \frac{v_i}{1-D} \tag{14}$$

$$v_{C2} = \frac{(1-n)Dv_i}{n(1-D)} \tag{15}$$

$$v_{C3} = \frac{Dv_i}{n(1-D)} \tag{16}$$

$$v_o = v_{Co} = Gv_i = \frac{n+D}{n(1-D)}v_i \tag{17}$$

By utilizing the current balance principle for capacitors using equations (4-6) and (11-13), the mean current passing through the inductor and the magnetizing inductor can be evaluated as described subsequently:

$$i_L = \frac{n+D}{n(1-D)} i_o \tag{18}$$

$$i_{Lm} = i_o \tag{19}$$

where v_i, v_o and i_o are the input voltage, output voltage and output current, respectively. The voltage gain curves of the proposed converter are plotted in Fig. 5 for different coupled inductor's turn ratios. To demonstrate the impact of leakage inductance (L_k) on voltage gain, consideration is given to the coupling coefficient (k) as follows:

$$k = \frac{L_m}{L_k + L_m} \tag{20}$$

Fig. 6 illustrates the voltage gain of the proposed converter across varying coupling coefficients and duty cycles. It is observed that an increase in leakage inductance leads to a reduction in both coupling coefficient and voltage gain.

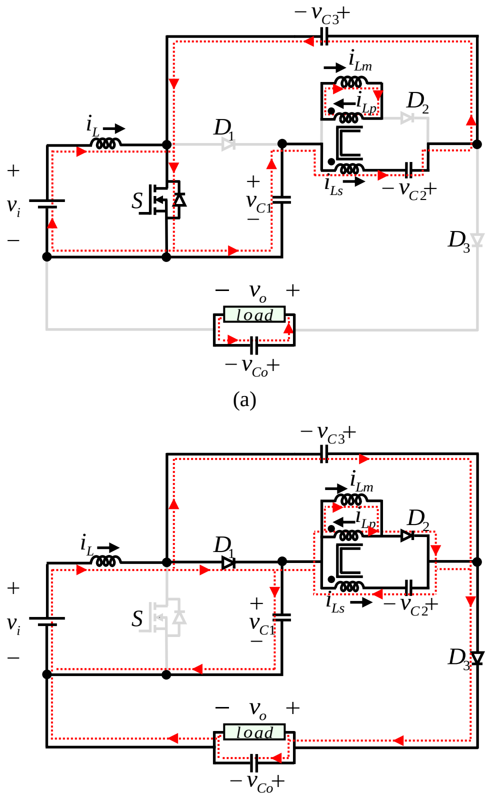

(a)

(b)

Fig. 4. Equivalent circuits of proposed converter. (a) ST. (b) NST.

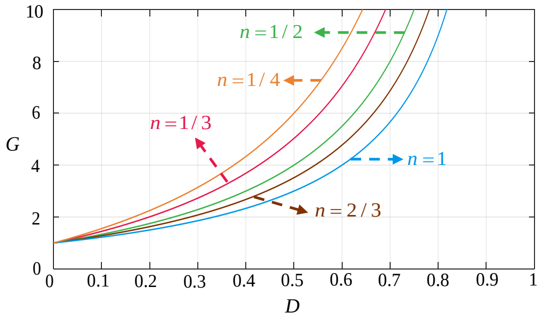

Fig. 5. Voltage gain versus duty cycle curves for four different coupled inductor's turn ratios.

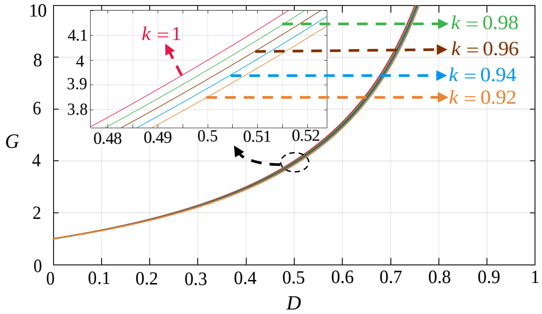

Fig. 6. Voltage gains versus duty cycle for different coupling coefficients (k) and n=0.5.

By applying KCL and the principle of current balance, it is possible to calculate the average currents of all capacitors during charging or discharging modes within a given time interval.

$$\begin{cases} i_{C1-charge} = i_{C2-charge} = \frac{Di_o}{n(1-D)} \\ i_{C1-discharge} = i_{C2-discharge} = -\frac{i_o}{n} \end{cases} \tag{21}$$

$$\begin{cases} i_{C3-charge} = \frac{i_o}{n} \\ i_{C3-discharge} = -\frac{Di_o}{n(1-D)} \end{cases} \tag{22}$$

$$\begin{cases} i_{Co-charge} = \frac{Di_o}{1-D} \\ i_{Co-discharge} = -i_o \end{cases} \tag{23}$$

Through the application of KVL to the equivalent circuit of the ST state, the voltages experienced across diodes D_1, D_2, and D_3 are determined using the following equations:

$$v_{D1} = v_{C1} = \frac{v_i}{1-D} \tag{24}$$

$$v_{D2} = v_{C1} - v_{C3} - v_{Lp} = \frac{(1-n)v_i}{n(1-D)} \tag{25}$$

$$v_{D3} = v_{C3} - v_o = \frac{v_i}{1-D} \tag{26}$$

Through the application of KVL to the equivalent circuit of the NST state, the voltage across the switch S is computed using the following equation:

$$v_S = v_{C1} = \frac{v_i}{1-D} \tag{27}$$

By utilizing KCL on the equivalent circuit during the ST state, the currents flowing through the switch S are determined using the ensuing equation:

$$i_S = i_L + i_{C3-charge} = \frac{(1+n)i_o}{n(1-D)} \tag{28}$$

Through the application of KCL to the equivalent circuit during the NST state, the currents flowing through diodes D_1, D_2, and D_3 are determined using the following equations:

$$i_{D1} = i_L + i_{C3-discharge} = \frac{i_o}{1-D} \tag{29}$$

$$i_{D2} = i_o + i_{Co-charge} + i_{C2-charge} + i_{C3-discharge} = \frac{i_o}{1-D} \tag{30}$$

$$i_{D3} = i_o + i_{Co-charge} = \frac{i_o}{1-D} \tag{31}$$

The root-mean-square (rms) values of the currents in the power switch, diodes and capacitors, as well as average currents of the switch and diodes play a crucial role in efficiency analysis, and they can be obtained as follows:

$$I_{S-rms} = \frac{\sqrt{D}(1+n)I_o}{n(1-D)} \tag{32}$$

$$I_{D1-rms} = I_{D2-rms} = I_{D3-rms} = \frac{I_o}{\sqrt{1-D}} \tag{33}$$

$$I_{C1-rms} = I_{C2-rms} = I_{C3-rms} = \sqrt{\frac{D}{1-D}\frac{I_o}{n}} \tag{34}$$

$$I_{Co-rms} = \sqrt{\frac{D}{1-D}}I_o \tag{35}$$

$$I_{S-ave} = \frac{D(1+n)I_o}{n(1-D)} \tag{36}$$

$$I_{D1-ave} = I_{D2-ave} = I_{D3-ave} = I_o \tag{37}$$

III. Parameter Design

The minimum value of the inductor is calculated by following equation:

$$L = \frac{|V_L|\Delta t}{\Delta I_L} \tag{38}$$

The voltage across the inductor during the $\Delta t = DT_S$ interval is represented by $|V_L|$. ΔI_L refers to the permissible percentage ripple inductor current, denoted as $\Delta I_L = x\% I_L$. By utilizing equations (1), (2), (18), (19) and (38), the minimum inductance values can be determined as such:

$$L \geq \frac{DV_i^2}{x\% f_S P_o} \tag{39}$$

$$L_m = \frac{D(n+D)V_i^2}{(1-D)x\% f_S P_o} \tag{40}$$

The minimum value of the capacitor is calculated by following equation:

$$C = \frac{|I_C|\Delta t}{\Delta V_C} \tag{41}$$

The current passing through the capacitor during the $\Delta t = DT_S$ interval is represented by $|I_C|$. ΔV_C denotes the voltage ripple across the capacitor, symbolized as $\Delta V_C = y\% V_C$. Thus, based on equations (4), (5), (14), (15), (16), (17) and (41), the necessary capacitances can be determined as follows:

$$C_1 \geq \frac{D(1-D)^2 P_o}{(n+D)y\% f_S V_i^2} \tag{42}$$

$$C_2 \geq \frac{n(1-D)^2 P_o}{(1-n)(n+D)y\% f_S V_i^2} \tag{43}$$

$$C_3 \geq \frac{n(1-D)^2 P_o}{(n+D)y\% f_S V_i^2} \tag{44}$$

$$C_o \geq \frac{n^2 D(1-D)^2 P_o}{(n+D)^2 y\% f_S V_i^2} \tag{45}$$

where, V_i, P_o, and f_s are the values of the input voltage, output power, and switching frequency, respectively. A methodological approach for the optimal selection of a magnetic core is outlined in [33]. The initial step involves the calculation of the geometrical constant (K_g) of the inductor and coupled inductor core utilized in the proposed converter, as defined by:

$$K_g = \frac{A_C^2 W_A}{MLT} \geq \frac{\rho L^2 I_{max}^2}{r_L K_u B_{max}^2} \tag{46}$$

Here, A_C represents the effective cross-sectional area of the core, MLT denotes the mean length turn, W_A represents the window area, ρ is the copper's resistivity, B_{max} stands for the maximum flux density of the ferrite core, and K_u signifies the window utilization factor. Substituting (18) and (39) into (46) allows for the determination of the geometrical constant (K_g) for the inductor L, as demonstrated below:

$$K_g = \frac{A_C^2 W_A}{MLT} \geq \frac{\rho}{r_L K_u B_{max}^2 \left(\frac{D(n+D)V_i^2 I_o}{n(1-D)x\% f_S P_o}\right)^2} \tag{47}$$

Substituting (19) and (40) into (46) allows for the determination of the geometrical constant (K_g) for the coupled inductor L_m, as demonstrated below:

$$K_g = \frac{A_C^2 W_A}{MLT} \geq \frac{\rho}{r_L K_u B_{max}^2 \left(\frac{D(n+D)V_i^2 I_o}{(1-D)x\% f_S P_o}\right)^2} \tag{48}$$

Upon selecting the most suitable core for the inductor and coupled inductor based on the A_C value, the calculations for the number of winding turns (n) and the air gap (l_g) are determined as outlined below:

$$n = \frac{LI_{max}}{A_C B_{max}} \tag{49}$$

$$l_g = \frac{\mu_0 L I_{max}^2}{2B_{max}^{2C}} \tag{50}$$

where μ_0 is the permeability of air.

IV. Power Loss of Components

The primary components of losses in DC-DC converters are categorized into conduction loss and switching loss. Switching losses necessitate scrutiny in both diodes and power switches. The substantial current flow through components leads to significant conduction losses in the majority of cases. Therefore, an examination of the conduction losses in power switches, diodes, inductors, and capacitors is conducted for the converter.

Power switch losses: The conduction loss in the power switch can be expressed as:

$$P_{SC} = r_S I_{S-rms}^2 \tag{51}$$

Here, (I_{S-rms}) represents the rms current flowing through the power switch, while (r_S) denotes the resistance of the switch. By employing (32) and (51), the ultimate expression for the switch conduction loss can be formulated as:

$$P_{SC} = r_S \left(\frac{\sqrt{D}(1+n)I_o}{n(1-D)}\right)^2 \tag{52}$$

The turn-on and turn-off losses pertaining to a power switch can be described by a shared equation, exemplified by (53), as derived for the switch utilized in the proposed converter, as shown in (54).

$$P_{SS} = V_S I_{S-ave}(t_r + t_f)\frac{f_S}{2} \tag{53}$$

$$P_{SS} = \frac{D(1+n)(t_r+t_f)f_S P_o}{2n(1-D)^2} \tag{54}$$

Here, the P_{SS}, t_r, t_f, V_S, I_{S-ave}, and f_s represent the switching loss, turn-on delay time, turn-off delay time, switch voltage, average switch current, and switching frequency, respectively.

Diode power losses: The power loss in diodes can be categorized into conduction loss, forward voltage drop loss, and switching loss. Equation (55) details the forward voltage drop loss of a diode (P_{DF}), enabling the calculation of losses for the diodes in the proposed converter. Equation (56) presents the total forward voltage drop loss of the diodes.

$$P_{DF} = V_F I_{D-ave} \tag{55}$$

$$P_{DF} = (V_{F1} + V_{F2} + V_{F3}) I_o \tag{56}$$

Where V_F and $I_{D\text{-}ave}$ denote the forward voltage drop of the diode and the average current through the diode, respectively. The next calculated loss for the diodes is conduction loss (P_{DC}). The total conduction loss of the diodes in the proposed converter is summarized as:

$$P_{DC} = (r_{D1} + r_{D2} + r_{D3}) \left(\frac{I_o}{\sqrt{1-D}}\right)^2 \tag{57}$$

The resistances r_{D1}, r_{D2}, and r_{D3} represent the resistances of the diodes in the proposed converter. The final aspect of diode losses is the switching loss (P_{DS}), for which a standard equation is presented as (58). Equation (59) is formulated specifically for the switching loss pertaining to the diodes in the proposed converter.

$$P_{DS} = V_D I_{D-ave} t_{rr} \frac{f_s}{2} \tag{58}$$

$$P_{DS} = \left(\frac{(1-n)}{n(1-D)} + \frac{2}{(1-D)}\right) P_o t_{rr} \frac{f_s}{2} \tag{59}$$

The parameters t_{rr}, V_D, and $I_{D\text{-}ave}$ denote the reverse recovery time, diode voltage, and average diode current, respectively.

Inductors conduction loss: The conduction loss for the inductors (P_{LC}) is computed based on equation (60) and is expressed as equation (61).

$$P_{LC} = r_L I_{L-rms}^2 \tag{60}$$

$$P_{LC} = r_L \left(\frac{n+D}{n(1-D)} i_o\right)^2 + r_{Lm} I_o^2 \tag{61}$$

Capacitors conduction loss: The conduction loss in the proposed converter stems from the resistance in capacitors. The converter in question incorporates four capacitors, the total conduction loss of which amounts to:

$$P_{CC} = (r_{C1} + r_{C2} + r_{C3}) \frac{D}{1-D} \left(\frac{I_o}{n}\right)^2 + r_{Co} \frac{D}{1-D} I_o^2 \tag{62}$$

The conduction loss of the capacitors and the resistance of the capacitors are denoted as P_{CC} and r_C, respectively. Consequently, the efficiency of the proposed converter can be ascertained:

$$\eta = \frac{P_o}{P_o + P_{Loss}} \tag{63}$$

To analyze the impact of parasitic elements in both passive and active components on the voltage gain of the proposed converter, the model of the converter was modified to incorporate these elements. Fig. 7 depicts the circuit of the proposed converter with the integrated parasitic elements. This non-ideal converter model accounts for several parasitic elements, including the series resistances of the inductors ($r_L = r_{Lm} \approx r_L$), the equivalent series resistances of the capacitors ($r_{C1} = r_{C2} = r_{C3} = r_{Co} \approx r_C$), the on resistance of the power switch (r_S), the forward resistances of the diodes ($r_{D1} = r_{D2} = r_{D3} \approx r_D$), and their corresponding forward voltages ($V_{F1} = V_{F2} = V_{F3} \approx V_F$). Considering these parasitic elements, a new equation was derived to characterize the static voltage gain of the proposed converter (G') in equation (64).

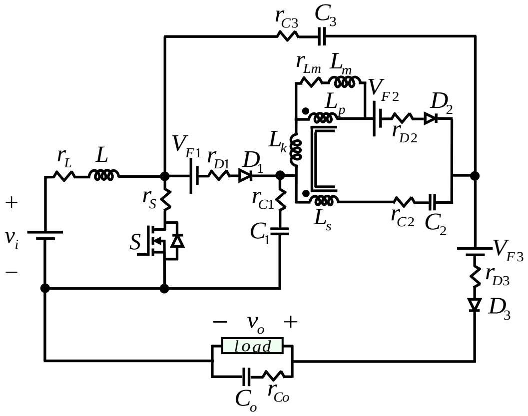

Fig. 7. The proposed converter with the parasitic elements.

V. Comparative Analysis

Table 1 presents a comparison of the characteristics of the proposed converter with similar converters. The results from Table 1 are illustrated in Figs. 8(a)-8(c). Fig. 8(a) displays the variation of voltage gain versus the duty cycle. It is evident that the proposed converter exhibits a higher voltage gain for n=0.5 compared to others with the same duty cycle except [28, 29]. However, the converters [28, 29] have a duty cycle limitation and suffer from high voltage stress on their semiconductors. For lower duty cycles, the converter described in [17, 31, 32] shows the highest voltage gain, although it may not be suitable for high-gain applications. Fig. 8(b) portrays the variation of normalized voltage stress on the main switch with respect to the duty cycle. The proposed converter demonstrates lower voltage stress on switch S compared to other converters. According to Fig. 8(c), the plot of normalized voltage stress across diodes for various duty cycles with n=0.5 reveals that the proposed configuration's stress is lower than of the most other converters except [2, 31]. Importantly, the proposed converter achieves higher voltage gain with lower voltage stress on the power switch compared to [2, 31]. In contrast to the converters discussed in references [9, 15, 28], the proposed converter introduces a common grounded feature, crucial for electrical systems, particularly in photovoltaic applications. This characteristic plays a vital role in mitigating leakage currents, a prevalent concern in PV-based converters. In contrast to the converters in references [15, 17, 28, 31], the proposed converter ensures continuous input current and eliminates the need for bulky input filters. Unlike the ZS and QZS converters described in references [27-29] with a restricted duty cycle range of 0 to 0.5, the proposed converter overcomes duty cycle limitations, enabling a duty cycle variation from 0 to 1. By comparing the proposed converter to similar converters, it becomes apparent that the proposed topology offers higher voltage gain with reduced stress on the semiconductors. Consequently, this design could be effectively utilized in renewable energy systems such as PV applications with low implementation costs.

TABLE 1: COMPARISON OF THE PROPOSED CONVERTER WITH COMPARABLE CONVERTERS

Ref.	$S^1/D^2/C^3/L^4/CL^5$	V_o/V_i	V_S/V_o	V_D/V_o	Common ground	Continuous input current	Duty cycle limitation
[2]	1/2/3/1/1	$\frac{1+nD}{1-D}$	$\frac{1}{1+nD}$	$\frac{n}{1+nD}$	Yes	Yes	No
[9]	1/4/4/3/1	$\frac{n}{1-D}$	$\frac{1}{n}$	1	No	Yes	No
[11]	2/2/4/1/1	$\frac{n}{1-D}$	$\frac{1}{n}$	1	Yes	Yes	No
[15]	2/5/4/-/1	$\frac{n(2-D)}{1-D}$	$\frac{1}{n(2-D)}$	$\frac{1}{2-D}$	No	No	No
[17]	1/3/3/-/1	$\frac{1+n}{1-D}$	$\frac{1}{1+n}$	1	Yes	No	No
[27]	1/2/3/2/-	$\frac{1}{1-2D}$	1	1	Yes	Yes	Yes
[28]	1/3/5/3/-	$\frac{1+D}{1-2D}$	$\frac{1}{1+D}$	$\frac{1}{1+D}$	No	No	Yes
[29]	1/5/3/3/-	$\frac{1+D}{1-2D-D^2}$	1	1	Yes	Yes	Yes
[31]	1/3/3/-/1	$\frac{1+n}{1-D}$	$\frac{1}{1+n}$	$\frac{n}{1+n}$	Yes	No	No
[32]	1/3/4/1/1	$\frac{1+n}{1-D}$	$\frac{1}{1+n}$	$\frac{1+n-D}{1+n}$	Yes	Yes	No
Proposed	1/3/4/1/1	$\frac{n+D}{n(1-D)}$	$\frac{n}{n+D}$	$\frac{n}{n+D}$	Yes	Yes	No

Number of 1. Switches, 2. Diodes, 3. Capacitors, 4. Inductors, 5. Coupled inductors

$$G^{'} = \frac{(n+D)(1-D)RnV_o}{(Rn^2(1-D)^2V_o+r_SD(1+n)^2(1-D)V_o+3r_Dn^2V_o(1-D)+r_L(n+D)^2V_o+r_Ln^2(1-D)^2V_o+3r_CDV_o(1-D)+r_CD(1-D)n^2V_o+3V_FRn^2(1-D)^2)} \tag{64}$$

VI. Simulation Results

To verify the efficacy and confirm the reliability of the proposed converter, simulation outcomes are showcased using PSCAD/EMTDC software. The simulation parameters utilized are detailed in Table 2.

TABLE 2: PARAMETERS USED IN THE SIMULATION

Parameters and Values						
V_i	f_S	D	n	C_1-C_3, C_o	L, L_m	load
$40\,V$	50KHZ	0.3	0.5	$220\mu F$	$400\mu H$	15Ω

The results of the simulation are presented in Fig. 9. In Fig. 9(a), the output voltage is around $87.24\,V$, which agrees with the calculated value (V_o=91.4 V) for an input voltage (V_i) of 40 V and utilizing the voltage gain equation (17) with a duty cycle of 0.3. This alignment between the simulation and theoretical outcomes confirms the precision of the voltage gain. Fig. 9(b) displays the current waveform, showing an output current of $5.82A$. The voltage and current stresses on the inductors are illustrated in Fig. 9(c)-9(f). The average current passing through inductors L and L_m is determined to be $13.34A$ and $5.73A$, respectively, as depicted in Fig. 9(d) and Fig. 9(f), which corresponds well with the theoretical predictions in equations (18)-(19). The waveforms of voltage stress on the capacitors, switches, and diodes are demonstrated in Fig. 9(g)-9(m). The calculated voltage stress values on the capacitors using equations (14)-(16), and on the switches and diodes using equations (24)-(27), closely correspond with the simulation results, as shown in Fig. 9(g) to Fig. 9(m).

VII. MPPT Simulation Results

In this section, the performance of the proposed converter under Maximum Power Point Tracking (MPPT) of a Photovoltaic (PV) system is evaluated using results obtained from PSCAD/EMTDC simulations. The setup of the proposed converter within a PV system is depicted in Fig. 10. A silicon module LG400N2W-A5 serves as the PV source, and its characteristics are detailed in Table 3 based on the manufacturer's datasheet. The P-V (power versus voltage) characteristic curves for radiations of $1000\,W/m^2$ and $800\,W/m^2$ at a temperature of T=298K are displayed in Figs. 11(a) and 11(b), respectively. As the change in radiation has a greater impact on the MPP compared to temperature variation, this study maintains a constant temperature and examines MPPT under various radiation conditions. Fig. 12 portrays the results obtained for the output power of the PV (P_{PV}), the output voltage of the PV (V_{PV}), the output voltage of the load (V_o), and radiation (G) during the extraction of maximum power from the PV with the proposed converter under step changes in radiation

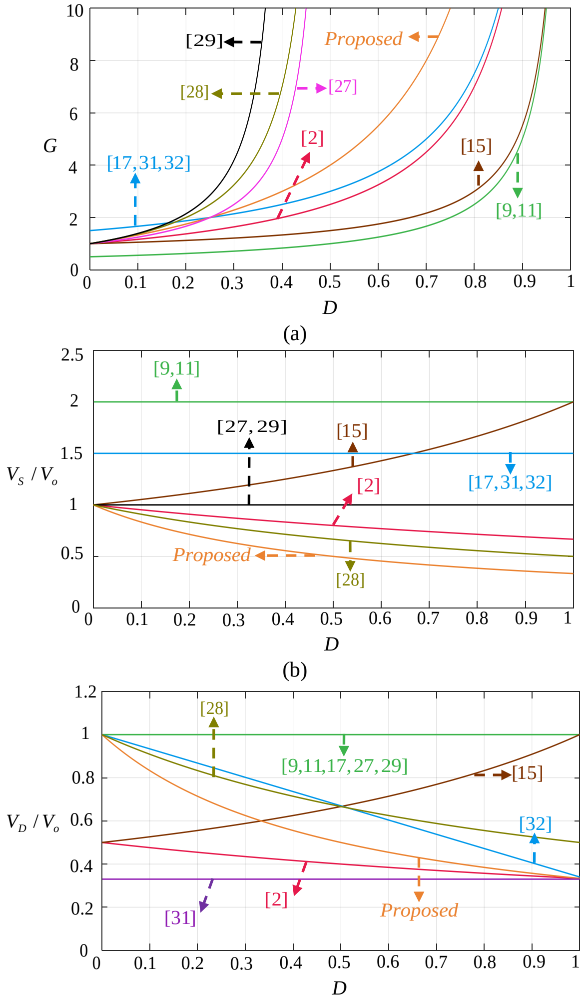

(a)

(b)

(c)

Fig. 8. Comparison results of the proposed converter and other converters. (a) voltage gain. (b) voltage stress on the switch. (c) voltage stress on diodes.

from 1000 W/m^2 to 800 W/m^2. The MPPT capability of the proposed converter is validated based on the P-V characteristics in Fig. 11 and the output power of the PV source in Fig. 12(a).

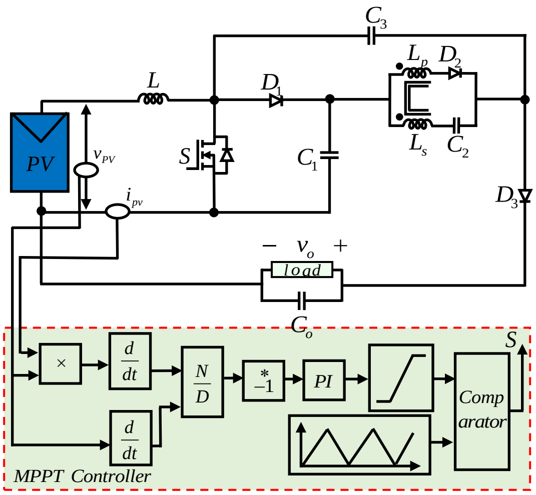

Fig. 10. Proposed converter and MPPT controller.

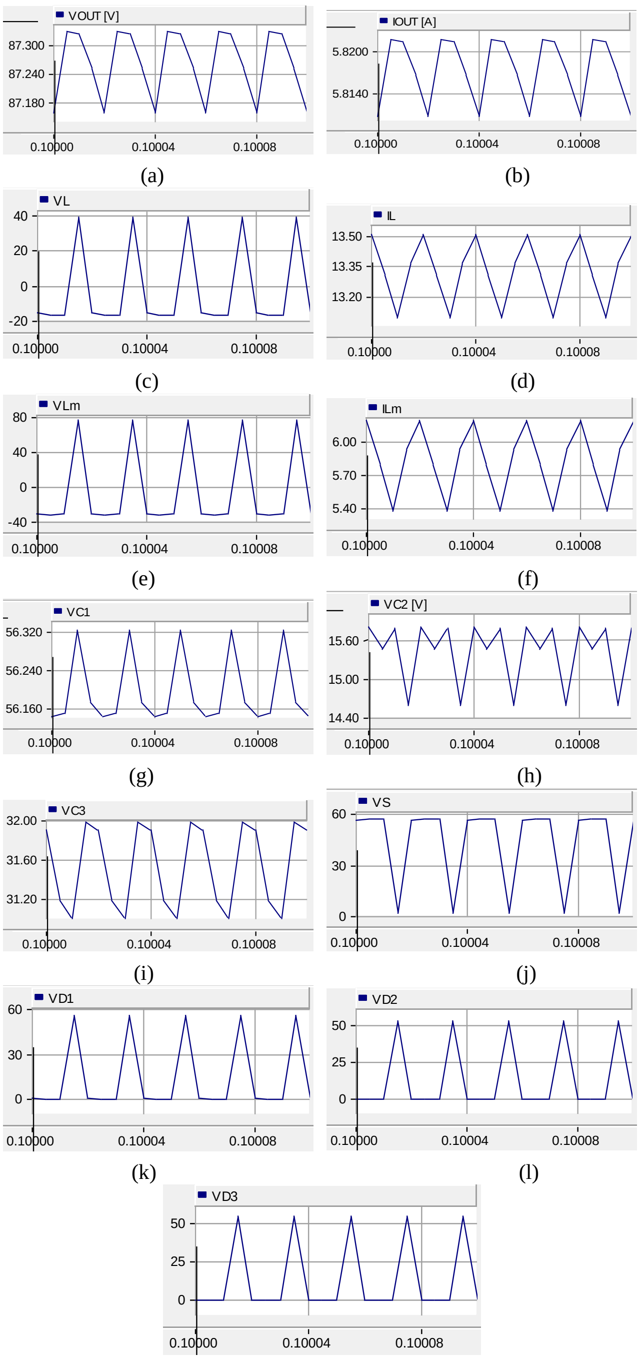

(a) (b)

(c) (d)

(e) (f)

(g) (h)

(i) (j)

(k) (l)

(m)

Fig. 9. Simulation results of the proposed converter.

TABLE 3: MONOCRYSTALLINE / N-TYPE MODULE PARAMETERS (LG400N2W-A5) PROVIDED BY THE MANUFACTURER FOR THE STANDARD CONDITION

Parameters and Values					
P_{MPP}	I_{sc}	V_{oc}	V_{mpp}	I_{mpp}	N_s
400 W	10.47A	49.3V	40.6V	9.86A	72

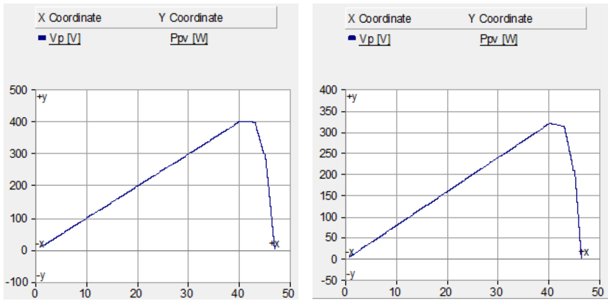

(a) (b)

Fig. 11. Power versus voltage characteristic curves for radiations 1000 W/m^2 and 800 W/m^2 at temperature T=298 K. (a) 1000 W/m^2. (b) 800 W/m^2.

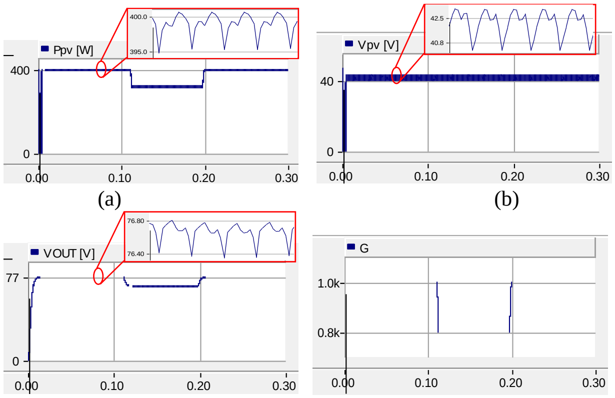

(a) (b)

(c) (d)

Fig. 12. MPPT simulation results for the proposed converter under step change of radiation from 1000 W/m^2 to 800 W/m^2 and 800 W/m^2 to 1000 W/m^2. (a) P_{PV}. (b) V_{PV}. (d) V_o. (a) irradiance (G).

VIII. Conclusion

In this research article, a single switch transformer-less DC-DC converter with continuous input current is introduced. This converter utilizes only a single power MOSFET, leading to a reduction in converter costs. Additionally, it features semiconductors with low blocking voltage, offering added advantages. A high voltage gain can be attained by decreasing the turn ratio of the coupled inductor, obviating the necessity for a high turn ratio to achieve a high voltage gain. Moreover, being transformer-less, the proposed converter circumvents associated drawbacks. A simple pulse width modulation technique is implemented for switch control. The converter incorporates MPPT control to optimize photovoltaic system power extraction. The theoretical analysis of the converter covers its operational modes, and the accuracy of the calculated outcomes is confirmed by comparing them with results from PSCAD/EMTDC software simulations.

REFERENCES

[1] S. Moosavi, “Efficiency improvement and inrush current reduction in a non-isolated dc-dc converter,” Int. J. Ind. Electron. Cont. Opt. (IECO), vol. 2, no. 2, pp.137-144, 2019.

[2] K.B. Park, G.W. Moon, and M.J. Youn, “Non-isolated high step-up boost converter integrated with sepic converter,” IEEE Trans. Power Electron., vol. 25, no. 9, pp. 2266-2275, 2010.

[3] P. Abolhassani, M. Maalandish, A. Nadermohammadi, M.B.B. Sharifian, M.R. Feyzi, and S.H. Hosseini, “A high step-up high step-down coupled inductor based bidirectional dc-dc converter with low voltage stress on switches,” IET Power Electron., vol. 17, no. 7, pp. 802-823, 2024.

[4] A. Nadermohammadi, M. Maalandish, A. Seifi, P. Abolhassani, S.H. Hosseini, and M. Farsadi, “A non-isolated single-switch ultra-high step-up dc-dc converter with coupled inductor and low-voltage stress on switch,” IET Power Electron. vol. 17, no. 2, pp. 251-265, 2024.

[5] S.M. Hashemzadeh, E. Babaei, S.H. Hosseini, and M. Sabahi, “Design and analysis of a new coupled inductor based interleaved high step-up dc-dc converter for renewable energy applications.,” Int. Trans. Electr. Energy Syst., 2022.

[6] M. Eskandarpour Azizkandi, F. Sedaghati, and H. Shayeghi, “A new boost dc-dc converter based on a coupled inductor and voltage multiplier cells,” Int. J. Ind. Electron. Cont. Opt. (IECO), vol. 2, no. 4, pp. 265-278, 2019.

[7] A. Nadermohammadi, P. Abolhassani, M. Maalandish, A. Seifi, P. Aghakhanlou, and S.H. Hosseini, “Soft-switching ultra-high step-up dc-dc converter featuring coupled inductor and low voltage stress on switches,” in proc. PEDSTC, 2024.

[8] H. Shojaeian, S. Hasanzadeh, and M. Heydari, “High efficient and high step-up dual switches converter based on three coupled inductors,” Int. J. Ind. Electron. Cont. Optim. (IECO), vol. 1, no. 2, pp. 143-152, 2018.

[9] M. Kim and S. Choi, “A fully soft-switched single switch isolated dc-dc converter,” IEEE Trans. Power Electron., vol. 30, no. 9, pp. 4883-4890, 2014.

[10] S.M. Hashemzadeh, S.H. Hosseini, and V. Marzang, “Increase of the photovoltaic resources power using multi-input dc-dc converter and model-based mppt algorithm,” Int. J. Ambient Energy, vol. 43, no. 1, pp. 7501-7512, 2022.

[11] A. Kumar and P. Sensarma, “Ripple-free input current high voltage gain dc–dc converters with coupled inductors,” IEEE Trans. Power Electron., vol. 34, no. 4, pp. 3418-3428, 2018.

[12] T. Nouri and T. Shaneh, “A new interleaved ultra-large gain converter for sustainable energy systems,” IET Power Electron., vol. 14, no. 1, pp. 90-105, 2021.

[13] S. Padmanaban, F. Blaabjerg, P. Wheeler, J.O. Ojo, and A.H. Ertas, “High-voltage dc-dc converter topology for pv energy utilization-Investigation and implementation,” Electric Power Compon. Syst., vol. 45, no. 3, pp. 221-232, 2017.

[14] B. Zhu, Q. Zeng, Y. Chen, Y. Zhao, and S. Liu, “A dual-input high step-up dc/dc converter with ZVT auxiliary circuit,” IEEE Trans. Energy Conv., vol. 34, no. 1, pp. 161-169, 2018.

[15] T.J. Liang, J.H. Lee, S.M. Chen, J.F. Chen, and L.S. Yang, “Novel isolated high-step-up dc-dc converter with voltage lift,” IEEE Trans. Ind. Electron., vol. 60, no. 4, pp. 1483-1491, 2011.

[16] A. Mostaan, J. Yuan, Y.P. Siwakoti, S. Esmaeili, and F. Blaabjerg, “A trans-inverse coupled-inductor semi-SEPIC dc-dc converter with full control range,” IEEE Trans. Power Electron., vol. 34, no. 11, pp. 10398-10402, 2019.

[17] S.M. Chen, T.J. Liang, L.S. Yang, and J.F. Chen, “A boost converter with capacitor multiplier and coupled inductor for ac module applications,” IEEE Trans. Ind. Electron., vol. 60, no. 4, pp. 1503-1511, 2011.

[18] Y.P. Hsieh, J.F. Chen, T.J. Liang, and L.S. Yang, “Novel high step-up dc-dc converter with coupled-inductor and switched-capacitor techniques,” IEEE Trans. Indus. Electron., vol.

59, no. 2, pp. 998-1007, 2011.
[19] F.Z. Peng, "Z-source inverter," IEEE Trans. Ind. Appl., vol. 39, no. 2, pp. 504-510, 2003.
[20] J. Zhang, and J. Ge, "Analysis of Z-source dc-dc converter in discontinuous current mode," in Proc. APPEEC, Chengdu, China, pp. 1-4, March 2010.
[21] F. Evran, and M.T. Aydemir, "Z-source-based isolated high step-up converter," IET Power Electron., vol. 6, no.1, pp. 117-124, 2013.
[22] B. Poorali, A. Torkan, and E. Adib, "High step-up Z-source dc-dc converter with coupled inductors and switched capacitor cell," IET Power Electron., vol. 8, no. 8, pp. 1394-1402, 2015.
[23] M. Zhu, K. Yu, and F.L. Luo, "Switched inductor Z-source inverter," IEEE Trans. Power Electron., vol. 25, no.8, pp. 2150-2158, 2010.
[24] Y. Shindo, M. Yamanaka, and H. Koizumi, "Z-source dc-dc converter with cascade switched capacitor," in Proc. IIES, Melbourne, Australia, pp. 1665-1670, Nov. 2011.
[25] Y. Tang, S. Xie, and C. Zhang, "An improved Z-source inverter," IEEE Trans. Power Electron., vol. 26, no. 12, pp. 3865-3868, 2011.
[26] Y. Tang, S. Xie, C. Zhang, and Z. Xu, "Improved Z-source inverter with reduced Z-source capacitor voltage stress and soft-start capability," IEEE Trans. Power Electron., vol. 24, no. 2, pp. 409-415, 2009.
[27] D. Vinnikov and I. Roasto, "Quasi-Z-source based dc/dc converters for distributed power generation," IEEE Trans. Ind. Electron., vol. 58, no.1, pp. 192-201, Jan. 2011.
[28] A. Raveendran, E. Paul, and A.P. Ommen, "Quasi-Z-source dc-dc converter with switched capacitor," Int. j. eng. res. gen. sci., vol. 3, no. 4, July 2015.
[29] M. Nguyen, Y. Lim, and G. Cho, "Switched-inductor quasi-Z-source inverter," IEEE Trans. Power. Electron., vol. 26, no. 11, Nov. 2011.
[30] Y. Tang, T. Wang, and D. Fu, "Multicell switched-inductor/switched-capacitor combined active-network converters," IEEE Trans. Power Electron., vol. 30, no. 4, pp. 2063-2072, 2014.
[31] H. Shayeghi, S. Pourjafar, S.M Hashemzadeh, and F. Sedaghati, "A dc-dc converter with high voltage conversion ratio recommended for renewable energy application," J. Oper. Autom. Power Eng., vol. 12, no. 3, pp. 186-194, 2024.
[32] N. Yousefi, D. Mirabbasi, B. Alfi, M. Salimi, and G.R. Aghajani, "A low input current ripple high step-up dc-dc converter with reduced voltage stress for renewable energy application," J. Oper. Autom. Power Eng., 2024, in press.
[33] C.W. McLyman, Transformer and Inductor Design Handbook, Third Edition, Revised and Expanded. CRC press, 2004.
[34] J. Farzaneh, R. Keypouror, and A. Karsaz, "A novel fast maximum power point tracking for a PV system using hybrid PSO-ANFIS algorithm under partial shading conditions, " Int. J. Ind. Electron. Cont. Opt. (IECO), vol. 2, no. 1, pp. 47-58, 2019.

Sirous Toofan received the B.Sc. degree in Electronic Engineering from Amirkabir University of Technology (Tehran Polytechnic) in 1999, and the MSc. and PhD degree in Electronic Engineering from Iran University of Science and Technology (IUST) in 2002 and 2008, respectively. From 2007 to 2008, During his sabbatical leave, he worked in the VLSI group of Politecnico di Torino and in the Microelectronics-Integrated Circuits Laboratory of Politecnico di Milano Universities in Italy. From August 2009 to September 2022, he was assistance professor and then associate professor of Electrical Engineering at the University of Zanjan.

He is currently an associate professor and he has been working with the Faculty of Electrical and Computer Engineering, University of Tabriz, since September 2022. His current research activities include design of CMOS analog/mixed mode integrated circuits, RF/MM integrated circuits, Integrated DC-DC Converters, and sensors interfaces.

Babak Fathipour was born in Tabriz, Iran, in 1999. He received a B.Sc. degree in Electrical Power Engineering, and an M.Sc. degree in Power Electronics Engineering from University of Tabriz, Tabriz, Iran in 2021 and 2023, respectively. His current research interests include power electronic converters and renewable energy systems.

Ebrahim Babaei (M'10, SM'16) received the Ph.D. degree in Electrical Engineering from the University of Tabriz, in 2007. He is the author and co-author of one book and more than 690 journal and conference papers. He also holds 26 patents in the area of power electronics. His current research interests include the analysis, modelling, design, and control of Power Electronics Converters and their applications, Renewable Energy Sources, and FACTS Devices.

Prof. Babaei has been the Editor-in-Chief of the Journal of Electrical Engineering of the University of Tabriz, since 2013. He was an Associate Editor of the IEEE Transactions on Industrial Electronics from 2015 to 2023. He is also currently an Associate Editor of the IEEE Transactions on Power Electronics, IEEE Open Journal of the Industrial Electronics Society, Iranian Journal of Science and Technology, Transactions of Electrical Engineering, and International Journal of Circuit Theory and Applications. He was selected by the Ministry of Science Research and Technology as the distinguished researcher of Iran in the field of engineering in 2022.

IECO
International Journal Of
Industrial Electronics Control and Optimization
Print ISSN: 3517-2645
Online ISSN: 3568-2645
Homepage: https://ieco.usb.ac.ir/

An Explicit and Accurate $I-V$ Characteristic for Photovoltaic Modules Based on Piecewise Quadratic Function

Ehsan Moshksar[1]

Faculty of Advanced Technologies, Shiraz University, Shiraz, Iran.[1]
Corresponding author's email: emoshksar@shirazu.ac.ir

Article Info

Article type:
Research Article

Article history:
Received: 20-April-2024
Received in revised form: 22-June-2024
Accepted: 12-July-2024
Published online: 21-Dec-2024

Keywords:
Explicit $I-V$ characteristic,
Linear least square,
Photovoltaic module,
Piecewise quadratic function.

ABSTRACT

Deriving an accurate and simple current-voltage ($I-V$) characteristic for photovoltaic (PV) module is highly significant for condition monitoring, fault detection, and maximizing power production in PV systems. Equivalent circuits consisting of one or more diodes are mostly utilized for $I-V$ curve modelling. However, these models are inherently implicit, relatively complex, and nonlinear in their parameters. Here, a piecewise quadratic function with four different intervals is generated from the measured $I-V$ data. The intervals are chosen such that the best model performance can be achieved, especially at maximum power point (MPP). Each quadratic function is obtained from least square technique according to the experimental data in the corresponding interval. It is easy to obtain the voltage value at MPP from the extracted model, analytically. Also, a suggestion is provided for extending the generated $I-V$ model to the real environmental condition by utilizing artificial neural network. The derived PV module model is highly suitable for maximum power point tracking, monitoring, and fault detection due to its simplicity, explicit structure, and accuracy.

I. Introduction

Recently, there is a high emphasis on the use of renewable energy sources all over the world [1]. In this regard, solar photovoltaic (PV) cells have attracted great attention. By series and parallel combination of solar cells a PV system with desired output power can be achieved [2-4].

Developing an accurate model for PV module is an essential task for improving and optimizing the performance of this system [5]. Also, condition monitoring of PV systems is significant for detecting the possible faults and maximizing power production [6].

The most common approach for PV module identification is to use the measured data from current–voltage ($I-V$) curve [7]. The $I-V$ curve is strongly affected by environmental conditions, such as irradiance (G) and PV module temperature (T). Since the PV model identification is mostly accomplished at standard test condition (STC), i.e., $G = 1000$ W/m^2 and $T = 25$ °C, the identified model has to be translated into the actual operating conditions [8]. Some identification techniques consider the whole measured $I-V$ curve data. On the other hand, some methods only consider some specific points such as open circuit $(0, V_{oc})$, short circuit $(I_{sc}, 0)$, and maximum power point (MPP) (I_{mp}, V_{mp}) [9]. Moreover, an accurate and reliable model of $I-V$ curve can be utilized for the fault diagnosis of PV systems [10]. Hence, the precise modelling and analysis of the module $I-V$ is vital for further applications.

Different models have been established to describe the $I-V$ characteristic as accurate as possible, the first of which are the black-box approaches that are based on the conventional artificial neural networks (ANN) [11] and their combination with fuzzy algorithm [12]. In general, these techniques are efficient, but they suffer from some disadvantages. First, a large set of data is required to obtain reliable model which is

Publisher: University of Sistan and Baluchestan

not always available. Second, no implicit or explicit mathematical formulations can be achieved for the $I-V$ characteristic. Also, equivalent circuits including single-diode model (SDM) [13, 14], double-diode model (DDM) [15-17], and three-diode model (TDM) [18, 19] are some common approaches for $I-V$ modelling. The SDM is the simplest equivalent circuit model, but with the least accuracy. The TDM has the highest complexity of mathematical relation, but with the highest accuracy. The DDM holds a trade-off between simplicity and prescience of the PV model. However, in all of these three models, current and voltage relations are expressed with inherent implicit formulations and high nonlinearities. Therefore, rapid and accurate estimation of unknown parameters in these circuits' models is a difficult task [20]. It should be noted that the inherent implicitly of equivalent circuits emerged from existence of series resistance (R_s) in these models [21].

Some works have been conducted to generate explicit equations for $I-V$ characteristic and write I as a function of V, or vice versa. The research in [22] can be considered as the first work in this regard. In this work, explicit and accurate functions are derived according to the Lambert W-function for both current and voltage. These equations represent the behavior of the SDM. Although these mathematical expressions have some advantages and explain SDM in an explicit form, they are complicated due to complexity of Lambert W-function. This complexity was revealed in [23] where a model-based maximum power point algorithm was applied for PV module with SDM. Moreover, in this $I-V$ model description, the unknown parameters are still presented in the nonlinear form. In [24, 25], pade approximants have been applied to form explicit $I-V$ relations. In [26, 27], Taylor's series expansion and Chebyshev polynomials have been utilized to express the exponential term of SDM and obtain an explicit analytical description of current. In [28], the mathematical expression $V+R_sI$ in the exponential term of SDM was approximated by cubic polynomial function of voltage V. In [29], an interesting approach has been applied to extract an explicit $I-V$ model for PV systems. The model was obtained according to three parameters including V_{oc}, I_{sc}, and a parameter introduced as shape parameter (S). Despite simplicity in the mathematical form, this method has some disadvantages. The S parameter should be adjusted, iteratively. Hence, small iterative step results in low rate of convergence, which is an issue especially for real time applications. On the other hand, large step lead to inaccurate model. Moreover, the model is nonlinear with respect to S. In [30], the solar cell characteristic curve was approximated by Bezier curve method. The presented model addressed the problems of nonlinearity, complexity, multivariate and multimodal of the characteristic's curve. Although many researches have been conducted to generate mathematical models for PV cell/module, developing more precise and less complicated models is still crucial. Since, some developed models are very complicated and may have implicit mathematical forms. On the other, some other models may not have desirable accuracy for additional investigations.

However, the developing of desirable model is complicated due to inherent nonlinearity of PV characteristic. Moreover, the PV characteristic highly depends on the environmental conditions such irradiance and temperature, which can be considered as another challenge for PV modelling.

In this paper, a piecewise quadratic function consisting of four separate quadratic function is derived to generate an explicit equation for $I-V$ characteristic. For this purpose, the experimental data are extracted non-uniformly from the whole $I-V$ curve (from zero voltage to open circuit voltage) at STC. In fact, more data is considered at the neighborhood of MPP. Intervals are considered as: $0 \le V \le 0.8V_{mp}$, $0.8V_{mp} \le V \le 0.95V_{mp}$, $0.95V_{mp} \le V \le 1.05V_{mp}$, and $1.05V_{mp} \le V \le V_{oc}$. A separate quadratic function is fitted for each interval by linear least square technique. It is shown that the proposed piecewise function simulates the real PV module $I-V$ curve with high accuracy, especially at MPP. Hence, this model can be easily used for maximum power point tracking to maximize energy harvesting from PV system. Moreover, it is suggested that how one can extend the coefficients of the piecewise function to generate another piecewise $I-V$ curve in the real environmental condition by utilizing ANN. The generated model has specific advantages over the equivalent circuits. First, the model defines an explicit relation between current and voltage of any PV module. Second, the generated model is linear in parameter and PV module identification can be easily achieved by simple numerical analysis. Moreover, it has less complexity, but higher accuracy than the equivalent circuit models. The main highlights and novelties of the proposed piecewise quadratic model can be itemized as:

- An explicit and linear in parameters equation for $I-V$ characteristic of photovoltaic module is derived according to piecewise quadratic function.
- The proposed model is highly accurate with unique model's parameters and less complexity compared with equivalent circuits.
- This model can be utilized for maximum power point tracking purpose and any model-based fault detection techniques.
- A reliable suggestion is provided for extension of the derived model to other real environmental conditions by utilizing of artificial neural network.

In the rest of this article, the implicit mathematical $I-V$ characteristic equations for a PV module with diodes equivalent circuits will be given in Section II. Section III presents a novel approach to generate a mathematical model for PV module with explicit $I-V$ characteristic equation and its extension to other environmental conditions. The results for modelling of the PV module KC200GT with the proposed approach and a comparison with other PV modelling methods are discussed in Section IV. Finally, the conclusion is drawn in Section V.

II. Diodes Equivalent Circuits

The mathematical $\boldsymbol{I-V}$ characteristic equation for a typical PV module is highly nonlinear. Utilization of equivalent circuits consisting of diodes is the most common approach for $\boldsymbol{I-V}$ modelling. In this regard, single-diode model, double-diode model, and three diode model are presented. SDM is the simplest circuit with least amount of accuracy. This model has five unknown parameters that should be estimated for PV model identification. DDM with seven unknown parameters has moderate accuracy and complexity among these three circuits. Finally, TDM with nine unknown parameters has the highest accuracy, but also the highest complexity with respect to the other two circuit models. The schematic representations of these circuit models are shown in Fig. 1. The corresponding $\boldsymbol{I-V}$ characteristics for SDM, DDM, and TDM are written in equations (1) to (3), respectively [14, 16, and 18].

$$I = I_{ph} - I_{01}\left(e^{\frac{V+R_sI}{a_1V_t}} - 1\right) - \frac{V + R_sI}{R_p} \tag{1}$$

$$I = I_{ph} - I_{01}\left(e^{\frac{V+R_sI}{a_1V_t}} - 1\right) - I_{02}\left(e^{\frac{V+R_sI}{a_2V_t}} - 1\right) - \frac{V + R_sI}{R_p} \tag{2}$$

$$I = I_{ph} - I_{01}\left(e^{\frac{V+R_sI}{a_1V_t}} - 1\right) - I_{02}\left(e^{\frac{V+R_sI}{a_2V_t}} - 1\right) - I_{03}\left(e^{\frac{V+R_sI}{a_3V_t}} - 1\right) - \frac{V + R_sI}{R_p} \tag{3}$$

where $\boldsymbol{I}$ and $\boldsymbol{V}$ are output current and voltage of the PV module. $\boldsymbol{I_{0i}}$ and $\boldsymbol{a_i}$ are saturation current and ideality factor of the $\boldsymbol{i^{th}}$ diode ($\boldsymbol{i = 1, 2, 3}$). $\boldsymbol{I_{ph}}$ is photocurrent, $\boldsymbol{R_s}$ is series resistance, and $\boldsymbol{R_p}$ is parallel resistance. Also, $\boldsymbol{V_t}$ is thermal voltage which is proportional to module temperature and number of series cells in the module. Despite accuracy and complexity of these circuit models, they have some common disadvantages. First, all the three equations are expressed in implicit mathematical forms with respect to current and voltage variables. Moreover, these equations generate nonlinear in parameters models for the PV module. Hence, model identification, parameter estimation, and $\boldsymbol{I-V}$ extraction are complicated to achieve by these equivalent circuits.

For the SDM in equation (1), an explicit relation between current and voltage was expressed as follows [22]:

$$I = g(V) = -\frac{V}{R_s + R_p} - \frac{W\left(\frac{R_sI_{01}R_p\exp\left(\frac{R_p\left(R_sI_{ph}+R_sI_{01}+V\right)}{a_1V_t\left(R_s+R_p\right)}\right)}{a_1V_t\left(R_s+R_p\right)}\right)a_1V_t}{R_s} + \frac{R_p(I_{01} + I_{ph})}{R_s + R_p} \tag{4}$$

where $W(.)$ is Lambert *W*-function. It is obvious that relation (4) is complicated and difficult to use, in practice. For example, calculation of the voltage at MPP (V_{mp}) is relatively difficult to achieve as shown in [23]. Moreover, to the best of author's knowledge, no explicit mathematical equations are derived for DDM and TDM.

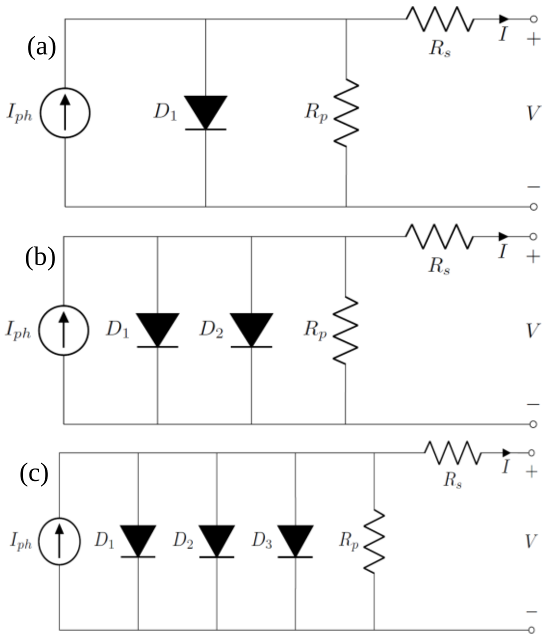

Fig. 1. Equivalent circuits of a PV module: (a) SDM, (b) DDM, (c) TDM.

III. Piecewise Quadratic Function

Here, a novel approach is presented to generate a mathematical model for PV module with explicit and linear in parameter $I-V$ characteristic equation.

In order to establish the $I-V$ curve equation, the experimental data have to be collected from the PV module from zero voltage (short circuit condition) up to its open circuit condition. Since MPP condition is the most significant operating point of the PV module, more data should be allocated to the neighborhood around this point. In general, maximum power extraction is a concerning challenge for researchers due to uncertainty of renewable energy sources, complex operational constraints, and non-convex cost functions [31].

To generate an explicit and precise $I-V$ characteristic equation, the whole operating conditions of the module are divided into four different ranges. The first interval is related to zero voltage up to $0.8V_{mp}$, which can be shown as $0 \leq V \leq 0.8V_{mp}$. The second interval can be considered as $0.8V_{mp} \leq V \leq 0.95V_{mp}$. The third interval consists of MPP and has the highest density of the collected data as $0.95V_{mp} \leq V \leq 1.05V_{mp}$. The last interval is started from zero and ends at V_{oc}, which can be shown as $1.05V_{mp} \leq V \leq V_{oc}$. For each interval ($i$), a quadratic polynomial function (f_i) is fitted to the corresponding experimental data by linear regression analysis, which can be written as:

$$I_i = f_i(V) = a_i V^2 + b_i V + c_i, i = 1, 2, 3, 4 \tag{5}$$

Here, ordinary least square method can be applied to estimate the unknown constant coefficients a_i, b_i, and c_i (for $i = 1, 2, 3, 4$). The ordinary least square formula is written as [32]:

$$\theta_i = (X_i^T X_i)^{-1} X_i^T y_i, \qquad i = 1,2,3,4 \tag{6}$$

where θ_i is vector of unknown constants, X_i is a known regressor matrix and y_i is the measured output vector. By applying equation (6) into equation (5), the constant coefficients a_i, b_i, and c_i can be achieved as:

$$\begin{bmatrix} c_i \\ b_i \\ a_i \end{bmatrix} = \begin{bmatrix} n_i & \sum_{j=1}^{n_i} V_{j,i} & \sum_{j=1}^{n_i} V_{j,i}^2 \\ \sum_{j=1}^{n_i} V_{j,i} & \sum_{j=1}^{n_i} V_{j,i}^2 & \sum_{j=1}^{n_i} V_{j,i}^3 \\ \sum_{j=1}^{n_i} V_{j,i}^2 & \sum_{j=1}^{n_i} V_{j,i}^3 & \sum_{j=1}^{n_i} V_{j,i}^4 \end{bmatrix}^{-1} \begin{bmatrix} \sum_{j=1}^{n_i} I_{j,i} \\ \sum_{j=1}^{n_i} V_{j,i} I_{j,i} \\ \sum_{j=1}^{n_i} V_{j,i}^2 I_{j,i} \end{bmatrix}, \tag{7}$$
$$i = 1, 2, 3, 4$$

where n_i, $V_{j,i}$, and $I_{j,i}$ are the number of data points, voltage, and current values in the i^{th} interval, respectively. Hence, the corresponding piecewise quadratic function can be obtained as:

$$I = f(V) = \begin{cases} f_1(V), & 0 \leq V \leq 0.8V_{mp} \\ f_2(V), & 0.8V_{mp} \leq V \leq 0.95V_{mp} \\ f_3(V), & 0.95V_{mp} \leq V \leq 1.05V_{mp} \\ f_4(V), & 1.05V_{mp} \leq V \leq V_{oc} \end{cases} \tag{8}$$

The main advantage of the least square technique is fast unbiased convergence of the estimated parameters with the lowest variance as verified in [32] for the case of uncorrelated error vector. Therefore, a precise $I-V$ characteristic model is achieved, explicitly and with linear in parameter from.

A. MPP of Explicit Characteristic

If one considers the power-voltage ($P-V$) curve at uniform environmental condition, then, there will be a unique MPP. This point is highly desirable and multiple maximum power point tracking (MPPT) algorithms have been implied to extract maximum power form the PV system [33]. At the voltage in which the maximum power occurs, the derivative of power with respect to voltage is zero. In the derived model, the MPP is located in the third interval which is related to $f_3(V)$. Hence, the voltage value at MPP can be achieved as:

$$\frac{dP}{dV} = \frac{d(V \times f_3(V))}{dV} = f_3(V) + V \times \frac{df_3(V)}{dV} = 0 \tag{9}$$

By substitution of $f_3(V) = a_3 V^2 + b_3 V + c_3$ in equation (9), we have:

$$3a_3 V^2 + 2b_3 V + c_3 = 0 \tag{10}$$

Hence, the voltage at MPP can be easily obtained by analytical solution of quadratic polynomial function in equation (10). Finally, by substitution of the calculated V_{mp} in $f_3(V)$, the maximum power current (I_{mp}) will be achieved. This easy computation of V_{mp} is not comparable with the analysis performed in [23] which considered SDM relation in (4) to obtain V_{mp} for the $I-V$ curve.

Unlike circuits' models which have infinite responses for their parameter estimations problem, here, there is only a unique response. Moreover, the proposed piecewise model guarantees only a unique MPP for a uniform environmental condition.

B. Extension to Other Environmental Conditions

In general, the $I-V$ characteristic will be changed according to the variations of G and T. The proposed approach for developing an explicit $I-V$ characteristic can be easily applied at any environmental condition in real time. In other words, one should collect the data from zero to V_{oc} with higher data density around the MPP. Then, dividing the whole voltage working condition into four intervals as in equation (8). Assign a quadratic function to each interval as in equation (5). Finally, the constant coefficients for each interval can be obtained by equation (7). Also, it is possible to achieve the corresponding V_{mp} by solving equation (10). Although this procedure results in a precise and explicit model at any environmental condition, it may not be acceptable for high rate applications such as MPPT. Moreover, this procedure requires to stop the PV module from working at its regular condition to collect the data, which is not desirable.

The ANN is an efficient approach for updating the estimated coefficients in real time ambient condition as shown in Fig. 2. More specifically, the real experimental data have to be collected for an acceptable wide range of environmental condition offline during a total year. Then, a separate piecewise quadratic function should be assigned for each weather condition according to equation (8). Finally, the ANN should be learned through collected data to realize a black box modelling between G and T as inputs and polynomial coefficients as outputs. This lead to a reliable $I-V$ characteristic model which is applicable for all the environmental conditions. It should be noted that effectiveness of the learned network is related to the reliability, accuracy, and diversity of the collected data.

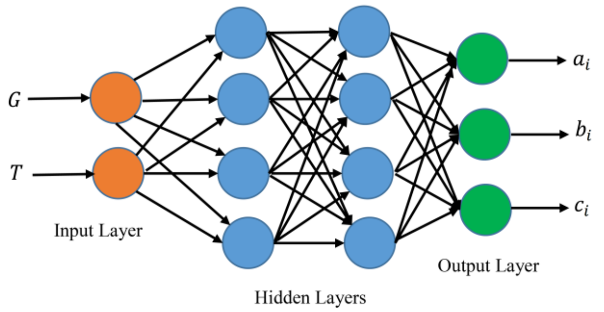

Fig. 2. Schematic representation of the ANN to achieve the model's coefficients for the real G and T values.

A block diagram is provided in Fig. 3 for better interpretation of the established PV model with explicit $I-V$ characteristic based on piecewise quadratic function.

IV. Results and Discussions

Without loss of generality, the popular KC200GT module is considered to validate the effectiveness of the proposed method. It should be noted that this modelling approach can be applied to other PV modules in a similar manner. All the simulations and implementation of the proposed algorithm are developed in MATLAB environment.

First, the experimental data are extracted from module KC200GT at STC. The corresponding data points and the three key working conditions (open circuit, short circuit, and MPP) are illustrated in Fig. 4. It can be observed from this figure that more amount of data is collected in the neighborhood of MPP due to its importance.

All the four quadratic polynomial functions are derived according to the least square technique in relation (7). For the module KC200GT these functions are achieved as:

$$\begin{cases} f_1(V) = -44\times10^{-6}V^2 - 0.0013V + 8.2092 \\ f_2(V) = -0.0154V^2 + 0.6487V + 1.3104 \\ f_3(V) = -0.0663V^2 + 3.1901V - 30.4071 \\ f_4(V) = -0.1639V^2 + 8.5790V - 104.84 \end{cases} \qquad (11)$$

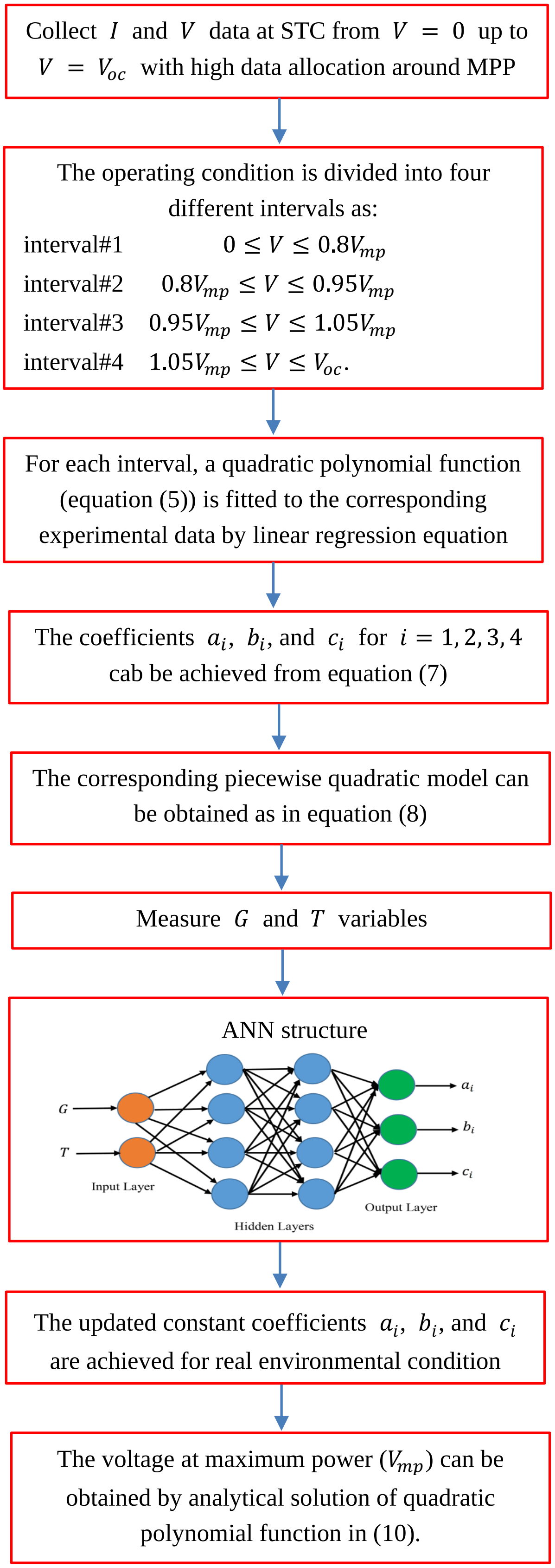

Fig. 3. A simple block diagram of the proposed piecewise quadartic model with an analytical procedure to find MPP

The established model in equation (11) can be easily generated in MATLAB by the command “polyfit(Vi,Ii,2)” where Vi and Ii are measured voltage and current data at the interval number i (i=1,2,3,4).

These polynomial functions are depicted in Fig. 5 for the whole operating condition, i.e., $0 \le V \le V_{oc}$. This figure verifies that each quadratic function has desirable performance at its corresponding voltage interval.

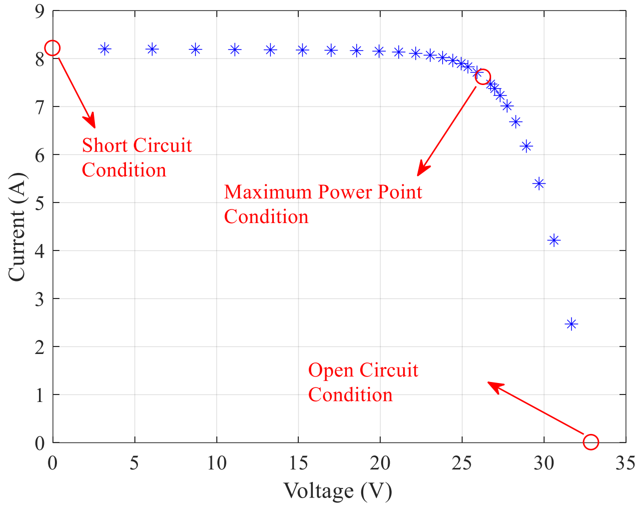

Fig. 4. Experimental data from $I - V$ characteristic of module KC200GT at STC.

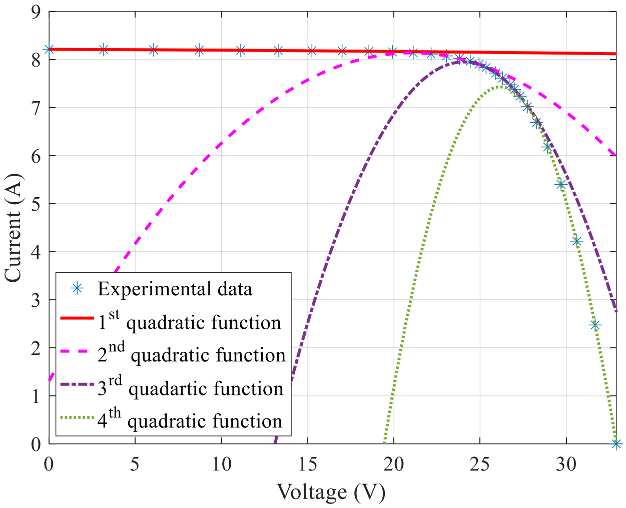

Fig. 5. Four extracted polynomial functions for the total operating condition $0 \le V \le V_{oc}$.

By considering each polynomial at its own extracted interval from equation (8), the derived $I - V$ characteristic can be obtained as it is illustrated in Fig. 6. It can be observed from this figure that a reliable model is achieved for the PV module all over its operating condition. To quantitatively verify the effectiveness of the proposed model, the root mean square error (RMSE) between the simulated current (I) from equation (11) and the measured experimental current (I_m) is calculated as [19]:

$$RMSE = \sqrt{\frac{\sum_{j=1}^{N}\left(I_{mj} - I_j\right)^2}{N}} \tag{12}$$

where N is the number of total experimental data. For the corresponding KC200GT module, we have $RMSE = 0.0068$ which is a very small value.

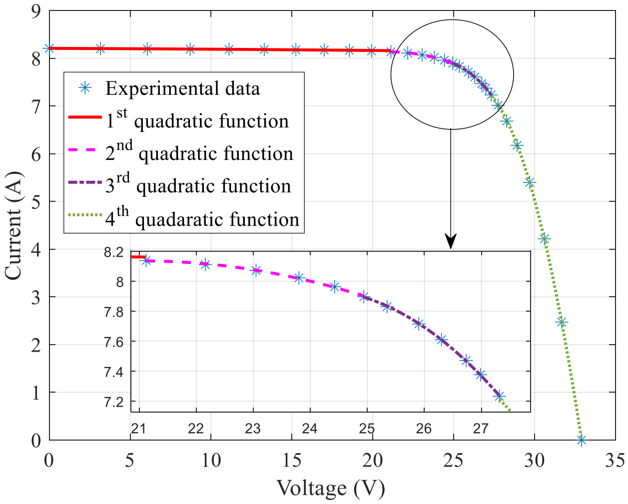

Fig. 6. Explicit piecewise quadratic function for $I - V$ characteristic at STC.

In order to investigate the preciseness of the proposed explicit function at MPP, the $P - V$ curve is illustrated in Fig. 7. For quantitative investigation, the third quadratic function ($f_3(V)$) which consists of MPP is considered again. It can be concluded from equation (10) that $-0.1989V^2 + 6.3802V - 30.4071 = 0$. By solving this quadratic equation for V, the maximum power voltage is achieved as $V_{mp} = 26.2546$ V. Substitution of the calculated V_{mp} in $f_3(V)$ results in obtaining $I_{mp} = 7.6468$ A. These calculated values are very close to the real values specified in the module’s datasheet. Hence, the results show the effectiveness of the proposed $I - V$ curve model at MPP.

A. Comparison with Other Methods

In order to verify the capability of the proposed approach, a comparison is provided with some recent methods including SDM [13], DDM [15], and TDM [19]. First, the generated $I - V$ curve from each method and the corresponding experimental data for the module KC200GT are illustrated in Fig. 8.

According to Fig. 8, for $V < V_{mp}$, the proposed method and the SDM has the best performance while the proposed method is still slightly better. The performance of the TDM is worse than SDM and DDM has the worst behavior for lower voltages. In the neighborhood of MPP, the proposed method and TDM has the best fitness with experimental data. However, the proposed approach shows slightly better fit with measured data. After these two methods, DDM has a better performance compared with SDM. Interestingly, all the four approaches have a desirable performance at the MPP itself. However, it should be noted that achieving MPP can be easily accomplished analytically by the proposed method (equation (10)). On the other hand, analytical calculation of MPP in SDM is relatively complicated and it is almost impossible for DDM and TDM. For $V > V_{mp}$, the piecewise quadratic function has the best modelling potential. After the designed approach, TDM and DDM has reliable performances, respectively. Finally, SDM has noticeably the lowest accuracy among all the four modelling methods.

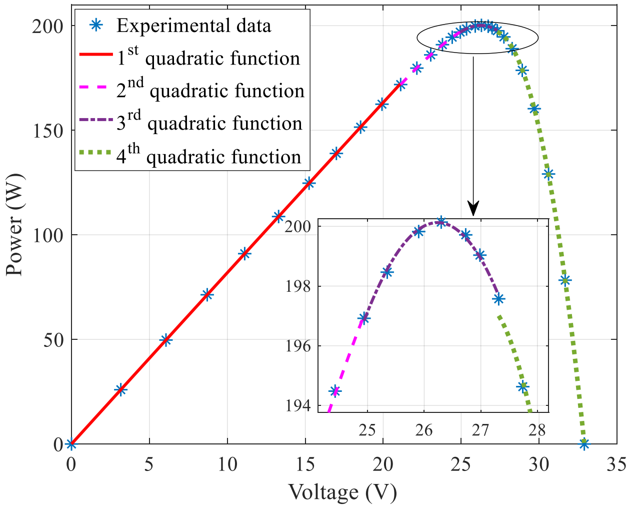

Fig. 7. Explicit piecewise quadratic function for $P - V$ characteristic at STC.

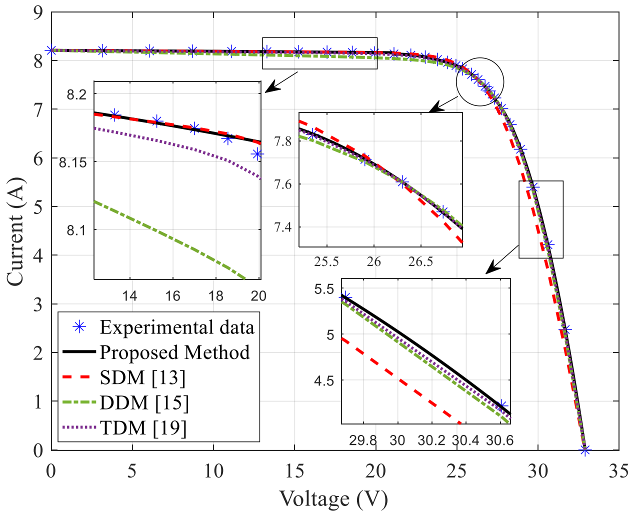

Fig. 8. Comparison between different approaches for $I - V$ characteristic at STC.

From the above discussion, one can conclude that the proposed method represents more reliable and accurate model with respect to circuit models at all operating conditions. For better insight on the performance of each method some quantitative and qualitative analyses are provided in Table 1. The quantitative indices are RMSE, maximum absolute current error (CMAE), maximum absolute power error (PMAE), maximum absolute current error at MPP (CMAE-MPP), and maximum absolute power error at MPP (PMAE-MPP). The qualitative indices include number of unknown parameters, linearity of model with respect to parameters, rate of modelling, complexity, and reliability.

TABLE 1 COMPARISON BETWEEN DIFFERENT PV MODELLING APPROCHES

Comparison indices	Proposed method	SDM [13]	DDM [15]	TDM [19]
RMSE	0.0068	0.1777	0.0628	0.0189
CMAE	0.0187	0.5151	0.1208	0.0554
CMAE-MPP	9.7e-04	0.0077	6.7e-04	3.2e-05
PMAE	0.5298	15.7651	3.8250	1.6962
PMAE-MPP	0.0255	0.2017	0.0176	8.4e-04
Parameters No.	12	5	7	9
Complexity	Very low	Low	High	Very high
Convexity	Yes	No	No	No
Simulation time	Very low	Low	High	Very high
Linear in parameters	Yes	No	No	No

It can be observed from Table 1 that the piecewise quadratic model has the highest accuracy among all the other methods considering the whole operating condition. However, at MPP specifically, DDM and TDM lead to more accurate model. But as previously discussed, analytical calculation of MPP from DDM and TDM is almost impossible. Hence, this specific preciseness is ineffective in practice.

From qualitative points of view, the proposed approach results into a model with very low complexity regardless of its 12 number of unknown parameters. Unlike the circuit models, the piecewise quadratic model is represented linear with respect to its parameters. Hence, it is easy to obtain the unknown parameters with common techniques such as linear least square. By the assumption of the known parameters, the simulated $I - V$ curve from the piecewise quadratic function can be rapidly generated in MATLAB environment. However, numerical simulation of $I - V$ curves for circuit models is much slower. Therefore, the piecewise quadratic model is highly desirable for real time applications of PV systems such as MPPT and fault detection. Moreover, the solution of estimated parameters for the proposed method is unique. On the other hand, all the circuit models lead to non-convex problems for their parameters' estimations. In other words, they all have non-unique solutions. Hence, the piecewise quadratic approach results in more reliable PV model with respect to equivalent circuits.

V. Conclusions

It is important to generate precise and simple model for a typical PV module. This task can be accomplished by using the measured data form $I-V$ characteristic. Although the equivalent circuits are popular modeling approaches, they result in models with an implicit mathematical structure and nonlinear in parameters forms. Hence, this leads to a highly complex, nonlinear, and non-convex model, in which the unknown parameter estimation is difficult and time consuming. These disadvantages may reduce the application of these equivalent circuits, in practice.

In this work, a piecewise quadratic function including four different quadratic functions is generated from the measured $I-V$ data at standard test condition (STC). The interval of each quadratic function is selected such that, the derived model is accurate and relatively simple. One of the intervals is allocated only to the MPP and its small neighboring. Hence, the generated model has high reliability at MPP and it is suitable for model-based maximum power point tracking algorithms. Moreover, the extracted model has high preciseness in all other operating conditions, verified by $RMSE = 0.0068$. Besides, the generated model has an explicit mathematical structure where all the parameters appear in the linear mathematical form. These advantages lead to a model which is desirable for maximum power point tracking, monitoring, and fault detection. Finally, one suggestion was provided to extend the derived model to the other ambient conditions through utilization of ANN.

REFERENCES

[1] A. A. Zamani, M. Shafiee, and M. Sajadinia, "Optimal self-tuning fractional order fuzzy load frequency control considering sustainable energy sources and electric vehicle," International Journal of Ambient Energy, vol. 44, pp. 2170-2184, 2023.

[2] M. A. Hasan and S. K. Parida, "An overview of solar photovoltaic panel modeling based on analytical and experimental viewpoint," Renewable and Sustainable Energy Reviews, vol. 60, pp. 75-83, 2016.

[3] J. Farzaneh and A. Karsaz, "Application of Improved Salp Swarm Algorithm Based on MPPT for PV Systems under Partial Shading Conditions," International Journal of Industrial Electronics, Control and Optimization, vol. 3, pp. 415-429, 2020.

[4] M. Sajadinia, "An adaptive virtual inertia control design for energy storage devices using interval type-2 fuzzy logic and fractional order PI controller," Journal of Energy Storage, vol. 84, Part A, p. 110791, 2024.

[5] R. Daxini, Y. Sun, R. Wilson, and Y. Wu, "Direct spectral distribution characterisation using the Average Photon Energy for improved photovoltaic performance modelling,". Renewable Energy, vol. 201, pp. 1176-1188, 2022.

[6] K. Lappalainen, M. Piliougine, S. Valkealahti, and G. Spagnuolo, "Photovoltaic module series resistance identification at its maximum power production," Mathematics and Computers in Simulation, 2023.

[7] K. Lappalainen, M. Piliougine, and G. Spagnuolo, "Experimental comparison between various fitting approaches based on RMSE minimization for photovoltaic module parametric identification," Energy Conversion and Management, vol. 258, p. 115526, 2022.

[8] H. K. Viljakainen, K. Lappalainen, and S. Valkealahti, "A novel procedure for identifying the parameters of the single-diode model and the operating conditions of a photovoltaic module from measured current–voltage curves," Energy Reports, vol. 8, pp. 4633-4640, 2022.

[9] F. J. Toledo, V. Galiano, J. M. Blanes, V. Herranz, and E. Batzelis, "Photovoltaic single-diode model parametrization: An application to the calculus of the Euclidean distance to an I –V curve," Mathematics and Computers in Simulation, 2023.

[10] Y. Liu, K. Ding, J. Zhang, Y. Lin, Z. Yang, X. Chen, Y. Li, and X. Chen, "Intelligent fault diagnosis of photovoltaic array based on variable predictive models and I–V curves," Solar Energy, vol. 237, pp. 340-35, 2022.

[11] Z. Chen, Y. Chen, L. Wu, S. Cheng, P. Lin, and L. You, "Accurate modeling of photovoltaic modules using a 1-D deep residual network based on I-V characteristics," Energy Conversion and Management, vol. 186, pp. 168-187, 2019.

[12] A. Chikh and A. Chandra, "Adaptive neuro-fuzzy based solar cell model," IET Renewable Power Generation, vol. 8, pp. 679-686, 2014.

[13] M. H. Qais and S. M. Muyeen, "A novel adaptive filtering algorithm based parameter estimation technique for photovoltaic system," IEEE Transactions on Energy Conversion, vol. 37, pp. 286-294, 2022.

[14] J. Xu, C. Zhou, and W. Li, "Photovoltaic single diode model parameter extraction by dI/dV-assisted deterministic method," Solar Energy, vol. 251, pp. 30-38, 2023.

[15] K. Chennoufi, M. Ferfra, and M. Mokhlis, "An accurate modelling of PV modules based on two-diode model," Renewable Energy, vol. 167, pp. 294-305, 2021.

[16] F. F. Liu, S. C. Chu, C. C. Hu, J. Watada, and J. S. Pan, "An effective QUATRE algorithm based on reorganized mechanism and its application for parameter estimation in improved photovoltaic module," Heliyon, vol. 9, p. e16468C, 2023.

[17] A. Şentürk, "A new recursive method based on datasheet information to calculate the double diode model parameters of commercially available photovoltaic modules," Renewable Energy, vol. 227, p. 120507, 2024.

[18] H. Rezk and M. A. Abdelkareem, "Optimal parameter identification of triple diode model for solar photovoltaic panel and cells," Energy Reports, vol. 8, pp. 1179-1188, 2022.

[19] A. M. Shaheen, A. R. Ginidi, R. A. El-Sehiemy, A. El-Fergany, and A. M. Elsayed, "Optimal parameters extraction of photovoltaic triple diode model using an enhanced artificial gorilla troops optimizer," Energy, vol. 283, p. 129034, 2023.

[20] T. N. Olayiwola and S. Choi, "Superellipse model: An accurate and easy-to-fit empirical model for photovoltaic panels," Solar Energy, vol. 262, p. 111749, 2023.

[21] L. E. Mathew and A. K. Panchal, "An exact and explicit PV panel curve computation assisted by two 2-port networks,"

Solar Energy, vol. 240, pp. 280-289, 2022.

[22] A. Jain and A. Kapoor, "Exact analytical solutions of the parameters of real solar cells using Lambert *W*-function," Solar Energy Materials and Solar Cells, vol. 81, pp. 269-277, 2004.

[23] E. Moshksar and T. Ghanbari, "A model-based algorithm for maximum power point tracking of PV systems using exact analytical solution of single-diode equivalent model," Solar Energy, vol. 162, pp. 117-131, 2018.

[24] S. Lun, C. Du, G. Yang, S. Wang, T. Guo, J. Sang, and J. Li, "An explicit approximate I–V characteristic model of a solar cell based on pade approximants," Solar Energy, vol. 92, pp. 147-159, 2013.

[25] A. K. Das, "An explicit *J–V* model of a solar cell using equivalent rational function form for simple estimation of maximum power point voltage," Solar Energy, vol. 98, pp. 400-403, 2013.

[26] S. Lun, C. Du, T. Guo, S. Wang, J. Sang, and J. Li, "A new explicit *I–V* model of a solar cell based on Taylor's series expansion," Solar Energy, vol. 94, pp. 221-232, 2013.

[27] S. Lun, T. Guo, and C. Du, "A new explicit I–V model of a silicon solar cell based on Chebyshev Polynomials," Solar Energy, vol. 119, pp.179-194, 2015.

[28] Y. Mahmoud, M. Abdelwahed, and E. F. El-Saadany, "An Enhanced MPPT Method Combining Model-Based and Heuristic Techniques," IEEE Transactions on Sustainable Energy, vol. 7, pp. 576-585, 2016.

[29] N. Boutana, A. Mellit, S. Haddad, A. Rabhi, and A. M. Pavan, "An explicit I-V model for photovoltaic module technologies," Energy Conversion and Management, vol. 138, pp. 400-412, 2017.

[30] M. Louzazni and S. Al-Dahidi, "Approximation of photovoltaic characteristics curves using Bezier Curve," Renewable Energy, vol. 174, pp. 715-732, 2021.

[31] M. Shafiee, A. A. Zamani, and M. Sajadinia, "Using Improved DDAO Algorithm to Solve Economic Emission Load Dispatch Problem in Presence of Wind Farms," International Journal of Industrial Electronics, Control and Optimization, vol. 6, pp. 161-169, 2023.

[32] R. A. Johnson and D. W. Wichern, "Applied Multivariate Statical Analysis," Pearson Printice Hall, Upper Saddle River, 6th ed., 2002.

[33] M. Rahideh, A. Ketabi, and A. H. Niasar, "Maximum Power Point Tracking Using a State-dependent Riccati Equation-based Model Reference Adaptive Control," International Journal of Industrial Electronics, Control and Optimization, vol. 3, pp. 115-124, 2020.

Ehsan Moshksar was born in Shiraz, Iran in 1985. He received the B.Sc. and M.Sc. degrees in Electrical Engineering from Shiraz University, Shiraz, Iran, in 2008 and 2011, respectively, and the Ph.D. degree in Chemical Engineering from Queen's University, Kingston, ON, Canada, in 2015. He is currently an Assistant Professor in the School of Advanced Technologies, Shiraz University, Shiraz, Iran. His research interests include nonlinear systems, adaptive control, parameter estimation, and real-time optimization with application to electrical, mechanical, and chemical systems.

IECO

This page intentionally left blank.

IECO
International Journal Of
Industrial Electronics Control and Optimization
Print ISSN: 3517-2645
Online ISSN: 3568-2645
Homepage: https://ieco.usb.ac.ir/

A Minimum Phase DC-DC Converter with High Voltage Gain and Continuous Input Current

Keyvan Yari[1] | Sara Hasanpour[2]

Department of Electrical engineering, TU Delft University, Mekelweg 4, 2628 CD Delft, Netherlands.
Department of Electrical engineering, Ramsar Branch, Islamic Azad University, Ramsar, Iran. [2]
Corresponding author's email: Sara.Hasanpour@iau.ac.ir

Article Info

Article type:
Research Article

Article history:
Received: 03-June-2024
Received in revised form:
20-July-2024
Accepted: 01-August-2024
Published online: 21-Dec-2024

Keywords:
High step-up converter,
Fast dynamic response,
Renewable energies,
Low ripple input current.

ABSTRACT

This paper presents a new design of a minimum phase high step-up DC-DC converter with a fast dynamic response for renewable energy systems. In addition to the common ground sharing between the input and output ports, the proposed converter draws a low ripple current from the input source, prolonging the input source's life cycle. Moreover, eliminating the right half plane zero from the control to output transfer function enables the converter to provide fast dynamic responses. Moreover, low voltage stress across the circuit components, simple structure, and low EMI are other merits of the suggested topology. Theoretical analysis, including the principle of operation, the mathematical calculation for steady-state operation, and small-signal modeling derivation, are clarified in detail. At last, to verify these analyses and the mentioned features of the proposed converter, a 25V input voltage, 100V output voltage and 100 W output power with 50 kHz switching frequency laboratory prototype has been implemented, and the main experimental results have also been outlined.

NOMENCLATURE

T	TIME DURATION OF A SWITCHING CYCLE
f_s	SWITCHING FREQUENCY
D	DUTY CYCLE OF THE POWER SWITCH
r_{Lk}	TOTAL PARASITIC RESISTANCE OF COUPLED INDUCTORS
$r_{Do(i)}, V_{FDo(i)}$	THE ITH DIODE PARASITIC RESISTANCE AND VOLTAGE DROP
t_{on}, t_{off}	THE SWITCH TURN-ON AND TURN-OFF TIMES
r_L	PARASITIC RESISTANCE OF THE INPUT INDUCTOR L
$r_{C(i)}$	THE ITH CAPACITOR PARASITIC RESISTANCE

I. Introduction

Global warming has been seen as an accelerating issue over the past decades that only gets worse. Needless to say, burning fossil fuels and the released greenhouse gases are the primary causes of this trend [1]. As a result of this worrying trend, researchers have paid ever-increasing attention to promising renewable energy sources such as wind and solar power and their penetration into the power grid [2-4]. Although solar power is the most convenient renewable power source across the planet, photovoltaic (PV) panels cannot be directly connected to the utility grid since their output voltage is much

Publisher: University of Sistan and Baluchestan

lower than the utility grid's demanded voltage. Hence, PV panels need an interface to inject their power into the power grid [5-7]. Conventional Boost Converter (CBC) is the most prevalent choice for step-up applications due to its simple structure and easy control. However, CBC suffers from multiple drawbacks, such as high voltage stress on its semiconductors, limited voltage gain, and low efficiency. To overcome these problems, extensive research has been done to report numerous DC-DC converters capable of realizing high efficiency and high voltage gain without extreme voltage stress across their semiconductors [8-12].

On the other hand, fast dynamic response is vital for many applications, namely portable electronic devices, DC microgrids, energy storage systems, and especially transformation electrification [13, 14]. In view of the fact that CBC's control to output transfer function has a Right-Half Plane Zero (RHPZ), it is a non-minimum phase system. Subsequently, many efforts have been put into improving the dynamic response of step-up DC-DC converters.

A damping network has been employed in several structures to eliminate RHPZ. These converters add a series Resistance-Capacitance (RC) to their structure to move the RHPZ to the left-hand side, hence improving the dynamic response of the converter. A damping network was added to the diode-capacitor-based boost and buck-boost converters to avoid the RHPZ in their structures [15]. Apart from the lack of common ground sharing between the input and output ports and the discontinuous input current of the buck-boost converter, both suffer from low voltage gain and low efficiency. In [16], a bidirectional switched capacitor DC-DC converter was reported, which uses a damping network to exclude right-half plane zero from its control to output transfer function. Also, a dual output AC/DC hybrid converter with a damping network was introduced in [17] to obtain minimum phase characteristic. All the same, the voltage gain is equal to the conventional buck-boost converter. On the other hand, using the RC networks leads to power losses in these converters, and the lack of high efficiency is a significant setback.

Complex control approaches have been used to realize minimum phase behavior for DC-DC converters. Time-based control technique was applied to CBC in [18] to remove the RHPZ and modify the dynamic response of the converter. The sampling position approach in a dual-loop digital average current mode controller was implemented to cancel the RHPZ in CBC [19]. Another method named Passivity-Based Control (PBC) was proposed and applied to CBC in [20] for better dynamic response. Yet, the non-minimum phase characteristic of CBC and Z-source converter was tackled with Active Disturbance Rejection Control (ADRC) and cascaded sliding mode controller in [21] and [22], respectively. Despite improving the dynamic response using advanced controllers, the power circuit of CBC and Z-source converter still faces several challenges, including limited voltage gain, high voltage stress across semiconductors, inefficient energy conversion, etc. The performance of the general predictive and linear controllers in overcoming the non-minimum phase feature of a multi-input boost converter [23]. This investigation confirms that General Predictive Control (GPC) accomplishes faster dynamic response and more robustness than linear controller.

Researchers have addressed removing the RHPZ by changing CBC's structure and turning it into Tri-state converters [24, 25]. These converters add a power switch and a diode to CBC to cancel the right-half plane zero from their control to the output transfer function. However, these structural modifications cause the ripple in the input current to rise. Hence, [26] offered an interleaved-based tri-state boost converter to tackle this issue. Nevertheless, with these enhancements, the voltage gain of these converters is still constrained, rendering them improper for high voltage gain demands. Similar to tri-state converters, a third-order boost converter was also introduced to increase voltage gain conversion [27]. But, the input and output ports do not share a common ground. Besides, due to the high ripple input current, the converter falls short of the imperative specifications for practical applications. Employing coupled inductors is another approach to cancel out the RHPZ in DC-DC converters. This technique was implemented in [28] for eliminating the RHPZ since it can establish a path from the input source to the output load when the main switch is in its ON state. Despite possessing a fast dynamic response, the converter has a voltage gain equal to CBC and employs a damping network, resulting in efficiency degradation. Three inductors were coupled in [29] and [30] to limit the input current ripple while transferring the RHPZ to the left-hand side. Like the converter in [28], the restricted voltage gain deteriorates the overall performance of the converters. Furthermore, the low coupling coefficient is another drawback that leads to energy loss of magnetic elements and construction complexity. To attain the requirements for high step-up voltage gain, coupled inductors have also been utilized to acquire simultaneous minimum phase feature and high voltage conversion ratios in several DC-DC converters [31-34]. By making a forward path from the input source to the output load during the ON time of the power switch, the boost-forward converter in [31] can offer minimum phase characteristic and higher voltage gain compared to all the previously mentioned converters. However, the input current ripple is large, reducing the input source's life span. The voltage gain was improved by utilizing switched capacitors and coupled inductors in the reported converters in [32, 33]. Despite improving voltage gain, the high input current ripple drawback still persists. To resolve the high input current ripple problem, an interleaved-based converter was proposed in [33]. Whilst the converter offered a lower input current ripple compared to [31], the ripple is still high due to using an asymmetrical structure of the coupled inductors [35, 36].

Juxtaposing all the pros and cons of the above-mentioned minimum phase converters, none can provide high voltage gain while drawing a low ripple current from the input source. Hence, the primary novelty of this paper is the proposal for a minimum phase DC-DC converter by combining boost forward [31] and conventional boost converter. In addition to the fast dynamic response, high voltage gain, low ripple input current, and common ground sharing between input and output ports are other merits of the presented converter. Thanks to these characteristics, the new converter is compatible with many applications.

The remainder of this paper is organized as follows: Section II describes the operation principles of the proposed converter. Voltage and current stresses have been derived in Section III. Section IV represents the small-signal modeling process. Performance comparison is introduced in Section V. Experimental results are discussed in Section VI. Lastly, Section VII concludes the paper.

II. Principles of Operation

The proposed converter is comprised of one power switch S, one inductor L, two diodes D_{o1}, and D_{o2}, three capacitors C_1, C_{o1} , and C_{o2} and two coupled inductors N_1 and N_2. The proposed converter equivalent circuit is shown in Fig. 1. The voltage and current associated with each element are shown separately.

With the object of simplifying calculation for steady-state analysis, the below assumptions are taken into account;

1) The capacitors' voltage is considered constant during one switching cycle.
2) All the circuit elements are ideal. Hence, the power switch's turn-on resistance, diodes' voltage drop during on state, and parasitic resistances of the capacitors and inductors are ignored.
3) A transformer with a leakage inductance L_k and a large magnetizing inductance L_M is used to model the coupled inductors.

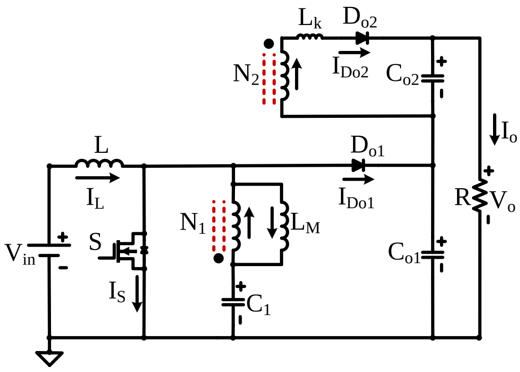

Fig. 1. The proposed converter.

4) The proposed converter operates in Continuous Conduction Mode (CCM).

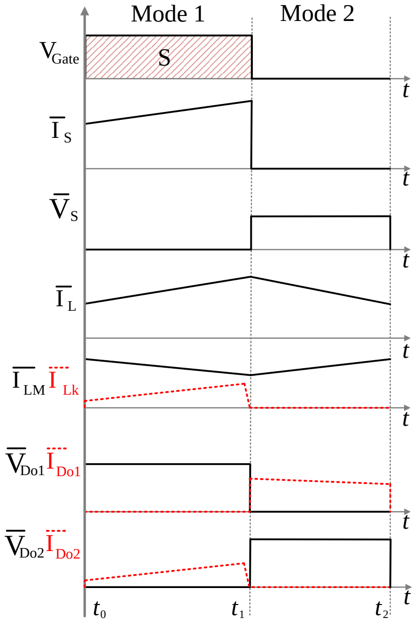

Fig. 2. Key waveforms of the proposed converter in a switching cycle.

Fundamental waveforms of the proposed converter are drawn in Fig. 2. The proposed converter has two operational stages. They are described in detail below.

Mode 1 $[t_0 - t_1]$: At $t = t_0$ switch S is turned ON by the driving circuit, and the diode D_{o1} is turned OFF. The input voltage source V_{in} gives energy to the inductor L. At the same time, the capacitor C_1 together with magnetizing inductance L_M charge capacitor C_{o2} and the output load through the coupled inductors and diode D_{o2}. Moreover, the output capacitors C_{o1} and C_{o2} supply the load at this time interval. The following equations are derived for this operational stage.

$$V_L = V_{in} \tag{1}$$

$$V_{Lk} = -V_{Co2} + nV_{C1} \tag{2}$$

$$V_{LM} = V_{C1} \tag{3}$$

$$V_o = V_{Co1} + V_{Co2} \tag{4}$$

$$I_{Lk} = I_{Co2} + I_o \tag{5}$$

Mode 2 $[t_1 - t_2]$: At $t = t_1$ switch S is turned OFF by the driving circuit, and the diode D_{o2} is turned OFF. Besides, diode D_{o1} is turned ON. Accordingly, the stored energy in the inductor L is released to magnetizing inductance L_M, capacitor C_1 and capacitor C_{o1}. Like the previous mode, output capacitors C_{o1} and C_{o2} supply the load. The following equations are derived in this operational stage.

$$V_L = V_{in} - V_{Co1} \tag{6}$$

$$V_o = V_{Co1} + V_{Co2} \tag{7}$$

$$V_{LM} = V_{C1} - V_{Co1} \tag{8}$$

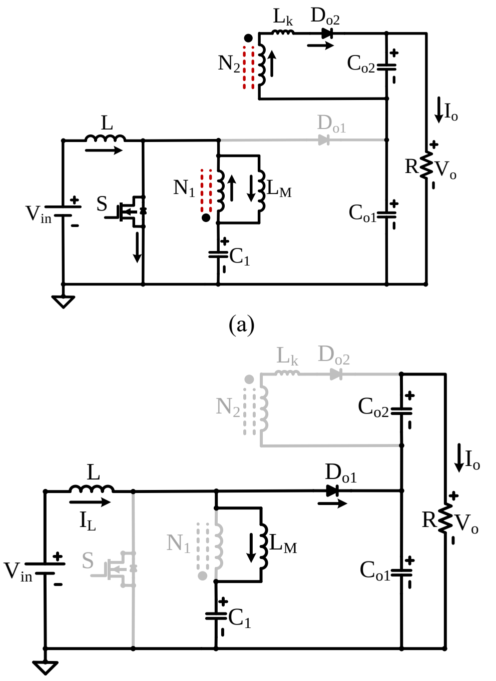

(a)

(b)

Fig. 3. Equivalent circuit of the proposed converter in a switching cycle (a) Mode 1 and (b) Mode 2.

$$I_{Do1} = I_o + I_{Co1} \tag{9}$$

The equivalent circuits for both operational stages are depicted in Fig. 3.

III. Steady-State Analysis of the Proposed Converter

A. *Voltage stress across circuit elements*

This section calculates all the elements' voltage stresses. Then, the voltage gain of the converter is derived. Since the input voltage source, input inductor L, magnetizing inductor L_M, and capacitor C_1 make a loop, the average voltage across the capacitor C_1 is equal to the input voltage;

$$V_{C1(avg)} = V_{in} \tag{10}$$

Hence, the voltage across the capacitor C_{o2} is derived as

$$V_{Co2} = nV_{in} \tag{11}$$

in which $n = \frac{N_2}{N_1}$ is the turns ratio of the coupled inductors. Moreover, by applying the volt-second balance law to the input inductor L, the below equations can be written.

$$\int_0^{DT} V_{in} dt + \int_{DT}^{T} (V_{in} - V_{Co1}) dt = 0 \tag{12}$$

$$V_{Co1} = \frac{V_{in}}{1-D} \tag{13}$$

Now, from (11) and (13), the voltage gain of the proposed converter equals (14).

$$M = \frac{V_o}{V_{in}} = \frac{1}{1-D} + n \tag{14}$$

One can see that the voltage gain of the converter can be controlled by both the duty cycle of the power switch and the turn ratio of the coupled inductors.

B. *Semiconductor's voltage stresses*

From operational principals, the power switch S and diode D_{o1} should tolerate a voltage equal to V_{C1} during their OFF state. As a result, their voltage stresses are calculated as

$$V_{Do1} = V_S = \frac{V_{in}}{1-D} \tag{15}$$

And the voltage stress of the diode D_{o2} can be written as (16).

$$V_{Do2} = V_{Co2} - V_{N2} = \frac{nV_{in}}{1-D} \tag{16}$$

C. *Current stress analysis of circuit elements*

Notably, the proposed converter's power losses and the inductors' current ripple are ignored to facilitate current stress analysis. Now, the average current of the input inductor L can be expressed as

$$I_{L1(avg)} = MI_o = \left(\frac{1}{1-D} + n\right) I_o \tag{17}$$

Additionally, by applying the charge-balance law to the capacitor C_{o1}, the following equations are obtained.

$$\int_0^{DT} -I_o \, dt + \int_{DT}^{T} (I_L - I_{LM} - I_o) dt = 0 \tag{18}$$

$$I_{LM(avg)} = nI_o \tag{19}$$

Given the above equations and doing some mathematical calculations, the average, maximum, and Root Mean Square (RMS) currents of the power switch and diodes are acquired as

$$I_{S(avg)} = DI_o \left(\frac{1}{1-D} + \frac{n}{D}\right) \tag{20}$$

$$I_{Do1(avg)} = I_{Do2(avg)} = I_o \tag{21}$$

$$I_{S(max)} = I_o \left(\frac{1}{1-D} + \frac{2n}{D}\right) \tag{22}$$

$$I_{Do1(max)} = \frac{2I_o}{1-D} \tag{23}$$

$$I_{Do2(max)} = \frac{2I_o}{D} \tag{24}$$

$$I_{S(RMS)} = I_o \sqrt{\frac{D}{(1-D)^2} + \frac{2n}{1-D} + \frac{4n^2}{3D}} \tag{25}$$

$$I_{Do1(RMS)} = I_o \sqrt{\frac{7}{3(1-D)}} \tag{26}$$

$$I_{Do2(RMS)} = \frac{2I_o}{\sqrt{3D}} \tag{27}$$

Finally, the RMS currents of the leakage inductance and the capacitors are given by

$$I_{Lk} = I_{C1(RMS)} = nI_o \sqrt{\frac{4-3D}{3D}} \tag{28}$$

$$I_{Co1(RMS)} = I_o\sqrt{\frac{D}{1-D}} \tag{29}$$

$$I_{Co2(RMS)} = I_o\sqrt{\frac{4-3D}{3D}} \tag{30}$$

The voltage gain of the proposed converter as a function of the duty cycle at multiple turns ratio is illustrated in Fig. 4.

Likewise, the power switch's normalized RMS current by considering various turn ratios is shown in Fig. 4. As evidenced, the voltage gain has a straightforward relation with both the duty cycle and turns ratio of the coupled inductors. On the contrary, the normalized RMS current of the power switch decreases as the duty cycle increases. Meanwhile, the coupled inductors' turn ratio limits the falling rate.

IV. Small Signal Modelling

This section explains the small-signal modeling process and its mathematical derivation. Since DC-DC converters contain nonlinear elements, such as switches and diodes, they are inherently nonlinear systems. Hence, the proposed converter's Nonlinear Time-Variant (NLTV) model is transformed into a linear time-invariant (LTI) model by employing the State Space Average (SSA) method.

Moreover, it is essential to note that the voltages across the capacitors and the currents through the inductors are considered state variables. In the interest of using the SSA method, differential equations associated with each mode, with the help of Kirchhoff's Voltage and Current Laws (KVL and KCL), are written as

Mode 1:

$$\frac{di_L}{dt} = \frac{-r_L i_L}{L} + \frac{V_{in}}{L} \tag{31}$$

$$\frac{di_{LM}}{dt} = \frac{v_{C1}}{L_M} \tag{32}$$

$$\frac{dv_{C1}}{dt} = \frac{-i_{LM}}{C_1} - \frac{n^2DT_s}{L_kC_1}v_{C1} + \frac{nDT_s}{L_kC_1}v_{Co2} \tag{33}$$

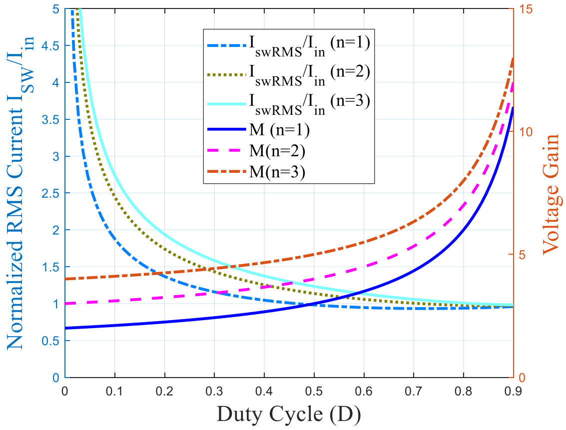

Fig. 4. Voltage gain and switch's normalized RMS currents for various coupled inductors turn ratio.

$$\frac{dv_{Co1}}{dt} = -\frac{(v_{Co1}+v_{Co2})}{RC_{o1}} \tag{34}$$

$$\frac{dv_{Co2}}{dt} = \frac{nDT_s}{L_kC_{o2}}v_{C1} - \frac{v_{Co1}}{RC_{o2}} - \left(\frac{1}{RC_{o2}} + \frac{DT_s}{L_kC_{o2}}\right)v_{Co2} \tag{35}$$

Mode2:

$$\frac{di_L}{dt} = \frac{-r_L i_L}{L} - \frac{v_{Co1}}{L} + \frac{V_{in}}{L} \tag{36}$$

$$\frac{di_{LM}}{dt} = \frac{v_{C1}}{L_M} - \frac{v_{Co1}}{L_M} \tag{37}$$

$$\frac{dv_{C1}}{dt} = -\frac{i_{LM}}{C_1} \tag{38}$$

$$\frac{dv_{Co1}}{dt} = \frac{i_L}{C_{o1}} + \frac{i_{LM}}{C_{o1}} - \frac{(v_{Co1}+v_{Co2})}{RC_{o1}} \tag{39}$$

$$\frac{dv_{Co2}}{dt} = -\frac{(v_{Co1}+v_{Co2})}{RC_{o2}} \tag{40}$$

The closed-form of the state equations can now be written by applying the time weight coefficients of every operational stage to equations (31)-(40) as follows.

$$\begin{cases}\dot{x} = Ax + Bu \\ y = Cx + Eu\end{cases} \tag{41}$$

in which $x, y,$ and u are the state variables, the output voltage, and the input matrix, respectively. Additionally, the final form of A, B, C, and E are expressed as

$$A = \begin{bmatrix} \frac{-r_L}{L} & 0 & 0 & \frac{D-1}{L} & 0 \\ 0 & 0 & \frac{1}{L_M} & \frac{D-1}{L_M} & 0 \\ 0 & \frac{-1}{C_1} & \frac{-T_sD^2n^2}{C_1L_k} & 0 & \frac{T_sD^2n}{C_1L_k} \\ \frac{1-D}{C_{o1}} & \frac{1-D}{C_{o1}} & 0 & \frac{-1}{RC_{o1}} & \frac{-1}{RC_{o1}} \\ 0 & 0 & \frac{T_sD^2n}{C_{o2}L_k} & \frac{-1}{RC_{o2}} & -\frac{(RT_sD^2+L_k)}{RC_{o2}L_k} \end{bmatrix} \tag{42}$$

$$B^T = \begin{bmatrix}\frac{1}{L} & 0 & 0 & 0 & 0\end{bmatrix} \tag{43}$$

$$C = \begin{bmatrix}0 & 0 & 0 & 1 & 1\end{bmatrix} \tag{44}$$

$$E = 0 \tag{45}$$

with the help of the following equations, the steady state value of all the variables can be determined as follows.

$$I_L = (n + \frac{1}{1-D})I_o \tag{46}$$

$$V_{Co1} = \frac{V_{in} - r_L I_L}{1-D} \tag{47}$$

$$V_{C1} = (1-D)V_{Co1} \tag{48}$$

$$V_{Co2} = \frac{L_kV_{Co1} - RT_sD^2nV_{C1}}{RT_sD^2 + L_k} \tag{49}$$

$$I_{LM} = \frac{T_sD^2n(V_{Co2} - nV_{C1})}{L_k} \tag{50}$$

Moreover, a comparison has been made to validate the modeling accuracy between the circuit's and model's responses. The result is depicted in Fig. 5. As shown, there is a step change in the input voltage value, from 50V to 60V at $t = 0.05s$, in which both responses have a wise agreement. Accordingly, the converter's model is valid for further analysis.

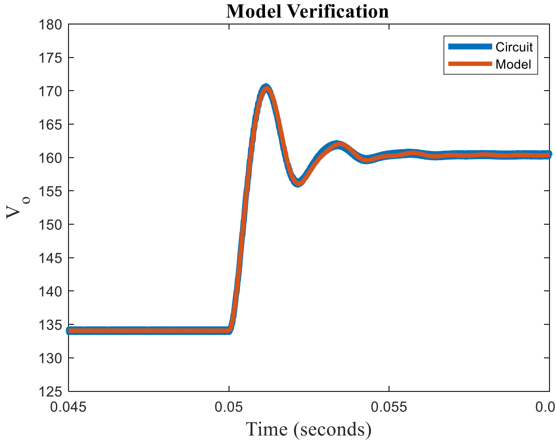

Fig. 5. Circuit's response and model's response comparison.

A small signal model is required to extract the conditions that make the proposed converter behave like a minimum-phase system. As a result, small ac perturbations (negligible compared to steady-state values) are added to the DC values of the state variables, the input voltage, and the duty cycle. These added ac perturbations with the "^" sign and the DC values in capital form are summarized in (51).

$$\begin{cases} x = X + \hat{x} \\ d = D + \hat{d} \\ v_{in} = V_{in} + \hat{v}_{in} \end{cases} with \begin{cases} |\hat{x}|"|X| \\ |\hat{d}|"|D| \\ |\hat{v}_{in}|"|V_{in}| \end{cases} \quad (51)$$

After applying (51) to (31)-(40), doing some calculations, and linearizing the model at the operation point via using (46)-(50), the small signal model of the proposed converter is determined as follows;

$$\begin{cases} \dot{\hat{x}} = A_s\hat{x} + B_s\hat{u} \\ \hat{y} = C_s\hat{x} + E_s\hat{u} \end{cases} \quad (52)$$

Where As is:

$$\begin{bmatrix} \frac{-r_L}{L} & 0 & 0 & \frac{D-1}{L} & 0 \\ 0 & 0 & \frac{1}{L_M} & \frac{D-1}{L_M} & 0 \\ 0 & \frac{-1}{C_1} & \frac{-T_sD^2n^2}{C_1L_k} & 0 & \frac{T_sD^2n}{C_1L_k} \\ \frac{1-D}{C_{o1}} & \frac{1-D}{C_{o1}} & 0 & \frac{-1}{RC_{o1}} & \frac{-1}{RC_{o1}} \\ 0 & 0 & \frac{T_sD^2n}{C_{o2}L_k} & \frac{-1}{RC_{o2}} & -\frac{(RT_sD^2+L_k)}{RC_{o2}L_k} \end{bmatrix} \quad (53)$$

$${B_s}^T = \begin{bmatrix} \frac{1}{L} & 0 & 0 & 0 \\ \frac{V_{Co1}}{L} & \frac{V_{Co1}}{L_M} & \frac{2T_snD[V_{Co2}-nV_{C1}]}{C_1L_k} & -\frac{I_L+I_{LM}}{C_{o1}} \end{bmatrix} \quad (54)$$

$$C_s = [0 \quad 0 \quad 0 \quad 1 \quad 1] \quad (55)$$

$$E_s = 0 \quad (56)$$

$$\hat{u} = \begin{bmatrix} \widehat{v_{in}} \\ \hat{d} \end{bmatrix} \quad (57)$$

$$\hat{x}^T = [\widehat{i_L} \quad \widehat{i_{LM}} \quad \widehat{v_{C1}} \quad \widehat{v_{Co1}} \quad \widehat{v_{Co2}}] \quad (58)$$

Hence, by employing the Laplace transformation, the control-to-output transfer function G_{vod} is obtained as

$$G_{vod}(s) = \frac{\widehat{v_o}}{\hat{d}} = C_s(SI - A_s)^{-1}B_s + E_s \quad (59)$$

Using (59), the control to output transfer function G_{vod} can be rewritten as (60).

$$G_{vod} = \frac{\widehat{v_o}}{\hat{d}} = \frac{a_4s^4 + a_3s^3 + a_2s^2 + a_1s + a_0}{b_5s^5 + b_4s^4 + b_3s^3 + b_2s^2 + b_1s + b_0} \quad (60)$$

From (60), the control to output transfer function has four zeros and five poles. To force the converter to function like a minimum phase system, all the zeros should be placed on the left-hand side of the s-plane. As a result, the Routh-Hurwitz condition must be met by coefficients $a_1 - a_4$. The following conditions are produced when the coefficients $a_1 - a_4$ are subjected to this criterion.

$$a_4 > 0, a_3 > 0, a_0 > 0, a_2a_3 - a_4a_1 > 0, a_1\left[\frac{a_2a_3 - a_4a_1}{a_3}\right] - a_0a_3 > 0 \quad (61)$$

Fig. 6 (a) sketches the pole-zero map of G_{vod}, by employing the parameters in TABLE 1 at various output loads. Obviously, the system does not have any right-hand side zeros after considering the conditions summarized in (61). Hence, the converter benefits from the minimum phase characteristic. This figure also demonstrates that zeros with relatively higher frequency move considerably farther as the output load rises. Conversely, high-frequency poles move toward the imaginary axis as the output load increases.

Moreover, the area near the imaginary axis has been enlarged for better understanding in Fig. 6(b). As seen, with the output load increment, zeros and poles with relatively lower frequencies are shifted toward $j\omega$ axis. Finally, the Bode diagram of G_{vod} is illustrated in Fig. 7 for different output loads.

TABLE 1. OPERATING POINT'S SPECIFICATIONS OF THE PROPOSED CONVERTER

Parameters	Value
V_{in}	25V
L, r_L	300µH, 22mΩ
$L_M(turnsratio = n_1{:}n_2)$	460µH (1:2)
L_k	5µH
C_1, C_{o1}, C_{o2}	50µF, 68 µF, 50µF
R	50-150 Ω
f_s	50kHz

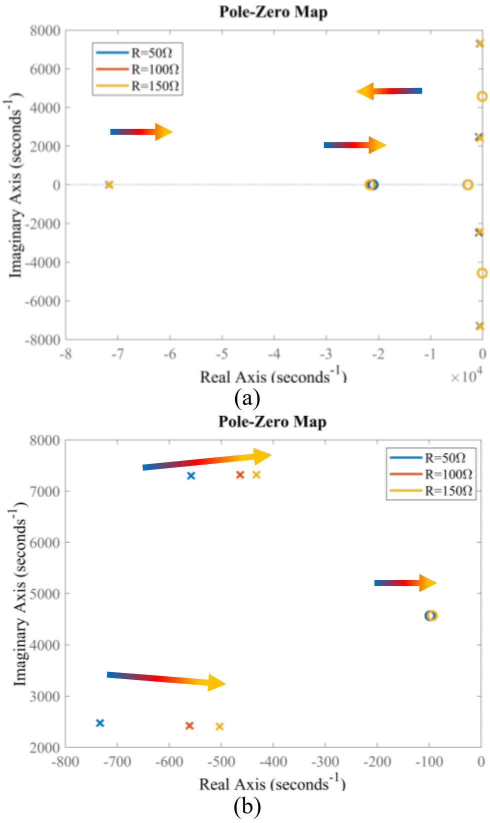

(a)

(b)

Fig. 6. Pole-Zero Map of G_{vod} at various output loads (a) Original Map, (b) Enlarged Map.

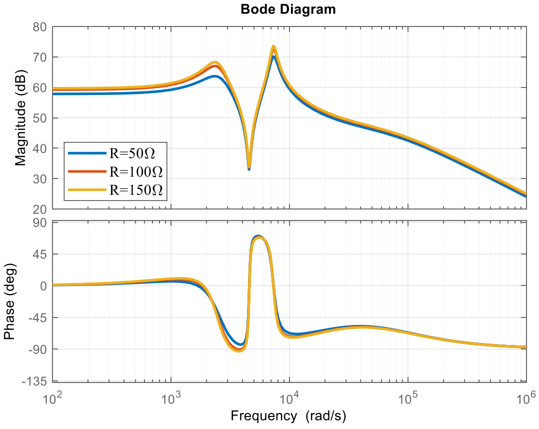

Fig. 7. Bode plot of G_{vod} at various output loads.

V. Comparison with Similar Converters

Since several studies about DC-DC converters with minimum and non-minimum phase features have been published, this section compares the proposed converter and its counterparts comprehensively.

Firstly, the normalized voltage stress of the power switch is compared for the proposed converter and DC-DC converters summarized in Fig. 8. Based on Fig.8 (a), the normalized power switch's voltage stress of [15]-boost, [32] and [33] are lower than the proposed converter. However, these converters suffer from high ripple input currents. Secondly, from Fig. 8 (b), the voltage gain of the proposed converter is higher than all the suggested converters except [12], [32] and [33]. It should be noted that the reported converter in [12] is a non-minimum phase converter and struggles with slow dynamic response. In the case of normalized input current ripple, Fig. 8 (c) confirms that only the converter in [26] can offer a lower input current ripple only for the duty cycle around 0.5.

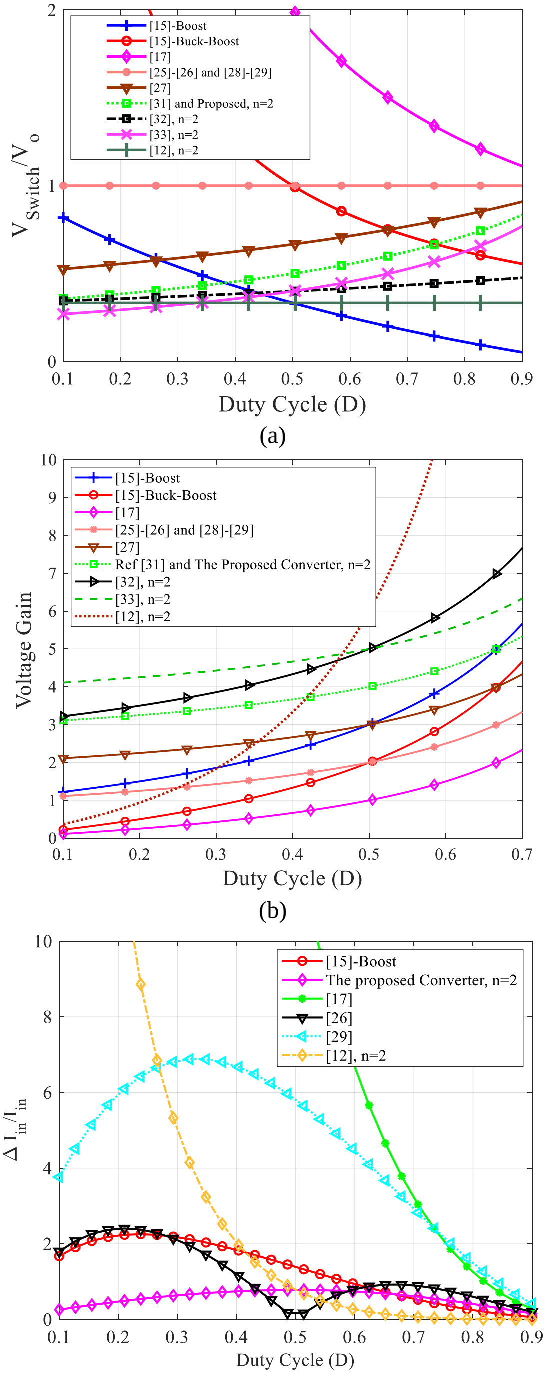

(a)

(b)

(c)

Fig. 8. Comparison with other minimum phase converters (a) Normalized voltage stress of the power switch, (b) Voltage gain comparison, and (c) Normalized input current ripple comparison.

TABLE 2 COMPARISON WITH OTHER SIMILAR CONVERTERS

Item / Converter	Voltage gain	Number of elements*						Voltage stress on switch(es)	Highest voltage stress on diodes	ICR**	C. G***
		MC	C	D	S	R_d	T				
Ref [15] Boost	$\frac{1+D}{1-D}$	2	5	2	1	2	12	$\frac{(1-D)V_o}{1+D}$	$\frac{(1-D)V_o}{1+D}$	Low	×
Ref [15] Buck-Boost	$\frac{2D}{1-D}$	2	5	2	1	2	12	$\frac{V_o}{2D}$	$\frac{V_o}{2D}$	High	×
Ref [17] DC Part	$\frac{D}{1-D}$	2	3	1	4	-	10	$\frac{V_o}{D}$	$\frac{V_o}{D}$	Low	✓
Ref [25]	$\frac{1}{1-D}$	1	1	2	2	-	6	V_o	V_o	High	✓
Ref [26]	$\frac{1}{1-D}$	2	1	4	4	-	11	V_o	V_o	Low	✓
Ref [27]	$\frac{2-D}{1-D}$	1	2	2	1	-	6	$\frac{V_o}{2-D}$	$\frac{V_o}{2-D}$	High	×
Ref [28]	$\frac{1}{1-D}$	1	2	1	1	1	7	V_o	V_o	High	✓
Ref [29]	$\frac{1}{1-D}$	1	3	1	1	-	6	V_o	V_o	Low	✓
Ref [31]	$n+\frac{1}{1-D}$	1	2	2	1	-	6	$\frac{V_o}{n(1-D)+1}$	$\frac{nV_o}{n(1-D)+1}$	High	✓
Ref [32]	$1+\frac{n}{1-D}$	1	3	3	1	-	8	$\frac{V_o}{1-D+n}$	$\frac{nV_o}{2+n-D}$	High	✓
Ref [33]	$n+\frac{2-D}{1-D}$	2	3	3	1	-	9	$\frac{V_o}{n(1-D)+2-D}$	$\frac{nV_o}{n(1-D)+2-D}$	High	✓
Ref [12]	$\frac{(1+n)D}{(1-D)^2}$	2	3	3	2	-	10	$\frac{V_o}{n+1}$	$\frac{nV_o}{(1+n)D}$	Low	✓
Proposed converter	$n+\frac{1}{1-D}$	2	3	2	1	-	8	$\frac{V_o}{n(1-D)+1}$	$\frac{nV_o}{n(1-D)+1}$	Low	✓

* MC= Magnetic core, C= Capacitor, D=Diode, S= Switch, R_d=Damping Resistor and T= Total **ICR=Input Current Ripple, *** C.G= Common Ground

Otherwise, the proposed converter and the converter in [12] have the lowest input current ripple among all the converters.

Moreover, the input and output ports of the converters in [15] and [27] do not share a common ground, which limits their applications. From an efficiency point of view, the converters in [15] and [27] are not proper due to using damping resistances in their structure. Although the reported converters in [25], [27], [29], and [31] have the minimum number of elements, the lack of high voltage gain or continuous input current is their main drawback.

Juxtaposing all these comparisons, while converters with higher voltage gain exist, the proposed converter is the only one capable of simultaneously offering high voltage gain, low ripple input current, and common ground features. Additionally, the proposed converter provides these features without using a high number of elements or compromising a vital characteristic.

Moreover, Fig. 9 illustrates and contrasts the dynamic response to an abrupt change in the duty cycle of the proposed converter and converters in [31-33]. It is noteworthy that all the converters deliver 100W power to the output load in this comparison and employ coupled inductors in their structure. Regarding Fig. 9, a sudden change in the duty cycle is applied at $t = 0.1s$ and the output voltage of the converters rises from 105V to 115V. While all the converters present relatively fast responses, the responses of the proposed converter and the converter in [33] are the fastest ones with lower oscillation, unlike the converters in [31] and [32].

At the end of this section, the frequency response of the control to output transfer function for the proposed converter, the converter in [31], and CBC are drawn and compared in Fig. 10 using the parameters in TABLE 1. As can be seen, CBC has a negative phase margin and a gain margin. Hence, it is unstable. To make this comparison more straightforward, the main parameters of the bode plot, such as phase margin, gain margin, stability, and bandwidth of the studied converters, are summarized in TABLE 3. Although the proposed converter

TABLE 3 DETAILED FREQUENCY RESPONSE COMPARISON

Item	CBC	Ref [31]	The proposed converter
PM (degree)	-47.9	90.2	90.3
GM (dB)	-46.7	∞	∞
Stable	×	✓	✓
Band Width (kHz)	2.24	5.1	3.54

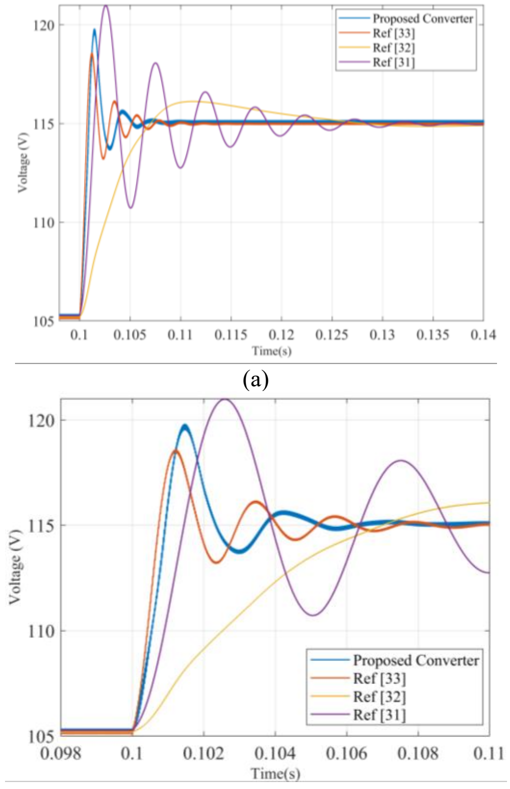

(a)

(b)

Fig. 9. (a) Response of the proposed converter and its peers against a sudden change in duty cycle, (b) Enlarged sketch of the responses.

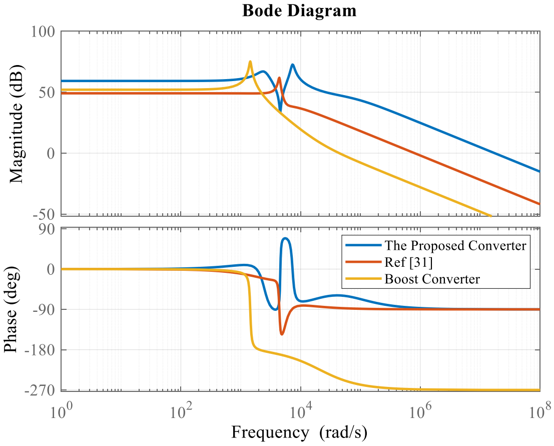

Fig. 10. Frequency response comparison.

and the converter in [31] have similar phase and gain margins, the proposed converter's bandwidth is less than [31].

VI. Experimental Results

Steady-state analyses are validated in this section using hardware-based experimental results. TABLE 4 also presents the laboratory prototype's elements and their values.

A 300 μH inductor is designed and implemented as the input inductor L. The implemented magnetizing inductance in the laboratory is 460μH. Fig. 13(a) sketches the applied pulse to the power switch's gate and the input current waveforms. This figure also confirms the proposed converter's low input current ripple characteristic. It should be noted that for the converter to behave like a minimum phase system, the size of elements should pass the criteria introduced in. The output voltage and leakage inductance's current waveforms are indicated in Fig. 13(b).

Time domain waveforms of the power switch's voltage and current are depicted in Fig. 13(c). Since the power switch's voltage stress is about 50V, half of the output voltage, a power switch with low $R_{DS(on)}$ can be chosen, resulting in lower power loss and higher power conversion efficiency.

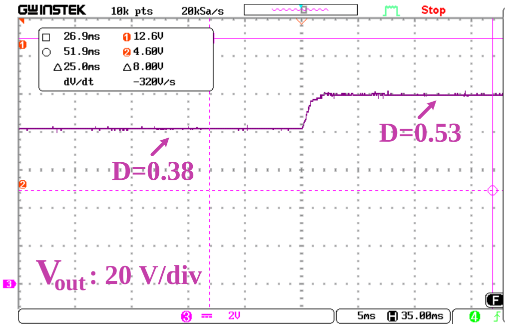

Fig. 11. Dynamic response of the proposed converter.

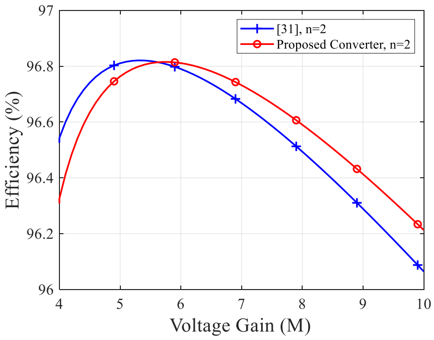

Fig. 12. Efficiency comparison of the proposed converter and [31].

Corresponding voltage and current waveforms of the diode D_{o1} are demonstrated in Fig. 13(d). Like the power switch, the voltage stress across D_{o1} is far lower than the output voltage. Besides, the measured voltage and current waveforms of the diode D_{o2} have been presented in Fig. 13(e). Even though the voltage stress of the diode D_{o2} is larger as compared to the power switch and the diode D_{o1}, it is not higher than the output voltage. Finally, Fig. 13(f) displays the implemented prototype of the converter.

Now, to corroborate the minimum phase performance of the proposed converter, the converter's dynamic response for a 40% step change in the duty cycle is shown in Fig. 11. As can be seen, the converter's output voltage does not have an undershoot as the duty cycle changes from 0.38 to 0.53. The efficiency of the proposed converter and the converter in [31] for a vast range of voltage gains is illustrated in Fig. 12 with the parameters outlined in TABLE 4. This figure reveals that although the proposed converter has more elements, it can

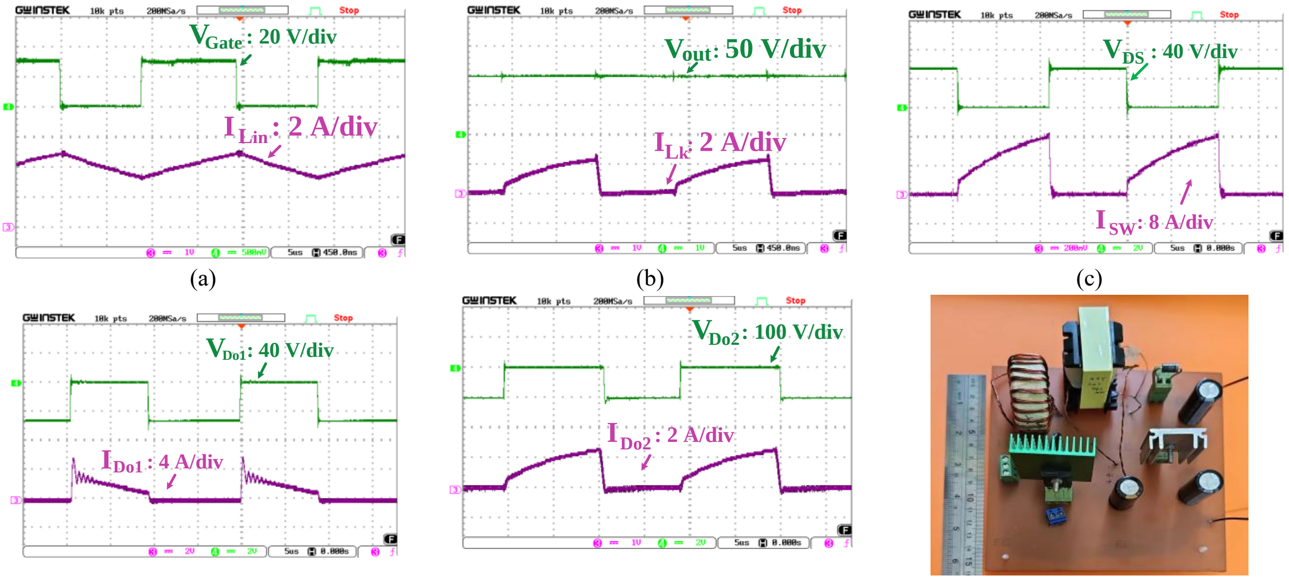

(a) (b) (c)

(d) (e) (f)

Fig. 13. Experimental results of the proposed minimum phase converter (a) Applied driving signal to the power switch and input current waveforms, (b) Output voltage and leakage inductance current waveforms, (c) Voltage and current waveforms of the power switch, (d) Voltage and current waveforms of the Diode D_{o1}, (e) Voltage and current waveforms of the Diode D_{o2}, and (f) Prototype of the converter.

offer better power conversion efficiency over a vast range of voltage gains compared to [31]. This sketch also approves that drawing a high ripple current from the input source leads to higher power loss. As a consequence of these results, the proposed converter can be utilized in various renewable energy applications and those requiring fast dynamic responses.

TABLE 4. HARDWARE SPECIFICATIONS.

Item		Specification
Output Power		100W
Output Voltage		100V
Input Voltage		25V
Switching Frequency		50kHz
Coupled Inductors (EE 42/21/15)	Turns Ratio	2
	Leakage Inductance	5 µH
	Magnetizing Inductance	460 µH
	Total Resistance	27mΩ
L_1		(T 184-52)/300 µH/ $r_L = 22m\Omega$
Capacitors (C_1, C_{o1}, C_{o2})		50 µF/65mΩ, 68 µF/47mΩ, 50 µF/65mΩ
Power Switch (S)		IRFB 4227 ($R_{DS} = 19.7m\Omega$)
Diodes	D_{o1}	MBR10100, ($V_f = 0.65V$)
	D_{o2}	MUR 440, ($V_f = 1.05V$)

VI. Conclusion

This paper proposes a minimum-phase DC-DC converter by making a path between the input source and output load. Accordingly, the converter can eliminate the right half plane zero inherently. Providing minimum phase feature and the following advantages altogether is the main contribution of this paper;

a) High voltage gain,

b) Low voltage stress across its semiconductors,

c) High power conversion efficiency,

d) Common ground sharing between its input and output ports,

and e) low input current ripple altogether. Despite the existence of converters with larger voltage gains, the proposed converter provides a respectable gain while maintaining the previously mentioned benefits. In addition, comprehensive theoretical and mathematical analysis, including steady-state analysis, small signal modeling, efficiency calculation, and so forth, have been done to lighten the novelty of the proposed converter. Aside from verifying the mentioned characteristics of the proposed converter through the experimental results, the presented comparison reveals its competitive features. Combining all the advantages of the proposed converter, one can inspect it as a proper choice for a vast range of applications.

References

[1] Selma B, Bounadja E, Belmadani B, Selma B, Fliess M. A novel intelligent control approach for wind energy conversion systems with synchronous reluctance generators. International Journal of Circuit Theory and Applications. Published online January 31, 2024.

[2] Hoseini S.M, Vasegh N, Zanganeh A. Robust hybrid control of output power for three-phase grid connected PV system. International Journal of Industrial Electronics, Control and Optimization (IECO). Vol 2, Issue 4, pp. 365-372, October 2019.

[3] Shajari S, Keypour R. New Enhanced Droop Controller for Seamless Load Sharing in AC Microgrids in Presence of Wind Turbine and Photovoltaic Source. International

Journal of Industrial Electronics, Control and Optimization (IECO). Vol 5, Issue 2, pp. 153-165, June 2022.

[4] Jalal Ali A, Shazdeh S, Bevrani H, Mirzaei R, Shafiee Q. An Effective Damping Control Approach in Grid-Connected Converters. International Journal of Industrial Electronics, Control and Optimization (IECO). Vol 6, Issue 4, pp. 271-281, December 2023.

[5] Jiang H, Han Y, Li W, et al. A line loss reduction optimization for renewable energy-based distribution networks using a probabilistic approach. International Journal of Circuit Theory and Applications. Published online October 18, 2023.

[6] Hasanpour S. New structure of Single-Switch Ultra-High-Gain DC/DC converter for renewable energy applications. IEEE Transactions on Power Electronics. vol. 37, no. 10, 12715-12728, 2022.

[7] Hasanpour S, Lee SS. New Step-Up DC/DC Converter with Ripple Free Input Current. IEEE Transactions on Power Electronics. vol. 39, no. 2, 2811-2821, 2024.

[8] Abbasi V, Varmenjeh A. R, Ahmadian S. Moghadam F. Y. Ultrahigh Step-Up DC–DC Converter Utilizing a Three-Winding Coupled Inductor and a Switched Capacitor Network with Reduced Input Current Ripple and Low Voltage Stress on the Power Switch. IEEE Transactions on Industrial Electronics, doi: 10.1109/TIE.2024.3395784.

[9] Hashemzadeh S.M, Hosseini S.H, Babaei E, Sabahi M. Design and modelling of a new three winding coupled inductor based high step-up DC–DC converter for renewable energy applications. IET Power Electronics. Vol. 15, Issue13, pp. 1322–1339, October 2022.

[10] Khan M. Y. A, Liu H, Hashemzadeh S. M, Yuan X. A Novel High Step-Up DC–DC Converter with Improved P&O MPPT for Photovoltaic Applications. Electric Power Components and Systems. Vol. 49, Issue 9–10, pp. 884–900, June 2021.

[11] Kumari A, Mahto C. B, Padhee S. Performance evaluation of coupled-inductor DC-DC converter for wind energy conversion system. International Journal of Electronics, pp. 1–26, May 2024, doi: 10.1080/00207217.2024.2354064.

[12] S. Hasanpour, A. Baghramian, and H. Mojallali. Analysis and modeling of a new Coupled-Inductor Buck–Boost DC–DC converter for renewable energy applications. IEEE Transactions on Power Electronics. Vol. 35, Issue 8, pp. 8088–8101, Aug. 2020, doi: 10.1109/tpel.2019.2962325.

[13] Cui X, Avestruz AT. Fast-Response variable frequency DC–DC converters using switching cycle Event-Driven digital control. IEEE Transactions on Power Electronics. vol. 38, no. 7, 8190-8207, 2023.

[14] Kalirajan K, Iruthayarajan MW, Kamaraja AS. Efficiency and dynamic characteristics of improved dual-stage power converter setup with advanced model predictive controller for electric vehicle battery charging. International Journal of Circuit Theory and Applications. vol. 51, no. 12, 5743-5775, 2023.

[15] Zhang Y, Liu J, Dong Z, Wang H, Liu Y. Dynamic performance improvement of Diode–capacitor-Based high step-up DC–DC converter through Right-Half-Plane Zero elimination. IEEE Transactions on Power Electronics. vol. 32, no. 8, 6532-6543, 2017.

[16] Ding K, Zhang Y, Liu J, Zeng P, Zhang J. Dynamic performance improvement of bidirectional Switched-Capacitor DC/DC converter by Right-Half-Plane Zero elimination. 2018 International Power Electronics Conference (IPEC-Niigata 2018 -ECCE Asia). Published online May 1, 2018.

[17] Bussa VK, Aman A, Singh RK. A Minimum-Phase dual output hybrid converter for standalone hybrid AC/DC supply systems. IEEE Transactions on Industry Applications. vol. 57, no. 1, 1044-1056, 2021.

[18] Leoncini M, Dago A, Bertolini A, Gasparini A, Levantino S, Ghioni M. A compact High-Efficiency Boost converter with Time-Based Control, RHP Zero-Elimination, and tracking error compensation. IEEE Transactions on Power Electronics. vol. 38, no. 3, 3100-3113, 2023.

[19] Balapanuru O, Lokhande MM, Aware MV. Performance improvement by sampling position approach in dual loop digital ACM controlled DC-DC boost converter. IEEE Transactions on Circuits and Systems II-express Briefs. vol. 70, no. 4, 1565-1569, 2023.

[20] Arora S, Balsara PT, Bhatia D. PBC for direct voltage regulation for the boost DC–DC converter. IET Power Electronics. vol. 12, no. 8,1942-1951, 2019.

[21] Ahmad S, Ali A. Active disturbance rejection control of DC–DC boost converter: a review with modifications for improved performance. IET Power Electronics. vol. 12, no. 8, 2095-2107, 2019.

[22] Ahmadzadeh S, Markadeh GA, Abjadi NR. Alleviating the right-half-plane zero effect on Z-source converter output voltage regulation using the cascaded sliding mode controller. IET Power Electronics. vol. 13, no. 15, 3419-3427, 2020.

[23] M. Ehsani, M. Saeidi, H. Radmanesh, A. Abrishamifar. Comparisons between Generalized Predictive Control and Linear Controllers in Multi-Input DC-DC Boost Converter. International Journal of Industrial Electronics Control and Optimization. Vol. 3, Issue. 1, pp. 27–34, January 2020.

[24] Viswanathan K, Oruganti R, Srinivasan D. A novel tri-state boost converter with fast dynamics. IEEE Transactions on Power Electronics. vol. 17, no. 5, 677-683, 2002.

[25] Kapat S, Patra A, Banerjee S. A Current-Controlled Tristate Boost converter with improved performance through RHP Zero elimination. IEEE Transactions on Power Electronics. vol. 24, no. 3, 776-786, 2009.

[26] Rana N, Kumar M, Ghosh A, Banerjee S. A novel interleaved Tri-State boost converter with lower ripple and improved dynamic response. IEEE Transactions on Industrial Electronics. vol. 65, no. 7, 5456-5465, 2018.

[27] Veerachary M. Third-order boost converter. IET Power Electronics. vol. 11, no. 3, 566-575. 2018.

[28] Garg M, Singh RK, Mahanty R. Magnetically coupled boost converter with enhanced equivalent series resistance filter capacitor for DC microgrid. IET Power Electronics. vol. 9, no. 9, 1943-1951, 2016.

[29] Gu Y, Zhang D, Zhao Z. Input/Output Current Ripple Cancellation and RHP Zero Elimination in a Boost Converter using an Integrated Magnetic Technique. IEEE Transactions on Power Electronics. vol. 30, no. 2,747-756, 2015.

[30] Cao Z, Yu G, Zhang D. A Novel Magnetic Integrated Boost-forward Converter. IEEE/IAS Industrial and Commercial Power System Asia (I&CPS Asia), Chengdu, China. Published online July 18, 2021.

[31] Poorali B, Adib E. Right-Half-Plane zero elimination of boost converter using magnetic coupling with forward energy transfer. IEEE Transactions on Industrial Electronics. vol. 66, no. 11, 8454-8462, 2019.

[32] Goudarzian A, Dehkordi BM, Abjadi NR, Adib E. Design of a switched-capacitor boost converter utilizing magnetic coupling with capability of right-half plane zero elimination. IET Power Electronics. vol. 14, no. 1, 211-224, 2020..

[33] Goudarzian A, Khosravi A, Raeisi HA. Modeling and implementation of a new boost converter with elimination of right-half -plan zero. International Transactions on Electrical Energy Systems. vol. 30, no. 9, 2020.

[34] Vaghela MA, Mulla MA. High Step-Up Gain Converter based on Two-Phase interleaved coupled inductor without Right-Hand Plane Zero. IEEE Transactions on Power Electronics. vol. 38, no. 5, 5911-5927, 2023.

[35] Pirpoor S, Rahimpour S, Andi M, Kanagaraj N, Pirouzi S, Mohammed AH. A novel and High-Gain Switched-Capacitor and Switched-Inductor-Based DC/DC boost converter with low input current ripple and mitigated voltage stresses. IEEE Access. 2022; 10:32782-32802.

[36] Naeini OH, Shaneh M, Mohammadi MR, Adib E. A new interleaved high step-up soft switching converter with simple auxiliary circuit and reduced voltage stress. IET Renewable Power Generation. vol. 17, no. 3, 528-538, 2022.

Keyvan Yari was born in Rasht, Iran, in 1990. He received the B.S. degree and the M.S. degree in electrical engineering (Hons.) from the University of Guilan, Rasht, in 2012 and 2015, respectively.,His current research interests include high-efficiency and high step-up dc–dc converters, soft-switching converters, efficient power conversion, and renewable energy-based power systems.

Sara Hasanpour was born in Iran, in 1979. She received the B.S. degree in electron ic engineering from Azad Islamic University, Lahijan Branch, Iran, in 2002, the M.S. degree from the Isfahan University of Technology, Isfahan, Iran, in 2005, and the Ph.D. degree in power electronics engineering from University of Guilan, Rasht, Iran, in 2019. She received the best Ph.D. thesis award in power electronics engineering in Iran, awarded by the Power Electronics Society of Iran, 2020. She is currently assistant professor at Azad Islamic University, Ramsar Branch, Ramsar, Iran. Her major research interests include design and implementation of step-up/step-down switch-mode DC/DC converters with high-power density, renewable energy technologies, control and modeling of switched-mode DC/DC converters and electronic ballasts

IECO
International Journal Of
Industrial Electronics Control and Optimization
Print ISSN: 3517-2645
Online ISSN: 3568-2645
Homepage: https://ieco.usb.ac.ir/

Optimal Placement of Plug-in Electric Vehicles Fast-Charging Stations Using Geographic Information System and Considering Power Distribution Network Indexes: A Case Study in Kabul

Fatemeh Keramati |Hamid Reza Mohammadi
Department of Electrical and Computer Engineering, University of Kashan, Kashan, Iran.[1,2]
Corresponding author's email: mohammadi@kashanu.ac.ir

Article Info

Article type:
Research Article

Article history:
Received: 02-May-2024
Received in revised form:
04-July-2024
Accepted: 06-August-2024
Published online: 21- Dec-2024

Keywords:
Electric Vehicle,
Fast-Charging Station,
Optimal placement,
Power loss,
Geographic Information System.

ABSTRACT

Concerning the increasing application of plug-in electric vehicles (PEVs), planning PEV fast-charging stations (PEVF-CS) has become an important research topic. Regarding the reactive power compensation capability, the optimal planning of PEVF-CS reduces voltage deviation and power loss in the distribution network. Also, one of the basic requirements for expanding electric transportation is the optimal placement of accessible PEVF-CSs, considering the geographic information data. Therefore, the optimal placement of PEVF-CS requires attention to different geographical criteria and power distribution network constraints. In this sense, this paper aims to propose an approach that integrates the Geographic Information System (GIS) technique, Multi-Criteria Decision-Making (MCDM) method, and Mixed-Integer Nonlinear Programming to find the optimal location of a PEVF-CS in Kabul city. The first stage is decision analysis based on the GIS technique and the MCDM approach. The second stage is suitability analysis of the power distribution network constraints to improve power quality. This paper considers ten different suitability criteria, and the Technique for Order Preference Similarity to Ideal Solution (TOPSIS) is applied to rank the different candidate locations. The analysis identified Junction 4 as the optimal choice and demonstrated a significant 3.6% reduction in power loss during peak hours, decreasing from 1071 kW to 1032 kW. These results demonstrate the effectiveness of our approach in optimizing PEVF-CS placement to enhance power quality and reduce the power loss.

NOMENCLATURE

AHP	Analytic hierarchy process.
EV	Electric vehicle.
GIS	Geographic information system.
MINLP	Mixed-integer nonlinear programming model.
MCDM	Multi-criteria decision-making.
PEV	Plug-in electric vehicle.
PDN	Power distribution network.
PEVCS	Plug-in electric vehicle charging station.
PEVF-CS	Plug-in electric vehicle fast-charging station.
TOPSIS	Technique for order preference similarity to ideal solution.
WLC	Weighted linear combination.
S^s	Set of reference bus.
S^{line}	Set of lines in DN.
i,j	Index of buses in DN.
t	Index of time.
$G_{i,j} - B_{i,j}$	Line conductance and susceptance.
C^{Volt}	Penalty factor for voltage deviation ($).
C_t^{Ploss}	Penalty factor for power loss ($/kWh).
C_i^u	Grid connection and AC/DC converter costs ($/MVA).
$P_{i,t}^l - Q_{i,t}^l$	Active/reactive power consumption of loads.
$P_{i,t}^{Fcs}$	Active power consumption of PEVF-CS.
P_t^{loss}	Power loss.
$P_{i,j,t}^{line} - Q_{i,j,t}^{line}$	Active/reactive power of lines.
$P_{i,t} - Q_{i,t}$	Active/reactive power generation.
$S_i^{Fcs} - Q_{i,t}^{Fcs}$	Apparent/reactive power of PEVF-CS.

$V_{i,t}$	Voltage magnitude.
$\delta_{i,t}$	Voltage angle.

All electrical quantities are stated per unit (PU).

I. Introduction

Environmental pollution resulting from burning fossil fuels, combined with the depletion of fossil energy resources, has compelled societies to focus more on transportation systems as significant consumers of these fuels. One effective way to decrease greenhouse gas emissions and dependency on fossil fuels is through the expansion of electric transportation. Advances in battery technology have significantly promoted the adoption of electric vehicles (EVs). Some researchers predict that EV production will soon overcome traditional vehicle production in the automotive industry. Additionally, improvements in rectifier design now enable EVs to function as mobile power sources and reactive power compensators [1]. One essential factor in expanding and promoting EVs is the availability of refueling infrastructure, specifically charging stations. Adequate and accessible charging stations accelerate the adoption of electric vehicles within transportation networks and contribute to their global proliferation. Therefore, the problem of determining the optimal location of charging stations has attracted more attention. In planning plug-in electric vehicle charging stations (PEVCS), mitigating adverse impacts on the Power Distribution Network (PDN) is crucial. Voltage stability, reliability, power loss, and power quality are pivotal concerns due to the potential harm from high EV penetration, which can affect grid performance [2, 3]. Various studies have addressed these challenges through optimization models for site selection and sizing of charging stations.

References [4, 5] propose models considering PDN constraints in optimizing PEVCS placement and sizing. Reference [4] integrates costs for distribution expansion, EV stations, voltage regulation, and protective devices into the objective function, preserving problem sensitivity and ensuring a global minimum through convex preservation. The results highlight the importance of voltage regulation and necessary upgrades to protection devices under high recharging demand. Reference [5] determines the optimal location and size of PEVCS in a PDN while maintaining stability conditions. The study analyzes the impact of PEVCS on the PDN by examining active and reactive power losses, power flow, and voltage deviation. Simulation results on the IEEE 33 bus distribution system indicate that up to 200 EVs can be charged without violating network constraints, and adding distributed generators, preferably renewable, is necessary to meet high EV demand while mitigating environmental pollution. Reference [6] proposes mixed-integer linear programming to optimize the sizing and placement of EVCSs in a real distribution system. The objective is to minimize the number of stations while meeting EV owners' needs and PDN constraints.

Using real EV charging data from a Turkish distribution network, the study validates the model's effectiveness through various case studies. It highlights potential cost reductions in installation and infrastructure upgrades while suggesting future research should focus on managing peak power impacts and utilizing ancillary services from EVs in distribution systems. However, these studies do not consider driver convenience in urban areas, which is crucial for EV adoption.

Reference [7] introduces a novel approach using stochastic power flow analysis to optimize the siting and sizing of PEVCSs, focusing on addressing uncertainties in power systems, such as load fluctuations and EV integration impacts. The model aims to maximize PEVCS investment returns by minimizing average wait times and charging distances prioritizing driver convenience. Additionally, it enhances system voltage stability through dynamic system voltage stability (DSVS) indices, demonstrating improved service quality even under high EV penetration scenarios. Reference [8] addresses the location planning of urban PEVCS and battery-swapping stations, considering user behavior and aiming to minimize total costs, maximize user satisfaction, and reduce energy consumption in route to stations. A multi-objective planning model is developed and solved using YALMIP/CPLEX, dynamically analyzing key parameters to determine optimal station locations. The results balance charging and battery-swapping pressures, ensuring even distribution and full utilization of facilities, thereby alleviating user anxiety and promoting EV adoption. These efforts demonstrate the importance of integrating technical and economic considerations in planning PEVCSs to sustain PDN performance. Yet they neglect the station's ability to compensate for voltage drop and power loss within the power network. In [9], a new model is introduced for optimal PEVF-CS siting and sizing, considering PEVF-CSs as power line conditioners to improve power quality and address traffic congestion by strategically placing stations. Reference [10] proposes a GIS-based method and a genetic algorithm for estimating charging demand and determining the optimal locations for charging stations. The primary goals of this study are to decrease investment costs and present an appropriate geographic distribution of charging stations. Additionally, the study investigates various aspects of electric vehicles by modeling electric and parallel hybrid vehicles in MATLAB/Simulink software. However, optimal planning for charging stations is a multi-criteria evaluation problem, with various conflicting criteria influencing the process. The recent studies mentioned above do not address geographical limitations, which are crucial in planning PEVF-CSs. The model needs to account for geographical barriers that could affect the practical suitability of the identified optimal charging station locations.

Furthermore, many studies have examined placing charging stations as the MCDM or the Analytical Hierarchy Process (AHP) for locating PEVCSs [11-15]. Reference [11] employed the fuzzy AHP to determine optimal placing EV charging stations in Ankara, Turkey. Their methodology included four stages: criteria identification, scoring the availability of EV charging station sites, criteria weighting through expert input, and ranking proposed sites using AHP. Meanwhile, in another study [12], AHP and FAHP methods are used to calculate criteria weights, with AHP initially determining weights that are subsequently averaged in the FAHP method. The study focused on accessibility, environmental impact, and economic considerations, including 13 sub-criteria, to identify optimal charging station locations within Istanbul, Turkey. In [16], an integrated strategy is proposed for ranking optimal locations and determining the number of charging stations in the Kadikoy and Ataşehir districts of Istanbul, Turkey. The methodology involves selecting alternatives based on different criteria utilizing the AHP method and ranking them by the TOPSIS method. Subsequently, the number of charging stations is optimized to maximize profitability using the LINGO tool. However, the paper does not introduce a new spatial siting solution. In [17], the study calculates criteria weights using the AHP method and prioritizes alternative locations using PROMETHEE and VIKOR methods for MCDM. Results indicate that the southeast of the European side and the southwest of Anatolian in Istanbul are most suitable for PEVCS deployment. Reference [18] analyzes critical factors in selecting optimal charging station locations in Greece, highlighting the importance of transportation hubs and parking lots over land usage. Public service criteria are comparatively less significant in location planning. Reference [14] identified optimal locations for EV charging stations in Upper Silesia and Dabrowa Basin, Poland. Their methodology is more straightforward than previous studies [12, 13], focusing on assessing and siting a limited number of off-road charging stations. However, to our knowledge, existing literature still needs to introduce a methodology to address the spatial sitting problem of EV charging points while simultaneously considering both geographical conditions and power constraints. It's important to note that PEVCSs can provide reactive power compensation through their power electronic converter, benefiting power networks, yet research still needs to integrate these parameters concurrently.

This paper addresses the optimal location for fast-charging stations in Kabul City, Afghanistan, to facilitate the transition from gasoline to electric vehicles and ensure proper geographic distribution. While some studies in Afghanistan have used MCDM methods for various purposes such as assessing the feasibility of wind energy for hydrogen production in Badakhshan [19], prioritizing locations for wind energy-based hydrogen production [20], and evaluating potential geothermal energy projects [21] none have focused on planning PEVF-CSs in Afghanistan, particularly in Kabul, the capital and largest city. Moreover, GIS-based studies have only focused on the optimal location of charging stations according to the proximity criterion to power transmission lines. However, by adding the PDN constraints and power quality issues, the optimal location of PEVF-CSs can be achieved from both the PDN and GIS aspects. Therefore, this paper addresses determining the optimal location for PEVF-CSs to satisfy the geographic criteria and power quality indexes as a distinguished feature. Improving the power quality of the PDN and finding an accessible location for placing PEVF-CSs are the two main goals of this paper. The paper is organized as follows: The next section presents the methodology for explaining all processes. The third section presents the results and discussion. Finally, the paper is concluded in section four.

II. Methodology

This paper proposes the integration of the GIS-based MCDM approach and a mathematical model for finding suitable locations of PEVF-CS. In this regard, the workflow of this study is shown in Fig. 1. This figure describes different steps in the proposed approach.

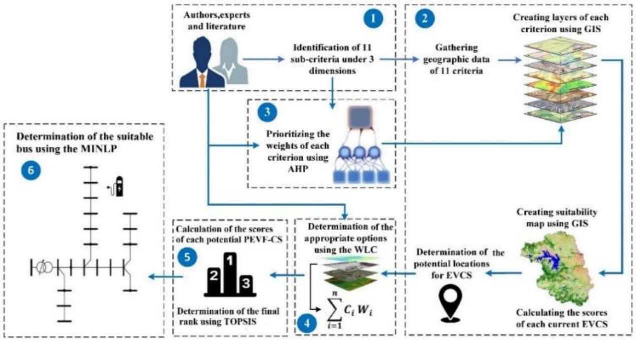

Fig. 1. The workflow of this study

In the first step, the essential criteria that affect the suitable location of PEVF-CS are chosen. In the second step, the geographic data of each criterion is gathered, and suitability layers for each criterion are produced using GIS-based analysis. The related data for each criterion is collected from different sources for spatial analysis. The GIS-based MCDM approach is implemented using the AHP and weighted linear combination (WLC) methods. In the following, the alternatives are ranked with the TOPSIS method. Also, QGIS software is used to analyze the GIS data. Finally, the most suitable alternative is analyzed as power network constraints. The proposed MINLP is used for selecting the optimal bus for connection of the PEVF-CS.

A. Analysis of the evaluation attributes

This paper considers eleven criteria to select the suitable location of PEVF-CS. Indeed, the criteria that affect the PEVF-CS location are chosen. Also, the criteria related to statistical data have been omitted due to the limited access to Kabul City's statistical data and the expense of preparing questionnaires to estimate some statistical data. In this study, eleven criteria have been extracted using various sources. The determined criteria are divided into three groups (Fig. 2).

Fig. 2. Criteria architecture of the PEVF-CS siting problem

1) Population density

The necessity for charging stations is more remarkable in areas with more population density than in other areas. For this reason, population density is used as a criterion to determine the candidate areas. In this paper, the raster layer of the Kabul population for 2020 is used [22]. A site with a high population density will be more suitable for placing PEVF-CS.

2) Shopping malls

Shopping malls can be considered as an evaluation factor for finding a suitable location for PEVF-CS. Placing PEV-FCS near shopping malls can cover a significant part of the demand for refueling. Google Maps has been used to determine the location of shopping malls and produce the shapefile layer of shopping malls.

3) Roads

In the transportation network, electric vehicles travel on the roads. Therefore, roads play a key role in determining the optimal location for installing charging stations. This study omits local streets, and just the main streets are considered. Places close to the roads are regarded as more suitable locations. The shapefile layer of roads is extracted from Ref. [23].

4) Income rate

The income rate factor can be considered in the PEVF-CS location selection. The income rate criterion is used as a determinative criterion in the TOPSIS method. A location with a high-income rate will be more suitable.

5) Transportation stations

However, these centers are located in high-traffic areas of the city. Therefore, places near these centers are more suitable for installing charging stations. The map layer of transportation stations is extracted using Google Maps and Ref. [23].

6) Park areas

Urban parks are green spaces used for recreation in cities. Many citizens visit these areas daily for exercise and recreation. Therefore, parks are one of the criteria that influence the optimal planning of charging stations. In other words, electric cars parked near parks can benefit from being changed by PEVF-CSs. The park map layer is produced using Google Maps and Ref. [23].

7) Green space

Green space has been chosen as an environmental factor to select the optimal location for installing charging stations. Green space layering was generated using Google Maps and Ref. [23]. Places far from green spaces are more suitable for installing charging stations.

8) Slope

The land slope can affect the location where charging stations are installed. The cost of placing PEVF-CS in high-slope areas is much higher than in low-slope areas. Since Kabul is located between mountains and rough plains, this criterion must be considered. The raster layer of elevation is extracted from Ref. [23], and the slope analysis tool of the QGIS software produces the raster layer of the slope. If the location has a low slope, it will be suitable.

9) Land values

Land value is an economic factor that can affect the suitable location selection of PEVF-CS. The land value criterion is used in the TOPSIS method for ranking alternatives. The land value is obtained from field research. The low-value land is more suitable for installing PEVF-CS.

10) Fuel stations

Fuel stations are one of the first places considered for the installation of PEVF-CS. Many studies considered fuel stations candidates for installing charging stations [24]. Since fuel stations are usually located in suitable places in terms of the transportation network and regional traffic, the places close to them can be suitable places to install the PEVF-CS. The map layer of petrol stations is extracted using Google Maps and Ref. [23].

11) Substations

PEVF-CSs should be installed near power lines with significant electrical demands. Since charging stations will encounter high power demands, proximity to high-voltage feeders is necessary to find the optimal location for placing PEVF-CS. On the other hand, the distribution network cannot accept charging stations as there is high electricity demand in each feeder, so with the recommendation of experts of Breshna Electric Company [25], eleven junctions are identified as suitable locations for the map layer of substations.

B. Kabul City

Kabul, the capital and the largest city of Afghanistan is located in the east of the country. Kabul with a population of about 5 million [26] is located between the coordinates 34° 31′ 31″ North and 69° 10′ 42″ East and at an altitude of 1.8 km from the sea level [27]. Fig. 3 shows the geographical location of Kabul city. Replacing gasoline cars with electric cars can be one of the appropriate solutions to reduce air pollution in Kabul city. The expansion of electric vehicles in Kabul requires determining the optimal location of PEVF-CSs according to effective criteria. Therefore, in this study, the optimal location of a PEVF-CS in Kabul is investigated using the GIS-based MCDM approach.

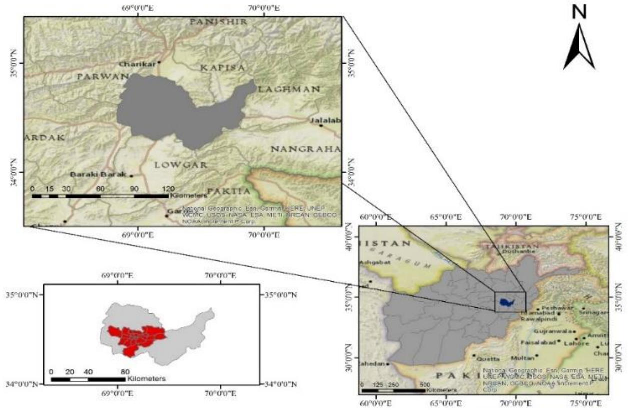

Fig. 3. Geographical area of the case study (Kabul City).

C. *The analytic hierarchy process (AHP)*

This study uses a GIS-based MCDM approach to find suitable locations for placing PEVF-CS. We first extracted maps related to critical criteria used in our research to analyze the optimal location for charging stations in Kabul's suburbs. These criteria include distance from power posts, population density, and road accessibility. We prepared distance maps for each criterion using the Proximity tool in QGIS software. After creating these distance maps, our next step was to evaluate and standardize them. The evaluation involved assigning values based on the desirability of each criterion's distance from the ideal placement. For example, shorter distances to power posts received higher desirability values per meter unit. Standardization ensured that the range of values across all criteria was consistent and comparable. This process is carried out using the Reclassify by Table tool in QGIS, following the guidelines specified in Table 1. Ultimately, this valuation and standardization process led to the production of merit maps for each criterion, illustrating the suitability of different areas for charging station locations. Fig.4 depicts these merit maps, displaying the spatial distribution of optimal criteria for siting charging stations in Kabul's suburbs. The AHP method uses the criteria that are essential for the decision-making process.

A detailed mythology of the AHP method can be found in [28]. Each criterion's superiority and value are compared by creating a pairwise comparison matrix. Finally, the weight of each criterion is determined. This process is done using Expert Choice software. The compatibility rate or ratio (CR) used to evaluate the precision of pairwise comparison must be computed. In the AHP method, CR signifies the level of compatibility in comparisons and provides insight into the accuracy of valuation made through pairwise comparisons. Pairwise comparisons are acceptable when their CR value is less than 0.1. If the CR exceeds 0.1, it is necessary to revisit the pairwise comparison matrix until the CR falls within the acceptable range [12, 29]. In this study, the CR is measured at 0.09, indicating that the judgments are reliable and acceptable. Consequently, the criteria can be weighted based on these reliable judgments. According to Fig. 5, the criteria of roads, petrol stations, and substations have the highest weight, respectively.

In this study, the PEVF-CS siting is determined using the MCDM approach, incorporating the WLC method to assign appropriate weights to different layers. The WLC method is the most common in MCDM analysis. This technique is also called the scoring method. After determining the weight of the criteria, the weight of each criterion is multiplied by the value of that attribute, and a final value is obtained as the new weight of the alternative [28].

D. *Technique for order preference by similarity to ideal solution (TOPSIS)*

Alternative locations or points are found using MCDM-based location selection studies. These alternatives are ranked according to two criteria, land value, and income rates.

TABLE 1 ATTRIBUTE CLASS INTERVALS AND SCORES [12]

Criterion	Population density					
Score	5	4	3	2	1	0
Limits $(1000/Km^2)$	33<	23-32	17-22	10-16	<9	-
Criterion	Shopping malls					
Score	5	4	3	2	1	0
Limits (m)	<250	250-500	500-750	750-1000	1000<	-
Criterion	Roads					
Score	5	4	3	2	1	0
Limits (m)	<250	250-500	500-750	750-1000	1000<	-
Criterion	Transportation stations					
Score	5	4	3	2	1	0
Limits (m)	<250	250-500	500-750	750-1000	1000<	-
Criterion	Fuel stations					
Score	5	4	3	2	1	0
Limits (m)	<250	250-500	500-750	750-1000	1000<	-
Criterion	Park areas					
Score	5	4	3	2	1	0
Limits (m)	<250	250-500	500-750	750-1000	1000<	-
Criterion	Green areas					
Score	5	4	3	2	1	0
Limits (m)	300<	250-300	200-250	150-200	100-150	<100
Criterion	Slope					
Score	5	4	3	2	1	0
Limits (degree)	<5	5-10	10-15	15-20	20-25	25<

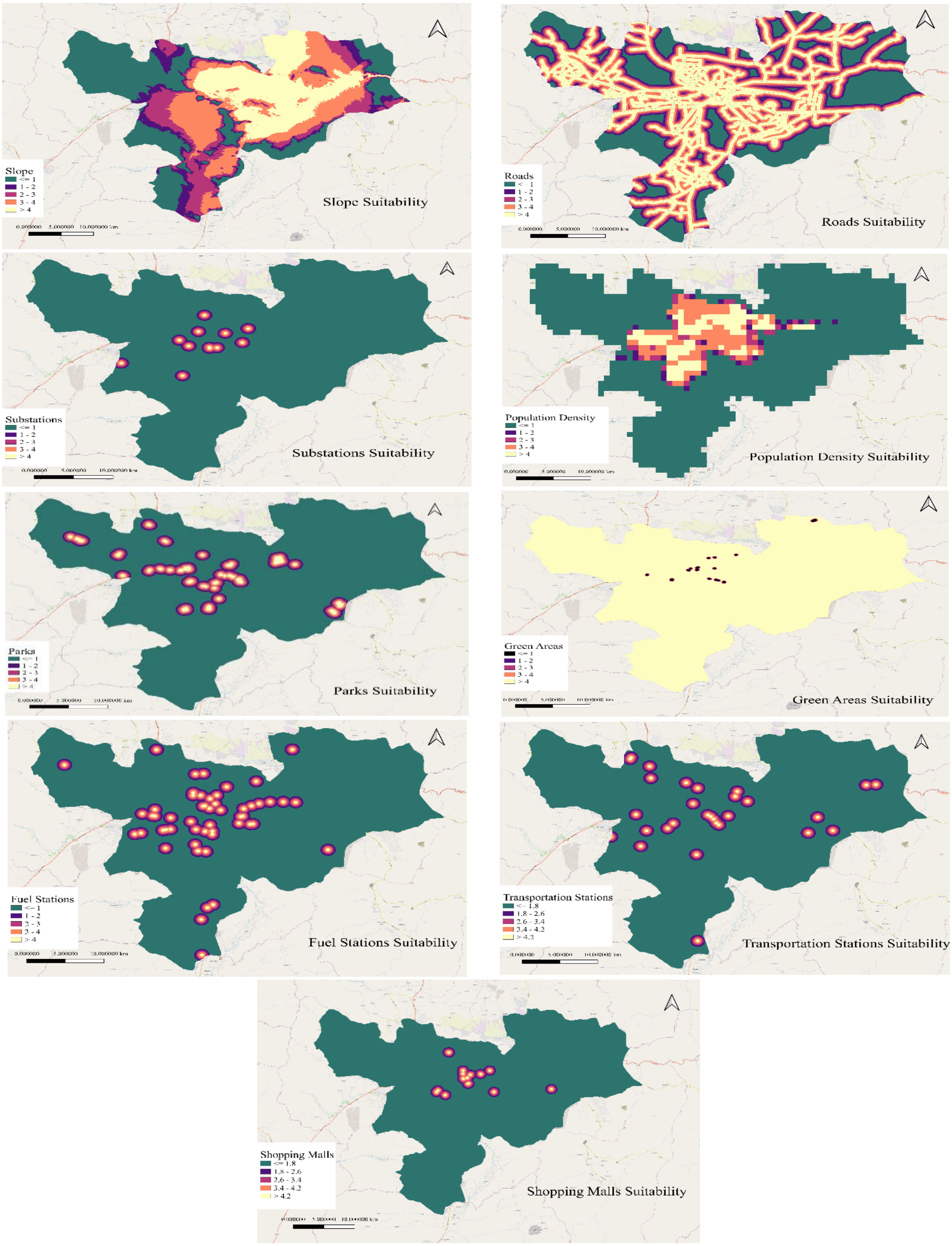

Fig. 4. Suitability maps for different criterion

Fig. 5. Weights of different criteria

The TOPSIS method is used to prioritize the optimal locations. In this method, each alternative's land cost and income rate are considered decisive criteria. First, the decision matrix is formed according to the alternative's land value and income rate. Next, the decision matrix is normalized, and the distances from each alternative to the worst and best conditions are calculated. High land value and high-income rate of points are the worst and best conditions, respectively. Finally, the similarity to the worst and the best conditions according to their distance are defined. A detailed methodology of TOPSIS can be found in [30]. Equations (1) and (2) illustrate the distance of each alternative from the best and worst alternatives.

$$S_i^* = \sqrt{\sum_{j=1}^{n} (V_{i,j} - V_j^*)^2} \tag{1}$$

$$S_i^- = \sqrt{\sum_{j=1}^{n} (V_{i,j} - V_j^-)^2} \tag{2}$$

Where j represents the desired criterion and i shows the alternative. S_i^* and S_i^- indicate the distances of i_{th} alternative from the best and worst solutions, respectively. $V_{i,j}$ is the performance of the i_{th} alternative concerning criterion j and V_j^* is the best value for the j_{th} criterion among all alternatives. V_j^- also shows the worst value of the j_{th} criterion among all alternatives. Equation (3) calculates the similarity index of each alternative.

$$C_i^* = \frac{S_i^-}{S_i^* + S_i^-} \tag{3}$$

$\boldsymbol{C_i^*}$ represents the similarity index. The range of $\boldsymbol{C_i^*}$ is between zero and one. The closer $\boldsymbol{C_i^*}$ is to one, the more similar the alternative is to the best solution. In other words, the alternative with the highest $\boldsymbol{C_i^*}$ is ranked first, and the alternative with the lowest $\boldsymbol{C_i^*}$ is ranked last.

E. Examination of junctions using a mathematical model

The GIS-based MCDM approach is analyzed considering the constraints of the DN. On the other hand, the PEVF-CS can compensate for reactive power using its power electronic converter. Therefore, placing the PEVF-CS in a suitable bus can enhance the voltage profile and decrease the power loss [9]. This study investigates the optimal location of the PEVF-CS obtained from the GIS-based MCDM approach according to power quality indexes. In other words, using the constraints of the DN and minimizing network power loss and voltage deviation, the optimal location (bus) for placing the PEVF-CS in the DN has been obtained.

As discussed, this study addresses the optimal location for placing the PEVF-CS to reduce network power loss and voltage deviation. According to equation (4), the objective function includes the penalty cost for voltage deviation and power loss.

$$\begin{aligned} F = (C^{Volt} \times \sum_t \sum_i (1 - V_{i.t})) \\ + \sum_t (C_t^{Ploss} \times P_t^{loss}) \\ + \sum_i (C_i^u S_i^{FCS} x_i) \end{aligned} \tag{4}$$

$V_{i,t}$ and P_t^{loss} represent bus voltage and network power loss, respectively. C^{Volt} and C_t^{Ploss} show the penalty cost for voltage deviation and power loss, respectively, and x_i is a binary variable that indicates the installation of PEVF-CS in bus i.

DN constraints are modeled with AC power flow [31]. In this study, the optimal location of the PEVF-CS has been determined considering the capability of reactive power compensation by the PEVF-CS. The constraints of the DN are as follows.

$$\begin{aligned} P_t^{loss} = \sum_{i,j} 0.5 \times G_{i,j} \\ +((V_{i,t})^2 + (V_{j,t})^2 \\ - 2V_{i,t}V_{j,t}\cos(\delta_{i,t} - \delta_{j,t})) \end{aligned} \quad \forall t \tag{5}$$

$$P_{i,j,t}^{line}=\frac{(V_{i,t})^2}{Z_{i,j}}\cos(\theta_{i,j})-\frac{V_{i,t}V_{j,t}}{Z_{i,j}}\cos(\delta_{i,t}-\delta_{j,t}+\theta_{i,j}) \quad \forall(i,j)\epsilon S^{line},t \qquad (6)$$

$$Q_{i,j,t}^{line}=\frac{(V_{i,t})^2}{Z_{i,j}}\sin(\theta_{i,j})-\frac{V_{i,t}V_{j,t}}{Z_{i,j}}\sin(\delta_{i,t}-\delta_{j,t}+\theta_{i,j}) \quad \forall(i,j)\epsilon S^{line},t \qquad (7)$$

$$P_{i,t}-\sum_i P_{i,t}^{l}+\sum_i (P_{i,t}^{FCS})*x_i==\sum_{j\in S^{line}} B_{i,j}P_{i,j,t}^{line} \quad \forall i,t \qquad (8)$$

$$Q_{i,t}-\sum_i Q_{i,t}^{l}+\sum_i (Q_{i,t}^{FCS})*x_i==\sum_{j\in S^{line}} B_{i,j}Q_{i,j,t}^{line} \quad \forall i,t \qquad (9)$$

$$\sqrt{(P_{i,t}^{FCS})^2+(Q_{i,t}^{FCS})^2}\leq S_i^{FCS} \quad \forall i,t \qquad (10)$$

$$-\overline{P_{\iota,t}}\leq P_{i,t}\leq\overline{P_{\iota,t}} \quad \forall i\in S^s,t \qquad (11)$$

$$-\overline{Q_{\iota,t}}\leq Q_{i,t}\leq\overline{Q_{\iota,t}} \quad \forall i\in S^s,t \qquad (12)$$

$$0.9\leq V_{i,t}\leq 1.05 \quad \forall i,t \qquad (13)$$

$$-\frac{\pi}{2}\leq\delta_{i,t}\leq\frac{\pi}{2} \quad \forall i,t \qquad (14)$$

Equation (5) shows the active power loss. Equations (6) and (7) show the line power between the network buses in each time. Equations (8) and (9) lead to the balance of active and reactive power in each bus and time interval, respectively. Equation (10) calculates the apparent power of the PEVF-CS in bus i. Equations (11) to (14) express the permissible limits of network variables, where $\overline{P_{\iota,t}}$ and $\overline{Q_{\iota,t}}$ show maximum active and reactive power generation.

III. Results and Discussion

In this study, the optimal location of PEVF-CS in Kabul city is determined using GIS-based MCDM and MINLP method. The results of each part are discussed separately.

A. *The GIS-based MCDM approach*

This study uses the WLC method and nine suitability layers to identify six optimal locations for installing PEVF-CS. Fig. 6 shows the suitable locations resulting from the WLC method. This figure shows that these six places are close to junctions 2, 3, 4, 5, 7, and 12. Fig. 7 shows the satellite images of these six junctions. Therefore, it is expected that if a PEVF-CS is installed in each of these places, it will be supplied by these junctions. Table 2 also shows the scores of these six places. Also, the optimal locations near junctions 4, 2, and 7 have the highest scores.

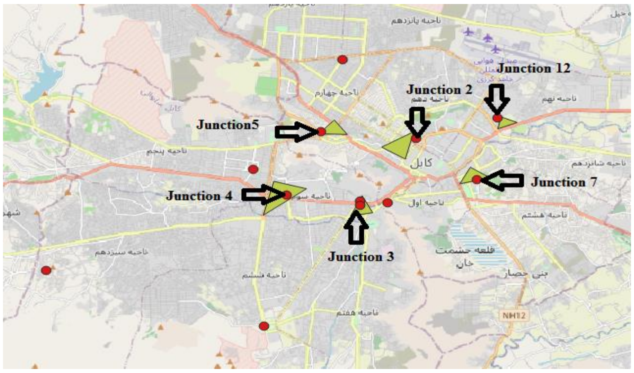

Fig. 6. Suitable locations for placing PEVF-CSs

In the following examination of alternative ranking, the TOPSIS method is used to identify the best location for installing the PEVF-CS. The decision matrix D_{ij} of the six candidate locations for placing PEVF-CS is obtained by considering land value criteria. The decision matrix is given by (15).

$$D_{ij}=\begin{bmatrix}3 & 1800\\ 3 & 1650\\ 5 & 1800\\ 2 & 2000\\ 2 & 1850\\ 4 & 1700\end{bmatrix} \qquad (15)$$

In this matrix, column 1 represents the criteria value, and column 2 represents the corresponding values for alternative land. It should be noted that the weights of the criteria are considered equal. Using the TOPSIS method, six alternatives are ranked, and their closeness to the ideal solution is shown in Table 3.

TABLE 2 SUITABLE LOCATIONS FOR PLACING PEVF-CS

Suitable location	Junction 2	Junction 3	Junction 4	Junction 5	Junction 7	Junction 12
score	4.289	4.012	4.673	4.073	4.183	3.881

TABLE 3 THE SIMILARITY OF ALTERNATIVES TO THE IDEAL SOLUTION

Alternative	Junction 4	Junction 12	Junction 3	Junction 2	Junction 5	Junction 7
C_i^*	0.909	0.668	0.35	0.332	0.1168	0
Rank	1	2	3	4	5	6

According to the two criteria of land price, three optimal locations near junctions 4, 12, and 3 are selected in terms of priority. The places around junction 4 are the most similar to the ideal solution. However, which bus at junction four should be the optimized place for the PEVF-CS connection? In other words, regarding DN constraints, which bus is the best for connecting a PEVF-CS? Therefore, the suitable bus for placing the PEVF-CS is investigated according to the DN constraint.

B. *MINLP method*

Using the MCDM approach, Junction 4 is the optimal area for installing the PEVF-CS, with the highest score and priority percentage. Junction 4 has 162 buses (Fig. 8). The distribution network line and bus data have been presented in [32]. The bus voltage and power loss of the 162-bus network during 24 hours are shown in Fig. 9 and 10, respectively. According to the power flow analysis, the minimum voltage and maximum loss of PDN are 0.85 pu and 1071 kW. In such a condition, placing PEVF-CS as a new demand and line conditioner device is sensitive. At peak hour (13), bus 114 (the worst bus) has the lowest voltage with a value of 0.85. The number of electric vehicles is assumed to be 250, 5 percent of the number of taxis in Kabul [33]. The power consumption is assumed to be 0.15 kWh/km, and the driving range is 100 km. The traffic flow during the day is presented in [34].

This study implements the mixed-integer non-linear model in GAMS software to place PEVF-CS and to improve the power quality in junction 4. Due to the constraints of the PDN, bus 4 is chosen as the optimal bus to connect the PEVF-CS. Fig. 11 shows the voltage of PDN after placing the PEVF-CS. Also, a comparison of the voltage of bus 114 (the worst bus) is shown in Fig. 12 for two cases: before and after placing the PEVF-CS. The power loss before and after placing PEVF-CS is shown in Fig. 13, as the results show that all PDN bus voltages increase between 1.8 and 2.07 percent.

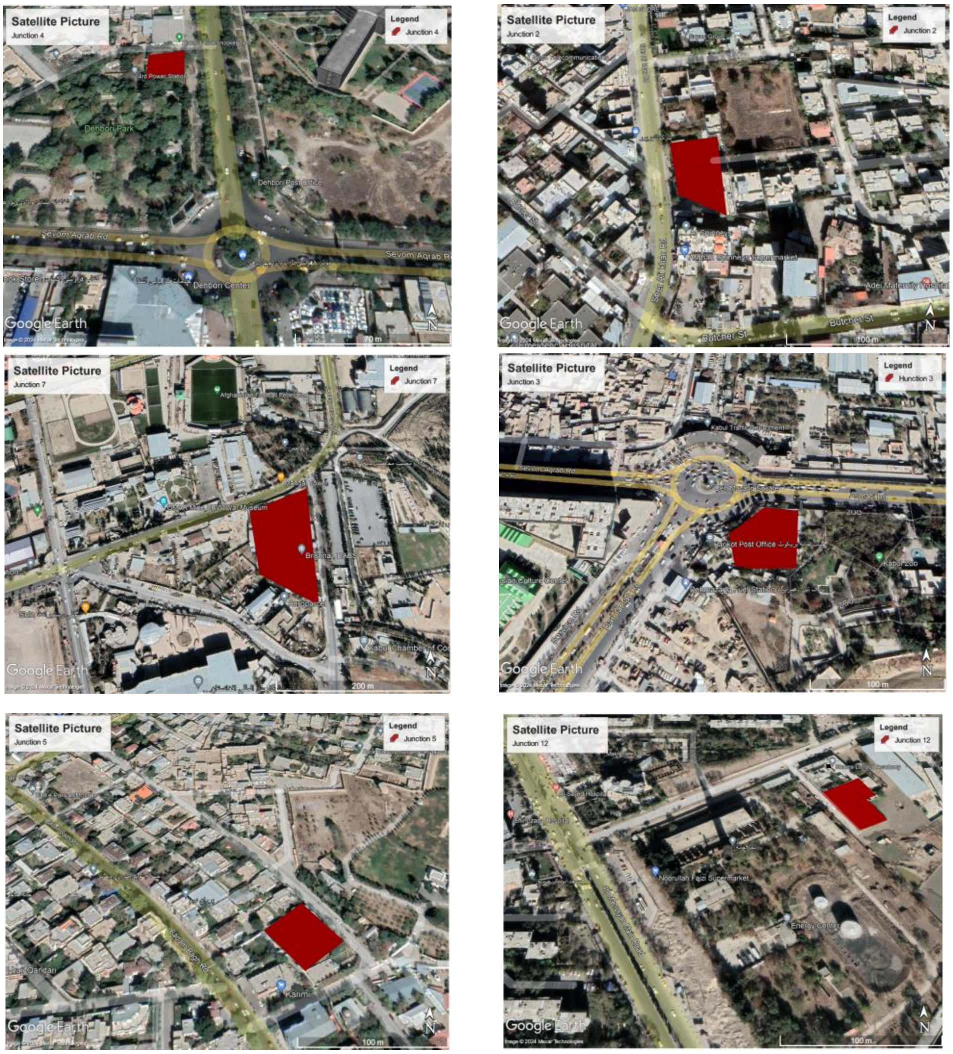

Fig. 7. The satellite pictures of the suitable junctions

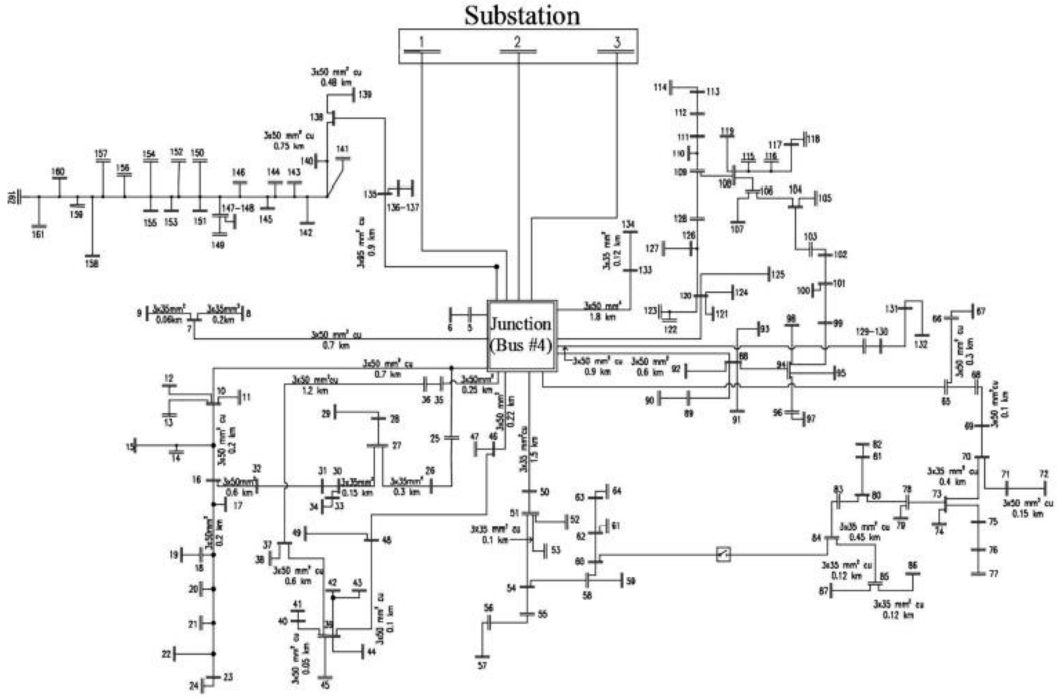

Fig. 8. Distribution network model (junction 4)

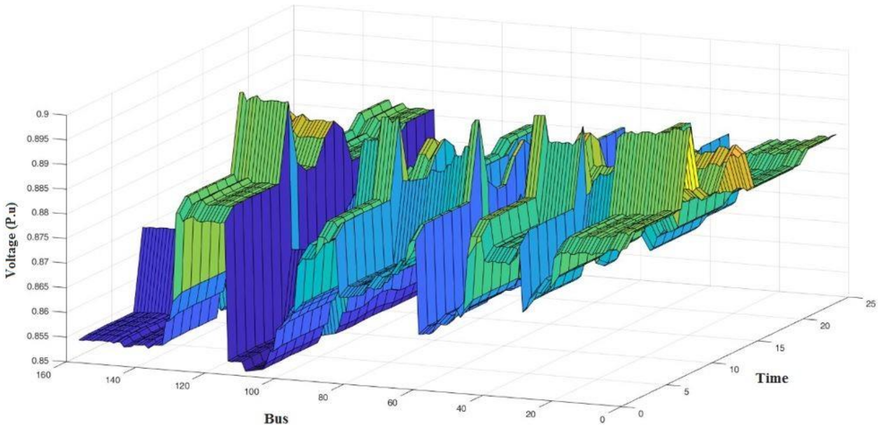

Fig. 9. Voltage profile of the DN before placing PEVF-CS

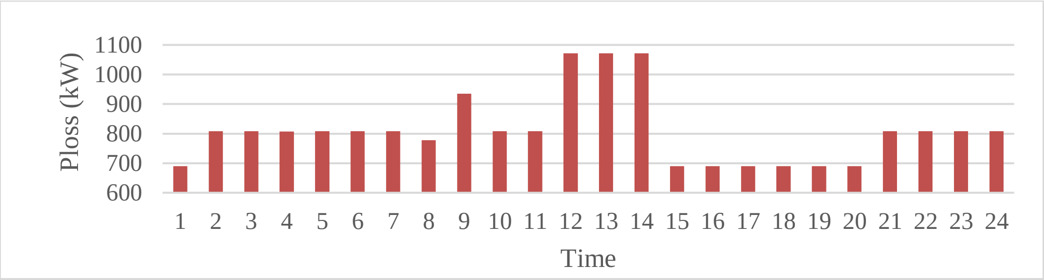

Fig. 10. Power loss before placing PEVF-CS

In addition, there is a 3.6% reduction in power loss during peak hours, decreasing from 1071 to 1032 kW. In other words, the power loss is significantly reduced, and the voltage profile improves after placing PEVF-CS. The PEVF-CS injects 850 kVAR at peak demand. The apparent power of the PEVF-CS is obtained equal to 1345 kVA. Fig. 14 shows the changes in active power consumption and reactive power generation of the PEVF-CS during 24 hours.

IV. Conclusion

This study addresses the critical need for optimal PEVF-CS locations in Kabul City, Afghanistan, during a global shift toward sustainable transportation. Integrating GIS tools, MCDM methods, and the MINLP model aims to balance geographic suitability with PDN constraints and power quality considerations. The research seeks to enhance infrastructure planning to support electric vehicle adoption and sustainable urban development in Kabul. Criteria such as population density, road accessibility, income rates, and proximity to essential facilities are analyzed using GIS tools. The AHP is applied for criteria weighting, while the TOPSIS ranks alternative locations. Subsequently, the MINLP model selects Junction 4 as the optimal area for PEVF-CS installation within the PDN, demonstrating significant improvements in voltage stability and power loss reduction during peak hours. Future studies could incorporate additional criteria, such as PEV distribution patterns, to enhance the proposed approach and improve result accuracy. Furthermore, considering the stochastic nature of PEV behavior and uncertainties in real-world conditions like weather and demand fluctuations would enhance the model's robustness. While this study focused on optimizing a single PEVF-CS in Kabul City, future research will expand to optimize multiple charging stations across urban networks, which is essential for scaling electric vehicle adoption strategies.

In conclusion, this research enhances the efficiency of PEVF-CS deployment and offers valuable insights into sustainable urban infrastructure planning. By using advanced decision support tools, such as GIS-based MCDM and MINLP modeling, this study promotes electric vehicle adoption. It enhances grid reliability in Kabul City, supporting its transition towards a sustainable urban future.

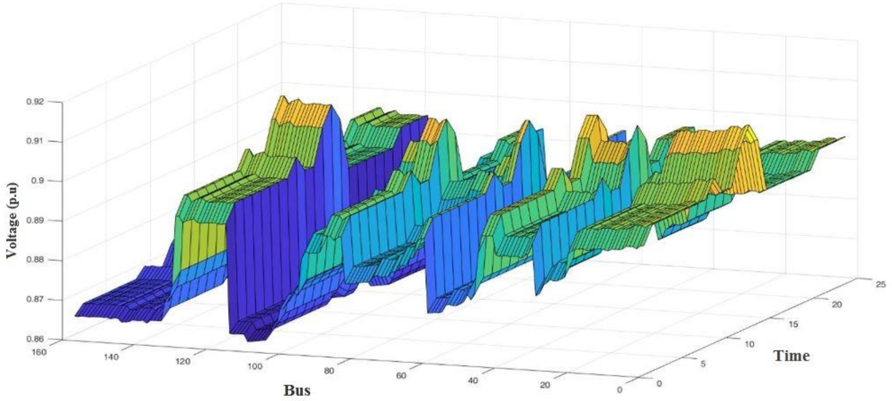

Fig. 11. The voltage profile of DN after placing the PEVF-CS

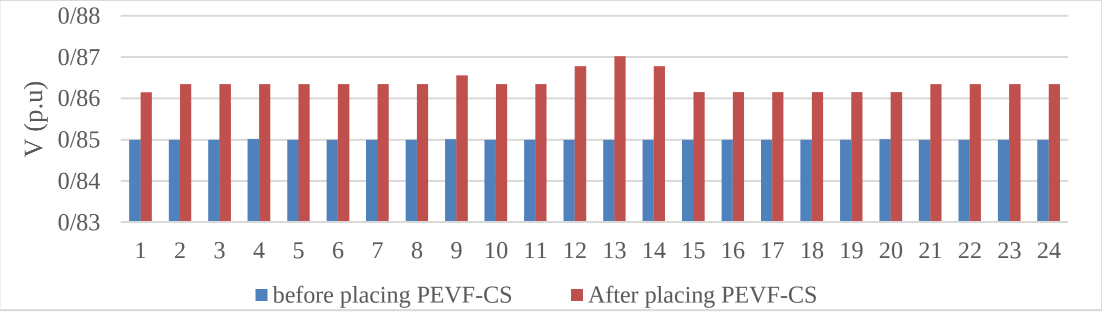

Fig. 12. The voltage of bus 114 before and after placing the PEVF-CS

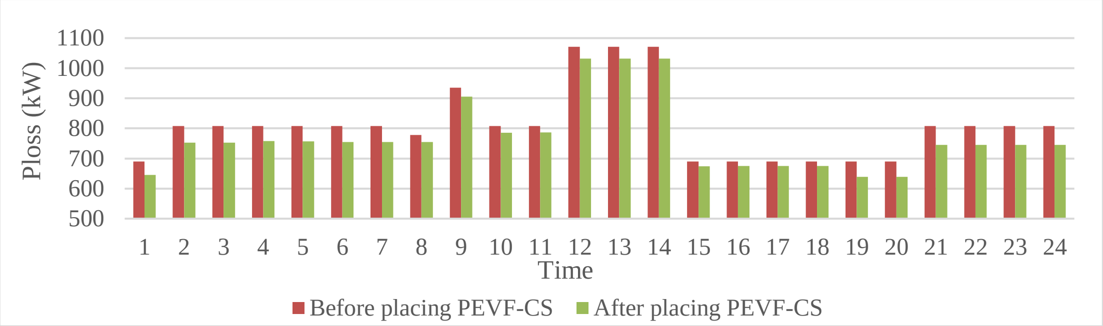

Fig. 13. The power loss before and after placing PEVF-CS

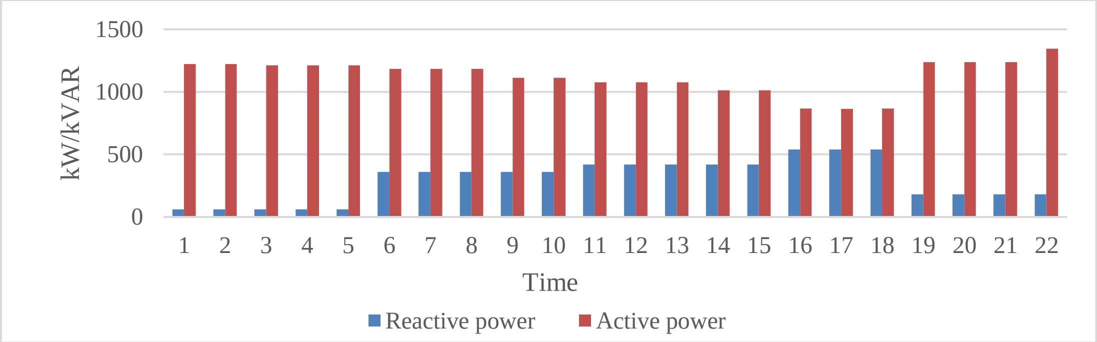

Fig. 14. Active power consumption and reactive power generation of the PEVF-CS during 24-hours

REFERENCES

[1] H. Soltani Gohari, K. Abbaszadeh, J. Gholami Gorji, "A Controllable Bidirectional Rectifier for EV Home Charging Station with G2H/G2VH/V2H/V2G Functions," International Journal of Industrial Electronics Control and Optimization ,vol. 4, no. 1, pp. 99-113, 2021.

[2] S. M. Alshareef, "Analyzing and mitigating the impacts of integrating fast-charging stations on the power quality in electric power distribution systems," Sustainability ,vol. 14, no. 9, p. 5595, 2022.

[3] P. Sivaraman, J. S. S. Raj, and P. A. Kumar, "Power quality impact of electric vehicle charging station on utility grid," in 2021 IEEE Madras Section Conference (MASCON), pp. 1-4, 2021.

[4] Q. Cui, Y. Weng, and C.-W. Tan, "Electric vehicle charging station placement method for urban areas," IEEE Transactions on Smart Grid, vol. 10, no. 6, pp. 6552-6565, 2019.

[5] T. Kunj and K. Pal, "Optimal location planning of EV charging station in existing distribution network with stability condition," in 2020 7th international conference on signal processing and integrated networks (SPIN), 2020, pp. 1060-1065.

[6] I. Sengor et al., "Optimal sizing and siting of different types of EV charging stations in a real distribution system environment," IET Renewable Power Generation ,vol. 16, no. 15, pp. 3171-3183, 2022.

[7] Y. Jin, M. A. Acquah, M. Seo, and S. Han, "Optimal siting and sizing of EV charging station using stochastic power flow analysis for voltage stability," IEEE Transactions on Transportation Electrification , vol. 10, no. 1, pp. 777-794, 2024.

[8] S. Zu and L. Sun, "Research on location planning of urban charging stations and battery-swapping stations for electric vehicles," Energy Reports ,vol. 8, pp. 508-522, 2022.

[9] F. Keramati, H. R. Mohammadi, G. R. Shiran, "Determining optimal location and size of PEV fast-charging stations in coupled transportation and power distribution networks considering power loss and traffic congestion," Sustainable Energy, Grids and Networks ,vol. 38, p. 101268, 2024.

[10] S. Alegre, J. V. Míguez, and J. Carpio, "Modelling of electric and parallel-hybrid electric vehicle using Matlab/Simulink environment and planning of charging stations through a geographic information system and genetic algorithms," Renewable and Sustainable Energy Reviews, vol. 74, pp. 1020-1027, 2017.

[11] M. Erbaş, M. Kabak, E. Özceylan, and C. Çetinkaya, "Optimal siting of electric vehicle charging stations: A GIS-based fuzzy Multi-Criteria Decision Analysis," Energy ,vol. 163, pp. 1017-1031, 2018.

[12] D. Guler and T. Yomralioglu, "Suitable location selection for the electric vehicle fast charging station with AHP and fuzzy AHP methods using GIS," Annals of GIS ,vol. 26, no. 2, pp. 169-189, 2020.

[13] S. Guo and H. Zhao, "Optimal site selection of electric vehicle charging station by using fuzzy TOPSIS based on sustainability perspective," Applied Energy,vol. 158, pp. 390-402, 2015.

[14] G. Sierpiński, M. Staniek, and M. J. Kłos, "Decision making support for local authorities choosing the method for siting of in-city EV charging stations," Energies, vol. 13, no. 18, p. 4682, 2020.

[15] Y. Zhang and K. Iman, "A multi-factor GIS method to identify optimal geographic locations for electric vehicle (EV) charging stations," in Proceedings of the ICA, 2018, vol. 1, pp. 1-6: Copernicus GmbH.

[16] M. E. Genevois and H. Kocaman, "Locating electric vehicle charging stations in Istanbul with AHP based mathematical

modelling," International Journal of Transportation Systems , vol. 3, 2018.

[17] Ö. Kaya, A. Tortum, K. D. Alemdar, M. Y. Çodur, "Site selection for EVCS in Istanbul by GIS and multi-criteria decision-making," Transportation Research Part D: Transport and Environment ,vol. 80, p. 102271, 2020.

[18] C. Karolemeas, S. Tsigdinos, P. G. Tzouras, A. Nikitas, and E. Bakogiannis, "Determining electric vehicle charging station location suitability: A qualitative study of greek stakeholders employing thematic analysis and analytical hierarchy process," Sustainability ,vol. 13, no. 4, p. 2298, 2021.

[19] K. Almutairi, S. S. H. Dehshiri, S. J. H. Dehshiri, A. Mostafaeipour, M. Jahangiri, and K. Techato, "Technical, economic, carbon footprint assessment, and prioritizing stations for hydrogen production using wind energy: A case study," Energy Strategy Reviews ,vol. 36, p. 100684, 2021.

[20] A. Mostafaeipour, S. J. H. Dehshiri, S. S. H. Dehshiri, and M. Jahangiri, "Prioritization of potential locations for harnessing wind energy to produce hydrogen in Afghanistan," International Journal of Hydrogen Energy, vol. 45, no. 58, pp. 33169-33184, 2020.

[21] A. Mostafaeipour, S. J. H. Dehshiri, S. S. H. Dehshiri, M. Jahangiri, and K. Techato, "A thorough analysis of potential geothermal project locations in Afghanistan," Sustainability ,vol. 12, no. 20, p. 8397, 2020.

[22] https://worldpopulationreview.com/world-cities/kabul-population.

[23] https://learnosm.org/en/osm-data/data-overview/.

[24] I. S. Bayram, U. Zafar, and S. Bayhan, "Could petrol stations play a key role in transportation electrification? a gis-based coverage maximization of fast ev chargers in urban environment," IEEE Access, vol. 10, pp. 17318-17329, 2022.

[25] https://main.dabs.af/Historyen.

[26] https://www.populationu.com/cities/kabul-population.

[27] https://de.wikipedia.org/wiki/Kabul.

[28] T. Höfer, Y. Sunak, H. Siddique, and R. Madlener, "Wind farm siting using a spatial Analytic Hierarchy Process approach: A case study of the Städteregion Aachen," Applied energy, vol. 163, pp. 222-243, 2016.

[29] J. Ma, N. R. Scott, S. D. DeGloria, A. J. Lembo, "Siting analysis of farm-based centralized anaerobic digester systems for distributed generation using GIS," Biomass and Bioenergy, vol. 28, no. 6, pp. 591-600, 2005.

[30] M. Jahangiri et al., "Prioritization of solar electricity and hydrogen co-production stations considering PV losses and different types of solar trackers: a TOPSIS approach," Renewable Energy, vol. 186, pp. 889-903, 2022.

[31] S. Pirouzi, J. Aghaei, T. Niknam, H. Farahmand, and M. Korpås, "Proactive operation of electric vehicles in harmonic polluted smart distribution networks," IET Generation, Transmission & Distribution, vol. 12, no. 4, pp. 967-975, 2018.

[32] M. Ahmadi, M. E. Lotfy, A. M. Howlader, A. Yona, T. Senjyu, "Centralised multi-objective integration of wind farm and battery energy storage system in real-distribution network considering environmental, technical and economic perspective," IET Generation, Transmission & Distribution ,vol. 13, no. 22, pp. 5207-5217, 2019.

[33] S. Faizi, N. R. Sabory, and A. H. Layan, "Fuel transportation impact on people, animals, and plant life in Kabul city," Repa Proc, pp. 89-95, 2020.

[34] S. N. Hashemian, M. A. Latify, and G. R. Yousefi, "PEV fast-charging station sizing and placement in coupled transportation-distribution networks considering power line conditioning capability," IEEE Transactions on Smart Grid, vol. 11, no. 6, pp. 4773-4783, 2020.

Fatemeh Keramati received her B.Sc. degree from the Islamic Azad University of Khomeini Shahr in 2018 and, her M.Sc. degree from the University of Kashan in 2023 all in electrical engineering. Her Current research interests include optimization, machine learning, power quality, power systems especially electric vehicle adoption in distribution networks.

Hamid Reza Mohammadi was born in Qom, Iran, in 1971. He received the B.Sc. degree from Sharif University of Technology, Tehran, Iran, in 1993, the M.Sc. degree from the University of Tabriz, Tabriz, Iran, in 1995, and the Ph.D. degree from Tarbiat Modares University, Tehran, Iran, in 2008 all in electrical engineering. Currently, he is an Associate Professor in the Electrical Engineering Department at the University of Kashan, Kashan, Iran. His research interests include power electronics, power quality, active filters, and different microgrid aspects including modeling and control of power converters, power quality, and energy management.

IECO

This page intentionally left blank.

IECO International Journal Of Industrial Electronics Control and Optimization
Print ISSN: 3517-2645
Online ISSN: 3568-2645
Homepage: https://ieco.usb.ac.ir/

Micro-Expression Recognition Using the Spatiotemporal Feature Extraction and Deep-Learning Methods

Vida Esmaeili[1] | Mahmood Mohassel Feghhi[2]

Faculty of Electrical and Computer Engineering, University of Tabriz, Tabriz, Iran[1,2]
Corresponding author's email: mohasselfeghhi@tabrizu.ac.ir

Article Info

Article type:
Research Article

Article history:
Received: 20-March-2024
Received in revised form:
14-July-2024
Accepted: 23-July-2024
Published online: 21-Dec-2024

Keywords:
Micro-expression recognition,
Spatiotemporal hand-crafted,
Spatiotemporal deep-learning.

ABSTRACT

The Micro-Expression (ME), which automatically reveals genuine human emotions, has gained significant attention. Recognizing the ME is crucial for many real-time applications. However, there are significant challenges to overcome. For instance, the number of ME frames is limited due to their short duration, and the subtle facial movements can be hard to detect due to their low intensity. These challenges need to be addressed to improve ME recognition. We propose a novel method for ME recognition in real-time. In this method, first, the apex frame is spotted using the rotated local binary pattern from six planes (RLBPS) and correlation coefficient (CC). Next, three hand-crafted methods such as the multi-color rotated local binary pattern from six planes (MRLBPS), the histograms of directed gradients from six planes (HDGS), and the histogram of image gradient direction from six planes (HIGDS) extract the features from the apex frame and its surrounding frames. Finally, the stacks of features as matrixes are fed into a three-dimensional convolutional neural network (3D-CNN), and the output is the maximum recognition rate by voting three results. The proposed method has shown promising results when compared to most state-of-the-art methods. According to the results, an average precision of 99% has been obtained using our proposed method. The combination of the RLBPS and the CC creates a strong method for spotting the apex frame. Also, feeding the stacks of spatiotemporal features into the 3D-ResNet increases the ME recognition rate in real-time.

I. Introduction

Over the past few years, the Micro-Expression (ME), as an automatic human emotion revelation, has attracted much attention. Recognizing it can provide insight into the emotional state (i.e., happy, scared, anxious, depressed, angry, and surprised). Also, analyzing it is valuable for various applications, such as social interaction, medicine, surveillance, law enforcement, teaching evaluations, psychology, interrogation, national security, etc. [1, 2].

The ME is the brief, spontaneous, subtle, involuntary, and fleeting facial expression that occurs in one-twenty-fifth to one-fifth of a second, which is challenging to detect by the naked eye and computer vision [3]. In other words, the ME is the facial muscle movements reacting to the emotional stimulus [4]. It may occur in high-risk situations when people attempt to conceal, manipulate, hide, or suppress their true feelings [5]. In fact, in these situations, the facial muscles work very cleverly to unveil the appearance of real emotions. Since this muscle action is uncontrollable, the ME can provide the essential clues to identify the criminal and detect lying.

Its association with thoughts and feelings was first declared by Ekman and Friesen in 1969 [6]. They found the MEs while examining videos of the psychiatric patients for lie detection. Indeed, one of the patients had decided to commit suicide. But she feigned to be glad and optimistic. While scrutinizing the patient interview video clip, Ekman surprisingly understood she was willing to hide her decision. He saw that the smile was replaced by a brief sadness. Later, the patient confessed to her lying.

In the following years, Ekman developed the ME Training Tool (METT) [7] to increase the human identification ability.

Publisher: University of Sistan and Baluchestan

Training by the MEET could slightly increase the recognition rate, and it was time-consuming [1]. Hence, researchers have endeavored to increase the recognition rate with the artificial intelligence methods [8-10]. In addition, they have tried to reduce the total elapsed time of the process. The hand-crafted methods extract the hand-engineered features relying on prior knowledge and heuristics, and deep-learning methods learn the high-level features automatically from very large datasets [1, 8-21].

The ME research is not limited to the recognition task. The detection and spotting of the apex frame are considered as its study bottleneck. The ME detection aims to capture the frames including the ME, excluding the ordinary facial expressions. Most importantly, the detection of a frame (i.e., the apex) that displays the expressive emotional state and the most facial muscle motions throughout the video sequence could be surprisingly utilized for the recognition task [1].

Still, there are severe challenges, which need to be solved. For example, there are a low number of involuntary public datasets as the ME happens under high-stakes, and collecting it is an arduous task. A scarce number of ME frames due to its short duration makes it also impossible to discover with computer vision. In addition, indiscernible subtle motions are not simple to describe due to the low intensity of facial muscular movements.

To address these challenges, in this study, we propose a novel method for the ME recognition in real-time. In this method, first, the apex frame is spotted using the rotated local binary pattern from six planes (RLBPS) and correlation coefficient (CC). We named this new method the RLBPS-CC. Second, the apex frame and surround frames are converted to a video to add the missed frames using the temporal interpolation model. Third, the subtle movements in the video are magnified, and the faces are aligned. Fourth, three hand-crafted methods such as the multi-color rotated local binary pattern from six planes (MRLBPS), the histograms of directed gradients from six planes (HDGS), and the histogram of image gradient direction from six planes (HIGDS) extract the features. Finally, the stacks of features as matrixes are fed into a three-dimensional convolutional neural network (3D-CNN), and the output is the maximum recognition rate by voting three results. Fig. 1 shows a framework of our proposed method.

To summarize, our main contributions are as follows:

- We propose a novel method by combining the spatiotemporal hand-crafted and deep-learning methods for the ME recognition in real-time.
- We propose a new method called the RLBPS-CC for spotting the apex frame.
- Unlike [13], we use the CC rather than the sum of squared differences (SSD) for the apex spotting. Also, we utilize the temporal interpolation model for the addition of the missed frames, since a low number of ME frames is recorded due to its short duration. In addition, the faces are alignment to remove the differences in the face shapes during the video recording. Furthermore, we add the HDGS and MRLBPS for feature extraction, and the outputs of three feature descriptors (the MRLBPS, HDGS, and HIGDS) are fed to a 3D-CNN for the ME recognition. Moreover, we apply our proposed method to four datasets, and we use the large-scale and balanced dataset (i.e., the CAS(ME)3).
- We have employed the rotated local binary pattern (RLBP) [22] on the three color channels rather than the simple local binary pattern (LBP) [23] and uniform LBP [23], and we also use the RLBP and CC for the apex detection task. Since this method is not only invariant to rotation, but also has a high discriminative power. To our knowledge, the RLBP has not yet been used for color channels feature extraction in six planes.
- In our proposed method, the matrixes obtained from MRLBPS, HDGS, and HIGDS are fed to a 3D-CNN by applying transfer learning. Although this method has more planes than the [2], [9], and [10] works, it does not consider as many planes as the [11], [19], and [17] works. Accordingly, it gives powerful spatiotemporal features to the 3D-CNN.
- Our proposed method increases the ME recognition rate compared to the previous state-of-the-art methods.

The rest of this article is organized as follows. Section II presents the related studies. Section III introduces the proposed method for the ME recognition in real-time. Section IV discusses the achieved experimental results. The conclusion and future directions are discussed in Section V.

II. Related works

In this section, initially, we review recent related works of literature in the field of ME. Then, we glimpse into the LBP on six planes (LBPS) which our proposed method derived from it.

A. Recent related works

Recently, it has been determined that temporal features can

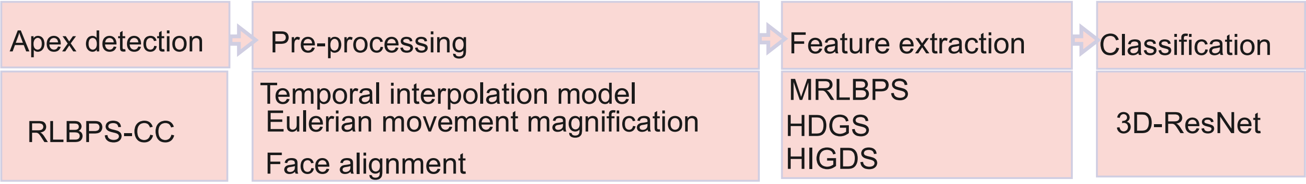

Fig. 1. A framework of our proposed method for the ME recognition in real-time.

reveal subtle movements [1]. In [9], four diagonal planes have been proposed for autonomous apex detection and ME recognition. In this work, these four temporal planes take the sequential images, which contain the magnified micro-motions. The pixels captured from these planes have been encoded using the LBP. The LBP histogram of the first plane is interconnected to the LBP histogram of the other planes for making a feature vector. The first feature vector, which obtains from three sequential images is compared with other feature vectors using the SSD for detecting the apex frame.

If the apex frame is the sixth frame, then, the fifth, sixth, and seventh frames are picked to feature extraction. The introduced feature extractor is a combination of the optical flow and the LBP from the four proposed planes [9]. Finally, the extracted features are classified using a linear support vector machine (LSVM) for the ME recognition.

In [10], the histogram of image gradient orientation (HIGO) method has been applied to the four diagonal planes, which consider sequential face images. Then, its histogram has been computed on each plane. Next, the obtained histograms have been concatenated to achieve the final histogram. Eventually, the final histogram has been fed to the LSVM for the ME recognition task.

In [11], the cubic-LBP feature descriptor has been presented for the first time. This method assumes fifteen planes in all possible directions. These planes can receive all temporal, spatial, and spatiotemporal features. Thus, the cubic-LBP is used for spotting the apex frame and other micro-movements [11, 17, 19]. Nonetheless, calculating the LBP code on the fifteen planes is time-consuming and expensive.

To reduce the processing time, in [19], one plane out of the 15 planes has been automatically selected using the partial differential equations (PDE) and the multivariate ridge regression as a simple linear classifier. This single plane specifies the main direction of the changes. Furthermore, in [17], the cubic-LBP has been made intelligent. In fact, a two-dimensional CNN (2D-CNN) intelligently learns to offer the particular planes for spotting the micro-movements. It identifies the direction/directions of the most movement.

To reduce the computational costs, the studies [13] and [8] choose the six planes with the best results according to several experiments. In [8], the apex frame is detected utilizing the LBP on the six planes and the SSD. Then, it is the input of a fast region-based 2D-CNN to recognize the ME. In addition to using these six planes for apex frame detection, these planes have been employed for feature extraction in [13]. At last, the features extracted from them have been classified by the LSVM.

Nevertheless, the spatiotemporal features can be learned by the spatiotemporal CNN (e.g., 3D-CNN) to lead to better performance. As far as the authors know, this work has not been done to recognize the ME.

A. Review of LBPS

Suppose a trail of images, and consider that they create a 3-dimensional (3D) volume (L, W, T). If $val_{\text{cen.pix.}}$ is corresponding to the gray value of the central pixel of the current frame, its coordinates are ($L_{\text{cen.pix.}}$, $W_{\text{cen.pix.}}$, $T_{\text{cen.pix.}}$). The coordinates of central pixel neighborhood in plane 1, plane 2, plane 3, plane 4, plane 5, and plane 6 are respectively given by:

$$\left(L_{\text{cen.pix.}} + \cos\left(\frac{2\pi x}{8}\right), W_{\text{cen.pix.}}, T_{\text{cen.pix.}} + \sin\left(\frac{2\pi x}{8}\right)\right) \tag{1}$$

$$\left(L_{\text{cen.pix.}}, W_{\text{cen.pix.}} - \sin\left(\frac{2\pi x}{8}\right), T_{\text{cen.pix.}} + \cos\left(\frac{2\pi x}{8}\right)\right) \tag{2}$$

$$\left(L_{\text{cen.pix.}} + \cos\left(\frac{2\pi x}{8}\right), W_{\text{cen.pix.}} - \sin\left(\frac{2\pi x}{8}\right), T_{\text{cen.pix.}} + \cos\left(\frac{2\pi x}{8}\right)\right) \tag{3}$$

$$\left(L_{\text{cen.pix.}} + \cos\left(\frac{2\pi x}{8}\right), W_{\text{cen.pix.}} - \sin\left(\frac{2\pi x}{8}\right), T_{\text{cen.pix.}} - \cos\left(\frac{2\pi x}{8}\right)\right) \tag{4}$$

$$\left(L_{\text{cen.pix.}} - \cos\left(\frac{2\pi x}{8}\right), W_{\text{cen.pix.}} - \sin\left(\frac{2\pi x}{8}\right), T_{\text{cen.pix.}} - \sin\left(\frac{2\pi x}{8}\right)\right) \tag{5}$$

$$\left(L_{\text{cen.pix.}} + \cos\left(\frac{2\pi x}{8}\right), W_{\text{cen.pix.}} - \sin\left(\frac{2\pi x}{8}\right), T_{\text{cen.pix.}} + \sin\left(\frac{2\pi x}{8}\right)\right) \tag{6}$$

where x is 0,1, ..., 7. When we suppose these six planes on the 3D volume, they have been intersected each other in the central pixel.

Then, the gray value of these neighborhood pixels are taken and compared with the gray value of the central pixel for computing the LBP. If their value is more, 1 is put. Otherwise, 0 is put. At last, all LBP feature vectors obtained from the six planes and concatenated to create LBPS feature vector.

III. Proposed method

This section presents the proposed method for ME recognition in real-time, which employs a combination of spatiotemporal hand-crafted and deep-learning methods. First, the apex frame is spotted using the RLBPS-CC. Then, the spatiotemporal features are extracted using spatiotemporal methods such as the MRLBPS, HDGS, and HIGDS from the apex and its surrounding frames.

Finally, the spatiotemporal features are fed to a spatiotemporal CNN (i.e., 3D-CNN). The flow diagram of the proposed method for the ME recognition is illustrated in Fig. 2.

A. *Apex Frame Detection Using the RLBPS-CC*

Initially, a video is recorded from the face of a person who wants to conceal her/his real emotions under special conditions. The video is converted into a trail of images, creating a 3D volume that includes the length (*L*) and width (*W*) of the images, as well as a time (*T*) dimension. Then, the spatiotemporal texture features are encoded using the RLBPS. In other words, the planes pictured in Fig. 3 take the pixels of the images in the spatiotemporal directions, and the RLBP operator codes them. Thus, the spatiotemporal directional changes are coded.

Clearly, the LBP weights are circularly shifting. Then, the maximum magnitude of the difference between neighbouring pixel's value ($\mathrm{val}_{\mathrm{neigh.pix.}}$) and the central pixel value ($\mathrm{val}_{\mathrm{cen.pix.}}$) in each plane is computed to find the dominant orientation (DO) as a reference. Next, the RLBP is calculated on each plane (see Equation 7). Finally, the RLBPS feature vector can be derived as follows:

$$\begin{gathered}
\mathrm{DO} = \max\left|val_{neigh.pix.} - val_{cen.pix.}\right| \\
\mathrm{RLBP} = \sum \mathrm{sign}\left(\mathrm{val}_{\mathrm{neigh.pix.}} - \mathrm{val}_{\mathrm{cen.pix.}}\right) \\
\times 2^{\mathrm{mod}(|\Lambda - \mathrm{DO}|,\Theta)} \\
\mathrm{RLBPS} = \sum v\{f(L,W,T) = \alpha\}; \\
\alpha = 0, \dots, l_p - 1; p = 0, \dots .5; \\
v(\beta) = \begin{cases} 0, if\ \beta\ is\ false \\ 1, if\ \beta\ is\ true \end{cases}
\end{gathered} \tag{7}$$

where the Λ is the neighbouring pixel's number, the Θ is the whole number of the neighbours, the *f(.)* is the obtained RLBP code, and the different numbers of its labels are defined by the l_p.

We can find the difference between the feature vectors of the various frames using the CC. The frame with the most difference in feature vector is considered the apex. The CC is calculated by:

$$\mathrm{CC} = \frac{\sum \mathrm{RLBPS_N} \times \mathrm{RLBPS_O}}{\sqrt{\sum \mathrm{RLBPS_N^2} \times \sum \mathrm{RLBPS_O^2}}} \tag{8}$$

where the $\mathrm{RLBPS_N}$ is the feature vector of the neutral face frame, and the $\mathrm{RLBPS_O}$ represents the feature vector of other frames.

The process of apex frame detection using the RLBPS-CC is shown in Fig. 4. First, a video is recorded from a person's face to create a 3D volume. Six planes (see Fig. 3) are applied to the trail images of the 3D volume. The RLBP code is calculated on each plane. Here, the DO is 32 – 25 = 7, and rotation is not needed. Values above threshold and the high weights corresponding to the thresholded neighbors are shown in orange color. Then, the RLBP map and its histogram are obtained from each plane. The RLBP histograms of six planes are concatenated to obtain the RLBPS feature vector. Finally, all histograms achieved from the images are compared using the CC for spotting the apex frame.

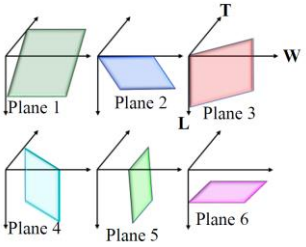

Fig. 3. The 6 planes.

B. *Pre-processing*

The apex frame, which was determined from section A, along with its surrounding frames are captured as a clip. The duration of ME short video clips should be increased and missed frames added using the temporal interpolation model [24] based on the Laplacian matrix. In this model, the video clip is a trail of images selected along a continuous curve, and the mapping between these frames has been learned to connect them. As a result, using this continuous-time function, it can generate by interpolation the frames that were not seen before at various time points (Fig. 5).

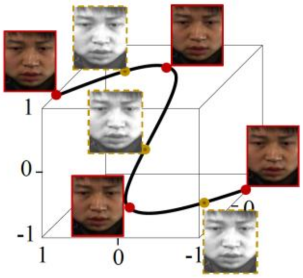

Fig. 5. The temporal interpolation model for generating the missed frames.

The next step is to import the video clip with more frames into a motion magnification method. We use the Eulerian movement magnification [25]. In this method, the Laplacian pyramid structure is utilized for separating the different frequency bands and applying a bandpass filter on them. The resulting signal is then amplified by a η factor. Finally, the original signal is added back to the amplified one to reconstruct the video. Mathematically, the movement magnification is [25]:

$$I(L,W,T+1) = I(L,W,T) + \sum \eta \frac{\partial I(L,W,T)}{\partial T} \tag{9}$$

where motion intensity has been shown by *I*. The process of the Eulerian movement magnification is shown in Fig. 6.

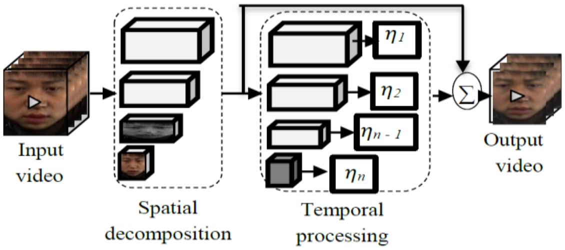

Fig. 6. The process of the Eulerian movement magnification.

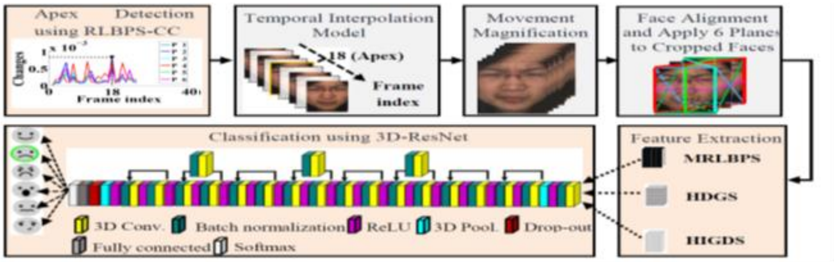

Fig. 2. The flow diagram of the proposed method for the ME recognition in real-time.

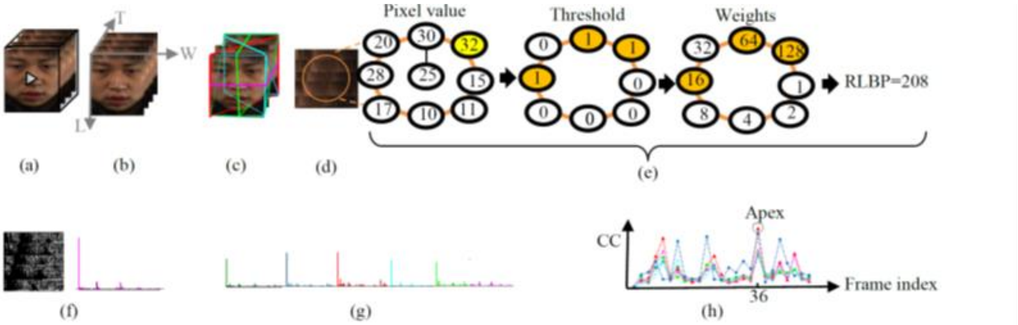

Fig. 4. Apex frame detection using the RLBPS-CC. (a) Video; (b) Creating a 3D volume using the trail of images; (c) Applying the six planes on the images of the 3D volume; (d) A sample of applying plane 6 to the trail of images; (e) Calculating the RLBP code on the plane 6; (f) The RLBP map (left) and its histogram (right) obtained from the plane 6; (g) Concatenating the RLBP histograms of six planes (obtaining RLBPS feature vector); (h) Comparing histograms achieved from all images of the trail (comparing RLBPS feature vectors) for spotting apex frame

Since the face shapes may be changed during the recording video, the face alignment should be performed. For the face alignment, the facial landmarks (with the *C* coordinates) of the front face (*F*) are detected by the discriminative response maps fitting (DRMF) [26]. The next frames (*R*) are reshaped using the local weighted mean (*Y*) for computing the transformation matrix (*M*) to register the face. Finally, the face regions are cropped according to the coordinates of the eyes in the first frame. Mathematically, the face alignment is as follows [2]:

$$M = Y\big(C(R), C(F)\big)$$

$$\mathrm{NR} = F \times M; \qquad (10)$$

where the NR is the normalized transformation frame. A sample of applying the DRMF on a face is illustrated in Fig. 7.

Fig. 7. A sample of applying the DRMF on a face.

B. Feature Extraction

In this step, the MRLBPS, HDGS, and HIGDS extract the features of the cropped face areas from the apex frame and its surrounding frames. The MRLBPS is applied to the color images to use their three channels (e.g., red, green, and blue). In this method, the RLBP (see Equation 7) separately codes the features of three channels on each of the six planes (Fig. 3). The results obtained from each channel are concatenated together. All achieved features from each plane are put into a matrix (Equation 11). This matrix represents the feature vector of the MRLBPS.

$$\mathrm{MRLBPS} = \begin{bmatrix} \mathrm{RedChannelRLBP1} & \mathrm{GreenChannelRLBP1} & \mathrm{BlueChannelRLBP1} \\ \mathrm{RedChannelRLBP2} & \mathrm{GreenChannelRLBP2} & \mathrm{BlueChannelRLBP2} \\ \mathrm{RedChannelRLBP3} & \mathrm{GreenChannelRLBP3} & \mathrm{BlueChannelRLBP3} \\ \mathrm{RedChannelRLBP4} & \mathrm{GreenChannelRLBP4} & \mathrm{BlueChannelRLBP4} \\ \mathrm{RedChannelRLBP5} & \mathrm{GreenChannelRLBP5} & \mathrm{BlueChannelRLBP5} \\ \mathrm{RedChannelRLBP6} & \mathrm{GreenChannelRLBP6} & \mathrm{BlueChannelRLBP6} \end{bmatrix} \qquad (11)$$

In the second feature descriptor (i.e., the HDGS), the Sobel operator with 90 and 0 direction masks as [-1 0 1] moves on the pixels in each plane to achieve the vertical and the horizontal derivatives (the D_L and D_W). Then, the gradient magnitude and its direction are calculated by

$$\text{Gradient magnitude} = \sqrt{{D_L}^2 + {D_W}^2}$$

$$\text{Gradient direction} = \tan^{-1}\frac{D_L}{D_W} \qquad (12)$$

To compute the feature vector, the pixels have the weighted voting for the direction channels based on the gradient calculation response. In the final feature vector, the histograms (the feature vectors) of the six planes are concatenated. Fig. 8 represents operating the HDGS.

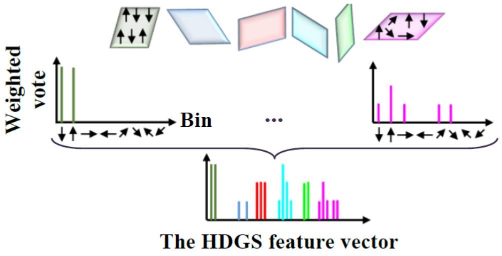

Fig. 8. The HDGS method.

The third feature extractor (i.e., the HIGDS) is applied to decrease the influence of the illumination and contrast. Although this method is similar to the HDGS, it utilizes the unweighted voting, since it gives up the gradient magnitude. The unweighted voting means a fixed amount of votes for each seen direction in the plane. Therefore, the gradient direction is independent of the brightness level of the pixel.

C. *Classification for ME Recognition*

The feature vectors obtained in the form of a 3D volume of matrices (224×224×224) are fed to a 3D-CNN (i.e., 3D-ResNet) by applying transfer learning. The core idea behind using the 3D-ResNet is the shortcut connections to resolve the vanishing gradient problem. In addition, we have assumed that the ResNet, which has already performed well on the ImageNet dataset, can be successfully applied to our achieved feature vectors as it could be generalized to our ME recognition task.

We follow a transfer learning approach for the 3D-CNN architecture, since it is not only optimized, but also resolves the issues of computational expensiveness and an insufficient number of samples. To avoid over-fitting in the training process, the pre-trained model and its learned parameters such as weight and bias are recommended [20].

To build the 3D-ResNet, 2D filters were extended in the third dimension to have 3D filters. Also, the 3D-ResNet includes the 3D-pooling and 3D-convolution layers. The depth of this model is eighteen, and it has a total of 71 layers. The architecture of the 3D-ResNet has been illustrated in Fig. 2. Finally, the ME classification was performed by voting.

IV. Experimental results

In this section, the experiments and achieved results are discussed. First, the used datasets containing the CASME, CASME II, CAS(ME)^3, and SMIC-NIR are explained. Then, implementation detail is brought to provide more details about the hyper-parameter setting, data augmentation, and the hardware and software. Finally, the experimental results and discussion will be expressed.

Used datasets

We employ four spontaneous and publicly available datasets. The first dataset, the CASME [27], has been tagged with the offset, onset, and apex frames. This dataset includes 195 samples of MEs at 60 fps with 1280 × 720 and 640 × 480 resolutions from 22 males and 13 females. The CASME II [28] contains 247 samples recording with a frame rate of two hundred fps from only Chinese participants. It consists of five classes of MEs. The resolution of the data is 280 × 240. The third is a large-scale dataset: the CAS(ME)^3 [29]. It offers 1,109 ME frames, which have been manually labeled. The CASME, CASME II, and CAS(ME)^3 have RGB images.

The fourth dataset is the SMIC-NIR [2], which is very close to the real situation. It contains 71 samples elicited from eight Caucasians and eight Asians participants (10 males and 6 females). In this dataset, the infrared data with a 640 × 480 resolution have been produced using a near-infrared camera. We employ this dataset for extracting the features using the HIGDS. A sample of the used datasets is shown in Fig. 9. Table 1 illustrates the summary of these datasets.

SMIC-NIR CASME II CASME CAS(ME)^3

Fig. 9. A sample of the used datasets.

TABLE 1
COMPARING THE SPECIFICATIONS OF USED DATASETS

Dataset	The number of Ethnicities	Emotion Classes	Frame rate (fps)	The ME samples
SMIC-NIR	2	3	25	71
CASME II	1	5	**200**	247
CASME	1	**7**	60	195
CAS(ME)^3	1	**7**	30	**1,109**

A. *Implementation detail*

Our method is implemented by MATLAB 2020 using a 3.5GHZ Intel Core i7 Duo processor. The experiments for training the model use Nvidia GTX950 GPU accelerator 8 GB memory. The hyper-parameter setting in the training step are listed in Table 2. To reduce the class imbalance and data augmentation, we have used rotation, flipping, and mirroring.

TABLE 2
TRAINING HYPER-PARAMETERS

Hyper-parameter	Value
Input size	224×224×224
Learning rate	0.0003
L2 regularization	0.0005
Max epoch	30
Bias/weight learning rate factor	10
Mini-batch size	8

B. *Experiments, results and discussion*

Initially, a video clip is recorded from the face of a person who wants to conceal her/his real emotions under special conditions. The video is converted into sequential images, which create a 3D volume. Then, the spatiotemporal texture features are encoded using the RLBPS. Next, the obtained feature vectors are compared using the CC, and the apex frame with a maximum changes is spotted using the RLBPS-CC. Fig. 10 shows a sample of the apex frame spotting using our RLBPS-CC method. In this sample (i.e., CASME\sub07\EP08_2), the frame index of the ground-truth apex is 11. Fig. 11 and Fig. 12 illustrate the errors of the apex frame spotting using our RLBPS-CC method and other previous methods.

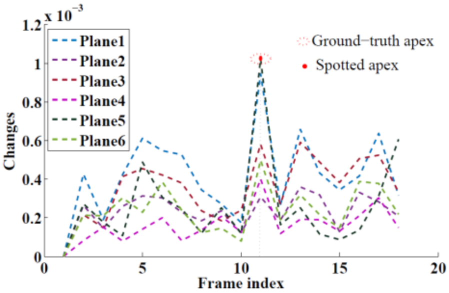

Fig. 10. The apex frame spotting using our RLBPS-CC method.

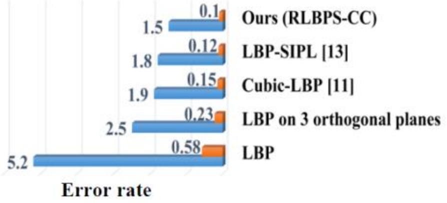

Fig. 11. The standard error (shown in orange color) and the mean absolute error (illustrated in blue color) for spotting the apex on the CASME.

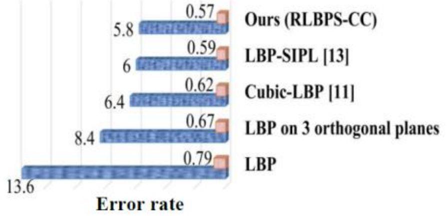

Fig. 12. The standard error (depicted in orange color) and the mean absolute error (pictured in blue color) for spotting the apex on the CASME II.

The apex frame along with its surrounding frames are captured as a clip video. The missed frames are added using the temporal interpolation model, and the sequential frames as a clip are imported into the Eulerian movement magnification method. The best motion magnification factor (η) based on several experiments is 8 (Fig. 13). According to the results, magnifying movements with a suitable factor improves the ME recognition performance. As seen in Fig. 13, excessive amplification reduces accuracy due to strengthening unwanted movements and artifacts, since these cases will hide the micro-movements in the MEs.

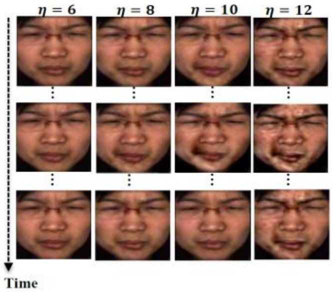

Fig. 13. Movement magnification with several η factors.

Since the face shapes may be changed, the face alignment is performed. For this task, the landmarks are determined using the DRMF. After the face alignment, the face regions are cropped according to the coordinates of the eyes in the first frame. Then, the spatiotemporal features of the cropped face areas are extracted using spatiotemporal methods such as the MRLBPS, HDGS, and HIGDS from the apex and its surrounding frames. The MRLBPS is applied to the color images of the CASME, CASME II, and CAS(ME)^3 to use their three channels (e.g., red, green, and blue). In this method, the RLBP separately codes the features of three channels on each of the six planes. The results obtained from each channel are concatenated together. All achieved features from each plane are put into a matrix, which represents the feature vector of the MRLBPS.

In the HDGS, the Sobel operator with 90 and 0 direction masks as [-1 0 1] moves on the pixels in each plane to achieve the vertical and the horizontal derivatives. To compute the feature vector, each pixel has a weighted vote for the direction channel, according to the gradient calculation response. In the final feature vector, the feature vectors of the six planes are concatenated.

The HIGDS ignores the gradient magnitude, and it utilizes the simple vote. This method is applied to the SMIC-NIR images.

The spatiotemporal feature vectors as a 3D volume of matrices (224×224×224) are fed to the pre-trained 3D-ResNet by applying transfer learning for the ME classification task. The fully-connected layer has been changed to adapt our work. Training the 3D-ResNet requires several hyper-parameters to be used in the back-propagation learning process. The optimization solver is an important parameter. We utilize the stochastic gradient descent (SGD) solver in the training process. It minimizes the loss function by moving in the direction of the negative gradient at each iteration. The other hyper-parameters are the learning rate, L2 regularization, mini-batch size, and drop-out. We set the L2 regularization=0.0005 and the drop-out=0. Stride is 1. Different values of the learning rate and the mini-batch size are implemented, and the best one is chosen. The obtained results are pictured in Fig. 14.

Finally, the best ME recognition rate is reported by voting. It is worth mentioning that we use the 10-fold cross-validation strategy, and we report the average of folds. Table 3 details the results for the ME recognition using our proposed method, which shows improvements over other methods.

Since the ME is more effectively revealed in a sequence of frames than in a single frame, it is best to use multiple frames. Our feature extraction methods can reveal changes in the previous and next frames using the six temporal planes. The six introduced planes code the changes over time in different directions. These planes have pixels, which carry valuable and impactful information. Moreover, the spatiotemporal features can be quickly classified with a high-accuracy rate using a 3D-CNN (i.e., the 3D-ResNet) compared to the LSVM.

The recognition rate of the ME using the feature extraction methods on the different planes (e.g., the 3 orthogonal planes, the 4 diagonal planes, and the 6 introduced planes) has been summarized in Fig. 15. As we have seen, the six planes (shown in Fig. 3) produce the best result. In addition, Fig. 16 shows the elapsed time for training of different 3D-CNN models.

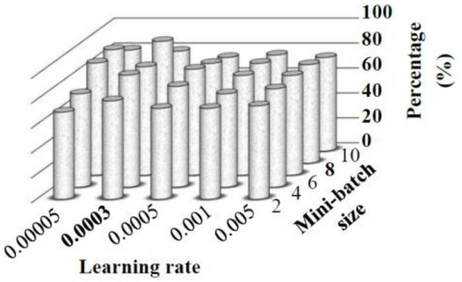

Fig. 14. The obtained results from different values of the learning rate and the mini-batch size.

TABLE 3

THE RESULTS FOR ME RECOGNITION ON THE COMPOSITE DATASETS. BOLD TEXT SHOWS THE BEST RESULT. UNDERLINE TEXT INDICATES SECOND-BEST PERFORMANCE.

Method	Accuracy (%)
HIGD on three orthogonal planes + LSVM [2]	55.9
LBP on three orthogonal planes + LSVM [2]	55.9
Dual-stream combining optical flow and dynamic image CNNs [30]	73.1
Combination of optical flow and LBP on diagonal planes [9]	79.6
HIGO on diagonal planes + LSVM [10]	82.6
HIGDS + LSVM [13]	83.7
Multi-color LBP on six intersection planes + LSVM [13]	86.2
µ-Pre-training of Deep Bidirectional Transformers (Micron-BERT) [31]	89.1
DenseNet + Efficient Channel Attention (ECA) [32]	95.76
Ours	**97.6**

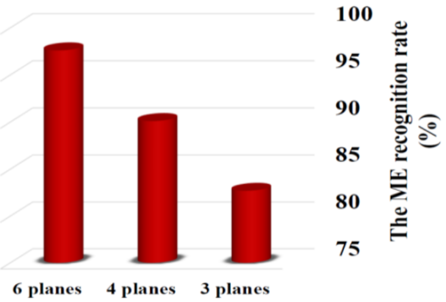

Fig. 15. The ME recognition rate using the feature extraction methods on the different planes.

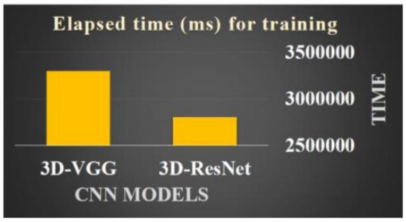

Fig. 16. The elapsed time (ms) for training of two different 3D-CNN models.

A. Experimental results using the evaluation metrics

In another experiment, the proposed method's usefulness is measured using the precision, F1-score, UF1, specificity, and sensitivity metrics [33]. These evaluation metrics can computed using the mathematical formulas in Table 4. Table 5 represents the achieved results of cross-validation using the proposed method. According to the results, an average precision of 99% has been obtained using our proposed method. Also, the average of other metrics is 97%. In addition, Table 6, Table 7, Table 8, and Table 9 compare the results of ours and other state-of-the-art methods on different datasets. The results show superior performance of our proposed method in comparison with others.

The possible reasons for increasing the ME recognition rate could be that (1) Unlike LBP, the RLBP circularly moves the weights to obtain the dominant direction; (2) Computing the RLBP on three channels of RGB images can provide the meaningful features; (3) Feature extraction on six small and temporal planes using the MRLBPS, HDGS, and HIGDS can reveal micro variants and changes; (4) Feeding the extracted temporal features to a 3D-ResNet can increase the ME recognition rate. Unlike 3D-VGG, the 3D-ResNet have advantages include requiring the feature learning only once, solving vanish/detonate gradients problem, reducing the training process time.

TABLE 4

THE EVALUATION METRICS

Name	Formula
Sensitivity	(true positives)/(false negatives+true positives)
Specificity	(true negatives)/(true negatives+ false positives)
Precision	(true positives)/(false positives+true positives)
F1-score	2×((Precision×Sensitivity)/(Precision+Sensitivity))
UF1	2×(∑ ((Precision×Sensitivity)/(Precision+Sensitivity)) /the number of classes)

TABLE 5
THE ACHIEVED RESULTS OF CROSS-VALIDATION USING THE PROPOSED METHOD ON THE COMPOSITE DATASETS

Fold	UF1	F1-score	precision	specificity	sensitivity
1	97%	98%	98%	98%	98%
2	96%	97%	99%	97%	97%
3	98%	98%	98%	98%	98%
4	96%	97%	99%	97%	95%
5	97%	96%	100%	98%	96%
6	97%	97%	99%	97%	97%
7	96%	97%	98%	96%	97%
8	98%	98%	99%	95%	98%
9	97%	98%	100%	99%	98%
10	98%	97%	99%	98%	97%
Average	97%	97%	99%	97%	97%

It is noteworthy that calculating the RLBP is time-consuming compared to the LBP. Also, feature extraction on six planes has computation complexity. Thus, the computational complexity of the proposed method is more than implementation a typical method or feeding raw images to a 3D-CNN.

TABLE 6
THE RESULTS FOR ME RECOGNITION IN TERM OF UF1 ON THE SMIC-NIR AND CASME II DATASETS. BOLD TEXT SHOWS THE BEST RESULT. UNDERLINE TEXT INDICATES SECOND-BEST PERFORMANCE.

Method	SMIC-NIR	CASME II
	UF1 (%)	UF1 (%)
Bi-Weighted Oriented Optical Flow (Bi-WOOF) [34]	57.27	78.05
Optical Flow Features from Apex frame Network (OFF-ApexNet) [35]	68.17	87.64
Shallow Triple Stream Three-dimensional CNN (STSTNet) [36]	68.01	83.82
Lightweight Apex-based Enhanced Network (LAENet) [37]	66.2	91.01
Hierarchical Transformer Network (HTNet) [38]	89	95.32
Ours	**96.8**	**97.5**

TABLE 7
THE RESULTS FOR ME RECOGNITION IN TERMS OF F1-SCORE AND ACCURACY ON THE SMIC-NIR AND CASME II DATASETS. BOLD TEXT SHOWS THE BEST RESULT. UNDERLINE TEXT INDICATES SECOND-BEST PERFORMANCE.

Method	SMIC-NIR		CASME II	
	F1-score (%)	Accuracy (%)	F1-score (%)	Accuracy (%)
Key Facial Components (KFC) [39]	78	77	73.75	72.76
Attention-based magnification-adaptive networks [40]	77	79.87	71	75.4
Shallow Triple Stream Three-dimensional CNN (STSTNet) [36]	68.01	70.13	83.82	86.86
Multi-scale 3D-ResNet50 [41]	75.1	74.6	88.9	91.35
Local Binary Pattern on Six Intersection Planes (LBP-SIP*l*) and Fast Region-based Convolutional Neural Network (FR-CNN) [8]	92	91.2	95.66	96.11
Ours	**97**	**97.4**	**97.5**	**97.8**

TABLE 8
THE RESULTS FOR ME RECOGNITION IN TERMS OF F1-SCORE AND ACCURACY ON THE CASME DATASETS. BOLD TEXT SHOWS THE BEST RESULT. UNDERLINE TEXT INDICATES SECOND-BEST PERFORMANCE.

Method	CASME	
	F1-score (%)	Accuracy (%)
Three-stream CNN (TSCNN) [42]	72.7	73.88
Knowledge distillation [43]	77	81.8
Dual-stream SpatioTemporal Attention Network (DSTAN) [44]	75	78
Local Binary Pattern on Six Intersection Planes (LBP-SIP*l*) and Fast Region-based Convolutional Neural Network (FR-CNN) [8]	80	81.56
Intelligent cubic-LBP [17]	93	93
Ours	**97.1**	**97.5**

TABLE 9
THE RESULTS FOR ME RECOGNITION IN TERMS OF F1-SCORE AND ACCURACY ON THE CAS(ME)^3 DATASETS. BOLD TEXT SHOWS THE BEST RESULT. UNDERLINE TEXT INDICATES SECOND-BEST PERFORMANCE.

Method	CAS(ME)^3
	UF1 (%)
Shallow Triple Stream Three-dimensional CNN (STSTNet) [36]	37.95
μ-Pre-training of Deep Bidirectional Transformers (Micron-BERT) [31]	56.04
Three-stream temporal-shift attention network based on self-knowledge distillation (SKD-TSTSAN) [45]	86.48
Ours	**97**

V. Conclusions

In this paper, a novel method called the RLBPS-CC has been proposed for the apex frame spotting. Also, a new method has been suggested for the ME recognition in real-time. In this method, three hand-crafted methods (i.e., the MRLBPS, HDGS, and the HIGDS) extract the features from the detected apex frame and its surrounding frames. Then, the stacks of the spatiotemporal features are fed into the 3D-ResNet, and the output is the maximum recognition rate by voting three results. The inference processing time took approximately 0.9 seconds. Based on the obtained results, the proposed methods show promising outcomes compared to most state-of-the-art techniques. In the future, this method could be used in other applications where subtle variations in features are required to be spotted.

ACKNOWLEDGMENT

This research was supported by Research grant of the University of Tabriz (number و/۲۷/۹۸۰).

REFERENCES

[1] V. Esmaeili, M. Mohassel Feghhi, and S. O. Shahdi, "A comprehensive survey on facial micro-expression: approaches and databases," Multimedia Tools and Applications, Vol. 81, No. 28, pp. 40089-40134, 2022.

[2] X. Li et al., "Towards reading hidden emotions: A comparative study of spontaneous micro-expression spotting and recognition methods," IEEE transactions on affective computing, Vol. 9, No. 4, pp. 563-577, 2017.

[3] G. Zhou et al., "Micro-expression action unit recognition based on dynamic image and spatial pyramid," The Journal of Supercomputing, pp. 1-24, 2023.

[4] Y. Li, J. Wei, Y. Liu, J. Kauttonen, and G. Zhao, "Deep learning for micro-expression recognition: A survey," IEEE Transactions on Affective Computing, 2022.

[5] G. Zhao, X. Li, Y. Li, and M. Pietikäinen, "Facial Micro-Expressions: An Overview," Proceedings of the IEEE, 2023.

[6] P. Ekman and W. V. Friesen, "Nonverbal leakage and clues to deception," Psychiatry, Vol. 32, No. 1, pp. 88-106, 1969.

[7] P. Ekman, Micro expressions training tool Emotionsrevealed. com, 2003.

[8] V. Esmaeili, M. Mohassel Feghhi, and S. O. Shahdi, "Automatic Micro-Expression Recognition Using LBP-SIPl and FR-CNN," AUT Journal of Modeling and Simulation, Vol. 54, No. 1, pp. 59-72, 2022.

[9] V. Esmaeili, M. Mohassel Feghhi, and S. O. Shahdi, "Autonomous apex detection and Micro-expression recognition using proposed diagonal Planes," International Journal of Nonlinear Analysis and Applications, Vol. 11, pp. 483-497, 2020.

[10] V. Esmaeili, M. M. Feghhi, and S. O. Shahdi, "Micro-expression recognition using histogram of image gradient orientation on diagonal planes," in 2021 5th International Conference on Pattern Recognition and Image Analysis (IPRIA), 2021: IEEE, pp. 1-5.

[11] V. Esmaeili and S. O. Shahdi, "Automatic micro-expression apex spotting using Cubic-LBP," Multimedia Tools and Applications, Vol. 79, pp. 20221-20239, 2020.

[12] V. Esmaeili, M. M. Feghhi, and S. O. Shahdi, "Automatic micro-expression apex frame spotting using local binary pattern from six intersection planes," arXiv preprint arXiv:2104.02149, 2021.

[13] V. Esmaeili, M. Mohassel Feghhi, and S. O. Shahdi, "Micro-Expression Recognition based on the Multi-Color ULBP and Histogram of Gradient Direction from Six Intersection Planes," Journal of Iranian Association of Electrical and Electronics Engineers, Vol. 19, No. 3, pp. 123-130, 2022.

[14] V. Esmaeili, M. M. Feghhi, and S. O. Shahdi, "Early COVID-19 Diagnosis from Lung Ultrasound Images Combining RIULBP-TP and 3D-DenseNet," in 2022 9th Iranian Joint Congress on Fuzzy and Intelligent Systems (CFIS), 2022: IEEE, pp. 1-5.

[15] V. Esmaeili and M. Mohassel Feghhi, "Real-time Authentication for Electronic Service Applicants using a Method Based on Two-Stream 3D Deep Learning," Soft Computing Journal, 2023.

[16] V. Esmaeili and M. Mohassel Feghhi, "Diagnosis of Covid-19 Disease by Combining Hand-crafted and Deep-learning Methods on Ultrasound Data," Journal of Machine Vision and Image Processing, Vol. 9, No. 4, pp. 31-41, 2022.

[17] V. Esmaeili, M. Mohassel Feghhi, and S. O. Shahdi, "Spotting micro - movements in image sequence by introducing intelligent cubic - LBP," IET Image Processing, Vol. 16, No. 14, pp. 3814-3830, 2022.

[18] V. Esmaeili and M. M. Feghhi, "COVID-19 Diagnosis: ULBPFP-Net Approach on Lung Ultrasound Data," Iranian Journal of Electrical & Electronic Engineering, Vol. 19, No. 3, 2023.

[19] V. Esmaeili, M. Mohassel Feghhi, and S. Shahdi, "Applying Partial Differential Equations on Cubic Uniform Local Binary Pattern to Reveal Micro-Changes," Journal of Electrical and Computer Engineering Innovations (JECEI), pp. 259-270, 2023.

[20] A. Ebrahimi, S. Luo, and R. Chiong, "Introducing transfer learning to 3D ResNet-18 for Alzheimer's disease detection on MRI images," in 2020 35th international conference on image and vision computing New Zealand (IVCNZ), 2020: IEEE, pp. 1-6.

[21] Z. Raisi and J. Zelek, "Investigation of Deep Learning Optimization Algorithms in Scene Text Detection," International Journal of Industrial Electronics Control and Optimization, Vol. 6, No. 3, pp. 171-182, 2023.
and Optimization, Vol. 6, No. 3, pp. 171-182, 2023.

[22] R. Mehta and K. Egiazarian, "Rotated local binary pattern (RLBP): rotation invariant texture descriptor," in 2nd International Conference on Pattern Recognition Applications and Methods, ICPRAM 2013, Barcelona, Spain, 15.-18.2. 2013, 2013, pp. 497-502.

[23] T. Ojala, M. Pietikäinen, and T. Mäenpää, "A generalized local binary pattern operator for multiresolution gray scale and rotation invariant texture classification," in Advances in Pattern Recognition—ICAPR 2001: Second International Conference Rio de Janeiro, Brazil, March 11–14, 2001 Proceedings 2, 2001: Springer, pp. 399-408.

[24] T. Pfister, X. Li, G. Zhao, and M. Pietikäinen, "Recognising spontaneous facial micro-expressions," in 2011 international conference on computer vision, 2011: IEEE, pp. 1449-1456.

[25] H.-Y. Wu, M. Rubinstein, E. Shih, J. Guttag, F. Durand, and W. Freeman, "Eulerian video magnification for revealing subtle changes in the world," ACM transactions on graphics (TOG), Vol. 31, No. 4, pp. 1-8, 2012.

[26] A. Asthana, S. Zafeiriou, S. Cheng, and M. Pantic, "Robust discriminative response map fitting with constrained local models," in Proceedings of the IEEE conference on computer vision and pattern recognition, 2013, pp. 3444-3451.

[27] W.-J. Yan, Q. Wu, Y.-J. Liu, S.-J. Wang, and X. Fu, "CASME database: A dataset of spontaneous micro-expressions collected from neutralized faces," in 2013 10th IEEE international conference and workshops on automatic face and gesture recognition (FG), 2013: IEEE, pp. 1-7.

[28] W.-J. Yan et al., "CASME II: An improved spontaneous micro-expression database and the baseline evaluation," PloS one, Vol. 9, No. 1, p. e86041, 2014.

[29] J. Li et al., "CAS (ME) 3: A third generation facial spontaneous micro-expression database with depth information and high ecological validity," IEEE Transactions on Pattern Analysis and Machine Intelligence, Vol. 45, No. 3, pp. 2782-2800, 2022.

[30] J. Tang, L. Li, M. Tang, and J. Xie, "A novel micro-expression recognition algorithm using dual-stream combining optical flow and dynamic image convolutional neural networks," Signal, Image and Video Processing,

Vol. 17, No. 3, pp. 769-776, 2023.

[31] X.-B. Nguyen, C. N. Duong, X. Li, S. Gauch, H.-S. Seo, and K. Luu, "Micron-bert: Bert-based facial micro-expression recognition," in Proceedings of the IEEE/CVF Conference on Computer Vision and Pattern Recognition, 2023, pp. 1482-1492.

[32] H. Yang, S. Sun, and J. Chen, "Deep Learning-Based Micro-Expression Recognition Algorithm Research," International Journal of Computer Science and Information Technology, Vol. 2, No. 1, pp. 59-70, 2024.

[33] C. Nicholson, "Evaluation metrics for machine learning—accuracy, precision, recall, and F1 defined,"Pathmind.http://pathmind.com/wiki/accuracy-precision-recall-f1, 2019.

[34] S.-T. Liong, J. See, K. Wong, and R. C.-W. Phan, "Less is more: Micro-expression recognition from video using apex frame," Signal Processing: Image Communication, Vol. 62, pp. 82-92, 2018.

[35] Y. S. Gan, S.-T. Liong, W.-C. Yau, Y.-C. Huang, and L.-K. Tan, "OFF-ApexNet on micro-expression recognition system," Signal Processing: Image Communication, Vol. 74, pp. 129-139, 2019

[36] S.-T. Liong, Y. S. Gan, J. See, H.-Q. Khor, and Y.-C. Huang, "Shallow triple stream three-dimensional cnn (ststnet) for micro-expression recognition," in 2019 14th IEEE international conference on automatic face & gesture recognition (FG 2019), 2019: IEEE, pp. 1-5.

[37] Y. Gan, S.-E. Lien, Y.-C. Chiang, and S.-T. Liong, "LAENet for micro-expression recognition," The Visual Computer, Vol. 40, No. 2, pp. 585-599, 2024.

[38] Z. Wang, K. Zhang, W. Luo, and R. Sankaranarayana, "HTNet for micro-expression recognition," arXiv preprint arXiv:2307.14637, 2023.

[39] Y. Su, J. Zhang, J. Liu, and G. Zhai, "Key facial components guided micro-expression recognition based on first & second-order motion," in 2021 IEEE International Conference on Multimedia and Expo (ICME), 2021: IEEE, pp. 1-6.

[40] M. Wei, W. Zheng, Y. Zong, X. Jiang, C. Lu, and J. Liu, "A novel micro-expression recognition approach using attention-based magnification-adaptive networks," in ICASSP 2022-2022 IEEE International Conference on Acoustics, Speech and Signal Processing (ICASSP), 2022: IEEE, pp. 2420-2424.

[41] H. Jin, N. He, Z. Li, and P. Yang, "Micro-expression recognition based on multi-scale 3D residual convolutional neural network," Mathematical Biosciences and Engineering, Vol. 21, No. 4, pp. 5007-5031, 2024.

[42] B. Song et al., "Recognizing spontaneous micro-expression using a three-stream convolutional neural network," Ieee Access, vol. 7, pp. 184537-184551, 2019.

[43] B. Sun, S. Cao, D. Li, J. He, and L. Yu, "Dynamic micro-expression recognition using knowledge distillation," IEEE Transactions on Affective Computing, Vol. 13, No. 2, pp. 1037-1043, 2020.

[44] Y. Wang et al., "Micro expression recognition via dual-stream spatiotemporal attention network," Journal of Healthcare Engineering, Vol. 2021, No. 1, 2021.

[45] G. Zhu et al., "SKD-TSTSAN: Three-Stream Temporal-Shift Attention Network Based on Self-Knowledge Distillation for Micro-Expression Recognition," arXiv preprint arXiv:2406.17538, 2024.

Vida Esmaeili received her B.S. degree in electrical engineering from the Azad University of Abhar, Iran, in 2015 and the M.S. degree in electrical engineering from the Azad University of Qazvin, Iran, in 2018. Since 2019, she has been working toward the Ph.D. degree in electrical engineering at the Tabriz University, Iran. Her research interests include the area of image processing, machine learning, data science, and pattern recognition. She has published more than 18 technical papers both at the national and international levels. Moreover, she served as a reviewer for several international journals, such as IEEE transactions on affective computing, Multimedia Systems, Scientific Reports, Visual Computer, Machine Vision and Applications, Signal, Image and Video Processing, etc.

Mahmood Mohassel Feghhi received the B.S. and M.S. degrees (Hons.) in electrical engineering from the Iran University of Science and Technology, Tehran, Iran, in 2006 and 2009, respectively, and the Ph.D. degree in electrical engineering from the College of Engineering, University of Tehran, Tehran, in 2015. From 2007 to 2016, he was a Senior Design Engineer in communication systems design with several communications industries and Inc. Since 2016, he has been with the Faculty of Electrical and Computer Engineering, University of Tabriz, Iran, where he is currently an Associate Professor. He has published more than 60 technical papers in international journals and conferences in the fields of information theory, wireless communications, signal and image processing, machine learning, data science, 5G/6G cellular networks, the Internet of Things (IoT), scheduling, and optimization . He is the Director-in-Charge of the Journal of Advanced Signal Processing (JASP), and the Executive Manager of the Tabriz Journal of Electrical Engineering (TJEE) . His current research interests include information theory, wireless communication networks, signal processing, machine learning, and optimization.

Dr. Mohassel Feghhi was the Chair of Scientific Committee at the 4th West Asian Symposium on Optical and Millimeter-wave Wireless Communications (WASOWC 2022), and the Scientific Committee Chair of the Communications section at the 28th Iranian Conference on Electrical Eng. (ICEE 2020) .Moreover, he served as a TPC member of several international conferences, and also serves as a reviewer for several international journals, such as IEEE Transactions on Green Communications and Networking, IEEE Transactions on Vehicular Technology (IEEE-TVT), IEEE Systems Journal, IET Communications, Ad Hoc Networks, Journal of the Franklin Institute, etc.

IECO

This page intentionally left blank.

International Journal Of
Industrial Electronics Control and Optimization
Print ISSN: 3517-2645
Online ISSN: 3568-2645
Homepage: https://ieco.usb.ac.ir/

Robust Beamforming for Ultrasonic Imaging using Wavelet-based Thresholding and Coherence Weighting

Mozhgan Ehsani[1] | Mehdi Bekrani[2] | Solyman Garousi[3]

Department of Electrical and Computer Engineering, Qom University of Technology (QUT), Qom, Iran [1,2,3]
Corresponding author's email: bekrani@qut.ac.ir

Article Info

Article type:
Research Article

Article history:
Received: 05-May-2024
Received in revised form:
05-Aug-2024
Accepted: 12-Aug-2024
Published online: 21-Dec-2024

Keywords:
Coherence weighting,
Covariance matrix,
Delay-and-sum beamformer,
MV beamformer,
Ultrasonic waves.

ABSTRACT

The delay-and-sum (DS) beamforming and delay-weight-and-sum (DWS) beamforming are primary methods in ultrasonic imaging with phased arrays. Total focusing method (TFM) and Minimum Variance (MV) based adaptive beamforming are well-known methods within DS and DWS beamforming, respectively. The MV-based adaptive beamforming significantly reduces interferences and provides high-resolution image compared to TFM beamforming, at the cost of high computational complexity, and sensitivity to input statistics for matrix inversion. To address these challenges, recently, iterative MV (IMV) has been proposed to alleviate computational burdens without the need for matrix inversion. The delay-multiply-and-sum (DMAS) beamforming enhances TFM beamforming performance by employing spatial information of the array signals. However, the resulting images remain susceptible to speckle and background noises in all of these beamformers. In this paper, we aim to improve these beamforming methods so that speckle and Gaussian background noise are reduced while preserving the quality of the reflective echoes in ultrasonic images. In the proposed method, a wavelet transform with a novel threshold function is applied to the received signals to initially reduce the noise, followed by the application of the beamformer. Subsequently, the coherence weighting using the denoised signals is derived, and the obtained coherence weighting is then integrated into the beamforming process. Simulation results demonstrate that the proposed method achieves a significant reduction in background noise and speckles of the above beamformer, and particularly reduces background noise and speckles of beamformer up to approximately -27dB while preserving the detection capability of reflective points.

I. Introduction

Today, ultrasound imaging systems commonly utilize Delay-and-Sum (DS) beamformers. These types of beamformers operate in a fast and simple manner but provide images with low resolution [1]. Synthetic Aperture Focusing Technique (SAFT) and Total Focusing Method (TFM) are two widely used DS based imaging methods[2-4].

One of the advanced beamforming methods in ultrasonic imaging with phased array is the Delay-Weight-and-Sum (DWS) beamforming, which operates by weighting the delayed signals and then summing them. The adaptive beamforming method based on the Minimum Variance (MV) theory is a well-known beamforming method within the context of DWS beamforming techniques.

In the MV adaptive beamformer, high-resolution and high-contrast images are generated. The associated weights are determined at each moment in such a way that the output power of the beamformer reaches the minimum possible value while preserving the desired signal.

The MV adaptive beamforming method involves a significant computational complexity. In recent years, approaches have been proposed to reduce the computational complexity of the MV beamforming technique[1]. In the Decimated MV (DMV) method, which prioritizes focusing during the ultrasonic wave transmission phase, a uniform reduction of array information is achieved by applying a

Publisher: University of Sistan and Baluchestan

spatial low-pass frequency filter. This reduction doesn't compromise the effective signal information contained within the reduced array covariance matrix[5]. Another approach to low-complexity MV beamforming involves transferring data to the beam space. This has been proposed utilizing various transformations such as the Discrete Fourier Transform (DFT), Discrete Cosine Transform (DCT), or Legendre Polynomial Transform[6]. The iterative MV (IMV) based adaptive beamforming method exploits the fact that received signals from two adjacent imaging points in ultrasonic imaging do not differ significantly. A new formula for updating the weights is presented, which eliminates the need for computing the covariance matrix inverse and results in faster optimization with just a few iterations for each imaging point [7].

In[8, 9], low-complexity and robust MV beamformers are proposed for ultrasound imaging systems using beamspace dominant mode rejection (DMR). In DMR technique, only eigenvectors corresponding to a few largest eigenvalues are computed. Computational complexity is reduced by predicting element-space data to the beam space domain and then employing dominant mode removal on the beam-space covariance matrix.

The Adaptive Spatial Smoothing MV (ASS-MV) method enhances the resolution and the ratio of contrast enhancement to noise of the MV method, by specifying subarray lengths for spatial smoothing, while preserving MV performance [10]. Moreover, the Generalized Sidelobe Canceller (CSG) partially suppresses MV method by dividing the weight vector into two parts in an adaptive manner [11]. Additionally, a Fast Adaptive Beamforming with sidelobe control is proposed, which minimizes the sidelobe level [12].

Recent advancements in ultrasonic imaging for non-destructive testing (NDT) have introduced innovative approaches to enhance defect detection and image quality. In[13], a full-matrix imaging method based on the search-vector imaging condition is proposed to detect the defects. The search-vector imaging condition integrates waveform inversion using first-order derivative vectors and approximated Hessian matrices to achieve highly accurate defect detection in complex-surface components.

Ref. [14] proposes a cost-effective imaging method utilizing Full Matrix Migration Total Focus Method (FM-TFM) and normalized cross-correlation (NCC) template matching, offering large-area scanned images without costly equipment.

In[15], a discretized tensor-based model for TFM, employing a sparse regularization strategy significantly enhances defect characterization and noise suppression, outperforming traditional TFM in both simulation and experimental studies. In[16], an optimized TFM based on delay-multiply-and-sum (DMAS) beamforming improves imaging performance through synthetic focusing in TFM, promising enhanced accuracy and quality in NDT applications.

Some recent studies in the field of NDT have focused on leveraging artificial neural networks, particularly deep learning techniques, to enhance inspection processes. In [17], a conditional Generative Adversarial Network (cGAN) was employed to replace conventional Full Matrix Capture (FMC) and Total Focusing Method (TFM) procedures with a simplified zero-degree plane wave. This approach demonstrated comparable resolution to TFM while significantly improving contrast in over 94% of reconstructions.

Reference [18] introduced a deep neural network (DNN) tailored for ultrasonic array tomography, specifically targeting subsurface crack recognition and pixel-wise cross-section image reconstruction in reinforced concrete structures. The DNN adopted an encoder-decoder architecture enhanced by skip connections and residual modules, effectively adapting to the semantic structure of ultrasonic B-scans. In[19], researchers developed a deep-learning surrogate model for rapid generation of realistic ultrasonic images in the Multi-modal Total Focusing Method (M-TFM). Using a Conditional U-Net (cU-Net), they facilitated controlled generation of high-resolution M-TFM images. This approach was validated with a case study involving planar defects in a complex weld-like profile, addressing uncertainties in image parameter reconstruction through numerical and experimental data.

While various beamforming methods aim to generate the ultrasonic image with high resolution and low complexity, they are sensitive to noises and may fail to detect the reflectors in noisy situations.

On the other hand, using deep learning in NDT offers significant benefits but also faces challenges. Deep learning models require large, labeled datasets for effective training, which can be costly and time-consuming to obtain, especially for diverse or rare defects. Additionally, their computational demands and concerns about robustness in noisy environments pose further obstacles.

In this paper, we propose a noise robust beamforming method to enhance the TFM, DMAS, MV, and IMV methods in a way that reduces background speckle and Gaussian noises in the resulting images. To achieve this, we employ a coherence weighting method [3] along with thresholding in the wavelet transform [20] to remove noise from ultrasonic images. An improved thresholding function, based on logistic function, is introduced to denoise images generated by the mentioned beamformers.

The remainder of this paper is organized as follows. In Section II, some well-known beamformers are introduced. In Section III, we propose a new noise robust beamforming method for ultrasonic imaging. The simulation and experimental results are conducted in Section IV. Conclusion is finally given in Section V.

II. Beamforming methods

In this section, we outline several beamforming methods. Our objective is to enhance their performance and make them more robust to noise using the proposed denoising method.

A. Delay-and-Sum (DS) beamformer

In the DS beamformer, suitable delays are initially applied to the received signals of the array elements to compensate for path delays. Subsequently, these signals are summed with constant weighting coefficients. If $z_j[n]$ represents the measured signal of element j at time index n, then

$$x_j[n] = z_j\left[n - \Delta_j[n]\right] \tag{1}$$

where $\Delta_j[n]$ represents the delay of element j relative to time index n, and $x_j[n]$ is the delayed signal received by element j .

To obtain the output of the DS beamformer, a constant weight is used, represented by:

$$y_{DAS}[n] = \sum\nolimits_{j=1}^{M} w_j^* x_j[n] = \boldsymbol{w}^H \boldsymbol{x}[n] \tag{2}$$

where $*$ denotes the conjugate transpose, H denotes the Hermitian transpose, and w_j^* is the weight applied to element j in the DS beamformer, which is obtained as a constant vector from [21, 22]:

$$w_{DS}(n) = \frac{1}{M}\vec{1} \tag{3}$$

where M is the number of array elements. In (2), we define vector $\mathbf{x}[n]$ as $\boldsymbol{x}[n] = \left[x_1[n], x_2[n], \ldots, x_M[n]\right]^T$ and $\boldsymbol{w} = [w_1^*, w_2^*, \ldots, w_M^*]^T$.

In the SAFT method, each array element transmits a signal and receives the signal reflection from the same element. Therefore, the brightness intensity of each pixel in the image is calculated as follows [22]

$$I_{SAFT}(n) = \sum_{i=1}^{M} A_i(x_{si}, 2\tau_i) \tag{4}$$

where x_{si} is the longitudinal coordinate (the length) of the ith element, $A_i(.)$ is the pulse-echo response of the ith element, and τ_i is the time it takes for the signal to travel from the ith element to the point of interest, which is the location of a specified pixel in the ultrasonic image.

In the TFM method, each array element individually transmits a signal, and the signal reflection is received by all array elements [22]. As a result, the brightness intensity of each pixel in the image is calculated as follows:

$$I_{TFM}(n) = \sum_{i=1}^{M}\sum_{j=1}^{M} A_{i,j}\left(x_{si}, x_{rj}, \tau_i + \tau_j\right) \tag{5}$$

where x_{si} and x_{rj} are the longitudinal coordinates of the transmitting and receiving elements, respectively, $A_{i,j}(.)$ is the pulse-echo response received by the jth element and transmitted by the ith element, and τ_i and τ_j are the times traveled from the transmitting element i to the point of interest and from the point of interest to the receiving element j, respectively.

B. Delay-Multiply-and-Sum (DMAS) beamformer

In[16], an optimized total focusing method using the delay-multiply-and-sum (DMAS) approach was proposed. For a given point z in the imaging area, the focused signal relative to z in DMAS is described as follows:

$$I_{DMAS}(z) = \sum_{i=1}^{M-1}\sum_{j=i+1}^{M} sign\{S_i(z)S_j(z)\}\sqrt{\left|S_i(z)S_j(z)\right|} \tag{6}$$

Here, the sign function denotes the signum function extraction operation, and the signed square root calculation ensures that the amplitude of each multiplication term is correctly scaled to match the dimensionality of the echo signals. S_j is the result of all echo signals received by the j -th element, calculated as:

$$S_j(z) = \sum_{k=1}^{M} A_{k,j}\left(x_{sk}, x_{rj}, \tau_k + \tau_j\right) \tag{7}$$

where, similar to TFM, $\tau_k$and τ_j are the travel times from the transmitting element k to the point of interest and from the point of interest to the receiving element j, respectively.

C. MV beamformer

The MV beamformer updates the weight vector for each point in the image based on the received data, adjusting the weights in such a way that the maximum level of interference and noise is removed from the desired signal. The output of this beamformer is obtained from:

$$y_{MV}[n] = \sum\nolimits_{j=1}^{M} w_{jMV}^* x_j[n] = \boldsymbol{w}_{MV}^H \boldsymbol{x}[n] \tag{8}$$

where x_j is the delayed signal received by element j, and w_{jMV}^* is the weight applied to element j in the MV beamformer. This beamformer minimizes the output power while preserving the desired signal unchanged, as described by:

$$\min_{w_{MV}}\{w_{MV}^H[n]x[n]w_{MV}[n]\}\ subject\ to\ w_{MV}^H[n]a = 1 \tag{9}$$

where $\mathbf{a}$ is the steering vector towards the desired signal. Since $\mathbf{x}[n]$ has been previously delayed, $\mathbf{a}$ is a column vector of size $M \times 1$ consisting of unit values, i.e., $\mathbf{a} = [1,1,\dots,1]_M^T$. The objective is to find $\mathbf{w}[n]$ such that the expression $\mathbf{w}_{MV}^H[n]\mathbf{x}[n]\mathbf{w}_{MV}[n]$ is minimized and the value of the beamforming gain $\sum_j w_j[n]$ is equal to one. To this end, optimized weights are obtained using the following equation:

$$\boldsymbol{W}_{MV}[n] = \frac{\boldsymbol{R}^{-1}[n]\boldsymbol{a}}{\boldsymbol{a}^H\boldsymbol{R}^{-1}[n]\boldsymbol{a}} \tag{10}$$

where $\boldsymbol{R}[n]$ is the autocorrelation function of the output data of the phased array elements, obtained from:

$$\boldsymbol{R}[n] = E\{\boldsymbol{x}[n]\boldsymbol{x}^H[n]\} \tag{11}$$

in which $E\{.\}$ represents statistical averaging. To accelerate the algorithm in online implementation, instantaneous values of the vectors are used instead of averaging for calculating the autocorrelation function. Therefore, the instantaneous autocorrelation function is given by:

$$\boldsymbol{R}[n] \approx \boldsymbol{x}[n]\boldsymbol{x}^H[n] \tag{12}$$

The covariance matrix of the array is estimated from the measured signals using[23, 24]:

$$\boldsymbol{R}[n] = \sum_{j=1}^{M} x_j[n]x_j^H[n] + \delta\boldsymbol{I} \tag{13}$$

where the regularization term $\delta\boldsymbol{I}$ is used to increase numerical stability and robustness of the MV method, in which $\boldsymbol{I}$ is the identity matrix and δ is a small positive constant close to zero.

D. IMV beamformer

To reduce the computational complexity of the MV method while preserving its performance, and increase its robustness against correlation matrix inverse errors, the IMV beamformer has been proposed [7]. In this approach, weights are updated iteratively using the steepest descent method. Therefore, the final equation for obtaining the weight vector is as follows:

$$\begin{aligned}\boldsymbol{w}_{D+1}[n] = {} & [\boldsymbol{I} - \boldsymbol{a}(\boldsymbol{a}^H\boldsymbol{a})^{-1}\boldsymbol{a}^H][\boldsymbol{I} - \mu\boldsymbol{R}]\boldsymbol{w}_D[n] \\ & +\boldsymbol{a}(\boldsymbol{a}^H\boldsymbol{a})^{-1}\end{aligned} \tag{14}$$

where the index D indicates the number of repetitions, and μ represents the step size. Due to the fact that the received signal from one imaging point does not change significantly compared to the received signal from another nearby point, the initial weight ($\mathbf{w}_0[n]$) is adjusted based on the last weight vector found for the previous point (i.e., $\mathbf{w}_0[n] = \mathbf{w}[n-1]$). This approach accelerates convergence speed [7]. The step size μ is also set to the maximum available value, calculated as $\mu = \frac{2}{\mathrm{trace}(\mathbf{R})}$[25].

By using the termination criterion $||y_D[n]|^2 - |y_{D-1}[n]|^2|$, where $y_D[n]$ represents the output of the array in the Dth repetition, the changes in output power can be determined at each iteration. When this criterion is less than a predefined threshold through trial and error, the iteration is terminated [7].

III. The Proposed Method

In the proposed method, we aim to eliminate noise generated in ultrasonic imaging and obtain higher quality images by using wavelet transform and coherence weighting. Fig. 1 illustrates the overall block diagram of the proposed approach. As shown, after receiving signals from the ultrasonic phased array, appropriate delays are applied to the signals to focus the beam on a target point (which will form a pixel of the ultrasonic image). We then use the wavelet transform to remove noise from the delayed received signals. Specifically, the signals are decomposed using the wavelet, and then the noise is reduced or removed using the threshold function proposed in this paper.

Finally, the noise-free signal is reconstructed using the inverse wavelet transform on the modified coefficients. These denoised signals are then used to compute coherence weighting and beamforming for the target point. The calculated coherence coefficients are multiplied at the output of the beamformer, and the brightness intensity of the target pixel in the image is obtained. This process is repeated for all pixels in the image, and the information of each pixel is stored in a buffer to create the final image. In this proposed method, the resulting image not only reduces the background noise and speckles but also enhances the resolution and the ability to distinguish reflective points of the test piece from each other.

The steps of the proposed method are as follows:

I. Wavelet Packet Transform (WPT) is used to decompose the signal and a proposed thresholding method is applied to remove noise from the received signals.

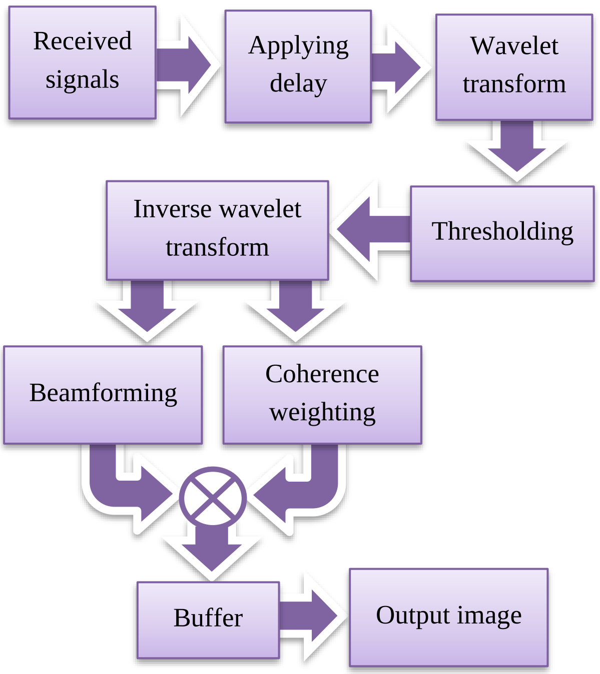

Fig. 1. Block diagram of the proposed method, illustrating the process from the received signals of the phased array to the output image construction.

II. Using the denoised signals and the optimization formula for weights in the TFM/MV/IMV methods, the ultrasound image of the under-test piece is obtained.

III. Using the denoised signals from the previous step, coherence weights are calculated for the image obtained by the beamformer.

IV. By applying the calculated coherence weights to the denoised beamformed image, an image with minimal noise is obtained.

The details of the wavelet transform and coherence weighting in the proposed method will be explained further.

A. *Wavelet Transform*

Removing Speckle and Gaussian noises using wavelet transform based on the fact that only a few wavelet coefficients contain the highest signal power, while the rest typically have low noise values, is feasible[26]. The wavelet transform performs noise reduction in three steps:

1) The signal is decomposed using various methods, one of which is the Wavelet Packet Transform (WPT). In this transform, the signal is divided into two parts: approximation and details, which respectively contain low-frequency and high-frequency information. The approximation part is successively decomposed into multiple stages with wavelet transform to obtain more details, and the details part is further divided into approximation and details at each level. This method provides high precision in signal reconstruction[27].
2) In this stage, the coefficients of the approximation and details parts are thresholded to remove coefficients that contain insignificant noise.
3) After thresholding the coefficients, the noise-reduced signal is reconstructed using the modified approximation and details coefficients through inverse wavelet transform.

The following effective threshold value for ultrasound signals has been applied as introduced in[28]:

$$T = \sqrt{\mu_j + k\sigma_j} \tag{15}$$

in which the parameter T represents the threshold value, μ_j denotes the mean value, and σ_j represents the standard deviation.

Two threshold functions, hard and soft, are commonly used for thresholding[29]. However, due to the issues these two thresholds create in signal reconstruction, we develop an alternative function to overcome the shortcomings of classical threshold functions. This alternative is based on the logistic function, which strikes a balance between the advantages and disadvantages of hard and soft thresholds.

The logistic function is a type of sigmoid function that is real-valued, bounded, and differentiable. It is defined for all real values, has a positive derivative for all its values, and is expressed by:

$$y = \frac{\alpha}{1 + e^{-\beta(x-\gamma)}} \tag{16}$$

in which, α represents the maximum value of the function, β determines the steepness of the curve, and γ specifies the center of the function. With the aid of this function, the improved threshold function is introduced. In this proposed improved threshold function, to ensure that coefficients' values are not zero for values smaller than the threshold level, the thresholding function is extended by incorporating the solution presented in[30]. This extension attenuates values between T and $-T$ instead of setting them to zero, as expressed by:

$$f(x)=\begin{cases} x - \left(\frac{T}{1+e^{-c(x-T)}}\right) & x > T \\ sgn(x)\left(\frac{|x|^d}{2T^{d-1}}\right) & |x| \le T \\ x + \left(\frac{T}{1+e^{-c(x+T)}}\right) & x < -T \end{cases} \tag{17}$$

where the parameter $c \ge 0$ controls the attenuation of values greater than the threshold level T and values smaller than $-T$, and the even parameter $d = 2k, k \in \mathbb{N}$ controls the attenuation of values between T and $-T$. In this threshold function, we have a better control over the impact of samples close to the threshold levels $\pm T$. If c and d tend to infinity, the threshold function behaves similarly to a hard threshold but remains continuous. This function possesses properties of continuity, uniformity, and differentiability over the entire domain interval $(-\infty, +\infty)$. The curves of the proposed function for $T = 3$ are shown in Fig. 2 for some values of c and d.

As shown in Fig. 2, when $c = 100$ and $d = 150$, the thresholding function behaves like a hard thresholding method. This means that wavelet coefficients within the range of (-3, +3) are set to zero, while those outside this range retain their values. Conversely, for smaller values of c and d, the function attenuates the magnitude of wavelet coefficients within the range of (-3, +3), with smaller coefficients being more heavily attenuated towards zero. For coefficients outside the range of (-3, +3), there is also attenuation, but the reduction in magnitude is less pronounced for larger coefficients. Specifically, when $c = 1$ and $d = 4$, the curves are smoothest, resulting in minimal attenuation for wavelet coefficients within the range of (-3, +3) and significant attenuation for those outside this range.

B. Coherence Weighting

The concept of coherence weighting was first introduced as the ratio between the coherence sum and the total addition of the signal magnitudes[31]. In order to minimize background noise and mitigate the effect of stray radiation in shaping different radiation patterns, coherence weighting can be employed. It is calculated according to the following equation[32]:

$$CF(s) = \left(\frac{|I(s)|^2}{M^2 \sum_{i=1}^{M} \sum_{j=1}^{M} \left| A_{i,j}\left(x_{si}, x_{rj}, \tau_i + \tau_j\right) \right|^2} \right)^{p_{cf}} \tag{18}$$

where $I(s)$ represents the intensity of each pixel in the image s, derived by the specified beamforming method, M is the number of elements in the array, x_{si} and x_{rj} represent the longitudinal coordinates of the transmitting and receiving elements, respectively. $A_{i,j}(.)$ signifies the pulse-echo response received by element j transmitted by element i, and τ_i and τ_j denote the time taken from the transmitting element i to the point of interest and from the point of interest to the receiving element j, respectively.

Additionally, p_{cf} (phase coherence factor) is the sensitivity factor, which governs the relationship between regions with different levels of coherence.

Multiplying the value of coherence weighting by the output images of the different beamformers results in their noise-removed images according to:

$$I_{CF}(x,y) = CF(x,y) I(x,y) \tag{19}$$

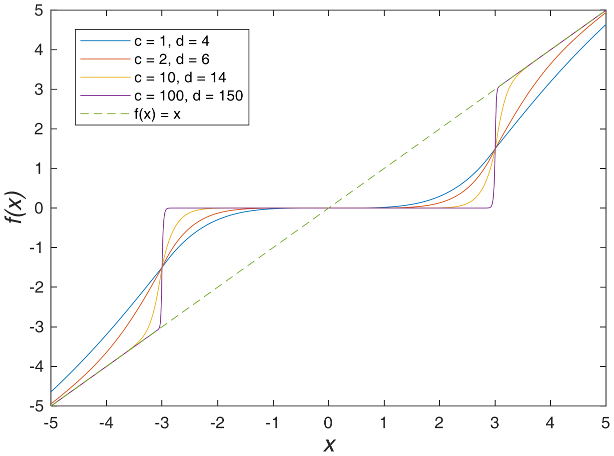

Fig. 2. The curves of the proposed thresholding function for various values of *c* and *d*.

where $CF(x,y)$ represents the coherence weighting, $I(x,y)$ denotes the image obtained from different beamformers, and $I_{CF}(x,y)$ is the denoised image.

In the proposed method, the WPT is utilized to decompose the signal using the effective threshold presented in (15) and the proposed threshold function using (17) to eliminate noise from the received signals. The signal decomposition levels are set to two, and the Daubechies wavelet of type 4 (db4) is employed for the ultrasonic signal. The beamformer weights are subsequently derived using (3), (10), and (14) for TFM, MV, and IMV, respectively, and the denoised image is generated. Using the denoised signals obtained in the previous stage and (18), the coherence weights are calculated. By applying the calculated weights to the denoised image generated by the specified beamformer, using (19), an image with minimal noise is obtained.

IV. Simulation and Experimental Results

The proposed method has been evaluated using simulation and experiments.

A. Simulation results

Simulation is conducted using MATLAB software. In the simulation, a steel specimen with dimensions of 75mm×50mm containing four point-defects, as depicted in Fig. 3, was tested. It is assumed in the simulations that there is no distance between the phased array and the steel specimen. Speckle noise with SNR=4 dB and Gaussian white noise with SNR=0dB have been added to the ultrasonic signals. To generate the speckle noise, we add some correlated extra peaks to the received signals of the phased array. These extra peaks are similar to the peaks of the actual reflections from defects. The simulation setup parameters are summarized in Table 1.

In our simulations, the values of c, d, and p_{cf} are determined empirically to achieve effective noise reduction from received ultrasonic phased array signals. The values of

TABLE 1 PARAMETERS OF SIMULATION SETUP

Material	Steel
Piece height (mm)	25
Number of array elements	16
Element pitch (mm)	2
Received signal type	5 cycles of modulated sinusoidal waveform
Probe frequency (MHz)	5
Sampling rate (MHz)	40
Speed of sound in steel (m/s)	3000
Image resolution (mm)	0.5
p_{cf}	4
c	5
d	30

other parameters are typically chosen to simulate realistic conditions.

To evaluate the performance of the beamformer, we utilize the following metrics:

1) Array Performance Index (API)

API is a dimensionless metric used to quantitatively compare the performance of array inspection methods in terms of their capability to detect and image reflector points[33]. A lower value of this index indicates better noise removal performance. API is computed giving:

$$API = \frac{A_{-6dB}}{\lambda^2} \tag{20}$$

where A_{-6dB} represents the area of the region where the value is at most, 6dB less than the maximum point, and λ denotes the wavelength of the ultrasonic signal.

2) Average Background Noise

Average noise (N_{avg}) is the mean intensity level of the pixels in the image corresponding to non-reflective points.

As N_{avg} decreases, the background brightness of the image decreases, leading to more accurate detection of reflective points.

3) Intensity Function

The intensity function is expressed as the normalized maximum intensity within the image depth range, obtained for each length x according to the following equation:

$$F(x) = 10\, log_{10}\left\{f(x)/\max_{x} f(x)\right\} \tag{21}$$

where the function $f(x)$ provides the maximum intensity level for each specified length x, thus $f(x) = \max_{z}\{I(x,y)\}$.

Based on the function $F(x)$, the separability of reflective points in the image from each other, the maximum attenuation level of the image for reflective points, and the average background noise level in the image are assessed [24].

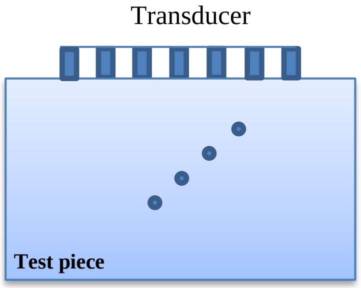

Fig. 3. The steel piece under test with four point-defects. The transducer, an ultrasonic phased array, is mounted directly over the piece.

Fig. 4 illustrates simulated images of TFM, DMAS, MV, and IMV beamforming methods without denoising (first column), with coherence weighting alone (second column), and the denoised images using the proposed wavelet thresholding along with coherence weighting (third column).

As observed in Fig. 4, applying coherence weighting alone to the beamforming methods has effectively increased image clarity to the extent that reflective points become more distinguishable from background noises. However, the amount of background noises is still high, which affect the image quality. As can be seen, the proposed method further enhances the image quality with lowering the background noises. Therefore, this approach exhibits a high capability in reflective point detection and background noise elimination. Particularly, in the IMV beamforming, it is clear through Fig. 4 that while coherence weighting alone reduces image noise substantially, our proposed denoising method enhances defect detection by producing brighter reflective points and lower background noise.

Fig. 5 depicts the intensity function for the TFM, MV, IMV, and DMAS methods in the noisy condition using (21). As evident in Fig. 5, in the presence of noise, IMV and DMAS methods present reflective points with higher discrimination compared to the other two methods. Additionally, Fig. 6 illustrates the intensity plots for the TFM, MV, IMV, and DMAS methods with the application of coherence weighting alone.

Comparing Fig. 6 with Fig. 5 demonstrates the positive impact of coherence weighting on the clarity of reflective points, the distinguishability of these points from each other, and significant background noise reduction. It is also noticeable that applying this weighting to these methods has led to the creation of more discriminated peaks in the intensity plot, indicating an enhanced ability to detect the reflective points.

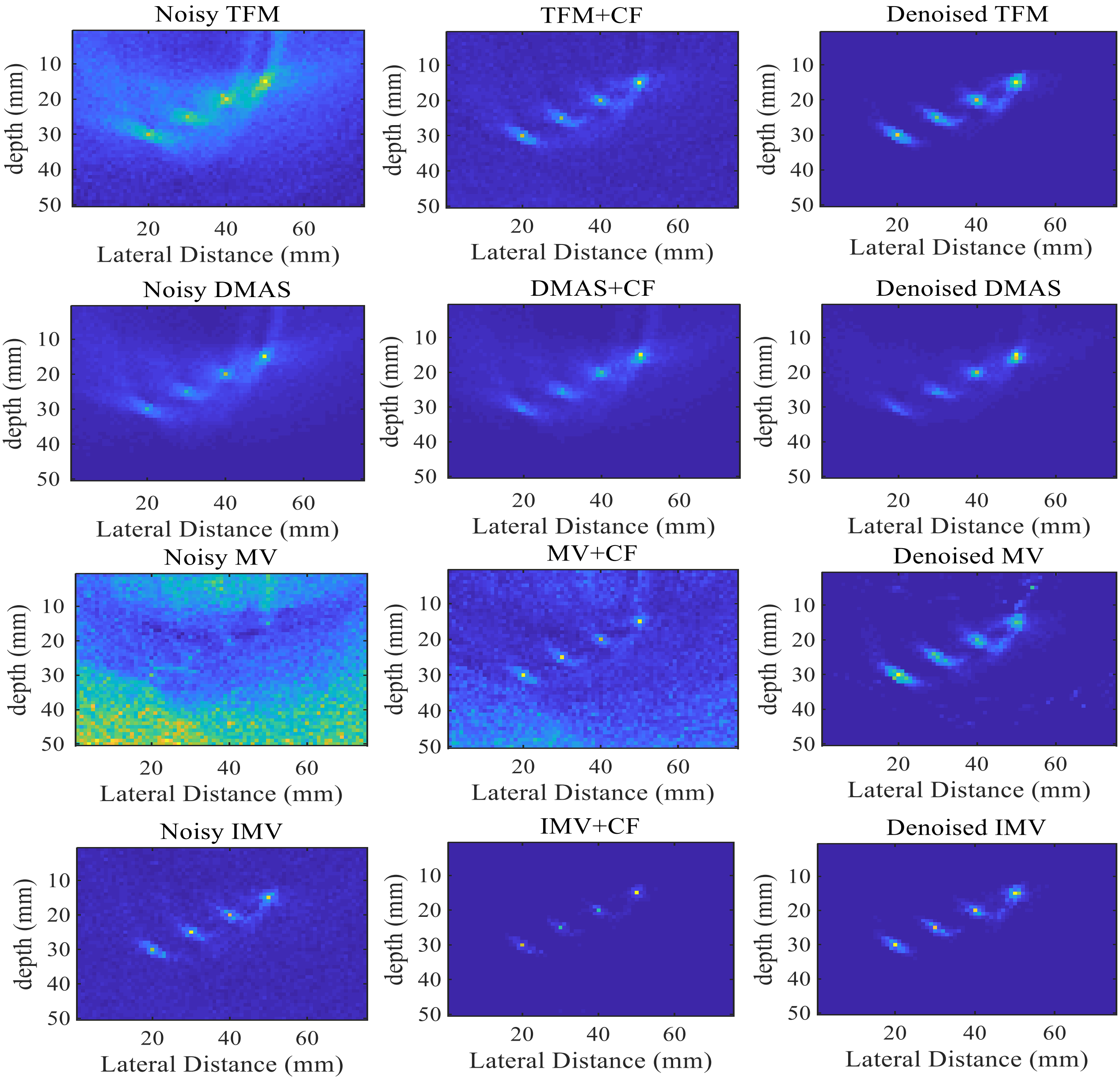

Fig. 4. Simulated images of TFM, DMAS, MV, IMV methods in three modes: Noisy mode (first column), Applying of coherence weighting alone (second column) and removal of noise by time thresholding and coherence weighting simultaneously (third column).

Fig. 7 displays the intensity plots of the proposed denoising methods. The increase in peak levels, representing the intensity of reflective points and the ability to detect defects, is well evident in the proposed methods.

It can be observed that the attenuation of peaks in this method is less than 1dB, whereas in the TFM method, this value is approximately 1.5dB, and the MV method has an attenuation of about 2dB. Additionally, with careful observation of this plot, we find that the depth of valleys between two peaks in the proposed method is lower compared to the other methods, indicating the superior ability to distinguish reflective points from each other.

Another notable point regarding the proposed denoised methods, is that background noise is reduced more than 5 dB for all of proposed beamforming methods, in comparison with their primary counterparts.

Table 2 presents the average noise level (N_{avg}), and the API metric values. It shows a reduction in API values in the proposed beamforming methods compared to the primary methods, which is considerable for TFM and MV.

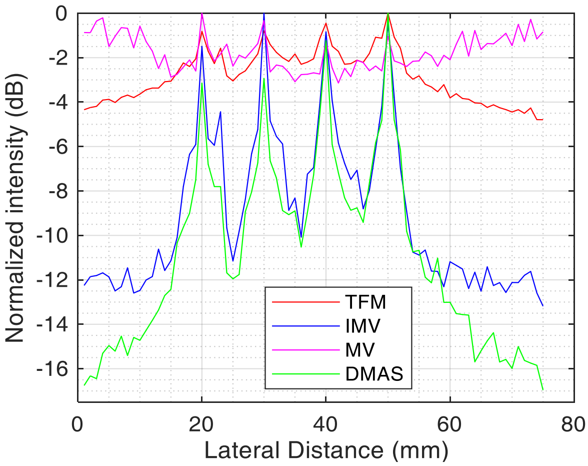

Fig. 5. Intensity function for TFM, MDAS, MV, and IMV in noisy conditions. IMV demonstrates superior noise reduction but exhibits more peak attenuation compared to the others.

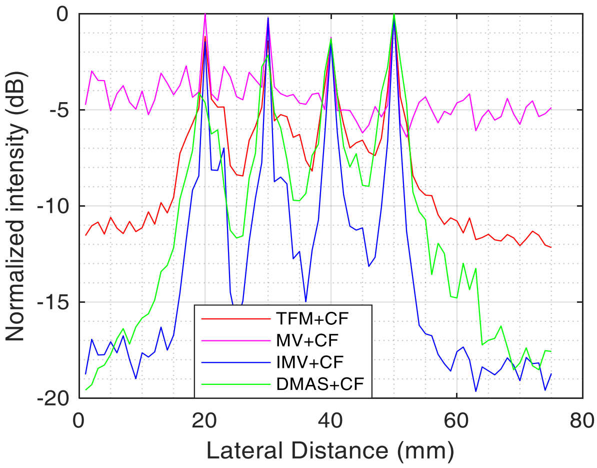

Fig. 6. Intensity function for TFM, DMAS, MV, and IMV with coherence weighting applied. IMV exhibits greater noise attenuation around the peaks, resulting in better peak distinguishing compared to the others.

Additionally, the average noise level has significantly decreased for all beamforming methods. Consequently, the proposed denoising approach has been able to demonstrate satisfactory performance in the removal of background Gaussian noise and speckle noise, while preserve the image quality of defects.

Furthermore, the performance of the proposed denoising method can be influenced by the value of p_{cf}. Table 3 shows API and N_{avg} values for four different p_{cf}. As p_{cf} increases, N_{avg} correspondingly decreases, and API slightly decreases, resulting in better resolution of reflective points. However, this improvement comes at the cost of peak attenuation, which reduces detectability for weak reflections. Moreover, computational complexity increases with higher p_{cf} values.

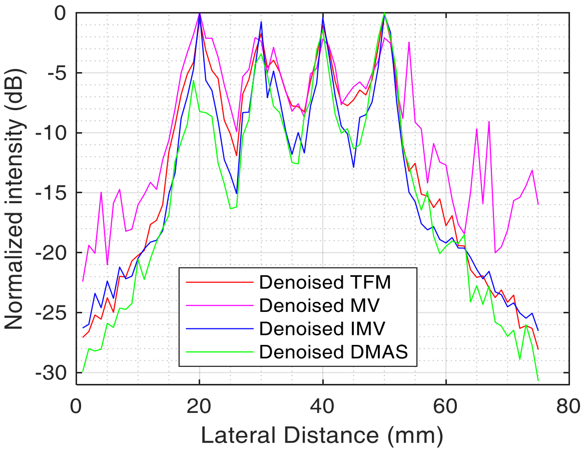

Fig. 7. Intensity function for TFM, DMAS, MV, and IMV with wavelet thresholding followed by coherence weighting. Denoised DMAS and Denoised IMV exhibit better noise attenuation than others, with Denoised IMV showing less peak attenuation compared to the others.

TABLE 2 AVERAGE BACKGROUND NOISE AND API FOR VARIOUS BEAMFORMING METHODS IN THE SIMULATION

	TFM	DMAS	MV	IMV
API	6.25	2.9	10.8	3
N_{avg}	-5.2 dB	-17.9 dB	-2 dB	-15.9 dB
	TFM+CF	DMAS+CF	MV+CF	IMV+CF
API	4.2	2.8	4.5	2.6
N_{avg}	-8.9 dB	-18.8	-7.4 dB	-19.4 dB
	Denoised TFM	Denoised DMAS	Denoised MV	Denoised IMV
API	3.8	2.8	4.8	2.9
N_{avg}	-15 dB	-23.9	-18.8 dB	-21.6 dB

TABLE 3 AVERAGE BACKGROUND NOISE AND API FOR DIFFERENT VALUES OF p_{cf} IN THE SIMULATION

p_{cf}		Denoised TFM	Denoised DMAS	Denoised MV	Denoised IMV
2	API	4.0	2.8	4.9	2.9
	N_{avg}	-12.5 dB	-23	-17.6 dB	-20.8 dB
4	API	3.8	2.8	4.8	2.9
	N_{avg}	-15 dB	-23.9	-18.8 dB	-21.6 dB
8	API	3.5	2.6	4.7	2.6
	N_{avg}	-18.6 dB	-29	-19.8 dB	-26.1 dB
12	API	3.4	2.4	4.6	2.3
	N_{avg}	-22.4 dB	-33.2	-21.1 dB	-31.2 dB

B. *Experimental results*

For the experiment, a phased array probe of model Olympus with 16 linear elements at a frequency of 7.5 MHz is used, mounted on a Rexolite wedge with the angle of 38.5 degrees[34]. The element pitch of the transducer is 0.5 mm. The width of the applied pulses is half the period of the probe, which equals 67 ns, and the amplitude of the applied pulse is 50 volts. The test piece is a cylindrical steel tube with a diameter of 60 mm and a thickness of 15 mm. The pulses received from the piece are sampled at a rate of 40 MHz. Fig. 8 shows the experimental setup.

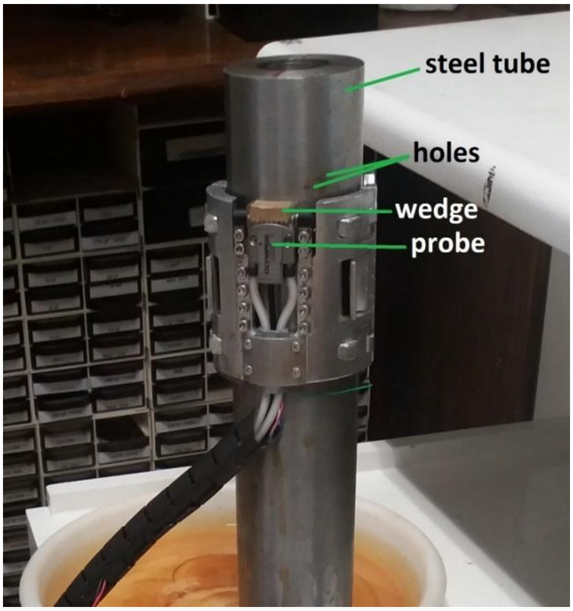

Fig. 8. The experimental setup, constructed by Niroo Research Institute (NRI) [34].

In the experiment, two small through-holes perpendicular to the axis of the steel tube at depths of 5 mm and 9 mm, each with a diameter of 0.8 mm, are provided as shown in Fig. 8. In this setup, due to the placement of the probe on the wedge, the ultrasonic waves are emitted and reflected obliquely. These waves, after passing through the wedge and entering the steel piece, are mainly transverse waves with a speed of about 3250 m/s. In this test, the lateral distance between the probe wedge and holes relative to the tube surface is 25 mm.

Figs. 9-a to 9-h show the images obtained from beamforming methods based on TFM (first row), DMAS (second row), MV (third row), and IMV (fourth row). The images in the left column show the classical methods, while the right column shows the denoised methods. The amounts of c, d, and p_{cf} are determined as before. It can be observed that in all images, the images of two holes are seen as bright spots, with their centers at depths corresponding to the locations of the holes in the steel tube. The bright areas in these images indicate background noise and speckles, which are due to the presence of noise in the signals received by the phased array and the limitations of the beamforming methods to mitigate the background noise.

It is observed that the hole images in the figures appear elongated, which is due to the significant lateral distance between the holes and the wedge compared to the length of the phased array.

According to Fig. 9, the background noise appeared in all the beamforming methods with considerable brightness, which lead to a possibility of detecting false defects, especially in the TFM and MV methods.

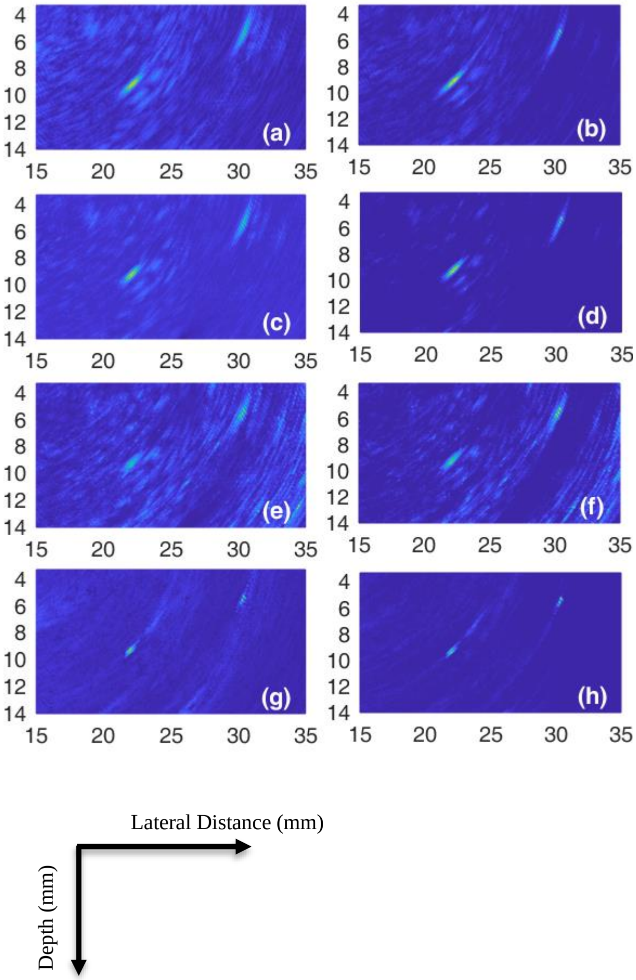

Fig. 9. The experimental images of TFM (a), Denoised TFM (b), DMAS (c), Denoised DMAS (d), MV (e), Denoised MV (f), IMV (g), Denoised IMV (h). The background noise and speckles in the proposed denoising method (the right column) are considerably less than the original images (the left column).

In the IMV and DMAS methods as shown in Fig. 9, the noise is somewhat reduced, and in IMV, the elongation of the holes reduces considerably. In the proposed denoising methods in the right column of Fig. 9, it is observed that the background noise and false reflections are significantly lower than in the counterpart methods, thereby improving the clarity of the hole images.

Table 4 presents the average background noise for the experiment. It shows a significant reduction in N_{avg} values in the proposed beamforming methods compared to the counterparts.

C. Discussion

In this study, we propose a solution to reduce background noise and speckles in phased array-based ultrasonic imaging. Our method has two main contributions: (i) denoising the phased array received signals using a novel wavelet-based thresholding technique, and (ii) applying a coherence

TABLE 4 AVERAGE BACKGROUND NOISE LEVELS FOR VARIOUS BEAMFORMING METHODS IN EXPERIMENT

	TFM	DMAS	MV	IMV
N_{avg}	-12.6 dB	-19	-10 dB	-15.4 dB
	Denoised TFM	Denoised DMAS	Denoised MV	Denoised IMV
N_{avg}	-17.4 dB	-26.6	-16.2 dB	-20.5 dB

weighting derived from the denoised signals to the output signal of the beamformer to construct the denoised images. We evaluated the proposed method on various ultrasonic beamforming techniques, including TFM, DMAS, MV, and IMV, through both simulations and experiments.

Fig. 4 qualitatively demonstrates that the combination of wavelet thresholding and coherence weighting significantly reduces background noise and speckles in beamforming techniques, while preserving the quality of reflective points. As a result, reflective points become more distinguishable in the images. The intensity functions illustrated in Figs. 5, 6, and 7 quantitatively confirm that reflective points are more discriminative after applying the proposed denoising method, consistent with the qualitative results from Fig. 4.

Additionally, the results show that DMAS and IMV provide better discrimination of reflective points and noise reduction compared to TFM and MV in both noisy and denoised versions. According to Table 2, the background noise is reduced by more than 5 dB across all beamforming methods when using the proposed denoising method, compared to their primary counterparts. Moreover, the API in the proposed denoised beamforming methods is slightly lower than in the primary counterparts, indicating improved image resolution with the proposed method.

In experiments, as shown in Fig. 9 and Table 4, the background noise is significantly lower with the proposed denoising methods than with the counterpart methods, which is consistent with the simulation results. Furthermore, Fig. 9 qualitatively shows a substantial reduction in false reflections caused by speckles in the proposed denoising methods, thereby enhancing the clarity of the holes in ultrasonic images.

V. Conclusions

In this study, we introduced a noise-robust beamforming technique aimed at reducing the speckle and background noises in ultrasonic imaging, while preserving the quality of reflective echoes. Our approach involved the utilization of a novel wavelet thresholding method on the input signals of the phase array, alongside the generation of images through total focusing method (TFM), delay-multiply-and-sum (DMAS), minimum variance (MV), and iterative MV (IMV) beamforming techniques. Subsequently, coherence weighting was derived from the denoised signals and integrated into the beamforming process to construct the denoised images. This proposed methodology not only effectively mitigates background noise but also enhances defect detection and improves the differentiation among reflective points, consequently elevating the quality and clarity of ultrasonic images.

REFERENCES

[1] J. Park, S. M. Wi, and J. S. Lee, "Computationally efficient adaptive beamformer for ultrasound imaging based on QR decomposition," *IEEE Transactions on ultrasonics, Ferroelectrics, and frequency control,* vol. 63, no. 2, pp. 256 - 265, 2016.

[2] J. Lambert, A. Pédron, G. Gens, F. Bimbard, L. Lacassagne, and E. Iakovleva, "Performance evaluation of total focusing method on GPP and GPU," *Conference on Design and Architectures for Signal and Image Processing,* pp. 1-8, 2012.

[3] L. P. Piedade, G. Painchaud-April, and P. B. A. Le Duff, "Minimum transmission events for fast ultrasonic TFM imaging: A comparative study," *NDT & E International,* vol. 128, 2022.

[4] T. Stepinski and F. Lingvall, "Synthetic aperture focusing techniques for ultrasonic imaging of solid objects," *8th European Conference on Synthetic Aperture Radar,* pp. 438-441, 2010.

[5] S. M. Sakhaei, "A decimated minimum variance beamformer applied to ultrasound imaging," *Ultrasonics,* vol. 59, pp. 119-127, 2015.

[6] A. M. Deylami and B. M. Asl, "A fast and robust beamspace adaptive beamformer for medical ultrasound imaging," *IEEE Transactions on Ultrasonics, Ferroelectrics, and Frequency Control,* vol. 64, no. 6, pp. 947-958, 2017.

[7] A. M. Deylami and B. M. Asl, " Iterative minimum variance beamformer with low complexity for medical ultrasound imaging," *Ultrasound in Medicine & Biology,* vol. 44, pp. 1882-1890, 2018.

[8] B. M. Asl and A. M. Deylami, "A low complexity minimum variance beamformer for ultrasound imaging using dominant mode rejection," *Ultrasonics, v*ol. 85, pp. 49-60, 2018.

[9] A. S. Vaidya and M. B. Srinivas, "A low-complexity and robust minimum variance beamformer for ultrasound imaging systems using beamspace dominant mode rejection," Ultrasonics, vol. 101, 2020.

[10] J. Pan, Y. Wang, Y. Wang, Z. Han, C. Zheng, and H. Peng, "Adaptive spatial smoothing-based minimum variance beamforming using signal coherence to improve image quality," IEEE International Ultrasonics Symposium (IUS), 2022.

[11] A. M. Deylami and B. M. Asl, "High resolution minimum variance beamformer with low complexity in medical ultrasound imaging," Ultrasound in Medicine & Biology, vol. 45, no. 10, pp. 2805-2818, 2019.

[12] Z. Shen, J. Li, and Q. Wu, "A fast adaptive beamformer with sidelobe control based on gradient descent ascent," Signal Processing, vol. 206, p. 108906, 2023.

[13] K. Ji, P. Zhao, C. Zhuo, H. Chen, J. Wang, and J. Fu, "High-accuracy ultrasonic imaging of the defects in the complex-surface components by the search-vector imaging condition," Mechanical Systems and Signal Processing, vol. 216, 2024.

[14] J. Wu, H. Hu, Y. Song, P. Ni, and X. Li, "Ultrasonic phased array imaging of multi-layered structures using full-matrix

migration and normalized cross-correlation matching technique," NDT & E International, vol. 145, 2024.
[15] Z. Zhao, L. Liu, W. Liu, D. Teng, Y. Xiang, and F. Z. Xuan, "Discretized tensor-based model of total focusing method: A sparse regularization approach for enhanced ultrasonic phased array imaging," NDT & E International, vol. 141, 2024.
[16] D. Teng, L. Liu, Y. Xiang, and F. Z. Xuan, "An optimized total focusing method based on delay-multiply-and-sum for nondestructive testing," Ultrasonics, vol. 128, 2023.
[17] N. Molinier, G. Painchaud-April, A. L. Duff, M. Toews, and P. Bélanger, "Ultrasonic imaging using conditional generative adversarial networks," Ultrasonics, vol. 133, 2023.
[18] H. Yang, J. Shu, S. Li, and Y. Duan, "Ultrasonic array tomography-oriented subsurface crack recognition and cross-section image reconstruction of reinforced concrete structure using deep neural networks," Journal of Building Engineering, vol. 82, 2024.
[19] G. Granados, R. Miorelli, F. Gatti, S. Robert, and D. Clouteau, "Towards a multi-fidelity deep learning framework for a fast and realistic generation of ultrasonic multi-modal Total Focusing Method images in complex geometries," NDT & E International, vol. 139, 2023.
[20] A. Ghaedi, R. Sedaghati, M. Mahmoudian, and S. Bazyari, "De-noising of partial discharge signals in HV XLPE cables by reference noise based on the wavelet transform," International Journal of Industrial Electronics Control and Optimization, vol. 6, no. 4, pp. 291-306, 2023.
[21] A. M. Deylami and B. M. Asl, "Improving the coherence coefficient resistance in ultrasonic beamforming," Twenty-Third Iranian Conference of Electrical Engineering, Sharif University of Technology, May 2015.
[22] J. Lester and W. Schmmer, "Fundamentals of ultrasonic phased arrays," Springer, 2014.
[23] M. Bekrani and V. Hamiyati-Vaghef, "An improved method for ultrasound imaging in weld inspection," Iranian Journal of Electrical and Electronic Engineering, vol. 17, no. 1, pp. 45-59, 2020.
[24] M. Bekrani, "Phased array ultrasonic imaging using improved total focusing method based on beamforming in non-destructive test," Journal of Welding Science and Technology of Iran, vol. 6, no. 1, pp. 115-132, 2020.
[25] B. Widrow and S. D. Stearns, "Adaptive signal processing," Prentice-Hall,1985.
[26] G. O. Y. M . Misiti, and J. M. Poggi, "Wavelets and their applications," John Wiley & Sons, 2013.
[27] F. Ping and L. Xinbao, "An improved denoising method for ultrasonic echo of non-destructive evaluation," IEEE International Conference on Anti-counterfeiting, Security, and Identification (ASID), 2016.
[28] R. S. V. Matz, S. Starman, and M. Kreidl, "Signal-to-noise ratio enhancement based on wavelet filtering in ultrasonic testing," Ultrasonics, vol. 49, pp. 752-759, 2009.
[29] D. L. Donoho, "De-noising by soft-thresholding," IEEE Transactions on Information Theory, vol. 41, no. 3, pp. 613-627, 1995.
[30] T. F. Sanam and C. Shahnaz, "Noisy speech enhancement based on an adaptive threshold and a modified hard thresholding function in wavelet packet domain," Digital Signal Processing, vol. 23, pp. 941-951, 2013.
[31] J. Camacho, M. Parrilla, and C. Fritsch, "Phase coherence imaging," IEEE Transactions on Ultrasonics, Ferroelectrics, and Frequency Control, vol. 56, no. 5, pp. 958-974, 2009.
[32] B. K. G. R. Baiotto, C. Nageswaran, and T. Clarke, " "Coherence weighting applied to FMC/TFM data from austenitic CRA clad lined pipes," Journal of Nondestructive Evaluation, vol. 37, no. 49, 2018.
[33] B. W. D. C. Holmes and P. D. Wilcox, "Post-processing of the full matrix of ultrasonic transmit–receive array data for non-destructive evaluation," NDT & E International, vol. 38, pp. 701-711, 2005.
[34] M. Bekrani and V. Hamiyati-Vaghef, "A new method for designing and implementation of NDT weld inspection of boiler tubes using ultrasonic phased array," Electronics Industries, vol. 12, no. 4, pp. 39-51, 2022.

Mozhgan Ehsani was born in Tehran, Iran. She received her Bachelor's degree in Electrical and Electronics Engineering in 2015 and her Master's degree from Qom University of Technology, Qom, Iran, in 2023. From 2019 to 2020, she worked as a designer at Matin Electronic Company. Her research has focused on ultrasound waves, with current interests in the development of ultrasonic beamformers.

Mehdi Bekrani received his B.Sc. degree in Electrical Engineering from Ferdowsi University of Mashhad, Iran, in 2002, and earned his M.Sc. and Ph.D. degrees in Electrical Engineering from Tarbiat Modares University, Tehran, Iran, in 2004 and 2010, respectively. From 2010 to 2012, he was a Research Fellow at Nanyang Technological University, Singapore. He then joined the Department of Electrical and Computer Engineering at Qom University of Technology, Qom, Iran, as an Assistant Professor and currently serves as an Associate Professor. His research interests focus on adaptive signal processing and its applications.

Solyman Garousi was born in Tehran, Iran, in 1991. He earned his Bachelor's degree in Electronics Engineering from Islamic Azad University, Karaj Branch, Alborz, Iran, in 2016, and his Master's degree in Electronics Engineering from Qom University of Technology in 2019. Since 2019, he has been a researcher at the Iran Electronics Technology Institute in Tehran, Iran. His research interests include audio and ultrasonic signal processing, navigation and communication signal processing, and image processing.